

PREDICTING BEHAVIOR OF FLEXIBLE PAVEMENTS WITH
GRANULAR BASES

A Thesis
Presented to
The Academic Faculty

by


Erol Tutumluer

In Partial Fulfillment
of the Requirement for the Degree
Doctor of Philosophy in Civil Engineering


Georgia Institute of Technology
September 1995

PREDICTING BEHAVIOR OF FLEXIBLE PAVEMENTS WITH
GRANULAR BASES

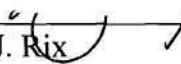
Approved:




Dr. Richard D. Barksdale




Dr. Paul W. Mayne



Dr. Glenn J. Rix



Dr. Gary R. Schmertmann



Dr. Charles E. Ueng

Date Approved By Chairperson 8/1/95

ACKNOWLEDGMENTS

I am deeply grateful to my advisor Professor Richard D. Barksdale for his constant support, valuable guidance and inspiration during the course of this research. I am fortunate to have had the opportunity of learning from him during my studies at Georgia Tech. I greatly appreciate his advice, encouragement, and guidance which made possible the completion of this dissertation. My very special thanks go to him for also the personal support his family gave me during the last four years.

I would like to thank the members of my graduate thesis committee, Dr. Paul W. Mayne, Dr. Glenn J. Rix, Dr. Charles E. Ueng, and Dr. Gary Schmertmann, for their contribution and helpful advice. The constant professional support on finite elements provided by Dr. Kenneth (Mac) Will is greatly appreciated. My special thanks go to Dr. Paul H. Wright who served in my advisory committee. I am also thankful to Dr. J. David Frost and Dr. Emir Macari for their help and valuable suggestions during the last two years at Geosystems Department.

It would have been impossible to even come this far without the friendship of the fellow graduate students: Dr. Barry S. Chen, Dr. Jorge L. Alba, Dr. Kevin Sutterer, Dr. Dayakar Penumadu, Dr. Roger Meier, Dr. Ronaldo Luna, Dr. Chun-Yi Kuo, Doug Brown, Pedro Arduino, Haroon Shami, Susan Burns, Wesley Spang, Carlo Lai, Gilberto

(Genco) D'Andria, my officemate Jie Han, and many others who I could not name here. They will always be remembered for the good time spent together. My special thanks go to the professional staff of the geotechnical group: Ken Thomas, Larry Westbrook, Vicki Clopton, and Seph Scott for their assistance and friendship.

I am very thankful to my Turkish friends who made me feel Atlanta as my home town during the last four years. Among them Selcuk Cimentalay, Ozgur Misman, Ismail and Sinan Lazoglu, Namik and Meral Ciplak, Ekrem and Eda Sabuncuoglu, and many others provided me with personal support and friendly advice. I will always appreciate the sincere support of my girlfriend Gunes Erdogan during the writing stages of this thesis.

Finally, and the most importantly, I would like to thank my parents Kemal and Sabahat Tutumluer for their consistent love and support. I am deeply indebted to them and my sister for all that they have done for me during my life.

TABLE OF CONTENTS

ACKNOWLEDGMENTS	iii
TABLE OF CONTENTS	v
LIST OF TABLES	viii
LIST OF ILLUSTRATIONS	ix
SUMMARY	xiv
CHAPTER	
I. INTRODUCTION	1
Statement of the Problem	1
Resilient Behavior	4
Outline of Thesis	5
II. REVIEW OF THE LITERATURE	9
Introduction	9
Theoretical Background	11
One-Layer Approach	13
Elastic Multi-Layered Theory	15
Linear Elastic Computer Programs	17
Resilient Material Characterization Models	19
Granular Materials	22
Subgrade Soils	41
Nonlinear Analysis	45
Summary	54
III. MODELING OF GRANULAR BASES	56
Introduction	56
Residual Stresses	59
Continuum Approach	66
Micromechanics Based Continuum Solutions	71

No Tension Analysis	72
Cross-Anisotropy Under Axial Symmetry	79
Summary	84
IV. NEURAL NETWORK MODELING OF RESILIENT MODULUS	85
Introduction	85
Background on Neural Networks	87
Literature Review: Material Modeling Using Neural Networks	95
Modeling Resilient Modulus of Granular Materials	97
Repeated Load Triaxial Tests	97
ANN Model	99
Validation Analysis	105
Summary	109
V. FINITE ELEMENT FORMULATIONS	111
Introduction	111
Isoparametric Eight Node Quadrilateral Element	113
Loading	125
Stress Computations	128
Six Node Interface Element	129
Stiffness Formulation	133
Summary	141
VI. COMPUTER CODE ORGANIZATION AND CAPABILITIES	142
General Description	142
Overview	143
GT-PAVE Program Organization	147
Nonlinear Analysis	153
Nonlinear Solution Technique	154
No Tension Modifications	165
Limitations of the Computer Code	175
Summary	177
VII. APPLICATIONS OF THE COMPUTER CODE	179
Introduction	179
Verification of the Computer Code	180
Example 1: Stress Distribution Boussinesq Type Problem	181
Example 2: Isotropic Three Layer System	184
Example 3: Cross-Anisotropic Three Layer System	189
Example 4: Modeling of Repeated Load Triaxial Tests	191
Effects of Compaction Induced Residual Stresses	196
Full-Scale Pavement Resilient Response Predictions	200

Georgia Tech Full-Scale Pavement Test Study	200
Modeling of the Pavement Test Sections	206
Test Section Resilient Response Predictions	211
Practical Design Considerations of Inverted Sections	217
Cost Comparison Analysis	221
Summary	227
VIII. NO TENSION ANALYSIS USING THE BLOCK MODEL	229
Introduction	229
Literature Review: Discrete Particle Approach	230
Load Transfer in Granular Materials	234
Block Model	238
Organization of Interface Elements in the Computer Code	243
Interface Behavior and Iterative Procedure for Equilibrium	249
The Block Model Iterative Equilibrium Procedure	257
Verification of Interface Elements	259
Example 1: Boussinesq Type Problem	259
Applications of the Block Model	263
Interface Properties	264
Example 2: Sliding Block Example	265
Example 3: Georgia Tech Conventional Test Sections	271
Summary	284
IX. CONCLUSIONS AND RECOMMENDATIONS	286
Conclusions	286
Practical Findings	291
Recommendations for Future Work	293
APPENDICES	
A. RESILIENT MODULUS DATA FOR POTENTIAL ARTIFICIAL NEURAL NETWORK VARIABLES	295
B. GT-PAVE NONLINEAR FINITE ELEMENT PROGRAM	303
Input and Output Capabilities	303
REFERENCES	308
VITA	321

LIST OF TABLES

Table

4.1	Mean Squared Errors Calculated Using Different Network Architectures After 10,000 Training Epochs	101
5.1	Shape Functions and Their Derivatives for the Eight Node Element	119
7.1	The Geometry and Performance Summary of Georgia Tech Pavement Test Sections (after Barksdale and Todres, 1983)	201
7.2	Aggregate Gradations and Material Properties Used in Flexible Pavement Test Sections	203
7.3	Detailed Summary of Resilient Test Section Response	205
7.4	Material Properties and Model Parameters Used in Modeling Pavement Test Section Response	209
7.5	Comparison of Predicted and Measured Response Variables	219
A.1	Georgia Tech Resilient Modulus Data For Potential ANN Variables	296
A.2	SHRP Resilient Modulus Data For Potential ANN Variables	298
A.3	North Carolina Resilient Modulus Data For Potential ANN Variables	301

LIST OF ILLUSTRATIONS

Figure

2.1	Generalized Multilayered Elastic System in Cylindrical Coordinates Under Axial Symmetry	12
2.2	Average Stress States in Aggregate Base for Use in Cyclic Testing for Light, Medium, and Heavy Pavements (after Barksdale and Itani, 1989)	20
2.3	Test Results and Predicted Behavior Using K- θ Model for A Dense Graded Aggregate (after Uzan, 1985)	24
2.4	Contour Model Cambridge q-p Stress Space (after Brown and Pappin, 1981)	27
2.5	Comparison of Contour Model with the K- θ Model (after Sweere et al., 1987)	29
2.6	Comparison of Test Results and Predicted Behavior Using Uzan Model for A Dense Graded Aggregate (after, Uzan, 1985)	31
2.7	Comparison of Predicted Resilient Modulus Behavior of Crushed Stone Using Brown's Model and Uzan's Model (after Uzan, 1985)	32
2.8	General Relationship Between Resilient Modulus and Deviator Stress for Fine-Grained Soils	43
3.1	Typical Granular Material Behavior Under Repeated Applications of Axial Deviator Load (after Jouve et al., 1987)	58
3.2	Schematic Representation of Stress Path During Compaction (after Uzan, 1985)	62
3.3	Distribution with Depth of Base and Subbase Moduli Under A Wheel Load (after Uzan, 1985)	64
3.4	The Three-Dimensional Continuum Model	68

3.5	Radial Tensile Stress and Vertical Pressure at the Bottom of Base As A Function of Modular Ratio (after Heukelom and Klomp, 1962)	74
3.6	Mohr-Coulomb Stress Modification for A No Tension Failure Condition (Zeevaert, 1980)	76
3.7	Stratified Anisotropic Material Under Axial Symmetry	81
4.1	A Typical Back-Propagation Neural Network	89
4.2	Summation and Transfer Functions of A Typical Artificial Neuron	90
4.3	Training Progress and Predicted Results for 6-5-5-1 Network	103
4.4	ANN Predictions of Resilient Modulus for Materials with Varying Stress Levels	104
4.5	Comparison of ANN Model Predictions with Uzan and UT-Austin Models	106
4.6	Computed Moduli Compared with Measured Values for A Sample Having Newly Introduced Material Property Set to the ANN Model	108
5.1	Finite Elements Used in the Model in Global Coordinates	114
5.2	Eight Node Isoparametric Quadrilateral Ring Element with Quadratic Displacements of Boundaries	116
5.3	Third Order Gauss Integration Point Locations in the Eight Node Quadrilateral Element	124
5.4	Six Node Interface Element	131
5.5	Uniform Load k Applied at the Boundary of An Eight Node Isoparametric Element with Unit Displacement Shown at Node 1	134
6.1	Flow Diagram of GT-PAVE Finite Element Program	148
6.2	Flow Diagram of QUADSTF Element Stiffness Subroutine	150
6.3	Flow Diagrams of SHAPE and EDGE Subroutines	151

6.4	Secant Modulus Approach for Newton-Raphson Scheme	156
6.5	Secant Newton-Raphson Scheme for the Hardening Granular Material Behavior	159
6.6	Resilient Modulus Search Technique Using Secant Stiffnesses for Flexible Pavements	160
6.7	Flow Diagram of NONLIN Nonlinear Analysis Subroutine	164
6.8	Effect of Principal Stress Rotation on the Computed Vertical Modulus	166
6.9	Horizontal Tension Zone in the Base As Predicted by Isotropic Linear Elastic Solution	168
6.10	Horizontal Tension Zone in the Base As Predicted by Cross-Anisotropic Linear Elastic Solution	169
6.11	Flow Diagram of Tension Modification Subroutine	172
7.1	Finite Element Mesh for the Boussinesq Type Problem	182
7.2	GT-PAVE FEM Stress Predictions for the Boussinesq Type Problem	183
7.3	Three-Layer Isotropic System Problem on Semi-Infinite Halfspace	185
7.4	GT-PAVE FEM Stress Predictions at Centerline for the Isotropic Three-Layer Problem	187
7.5	GT-PAVE Stress Predictions at 5 in. Radial Distance for the Isotropic Three-Layer Problem	188
7.6	GT-PAVE FEM Stress Predictions at Centerline for the Cross-Anisotropic Three-Layer Problem	190
7.7	Axisymmetric Finite Element Mesh Used to Model Repeated Load Triaxial Tests on Granular Materials	192
7.8	Comparisons of the GT-PAVE Nonlinear Resilient Response Predictions with the Measured Experimental Results	195

7.9	The Effect of Compaction Induced Residual Stresses on the Predicted Centerline Radial Stresses	199
7.10	Typical Cross Sections of Pavement Test Sections	207
7.11	Vertical Stiffnesses Predicted for the Conventional Sections	214
7.12	Predicted Vertical Stress Distribution on the Centerline of Loading	216
7.13	The Variation of Radial Tensile Stresses Throughout the Unstabilized Aggregate Base and Cement Stabilized Subbase in Section 12	218
7.14	The Variations of Horizontal Tensile Strain in AC and Vertical Stress on Subgrade with Base Thickness in Section 11	220
7.15	The Variation of Horizontal Tensile Strain at the Bottom of AC with AC Thickness	222
7.16	The Variation of Horizontal Tensile Stress Beneath the Centerline at the Bottom of Cement Stabilized Subbase with Subbase Thickness	222
7.17	Equal Cost Inverted and Conventional Field Section Constructions	224
7.18	Predicted Performance of the Equal Cost Inverted and Conventional Field Sections	225
7.19	Predicted Fatigue Performance of the Equal Cost Inverted and Conventional Field Sections	225
8.1	Contact Forces for Two-Dimensional Numerical Simulation - Anisotropic Loading (after Dobry et al., 1989)	236
8.2	Deformation of the Base Layer	237
8.3	Load Transfer in the Base Layer	237
8.4	Base Layer As A Set of Coupled Springs (after Allaart, 1992)	238
8.5	Granular Base Consisting of Blocks of Granular Particles Interacting Through Normal and Shear Springs	240

8.6	The Block Model Representation of the Granular Layers in the Finite Element Mesh: Example 2	244
8.7	Flow diagram of INTSTIF Element Stiffness Subroutine	245
8.8	Flow Diagram of INTSTRES Interface Element Stress Subroutine	248
8.9	Interface Behavior with Relative Displacements and Stresses	250
8.10	Algorithm for the Selection of Interface Behavior Mode and Computation of Balancing Forces	253
8.11	Finite Element Mesh with Interface Elements Used in the Middle 8.0 in. (203 mm) Zone: [Examples 1 and 3]	261
8.12	Interface Element Stress Predictions for the Boussinesq Type Problem	262
8.13	Interpretation of Element Normal and Shear Stresses in r-z Plane	268
8.14	Example 2: Deformed Mesh and the Variation of Interface Shear Stresses Throughout the Middle (Base) Layer for Loading Condition 1	270
8.15	Example 2: Deformed Mesh and the Variation of Interface Shear Stresses Throughout the Middle (Base) Layer for Loading Condition 2	272
8.16	Example 3: The Variation of Radial Stresses In the Crushed Stone Base - Nonlinear Analysis Using Elastic Continuum Approach	274
8.17	Example 3: The Variation of Radial Stresses Obtained from the Vertical Interface Elements in the Crushed Stone Base	276
8.18	Example 3: The Variation of Vertical Stresses Obtained from the Horizontal Interface Elements in the Crushed Stone Base	277
8.19	Example 3: The Variation of Interface Shear Stresses Obtained from Interface Elements in the Crushed Stone Base	279
8.20	Frictional Shear Resistance Under Normal Stress in A Three-Grain Assembly	280
8.21	Example 3: Comparison of Radial Tension Forces in the Base from Elastic Continuum and Block Models	282

SUMMARY

A theoretical and analytical study has been undertaken in this thesis to develop an improved analysis method for calculating the performance of flexible pavements with granular bases. A finite element program named GT-PAVE has been developed to predict the resilient response of flexible pavements. The program accounts for: 1) material nonlinearity due to the stress dependent nature of pavement materials, 2) cross-anisotropic behavior observed in granular bases, 3) horizontal residual stresses due to initial compaction, and 4) correction of tensile stresses at the bottom of the base layer obtained in elastic analyses. Finite element predictions of eight different response variables such as stress, strain, and deformation at different locations in the pavement are compared to the results obtained from experiments with instrumented full-scale test sections. The comparisons show very good agreement when a nonlinear elastic analysis is performed with cross-anisotropic material behavior assumed in the base layer. A new method of modeling the resilient response behavior of granular materials is proposed using artificial neural networks. A new block model approach of modeling unstabilized granular bases is also introduced to analyze the particulate media as blocks of aggregates enabling the particulate material behavior such as translation, sliding and separation. The so-called "no tension" problem is investigated using the block model to explain the deficiency of classical continuum solutions which predict inadmissible radial tension in the granular base.

CHAPTER I

INTRODUCTION

Statement of the Problem

Today, more than 2.2 million miles (3.5 million km.) of paved roads exist in the United States of which 94% consist of flexible pavements (FHWA, 1990). Flexible pavements are multilayered systems comprised of an asphalt concrete (AC) surfacing, base, and sometimes subbase layers. These layers are supported by a subgrade. The structural design principle of conventional flexible pavements is usually based on using higher quality materials at the top, where the intensity of stress from the wheel load is high, and materials of decreasing quality with increasing depth. To achieve maximum economy in a pavement section, each material should be located to take full advantage of its best engineering properties. When compacted properly, a granular base shows excellent compressive characteristics in spreading the wheel load over the weaker subgrade soils. The primary objective of this thesis is to study the factors affecting the engineering behavior of granular bases and to develop analytical models to define the stress distribution and load deformation characteristics in flexible pavements.

Since the development of microcomputers, mechanistic analysis has become widely used in flexible pavement design due to its ability to predict fatigue and rutting distress. Most of the currently used mechanistic design methods, however, still employ classical linear elastic analysis to predict the deflections, stresses and strains developed within a pavement due to a wheel load. In conflict with the assumptions of classical linear elasticity, neither the unstabilized aggregate base nor the subgrade soil is homogeneous and isotropic. The nonlinear behavior of both layers are well documented (Brown and Pappin, 1981, Thompson and Elliot, 1985). Recent research (Barksdale et al., 1989) also showed that granular bases with assigned cross-anisotropic material properties result in better predictions of general pavement response than those obtained from the isotropic solutions.

Unstabilized granular bases, which are composed of a discrete assembly of unbound aggregates, can not take any significant levels of tensile stress. The usually employed classical elastic continuum solutions of the pavement system problem, on the other hand, predict large horizontal tensile stresses in the bottom of the base which implies the base is in a state of failure. However, pavements generally do not fail in the field under the traffic load. Selig (1987) proposed that these predicted tensile stresses are actually offset by compressive compaction induced residual stresses which are locked in the granular layer and usually not included in the analysis. These residual stresses, as measured by several researchers (Uzan, 1985; Barksdale and Alba, 1993), must undoubtedly be considered in a proper analytical model for the base. Nevertheless,

whether or not this “no tension” problem can be fully explained with residual stresses is questionable since the predicted horizontal tensile stresses are usually higher than the compressive residual stresses.

Due to the apparent need for improved pavement modeling using proper geometry and material description for the unbound materials, a theoretical and analytical study has been undertaken in this thesis to develop an analysis method for correctly calculating the performance of flexible pavements. The finite element method is used in this study to predict the state of stresses and deformations of the axisymmetric multilayered pavement system when subjected to vehicle wheel load on the surface. A finite element program named GT-PAVE is developed to incorporate the analytical solution which includes the following essential considerations: (1) nonlinear behavior of granular bases and subgrade soils through realistic elastic constitutive behavior laws, (2) cross-anisotropic representation of the granular materials, (3) incremental loading, (4) the compaction induced residual stresses, and (5) “no tension” modifications. The response predictions for full-scale test sections obtained using the GT-PAVE program are found to be in good agreement with the observed results.

A new block model approach for modeling unstabilized granular bases is also proposed in this thesis to analyze in a practical way the particulate media as blocks of aggregates. The new model incorporates both the constitutive relations of the continuum and at the same time, handles the particulate material characteristics such as translation, sliding and separation. The “no tension” problem is investigated using the block model in

an attempt to explain the deficiencies of the classical continuum solutions which predict the inadmissible radial tension in the granular.

Resilient Behavior

The resilient behavior of flexible pavements is the elastic behavior which occurs in the pavement after a large number of repeated wheel load applications. Although most pavements experience permanent (irrecoverable) deformations after each load application, when the loads are small and repeated for a large number of applications, the deformations become almost completely recoverable. As these recoverable deformations become proportional to the load, as an engineering approximation, they can be considered elastic. It is, therefore, possible to select a reasonable elastic modulus commensurate with the speed of moving loads (Huang, 1993).

Repeated load triaxial tests are commonly performed in the laboratory to obtain the resilient properties of unstabilized granular and cohesive materials (Barksdale and Itani, 1990). The resilient modulus (M_R), generally obtained from repeated load triaxial tests, is the elastic modulus calculated based on the axial recoverable strain under repeated axial loads and is defined by

$$M_R = \frac{\sigma_d}{\epsilon_{rec}} \quad (1.1)$$

in which σ_d = the applied repeated deviator stress = $\sigma_1 - \sigma_3$, and ϵ_{rec} is the axial recoverable strain. The resilient modulus is an essential input variable for design of flexible pavements using mechanistic concepts. Throughout this thesis, the elastic behavior of pavement materials is referred to as the resilient behavior, and the elastic analyses are performed using the resilient modulus.

Outline of Thesis

In Chapter 2, a detailed historical review of the classical elastic layered theories are presented. First, the one layer Boussinesq elastic half space problem is considered. Later, Burmister's elastic multilayered approach is applied to the axisymmetric flexible pavement analysis. Within the scope of elastic layered theory, capabilities of some of the commonly used linear elastic computer programs are summarized. Several existing nonlinear material characterization models for unstabilized aggregate bases and the cohesive subgrade soils are also given in detail and compared for consistency and performance. The development of the nonlinear elastic flexible pavement analysis procedures are summarized, and their implementations in the current state-of-the-art nonlinear finite element programs are described.

The resilient response of granular bases is studied in Chapter 3. Some of the essential geometrical and material modeling aspects of unbound granular materials are explained within the framework of the elastic continuum approach. These modeling

aspects include: (1) compaction induced residual stresses, (2) cross-anisotropic representation of granular material behavior, and (3) several analyses aimed to solve the so-called “no tension” problem.

Artificial neural network modeling of the resilient modulus of unstabilized granular bases from laboratory test results is attempted in Chapter 4. After giving a brief background on artificial neural networks, neural network models are trained using experimental data and then used for predicting the resilient modulus given the appropriate stress state and granular material properties. The performance of a neural network model is evaluated for the following two categories: (1) the feasibility of using neural computations as an alternative to conventional stress state dependent resilient response modeling, and (2) how the model works for different material types with different granular material properties such as gradation, dry density, aggregate size, percent fines content, moisture content, etc.

Chapter 5 presents formulations for two types of elements used in the axisymmetric finite element program developed for predicting the behavior of flexible pavements with granular bases. The nonlinear finite element program, named GT-PAVE, employs both the eight-node quadrilateral element and also a six-node interface element which is compatible with the eight-node element. The complete derivations for the stiffness and load matrices are given for both elements, and the interface element parameters used in the new block model in Chapter 8 are summarized.

In Chapter 6, the organization of the GT-PAVE main program and its subroutines are described using flow diagrams. The important features of the program are discussed for the classical continuum representation of the granular base layer. These features include the nonlinear analysis procedure, incremental loading, no tension modification procedures, pre-and post-processing capabilities and the limitations of the finite element model.

The GT-PAVE nonlinear finite element program is verified in Chapter 7 using several example problems involving both linear and nonlinear analyses. The effects of the compaction induced residual stresses on the horizontal tension zone in granular bases is demonstrated through one example problem. The resilient response of five well instrumented full-scale pavement test sections are calculated using GT-PAVE program. The predictions obtained using the nonlinear analysis with the cross-anisotropic granular base representation are shown to be in good agreement in the test sections with up to 8 measured response variables. The GT-PAVE program is also used to predict the potential performance of different pavement section types and geometries.

The new block model analysis for unstabilized granular bases is proposed in Chapter 8. Granular bases are modeled as particulate media composed of blocks of aggregates. Granular particle characteristics including translation, sliding and even separation, are permitted in the new block model. The model and organizations of the related subroutines in the GT-PAVE program are first described using flow diagrams. The iterative block model equilibrium procedure is outlined and how the model works is

demonstrated in a simple three-layered sliding block example. The block model is later applied to the granular bases of the pavement test sections. Important findings are presented related to the shear resistance of the granular bases represented as particulate media.

In Chapter 9, conclusions are drawn and recommendations are given for future research in modeling flexible pavement behavior. Finally, Appendix A gives the experimental resilient modulus data used in Chapter 4 for the neural network modeling of resilient modulus in granular bases, and Appendix B presents a short summary of the input and output capabilities of the GT-PAVE nonlinear finite element program.

CHAPTER II

REVIEW OF THE LITERATURE

Introduction

Over the past three decades, there has been an increasing tendency toward designing flexible pavements using mechanistic-empirical methods. Mechanistic design methods calculate the pavement response variables such as the deformations, stresses and strains due to wheel loads. The pavement distresses are then predicted empirically based on laboratory tests and field performance data. The mechanistic-empirical method is realistic since the theory is combined with observed performance in the design procedure. With the availability of today's high-speed microcomputers and sophisticated test methods, the trend towards mechanistic methods is both natural and beneficial.

Dormon and Metcalf (1965) suggested first the use of design curves for flexible pavements based on the elastic layered theory in the United States. Since then, two main failure criteria have often been used in design of flexible pavements: (1) a limiting vertical compressive strain on the surface of subgrade to reduce permanent deformation and (2) a limiting horizontal tensile strain at the bottom of the asphalt concrete layer to

minimize fatigue cracking. Some of the mechanistic design methods currently in use such as the Asphalt Institute method (Shook et. al., 1982) and Shell Petroleum method (Claussen et. al., 1977) have defined failure, for example, by limiting the rutting to a tolerable amount of 0.5 in. or setting an allowable number of load repetitions for the horizontal tensile strain based on laboratory fatigue testing. Most methods, however, still use isotropic linear elastic theory to predict the pavement response variables.

The behavior of the pavement materials has been well documented to be dependent upon the stress and strain states to which each small element of material is subjected. To properly characterize especially the unstabilized aggregate base and the subgrade layers, it is essential that variations in resilient modulus both vertically and radially within a layer should be considered in the analysis. Additionally, the asphalt concrete surfacing is viscoelastic undergoing time and temperature dependent creep deformations under sustained loading. Therefore, the ultimate goal should be to design a flexible pavement using mechanistic based methods which incorporate nonlinear elastic and viscoelastic material properties.

This chapter presents a historical review of elastic layered theories which currently constitute the backbone of the presently used mechanistic flexible pavement design procedures. Within the scope of elastic layered theory, some commonly used linear elastic computer programs are given. Nonlinear material characterization models are reviewed, and current state of the art nonlinear elastic flexible pavement analysis procedures and finite element programs are also summarized.

Theoretical Background

Flexible pavements are usually represented as elastic layered systems resting on a homogeneous semi-infinite halfspace (Figure 2.1). The wheel load applied on the surface is considered as a uniform load distributed over a circular area where the contact pressure is usually taken as the pressure in the vehicle tire. Due to the special nature of this axisymmetric problem, a cylindrical coordinate system with coordinates r , θ , and z is used to represent radial, tangential, and vertical stress conditions respectively (Figure 2.1).

Boussinesq (1885) solved the problem of a point load P acting on the surface of a semi-infinite linear elastic homogeneous halfspace (i.e., a single deep layer) by combining equilibrium equations together with the constitutive and kinematic equations to obtain:

$$\nabla^2 \nabla^2 \phi = 0 \quad (2.1)$$

where $\phi = (P/2\pi) \cdot (r^2 + z^2)^{1/2}$ is the Airy stress function and ∇^2 is the Laplace operator. The stress, strain and displacement components at any depth z and radial distance r away from the point load P were obtained by solving Equation 2.1.

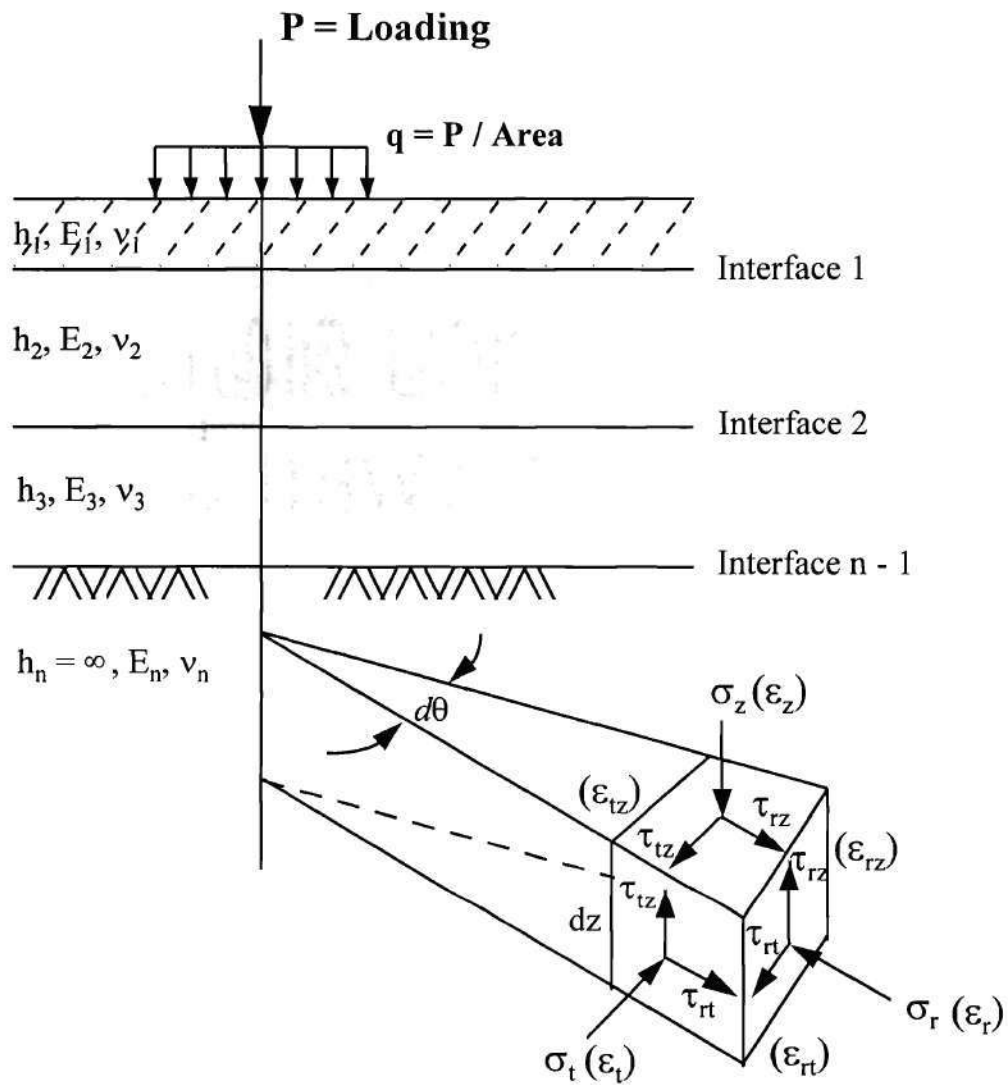


Figure 2.1. Generalized Multilayered Elastic System In Cylindrical Coordinates Under Axial Symmetry.

Foster and Ahlvin (1958) integrated the point load Boussinesq solution over a uniformly loaded circular area for use in flexible pavement analysis. Charts were prepared to give horizontal stress, vertical stress and elastic strains in the semi-infinite halfspace for an incompressible solid ($\nu = 0.5$). Ahlvin and Ulery (1962) later tabulated the complete pattern of stress, strain, and deflection results at a large number of points for different values of Poisson's ratios ν in the homogeneous halfspace.

One-Layer Approach

When the load is applied over a circular area, the most critical stress, strain, and deflection components occur under the centerline on the axis of symmetry. The shear stress τ_{rz} becomes zero under the centerline, and the principal stresses are equal those stresses in r, θ , and z directions. Considering the tire pressure on the pavement as a flexible plate of uniform load q having radius a , the stresses (σ_r , and σ_z) strains (ϵ_r , and ϵ_z) and the surface deflection (δ) can be determined beneath the center of the load from the following:

$$\sigma_r = \frac{q}{2} \left[1 + 2\nu - \frac{2(1+\nu)z}{(a^2 + z^2)^{1/2}} + \frac{z^3}{(a^2 + z^2)^{3/2}} \right] \quad (2.2)$$

$$\sigma_z = q \left[1 - \frac{z^3}{(a^2 + z^2)^{3/2}} \right] \quad (2.3)$$

$$\epsilon_r = \frac{(1 + \nu)q}{2E} \left[1 - 2\nu - \frac{2(1 - \nu)z}{(a^2 + z^2)^{1/2}} + \frac{z^3}{(a^2 + z^2)^{3/2}} \right] \quad (2.4)$$

$$\epsilon_z = \frac{(1 + \nu)q}{E} \left[1 - 2\nu + \frac{2\nu z}{(a^2 + z^2)^{1/2}} - \frac{z^3}{(a^2 + z^2)^{3/2}} \right] \quad (2.5)$$

$$\delta = \frac{(1 + \nu)qa}{E} \left\{ \frac{a}{(a^2 + z^2)^{1/2}} + \frac{1 - 2\nu}{a} [(a^2 + z^2)^{1/2} - z] \right\} \quad (2.6)$$

where a = radius of loading, z = depth of interest, q = magnitude of uniform loading, E = modulus of elasticity, and ν = Poisson's ratio.

The Boussinesq equations for the circular loading over a homogeneous halfspace summarized above can not be applied directly to a flexible pavement structure. A flexible pavement usually consists of two or more layers with asphalt concrete (AC) surfacing on the top, an unstabilized aggregate base or base and subbase in the middle, and a subgrade layer at the bottom. These layers have different elastic moduli which are changing with depth and different Poisson's ratios. Early applications of Boussinesq's

theory to pavement analysis, therefore, involved an approximation known as the method of equivalent layer thickness (Odemark, 1949). To model a layered system, Odemark method simply changes the thicknesses of different layers to make possible the use of one elastic modulus E and one Poisson's ratio ν . Several transformations were needed to calculate the stresses, strains, and deflections in the lower subgrade layer.

Elastic Multi-Layered Theory

True elastic layered theory was first developed by Burmister (1943) for the solution of a two-layer system, and then extended two years later for three layer systems more suitable for modeling pavements (Burmister, 1945). Based on the three-dimensional continuum, the elastic layered theory gives stresses, strains and displacements in multilayer systems upon making the following basic assumptions:

1. All layers are weightless and infinite in horizontal directions.
2. All layers are homogeneous, isotropic and linearly elastic.
3. All layers have a finite thickness except the bottom layer which is infinite.
4. Between any two layers, perfect bonding exists.
5. The upper layer is subjected to a single uniformly distributed circular load.
6. At infinite depth, all stresses and displacements are zero.

The fourth-order governing differential equation given by Equation 2.1 is satisfied for each layer using a stress function with four constants. Since this stress function must vanish at infinite depth, two constants become zero for the bottom most layer which as a

result has only two constants. For the n -layer system shown in Figure 2.1, the total number of constants or unknowns is $(4n - 2)$, which is evaluated by two boundary conditions and $(4n - 1)$ continuity conditions. The other two conditions are the vertical stress under the circular loaded area q and the surface is free of shear stress. The four conditions at each of the $(n - 1)$ interfaces are the continuity of vertical stress, vertical displacement, shear stress and radial displacement.

The multilayer system equations are first solved for the stress components in r, θ , and z directions including the shear stress τ_{rz} for the axisymmetric problem. Solutions for linear elastic multilayer systems under a single load then can be extended to cases involving multiple loads by applying the superposition principle. The principal stresses $(\sigma_1, \sigma_2, \text{ and } \sigma_3)$ are obtained by using the following equation where the intermediate principal stress is equal to the tangential stress $(\sigma_2 = \sigma_t)$:

$$\sigma_{1,3} = (\sigma_r + \sigma_z) / 2 \mp \sqrt{(\sigma_r - \sigma_z)^2 / 4 + \tau_{rz}^2} \quad (2.7)$$

The principal strains $(\epsilon_1, \epsilon_2, \text{ and } \epsilon_3)$ are then determined by

$$\epsilon_1 = \frac{1}{E} [\sigma_1 - \nu(\sigma_2 + \sigma_3)] \quad (2.8)$$

$$\varepsilon_2 = \frac{1}{E}[\sigma_2 - \nu(\sigma_1 + \sigma_3)] \quad (2.9)$$

$$\varepsilon_3 = \frac{1}{E}[\sigma_3 - \nu(\sigma_1 + \sigma_2)] \quad (2.10)$$

where E and ν are the elasticity modulus and Poisson's ratio, respectively.

The weightlessness and vastness of the layers are assumptions made in the linear elasticity and do not much affect the solutions as predicted by the elastic layered theory. The material properties assigned to the layers, however, have dramatic effect on response. The material properties can be represented by the ratio of the moduli of adjacent layers (E_1/E_2 , E_2/E_3 , etc.) and Poisson's ratio of each layer. The effect on response of stiff reinforcing layers is pronounced. In the early development of elastic layered theory, a Poisson's ratio of 0.5 was chosen to simplify the solution and resulting equations. A change of Poisson's ratio from 0.35 to 0.5 can, however, create a 25% change in vertical strain as noted by Burmister (1945). When compared to the measured response in pavements, elastic layered theory has been observed to predict stresses more accurately than the Boussinesq equations.

Linear Elastic Computer Programs

Several linear elastic layered computer programs have been developed over the years for the solution of the pavement problem. One of the earliest ones was the

CHEVRON program developed by the Chevron Research company (Warren and Dieckman, 1963). Hwang and Witczak (1979) later modified the program to approximately account for the nonlinear elastic granular base behavior and incorporated it into the DAMA pavement design program for use by the Asphalt Institute.

Also using Burmister's theory, Shell researchers developed the computer program, BISAR, for calculating the response of multi-layer structures with linearly elastic material behavior (De Jong et al., 1973). BISAR analyzes multiple loading conditions where more than one distributed circular load can be applied on the pavement. Different elastic moduli, Poisson's ratios, and thicknesses can be assigned to each layer where either slip or perfect bonding can be specified in the interface.

Another well-publicized linear elastic layered system program was developed at the University of California, Berkeley (Kopperman et al., 1986). Named ELSYM5, the program runs on a microcomputer and can analyze up to a maximum of 5 layers as elastic systems under multiple wheel loads. The program superimposes various loads and can compute the principal stresses, strains, and displacements at locations specified by user which is common to all linear elastic programs. ELSYM5 has become very popular in the US especially among the state transportation agencies for its easy use in routine flexible pavement design.

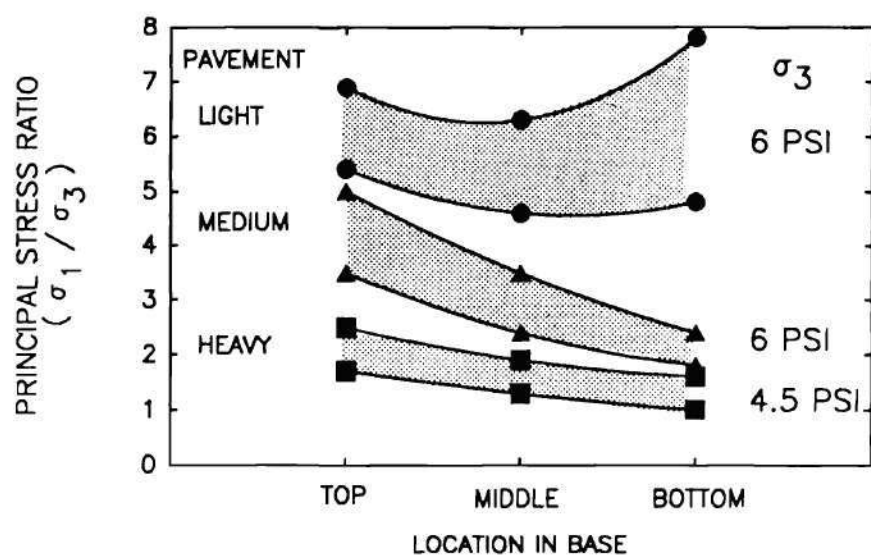
Recently, Huang (1993) presented the computer program KENLAYER for the analysis of elastic and viscoelastic layered systems. Named after University of Kentucky, the program is applied to flexible pavements as layered systems. The superposition of

multiple wheel loading is considered for single, dual, dual-tandem, and dual-tridem wheels with each layer in the system behaving differently, either linear elastic, nonlinear elastic, or viscoelastic (Huang, 1993). Damage is also included in the analysis by dividing one year into different periods, each assigned with a different set of material properties.

Resilient Material Characterization Models

The engineering behavior of the materials used in flexible pavements is usually characterized by using mathematical models. For selecting these models, several steps have to be followed. First a good theoretical background is a prerequisite for the total understanding of the idealizations and assumptions made in developing the models. Secondly, a laboratory testing program must be undertaken to represent the material behavior under similar service conditions which exist on the roadways. These are the conditions such as (1) loading, (2) environmental conditions, and (3) construction effects under which the material is expected to perform in service. The next step is to study the collected laboratory data sets to investigate a possible correlation between the data and response variables for the selection of a model. The model predictions should be verified using measured pavement response to determine the acceptability of the model.

Among the service conditions discussed above, the correct field stress states (see Figure 2.2), repeated application of moving traffic loads, field temperature and moisture,



Note: 1psi = 6.895 kPa

Figure 2.2. Average Stress States in Aggregate Base For Use in Cyclic Testing For Light, Medium, and Heavy Pavements (after Barksdale and Itani, 1989).

and induced pavement compaction stresses (Uzan, 1985; Selig, 1987) are the most important to be simulated in the analysis. Under the repeated application of moving traffic loads, most of the deformations are recoverable and thus considered elastic. Therefore, it has been customary to use resilient modulus (M_R) for the elastic stiffness of the pavement materials. Repeated load triaxial tests are commonly employed to evaluate the resilient properties of granular and cohesive materials (Barksdale and Itani, 1989).

For asphalt concrete surfacing, the repeated load diametral test is popular for evaluating the resilient characteristics. The resilient modulus of asphalt mixtures can also be determined by the repeated load indirect tension test (Huang, 1993). The resilient modulus is then empirically computed by

$$M_R = \frac{P(v + 0.2734)}{\delta t} \quad (2.11)$$

in which P is the magnitude of the dynamic load (lbs.), v is Poisson's ratio, δ is the total recoverable deformation (in.), and t is the specimen thickness (in.).

The resilient material characterization models reviewed in this section include granular materials used in base, subbase and granular subgrade as well as mostly cohesive fine-grained soils used in subgrade. The nonlinearity observed in both material types is usually presented in the form of stress dependent moduli which is reviewed in the

following section in chronological order of the development of these resilient response models.

Granular Materials

K-θ Model. Usually referenced back to Hicks and Monismith (1971), the K-θ model has been the most common one for characterizing the resilient response of the unbound aggregate in granular bases. The resilient modulus (M_R) is given as follows:

$$M_R = K_1 \sigma_\theta^{K_2} \quad (2.12)$$

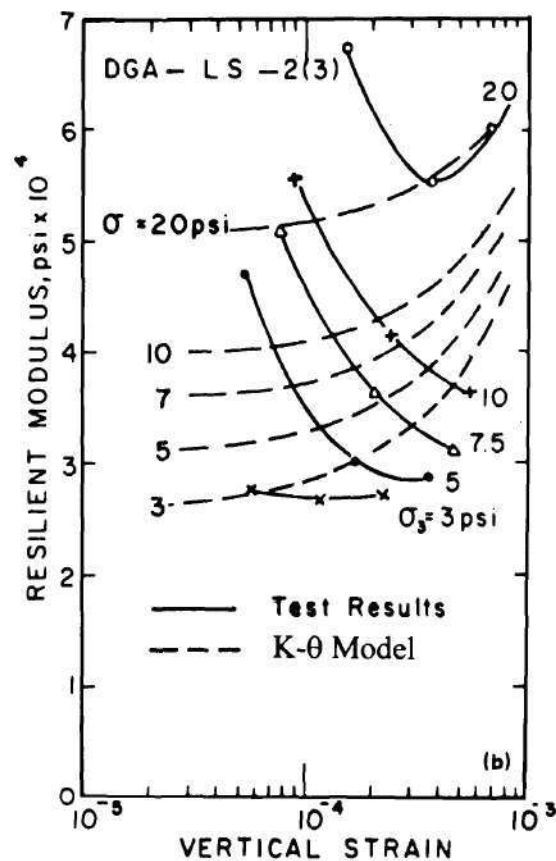
where $\sigma_\theta = \sigma_1 + \sigma_2 + \sigma_3$ = bulk stress and K_1 , and K_2 are material regression constants obtained from repeated load triaxial tests performed on granular materials.

The K-θ model has become the cardinal mathematical relation between the modulus and the stress states in most laboratory and full-scale research work related to unbound aggregates since late 1960's. The characteristic plot of the modulus varying with bulk stress is generally drawn on a log-log scale and represented by a straight line. Although it is simple, the K-θ model can give inaccurate results since it neglects the important effect of shear stress on the resilient modulus (May and Witczak, 1981; Uzan, 1985). Similarly, Brown and Pappin (1981) also observed that the K-θ model can only

represent a very limited range of stress paths and thus is likely to lead to erroneous results. Figure 2.3 compares measured resilient moduli with those predicted using the model for a dense-graded aggregate (Uzan, 1985). The discrepancy between the measured and predicted values of moduli is mainly due to neglecting the effect of shear stress and shear strain effects when calculating the response using the K- θ model. The K- θ model does not describe the descending behavior of the resilient modulus with axial strain.

Bulk-Shear Modulus Models. Boyce (1976) performed a series of repeated load triaxial tests on samples of well-graded crushed limestone. The resilient strain was found to be influenced by (1) mean normal stress p , and also (2) ratio of deviator stress to normal stress. A model of resilient behavior was developed in terms of the secant bulk modulus (K) and the secant shear modulus (G), which are functions of stress level. The origin of the non-linearity in the model was traced to the particulate nature of the materials by using the theory of contacting elastic spheres. Boyce (1980) developed the following equations for the incremental stress-strain behavior with a power dependence of both moduli on the isotropic mean stress:

$$K = \frac{K_i p^{(1-\mu)}}{1 - \beta \left(\frac{q}{p} \right)^2} \quad (2.13)$$



Note: 1psi = 6.895 kPa

Figure 2.3. Test Results and Predicted Behavior Using K- θ Model For a Dense Graded Aggregate (after Uzan, 1985).

$$G = G_i p^{(1-\mu)} \quad (2.14)$$

where K_i and G_i are initial values of bulk and shear moduli respectively, μ is a model constant less than 1, $\beta = (1-\mu) K_i / (6 G_i)$, and q is the deviator stress.

Equations 2.13 and 2.14, also known as the K-G model, satisfy Maxwell's reciprocity theorem. The theorem implies that the second order partial derivatives of a stress potential function are independent of the order of differentiation with respect to volumetric and deviatoric stress components. Alternatively, the strain invariants (volumetric and deviatoric strains) are related to mean normal stress p and the deviator stress q by the following expressions:

$$\varepsilon_v = \left(\frac{1}{K_i} \right) p^\mu \left[1 - \beta \left(\frac{q}{p} \right)^2 \right] \quad (2.15)$$

$$\varepsilon_q = \left(\frac{1}{3G_i} \right) p^\mu \left(\frac{p}{q} \right) \quad (2.16)$$

where all terms have been previously defined.

Using only the three parameters, i.e., μ , K_i , and G_i , the K-G model (Boyce, 1980) was found to give reasonably good agreement with measured strains when predicting the

resilient modulus of granular materials. The exponent “ μ ” is a measure of nonlinearity of the elasticity including the phenomenon of “elastic dilation” via the coupling terms (p and q) in the tangential description of the model.

Contour Model. Brown and Pappin (1981) extended the three parameter model of Boyce (1980) to the five parameter contour model in which a stress path dependency was added in the formulation. The volumetric and shear strains were found to be influenced by the length of the stress path followed. Using a special triaxial apparatus, granular materials were tested for different realistic stress paths varying independently the axial and confining pressures. Figure 2.4 shows the normalized volumetric and shear strain contours plotted in Cambridge q - p stress space in which $p = (\sigma_1 + \sigma_2 + \sigma_3)/3$ and $q = (\sigma_1 - \sigma_3)$. The contour model predicts the volumetric and shear strains by the following equations:

$$\epsilon_v = \frac{1}{K_i} \left(\frac{p}{p_0} \right)^{\mu-1} \left[1 - \beta \left(\frac{q}{p_0} \right)^2 \right] p \quad (2.17)$$

$$\epsilon_q = \frac{1}{3G_i} \left(\frac{p}{p_0} \right)^{\kappa-1} q \quad (2.18)$$

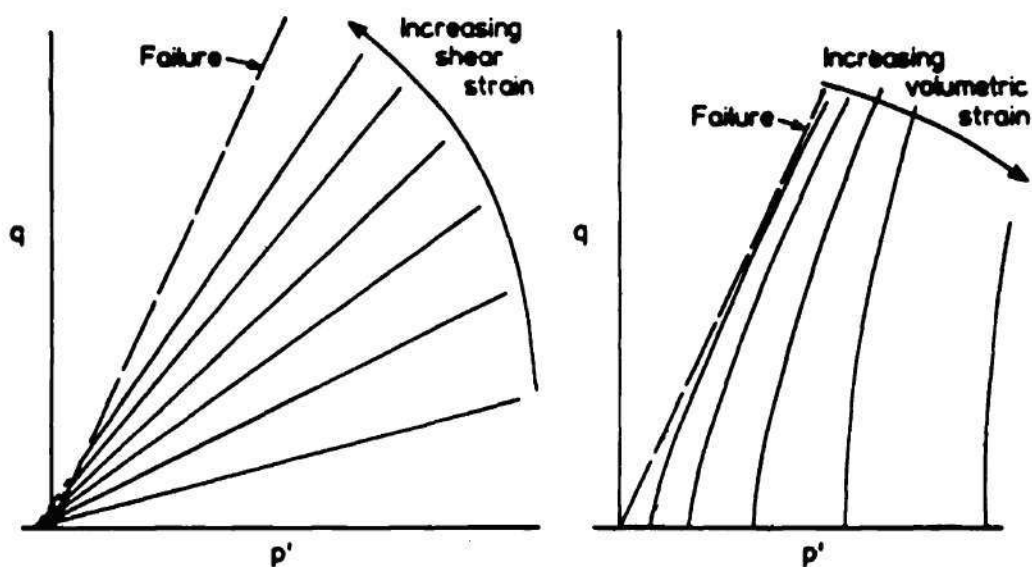
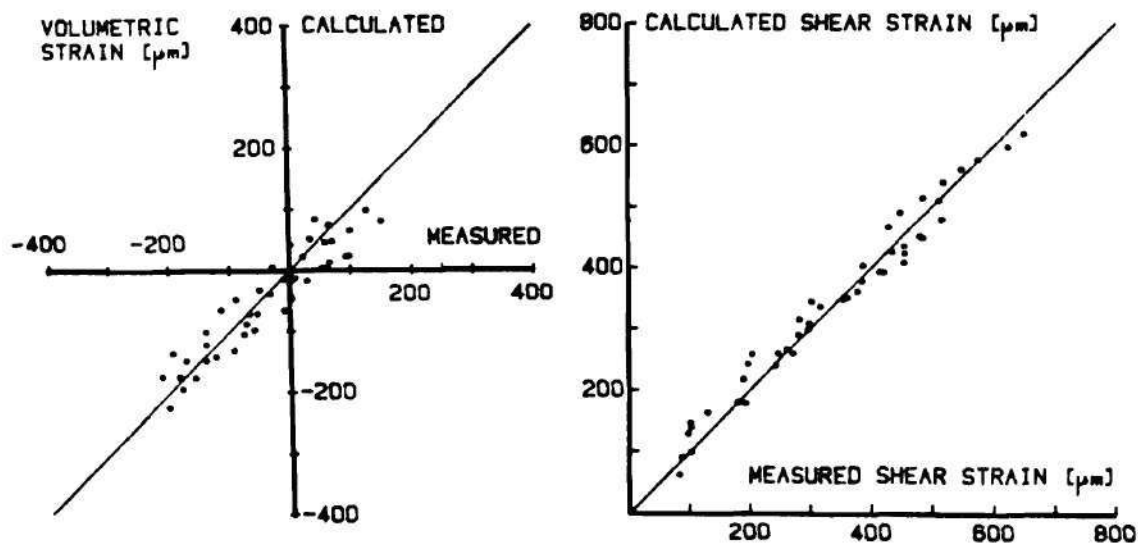


Figure 2.4. Contour Model Cambridge q - p Stress Space (after Brown and Pappin, 1981).

$$\Delta \epsilon_q = \frac{1}{3G_i} \left[\left(\frac{p_2}{p_0} \right)^\kappa \frac{q_2}{p_2} - \left(\frac{p_1}{p_0} \right)^\kappa \frac{q_1}{p_1} \right] \ell^r \quad (2.19)$$

where κ and r are statistical material constants, p_0 is the reference pressure, and $\ell = (\Delta p^2 + \Delta q^2)^{1/2}$ is the path length between stress state 1 and stress state 2. Equations 2.18 and 2.19, therefore, incorporate in the formulation the new parameters κ and r which establish improvement of the contour model over Boyce's K-G model. The path dependency of the shear strain ϵ_q is calculated from Equation 2.19 between the two stress and strain states: $\Delta \epsilon_q = \epsilon_{q2} - \epsilon_{q1}$.

The contour model is capable of predicting resilient test results (M_R) very well. However, the required resilient modulus testing is complicated and material constant evaluation is cumbersome when compared to other simpler approaches. Figure 2.5 gives a comparison of the volumetric and shear strain predictions using both the K- θ model and the more sophisticated contour model. The contour model predictions agree quite well with the measured values whereas the volumetric strains predicted by K- θ model deviate drastically from reality. On the other hand, due to the addition of two extra constants, the five parameter contour model no longer satisfies the reciprocal theorem and hence the model is not truly elastic.



(a) Based on contour model

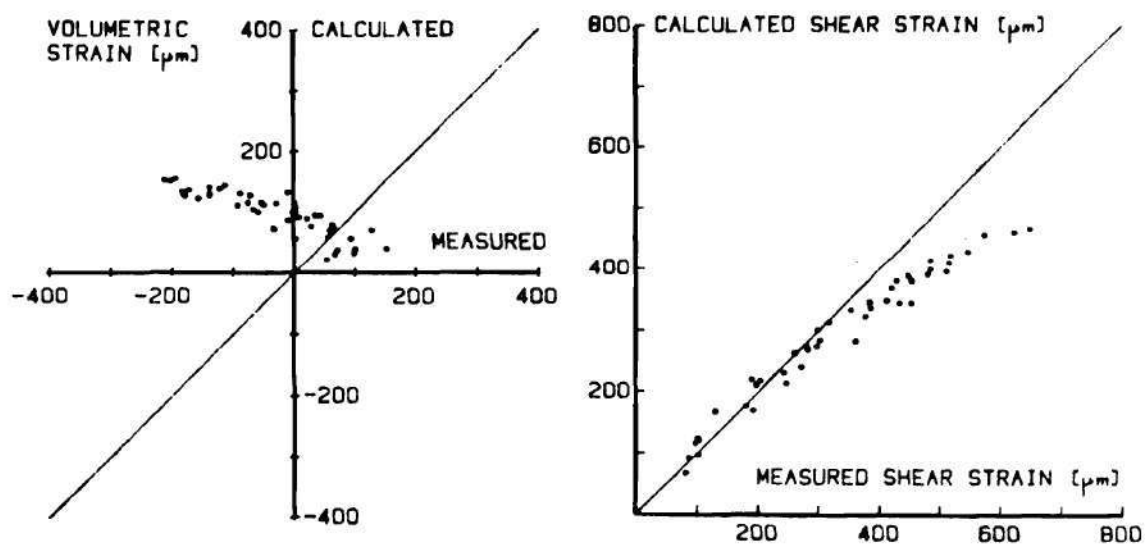
(b) Based on K- θ model

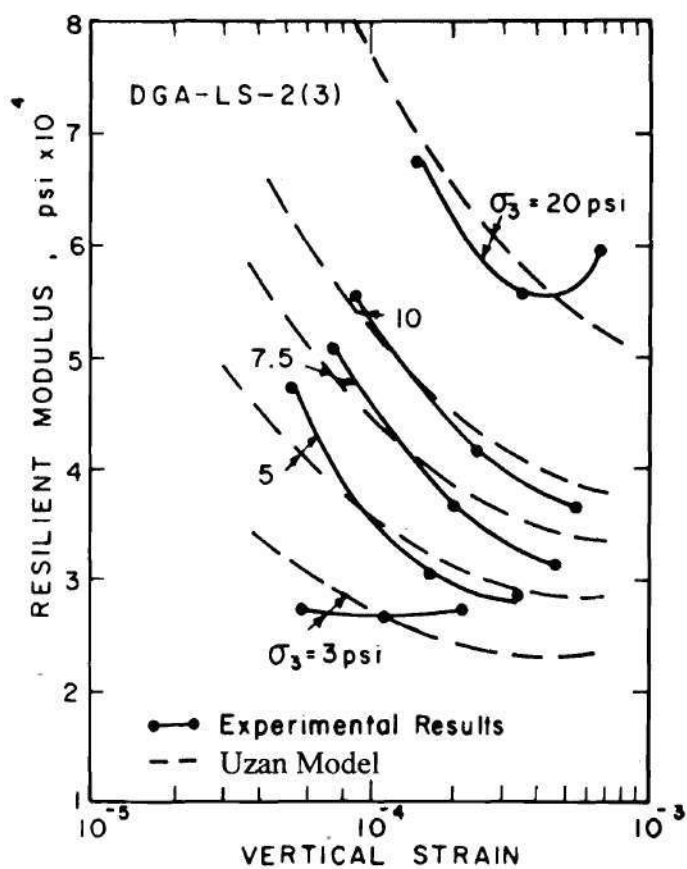
Figure 2.5. Comparison of Contour Model with the K- θ Model (after Sweere et al., 1987).

Uzan Model. Uzan (1985) proposed an improvement to the well-known K- θ model by including shear stress effects. An additional deviator stress term was included in the formulation of the K- θ model requiring a new constant parameter to be evaluated from laboratory tests. The Uzan model is expressed as follows:

$$M_R = K_3 \sigma_\theta^{K_4} \sigma_d^{K_5} \quad (2.20)$$

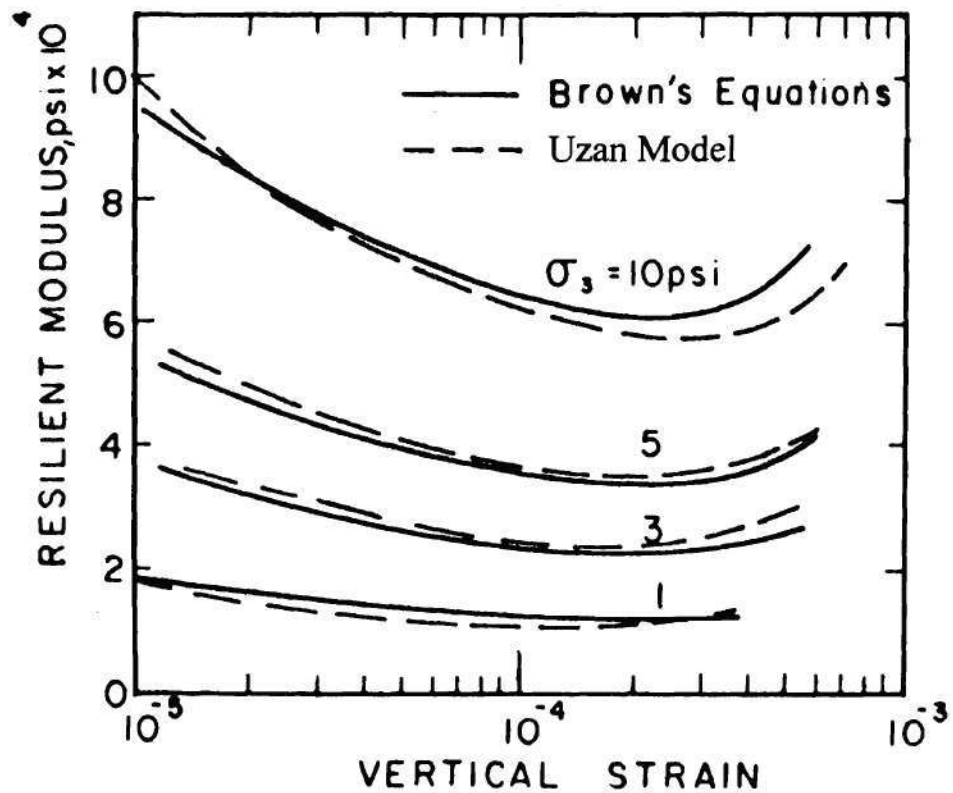
where $\sigma_\theta = \sigma_1 + \sigma_2 + \sigma_3 = \sigma_1 + 2\sigma_3$ = bulk stress, $\sigma_d = \sigma_1 - \sigma_3$ = deviator stress, and K_3 , K_4 , and K_5 are multiple regression constants obtained from repeated load triaxial test data on granular materials.

The resilient moduli predicted by the Uzan model are plotted in Figure 2.6 together with the experimental results obtained from repeated load triaxial tests for a dense graded aggregate. The Uzan model, when compared to the more complicated shear and volumetric strain contour model, also gives reasonably good agreement (Figure 2.7). This is mainly due to the Uzan model's ability to incorporate shear stress and strain effects in a realistic representation of the granular material behavior. Considering that horizontal residual stress levels are not well documented, the Uzan model also handles very nicely the behavior of granular bases used in the layered system analysis. Due to its simplicity and ease in material constant evaluation, the Uzan model can be used routinely as an improved nonlinear model in flexible pavement design procedures.



Note: 1psi = 6.895 kPa

Figure 2.6. Comparison of Test Results and Predicted Behavior Using Uzan's Model for A Dense Graded Aggregate (after Uzan, 1985).



Note: 1psi = 6.895 kPa

Figure 2.7. Comparison of Predicted Resilient Modulus Behavior of Crushed Stone Using Brown's Model and Uzan's Model (after Uzan, 1985).

Modified K-G Model. Jouve et al. (1987) presents a modified version of Boyce's (1980) equations for the bulk stress and shear stress of granular material. The modified K-G model follows the stress paths chosen in the triaxial tests (Brown and Pappin, 1981), but ignores the dilatancy phenomenon ($K \leq 0$) which is incompatible with the elastic model and the reciprocal theorem. For the modified K-G model, the bulk and shear moduli are defined by relationships:

$$K = K_i p^{(1-\mu)} \left\{ 1 + \gamma \left(\frac{q}{p} \right)^2 \right\} \quad (2.21)$$

$$G = G_i p^{(1-\kappa)} \quad (2.22)$$

where p = mean normal stress, q = deviator stress, and K_i , G_i , γ , κ , and μ are constants evaluated from test data. The experimental results also showed that shear strain could be represented by:

$$\epsilon_q = \frac{1}{3G_i} \left(\frac{q}{p} - c \right) p^\kappa \quad (2.23)$$

where $c = p_1^{(\kappa-1)} q_1 / (p_2^\kappa)$ is a parameter ≤ 1 with p_1, q_1 being initial stresses at stress state 1 and p_2, q_2 being the final stresses at stress state 2. The above interpretation takes into account the self weight of the sample, weight of the measurement equipment which is applied on the sample, and the residual lateral pressure in the triaxial cell.

Jouve et al. (1987) used the modified K-G model to verify the Boyce's relationship (1980) concluding that $\mu = \kappa$ is statistically true. The aggregate particle shapes used in the tests were also found to influence the elastic behavior of completely crushed unbound granular material.

Thom Model. Thom (1988) proposed a new elastic stress strain model for dry granular material for the range of stress paths which can be applied using triaxial and hollow cylinder testing apparatus. Based on the original work by Brown and Pappin (1981), Thom considered the resilient response separately for volumetric and shear strain components. The proposed model accounted also for microtexture, and particle shape and size of the unbound aggregates. As a result, the model required more material constants to relate the volumetric and shear strains to the principal stresses and shear stresses:

$$\varepsilon_v = A\Delta(\ln p)^B (\Delta p)^C - D \left[\Delta \left(\ln \frac{\sigma_1}{\sigma_3} \right)^2 \right]^E \quad (2.24)$$

$$\varepsilon_q = F \Delta \left(\ln \frac{\sigma_1}{\sigma_3} \right)^G \left[\Delta \tau + \frac{1}{3} \Delta S \right]^H \quad (2.25)$$

where σ_1 , σ_3 are principal stresses, p is mean normal stress, S is in-plane mean stress, τ is shear stress, Δ means change in, and A , B , C , D , E , F , G , and H are the statistically evaluated material constants determined experimentally. Comparing the model with laboratory data, quite good agreement was obtained. Later, Thom concluded that specimens comprised of aggregates containing large particles had greater elastic stiffness and shear strength compared to those having smaller particles. The elastic stiffness of a dry granular materials were also largely dependent on microtexture at particle contacts which determined interparticle friction.

Octahedral Shear Stress Model. Witzak and Uzan (1988) proposed a modification to the Uzan model by replacing the deviator stress term in Equation 2.20 by an octahedral shear stress term. This octahedral shear stress model also considers the dilation effect that takes place when a pavement element is subjected to a large principal stress ratio (σ_1 / σ_3). The model involves normalized values of the bulk and octahedral shear stress and is given as follows:

$$M_R = K_6 p_a \left(\frac{\sigma_\theta}{p_a} \right)^{K_7} \left(\frac{\tau_{\text{oct}}}{p_a} \right)^{K_8} \quad (2.26)$$

where $\sigma_\theta = \sigma_1 + \sigma_2 + \sigma_3 = \sigma_1 + 2\sigma_3$ = bulk stress, τ_{oct} = octahedral shear stress, p_a = atmospheric pressure, and K_6 , K_7 , and K_8 are multiple regression constants evaluated from resilient modulus test data.

Itani Model. Itani (1990) performed an extensive multiple regression analysis using many models relating the resilient modulus by different combinations of deviator stress, mean stress, confining stress, and axial strain. Laboratory test data for different aggregate gradations were used in this study to find better models to characterize the resilient modulus. Itani's best model fit the laboratory test data very nicely with a high determination coefficient ($R^2=0.96$) and was given as follows:

$$M_R = K_9 \left(\frac{\sigma_\theta}{3} \right)^{K_{10}} \sigma_d^{K_{11}} \sigma_3^{K_{12}} \quad (2.27)$$

where $\sigma_\theta = \sigma_1 + \sigma_2 + \sigma_3 = \sigma_1 + 2\sigma_3$ = bulk stress, $\sigma_d = \sigma_1 - \sigma_3$ = deviator stress, σ_3 = confining stress and K_9 , K_{10} , K_{11} , and K_{12} are multiple regression constants obtained from repeated load triaxial tests performed on granular materials. Equation 2.27 is

basically a modification to the Uzan Model (Equation 2.20) with the addition of the confining stress term. Itani concluded that although there was a slight multi-collinearity problem in this model (σ_3 , σ_θ , and σ_d are related), it was still useful in predicting the resilient modulus.

Crockford et al. Model. Crockford et al. (1990) studied the elastic constitutive relationships that best model the actual stress or recoverable strain states in pavement structures incorporating thick granular layers. The elastic response was taken primarily because previous research showed that falling weight deflectometer (FWD) equipment excited pavements elastically. A new resilient response was developed in which the modulus was expressed as a function of volumetric water content (V_w/V_t), suction stress (Ψ), octahedral shear stress (τ_{oct}), unit weight of material normalized by the unit weight of water (γ/γ_w), and the bulk stress (σ_θ). The final form of the model was given by

$$M_R = \beta_0(\sigma_\theta + 3\Psi V_w / V_t)^{\beta_1} (\tau_{oct})^{\beta_2} (\gamma / \gamma_w)^{\beta_3} \quad (2.28)$$

where β_0 , β_1 , β_2 , and β_3 are material constants. The moisture term $3\Psi V_w/V_t$ was found to affect only the bulk stress σ_θ . Very few experimental studies have been reported about suction which influence the moisture term. If a model is developed with laboratory data obtained only at one moisture content, Crockford et al. suggests eliminating this moisture

term. Moreover, if only one unit weight is again considered, the further elimination of the normalized unit weight term was suggested which simplifies the equation to the octahedral shear stress model of Witczak and Uzan (1988).

UTEP Model. An overparametrized resilient response model was proposed recently at University of Texas, El Paso (Feliberti, 1991) for unbound aggregate behavior. The model, called herein the UTEP model, predicts the resilient modulus using bulk stress and the induced resilient axial strain from the repeated load triaxial tests and is as follows:

$$M_R = K_{13} \sigma_\theta^{K_{14}} (\epsilon_a)^{K_{15}} \quad (2.29)$$

where $\sigma_\theta = \sigma_1 + \sigma_2 + \sigma_3 = (\sigma_d + 3\sigma_3)$ = bulk stress, ϵ_a = induced resilient axial strain, and K_{13} , K_{14} , and K_{15} are multiple regression constants. In the UTEP model, both σ_d (in σ_θ term) and ϵ_a are the predictor variables (on the right hand side of the equation) whereas in the Uzan model, only the deviator stress σ_d is a predictor variable. The UTEP model is then overparametrized since the resilient modulus M_R is by definition calculated by dividing the applied deviator stress σ_d by the measured axial strain ϵ_a . Alba (1993) reported that the UTEP model, compared to the other models studied, gave the best statistical curve fitting results to an extensive experimental data set. This is probably due

to the fact that the UTEP model has enough number of redundant constants to smoothly fit the measured data using the two predictor variables included in the model.

UT-Austin Model. Pezo (1993) presented a new general method of reporting resilient modulus tests on the pavement materials. The resilient modulus was suggested to be plotted with the measured axial strain as the main response variable. First, a multiple regression analysis was performed to express the axial strain in terms of the applied confining and deviator stresses from the laboratory tests. The UT-Austin model then incorporated the deviator stress and the confining stress terms for predicting the resilient modulus of granular materials as follows:

$$M_R = K_{16} \sigma_d^{K_{17}} \sigma_3^{K_{18}} \quad (2.30)$$

where $\sigma_d = \sigma_1 - \sigma_3$ = deviator stress, σ_3 = confining stress and K_{16} , K_{17} , and K_{18} are multiple regression constants obtained from repeated load triaxial tests. Alba (1993) obtained a very good statistical fit of resilient moduli from dynamic testing on granular materials ($R^2 = 0.96$).

Because the multiple regression constants are obtained mainly from the measured axial strain, the model is not overparametrized as it is in the case of the UTEP model. The model is also statistically sound, since the prediction variables are independent from

the response variables. Pezo (1993) has pointed out that bulk stress dependent models such as the K- θ model can not distinguish between two different test conditions with (1) $\sigma_d = \text{small}$ and $\sigma_3 = \text{large}$ and (2) $\sigma_d = \text{large}$ and $\sigma_3 = \text{small}$, even if $\sigma_\theta = \sigma_1 + \sigma_2 + \sigma_3 = (\sigma_d + 3\sigma_3)$ is the same for both tests. In such circumstances, the resilient moduli are not expected to be the same (using the same σ_θ) simply because cohesionless materials subjected to higher σ_3 also show higher moduli than if subjected to lower σ_3 .

Summary. All the resilient response models reviewed in this section except the K- θ model can be categorized into two main groups: (1) Simplified shear stress related models, and (2) more sophisticated volumetric and shear strain related models. The K- θ model can be considered as a simplified but inadequate model since it neglects the shear stress effects and is not capable of describing the resilient modulus decrease when the vertical strain is increased.

Among the simplified shear stress related models, the Uzan model and its modified versions (i.e., Witczak-Uzan and Itani models), and the UT-Austin model (Pezo, 1993) consider both the confining and the deviator stress effects and handle very well the stiffness reduction with the increase in strain. In the second category, the K-G, contour, modified K-G, and Thom models originate from the same concept of defining the resilient response based on the volumetric and shear strain behavior. Although these

models are more complicated and not well suited for routine design use, they are admittedly more sophisticated and very promising for theory related future research.

Due to the simplicity of the first group of models, the regression constants used in these models can be readily determined from routine resilient modulus tests. Even though the simplified models are not as fundamentally sound as the contour model, they do give reasonably good results. Therefore, for a practical, accurate approach, the Uzan model or the UT-Austin model, as a minimum should be employed when characterizing resilient behavior of granular materials. Such models can also be easily incorporated into a finite element code and used by state transportation agencies in mechanistic flexible pavement design procedures.

Subgrade Soils

The resilient modulus of fine-grained cohesive subgrade soils is dependent upon the stress state. The most important factor affecting the resilient modulus is the deviator stress. There is also some influence from confining pressure and the number of stress applications but this influence is less significant on resilient modulus M_R compared to the effect of deviator stress. Therefore, constitutive relationships are primarily established between the resilient modulus and the deviator stress for fine-grained subgrade soils. Some of the more commonly used resilient modulus models are as follows:

Empirical Relations. Charts for estimating the resilient modulus of subgrade soils from empirical strength test results have been frequently used in practice. These charts are often based on simple equations which empirically relate the resilient modulus of specific soil types to the soil strength parameters such as California Bearing Ratio (CBR) or stabilometer resistance value (R). Some of the commonly used relations are:

- M_R (psi) = 1500 CBR, or M_R (MPa) = 10 CBR (Heukelom and Klomp, 1962)
- M_R (psi) = 1155 + 555 R (The Asphalt Institute, 1982)
- M_R (MPa) = 17.6 (CBR)^{0.64} (Lister and Powell, 1987)

Bilinear Approximation. For many slightly cohesive and cohesive fine-grained soils, the resilient moduli obtained from the repeated load triaxial tests can be described by a bilinear function of the applied deviator stress σ_d . The bilinear behavior is usually expressed as follows (refer to Figure 2.8):

$$M_R = K_{19} + K_{21}(K_{20} - \sigma_d) \text{ when } \sigma_d < K_{20} \quad (2.31a)$$

$$M_R = K_{19} - K_{22}(\sigma_d - K_{20}) \text{ when } \sigma_d > K_{20} \quad (2.31b)$$

where K_{19} , K_{20} , K_{21} , and K_{22} are material constants obtained from laboratory repeated load tests. As indicated by Thompson and Elliot (1985), the value of the resilient

modulus at the breakpoint in the bilinear curve, K_{19} , (see Figure 2.8) can be used to classify fine-grained soils as being either soft, medium or stiff.

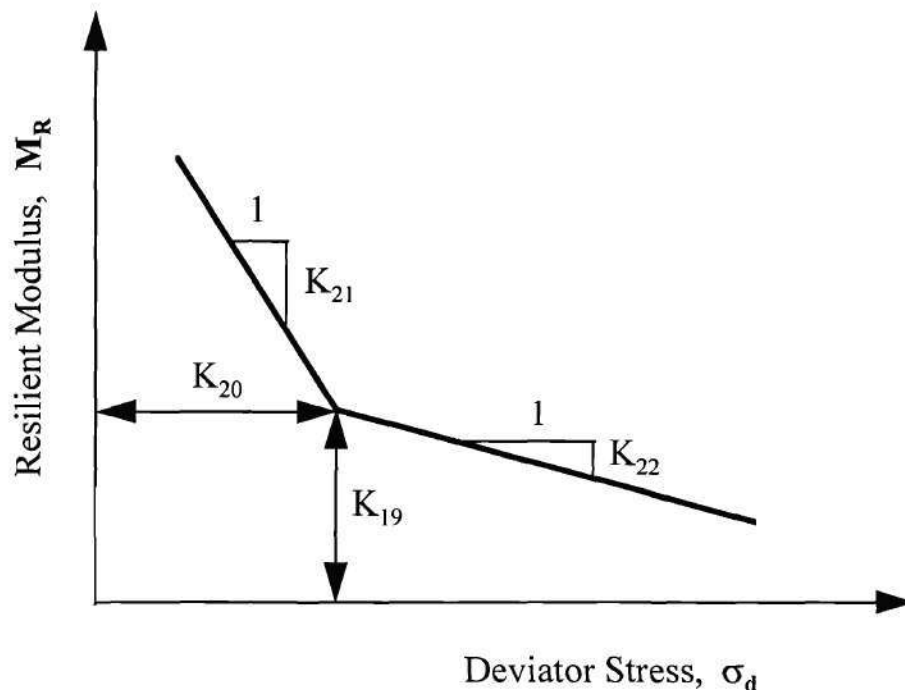


Figure 2.8. General Relationship Between Resilient Modulus and Deviator Stress For Fine-Grained Soils.

Brown and Loach Models. Brown (1979) proposed a nonlinear resilient response model for the subgrade developed from repeated load triaxial testing. The model realistically takes into account the effect of mean normal stress caused by overburden in the pavement subgrade layers. Moreover, the deviator stress calculated within the subgrade was considered to be caused only by the wheel loading. This

minimized the problem of increasing deviator stress, $\sigma_d = \sigma_1 - \sigma_3$, in deep subgrade layers due to the increase in overburden stresses. The model was expressed by:

$$M_R = A \left(\frac{p'_0}{q_R} \right)^B \quad (2.32)$$

where p'_0 is effective mean normal stress caused by overburden, q_R is deviatoric stress caused by wheel loading, and A and B are material constants. Typical ranges of A and B are 2.9 to 29.0 ksi (20 to 200 MPa), and 0 to 0.5, respectively for subgrade soils.

Later, in 1987, Loach proposed a modified version of Brown's model (Loach, 1987; Brown et al., 1987) in which an additional deviatoric stress term q_R was included in Equation 2.32 as follows:

$$M_R = C q_R \left(\frac{p'_0}{q_R} \right)^D \quad (2.33)$$

where C and D are material constants in the range of 10 to 100, and 1 to 2, respectively. The soil used in triaxial testing was a silty clay, known as Keuper Marl, which had been used extensively as the subgrade in the Pavement Test Facility at University of Nottingham. During testing, the effect of mean normal stress due to overburden p'_0 in the

model was simulated by the cell pressure and soil suction. Loach's model was believed to constitute an improvement to Brown's model since it was formulated after completing a comprehensive set of cyclic triaxial tests on samples more representative of soil in the ground than tests reported by Brown (1979).

Nonlinear Analysis

Modifications to the linear elastic layered theory to incorporate nonlinear elastic material properties into the solutions for unstabilized aggregate bases and subgrades started as early as late 1960's. Initial attempts were made to account for a nonlinear modulus changing with stress levels at different depths in the layers, and the assumption of using constant Poisson's ratio was also investigated. In this section, the development will be reviewed of some of the nonlinear solution techniques including finite element methods currently used in pavement analysis.

Early work in nonlinear analysis concentrated on making use of the classical elastic layered solutions in which the modulus was varied with depth only (Kasianchuk, 1968; Huang, 1968). Kasianchuk divided each pavement layer into thinner sublayers to model the variation in moduli with discrete changes. Initial estimates of moduli were input in the first iteration to solve for the stresses due to the circular wheel loading. These stresses were then added to the gravity stresses and new moduli were calculated using laboratory determined material characterizations for base and subgrade. Resilient

moduli were functions of bulk stress [$\sigma_\theta = \sigma_1 + \sigma_2 + \sigma_3$] and deviator stress [$\sigma_d = \sigma_1 - \sigma_3$], respectively. The iterative process continued until the moduli used were compatible with the stress distribution. The major approximation used in this method is that the modulus of each sublayer is assumed constant in the horizontal direction.

Huang (1968) divided a half-space into seven layers to show the effect of nonlinearity of granular materials on vertical stresses and deflections. The lowest layer was taken as a rigid base with a very large modulus. Using a similar method of successive approximations, the modulus of each layer was first estimated and the stresses calculated by layered theory. Using the sum of the computed stresses and geostatic stresses, a new set of moduli were estimated from a nonlinear, bulk stress dependent material model. New stresses were then calculated for the next iteration. The process was repeated until the moduli between two consecutive iterations converged to a specified tolerance.

Shifley (1967) and Duncan et al. (1968) were among the first researchers who applied finite element procedures to pavements thus incorporating nonlinear material behavior in the analysis. The finite element method discretizes the elastic layered system so that the resilient modulus can vary not only with depth but also in the radial direction. Both Shifley and Duncan et al. used iterative techniques to account for the nonlinearity of the granular materials as characterized by the bulk stress and confining stress dependent models. The asphalt concrete and the clayey sand subgrade were considered as linear

elastic. Duncan et al. analyzed the pavements for winter and summer conditions. They found that, especially for the summer condition, tensile stresses were developed beneath the wheel load in the granular base. Shifley applied similar techniques to predict the response on several sections of a full-scale test road.

Dehlen (1969) applied finite element techniques in evaluation of pavements in which an incremental loading procedure was used to account for the variations in both modulus and Poisson's ratio with stress level. For the first increment, the material properties were determined from gravity stresses and the tire pressure was loaded in five equal increments. The elements were checked at each increment with Poisson's ratio not being allowed to be greater than 0.5. The next load increment was then added and the process continued until the full load was applied. The results indicated that the surface deflection pattern was more concentrated and peak deflections were 3 to 13% higher than for a simple linear analysis. Little difference existed between the computed horizontal strains in the asphalt layer using the linear and nonlinear analyses. Also, the maximum vertical stress on the subgrade was 15 to 20% greater for the nonlinear compared to the linear analysis. Dehlen also showed that accurate estimates of the stresses and displacements could be obtained with a depth to the lower boundary of 50 radii and a radial distance of 12 radii to the cylindrical boundary.

Hicks (1970) considered a three layer system consisting of 4 inches (102 mm) of asphalt concrete, 12 inches (305 mm) of granular base over a clay subgrade subjected to a tire pressure uniformly distributed over a circular area. The finite element method was

employed to illustrate the potential differences in the behavior of the total system for two material models used in characterization of granular bases. These models related (1) resilient modulus to bulk stress, and (2) resilient modulus to the confining pressure. Using each model, the problem was solved with the wheel load applied in four equal load increments. The initial moduli were due to the gravity stresses alone, and the moduli for successive increments were computed from the stresses obtained after application of the previous increment.

The surface displacement basin was found by Hicks to be linearly varying for both models with lower displacements predicted by the confining pressure dependent model due to the differences in the states of stress. Similarly, the horizontal stresses predicted by confining pressure dependent model were also lower compared to the bulk stress dependent model, even though the vertical stresses obtained by using each model were nearly the same. In all instances, the principal stress ratios (σ_1 / σ_3) given by the confining pressure model was considerably greater than those obtained given by the bulk stress model. The calculations performed for 3 different Poisson's ratios of the base indicated that a change in Poisson's ratio from 0.35 to 0.5 reduced the principal stress ratio near the surface from about 10 to less than 4.

Later, in 1971, Hicks and Monismith used a similar nonlinear finite element program which applied the wheel load in five increments. At each increment, a tangent modulus and Poisson's ratio were calculated and the values of the resulting incremental strains were determined. This technique was used to predict the resilient response of a

test pavement. The results were consistently better than linear solutions but, in some cases, deviated significantly from measured stresses and strains.

Kirwan and Glynn (1969) first used a finite element program that added horizontal compressive stresses to elements under the load for handling any tensile stresses developed in the granular base. This program was later modified to incorporate nonlinear material behavior by Kirwan and Snaith (1975). The material characterization consisted of a stress dependent modulus and a set of properties for the elements within the granular layer. The load was applied and the new values were calculated for each element using the recently computed stresses. The program, however, had some convergence problems since it used one-step loading rather than an incremental loading scheme.

Stock et al. (1979) followed a similar approach for investigating nonlinear behavior of granular bases using finite element analysis. The granular layer was divided into four sublayers with the wheel load applied in one increment. In each sublayer, the modulus was computed using the stress states existing in the center of each sublayer underneath the load. Granular materials were characterized by using the bulk stress dependent K- θ model (Hicks and Monismith, 1971) with a stress state failure criterion superimposed. Stock et al. concluded that the characteristics of the granular material did not have a significant effect upon the vertical subgrade strain but considerably influenced the lateral tensile strain at the bottom of the asphalt concrete layer.

One of the most comprehensive finite element programs developed to date for the analysis of flexible pavements was the GAPPS7 program which also considered the

analysis of soil-fabric systems (Zeevaert, 1980; Barksdale et al., 1982). Included in the mathematical formulation were such features as: nonlinear soil and fabric materials, friction parameters of the fabric interface, tension stiffness of the fabric, ability to handle large displacements, "no tension" conditions of the granular materials, and the yielding of plastic materials. The nonlinear material stiffness behavior was described by a uniaxial stress strain curve. Resilient response of granular and cohesive layers were represented by using the K- θ model and subgrade bilinear approximations, respectively. The program was also capable of handling geometric nonlinearities which are due to large displacements caused by the change in geometry. The nonlinear analysis of the system was performed using an incremental and iterative procedure. The piecewise incremental solutions were verified after each load increment and iterations were performed to insure equilibrium. The program was verified with several theoretical studies and laboratory measurements especially for the complex soil-fabric behavior at interfaces.

Brown and Pappin (1981) designed the finite element program SENOL to specifically apply the contour model of Pappin (1979) for granular materials to flexible pavement analysis. SENOL uses nonlinear bulk and shear moduli in the granular material. Initial values of these moduli due to overburden stresses are first assigned in the elements. The effects of the wheel load are then computed by applying the load in 10 increments and iterating until satisfactory convergence is reached. A secant modulus approach was followed in the program where the moduli were calculated after each iteration from the total accumulated response until the present load increment. The

SENOL program was also developed to compute an equivalent Young's modulus and Poisson's ratio for calibrating simpler linear elastic layered system programs. The results obtained from the program showed good agreement between the measured and computed stresses and strains. The main advantage of using the contour model for the nonlinear characterization of granular bases is that the horizontal tensile stresses usually encountered in the lower part of the base using linear elastic solutions are no longer predicted.

Another finite element program similar to SENOL is DIANA developed at Delft Technical University in Netherlands (Sweere et al., 1987). The stress dependent resilient behavior of both granular materials and subgrades are modeled in the program by using the contour model with the simplifications applied to the model suggested by Mayhew (1983). The nonlinear iterative and incremental procedures adopted in DIANA were in essence also similar to SENOL program where a secant modulus was calculated using the response due to both overburden stresses and the wheel loading. As compared to the measured stresses and strains in a full-scale test pavement, DIANA predictions, however, were not satisfactory. The measured values for the asphalt tensile strain were typically about half the values calculated with DIANA, while the measured values for the vertical stresses in the base and the subgrade layers were higher than the predicted ones (Sweere et al., 1987).

Crockford (1990) developed an unusual type of nonlinear resilient response model for characterization of granular layers and pavement evaluation in conjunction with the

use of a falling weight deflectometer (FWD). The model included the first stress invariant, octahedral shear stress, unit weight of aggregates and moisture content in the formulation. He incorporated the model and some of the other commonly used ones such as the K- θ and Uzan (1985) models into an user-friendly finite element program named TTIPAVE. The program can handle residual stresses, cross-anisotropic material, and slip condition at layer boundaries using interface elements. Pavements are analyzed as axisymmetric or plane strain layered systems using linear and nonlinear constitutive material models. The program was verified by comparing predicted response with known exact solutions and also with measured response from a full-scale test section. The nonlinear iterations used in TTIPAVE for the material characterizations are usually terminated without convergence due to some limiting values of modulus encountered in the analysis. Another shortcoming of the program a simple, coarse finite element mesh is used for all layered systems. The use of one grid creates geometric limitations and also causes important errors even for a linear elastic problem.

ILLI-PAVE is a commonly used finite element program developed at the University of Illinois (Raad and Figueroa, 1980). The MICH-PAVE program was developed at the Michigan State University (Harichandran et al., 1989) for the analysis of flexible pavements. Both programs consider the pavement as an axisymmetric solid of revolution and use the following resilient response models; K- θ model (Hicks and Monismith, 1971) for granular materials, and a deviator stress dependent bilinear approximation for fine-grained subgrade soils. The principal stresses in the granular and

subgrade layers, following the method of Raad and Figueroa (1980), are modified at the end of each iteration so they do not exceed the strength of material as defined by the Mohr-Coulomb theory of failure. MICH-PAVE uses a flexible bounday at a limited depth beneath the surface of the subgrade, instead of a rigid boundary placed deeper in the subgrade. As a result, MICH-PAVE has a reduced run time and storage requirements compared to most programs.

Huang (1993) has compared the performance of the KENLAYER program which considers nonlinear elastic and viscoelastic multilayer systems with both ILLI-PAVE and MICH-PAVE programs. The KENLAYER program is essentially a layered system program (not a finite element one) where the materials can be modeled as nonlinear and the layers are divided into sublayers. The comparisons are as follows:

- The results of MICH-PAVE appear to be more reasonable than those of ILLI-PAVE when the same material models are used to characterize nonlinear behavior.
- A comparison of deflection basins calculated using the same nonlinear model parameters show that MICH-PAVE and KENLAYER give good aggrement whereas ILLI-PAVE results do not match with the field data.
- A linear elastic analysis indicates that MICH-PAVE gives significantly different results than KENLAYER and ELSYM5 programs.

For linear elastic systems, the correctly developed finite element and layer system programs should yield the same results. Therefore, Huang (1993) concludes that this

failure of MICH-PAVE and ILLI-PAVE to obtain linear elastic solutions should be resolved before using them in practice.

To simulate the resilient behavior of fine grained soils, Brunton and De Almeida (1992) developed a new finite element code named FENLAP for structural analysis of pavements. The program incorporates various nonlinear stress-strain models such as Brown's (1979) model and Loach's model (Brown et al., 1987) for subgrades but only the popular K- θ model for granular materials. An incremental and iterative procedure very similar to the one used in SENOL program was employed for nonlinear analysis. Chord moduli were obtained for the elastic stiffnesses which provided estimations of the average resilient moduli in the linear elastic layers to be used with FWD backcalculation procedures. Although the K- θ model was inadequate for characterization of the granular layers, the model gave reasonable results in terms of vertical displacements for the backanalysis of pavements from the FWD results.

Summary

A historical review of elastic layered theories was presented in this chapter. The one layer Boussinesq semi-infinite halfspace and Burmister's layered theory can give closed form solutions for pavement system problems assuming isotropic homogeneous material properties. The closed form solutions can be readily obtained using several commonly used linear elastic computer programs. Several material characterization

models used for predicting resilient response behavior of unbound granular materials and cohesive subgrades were described in detail. The models which consider both confinement and shear effects in characterization were recommended for practical pavement design use. A complete survey of the existing computer programs, which consider nonlinear material behavior in the analysis, were reviewed in chronological order. The deficiencies of most of the commonly used finite element programs, such as ILLI-PAVE and MICH-PAVE, were discussed to emphasize the apparent need for an improved method of pavement analysis.

CHAPTER III

MODELING OF GRANULAR BASES

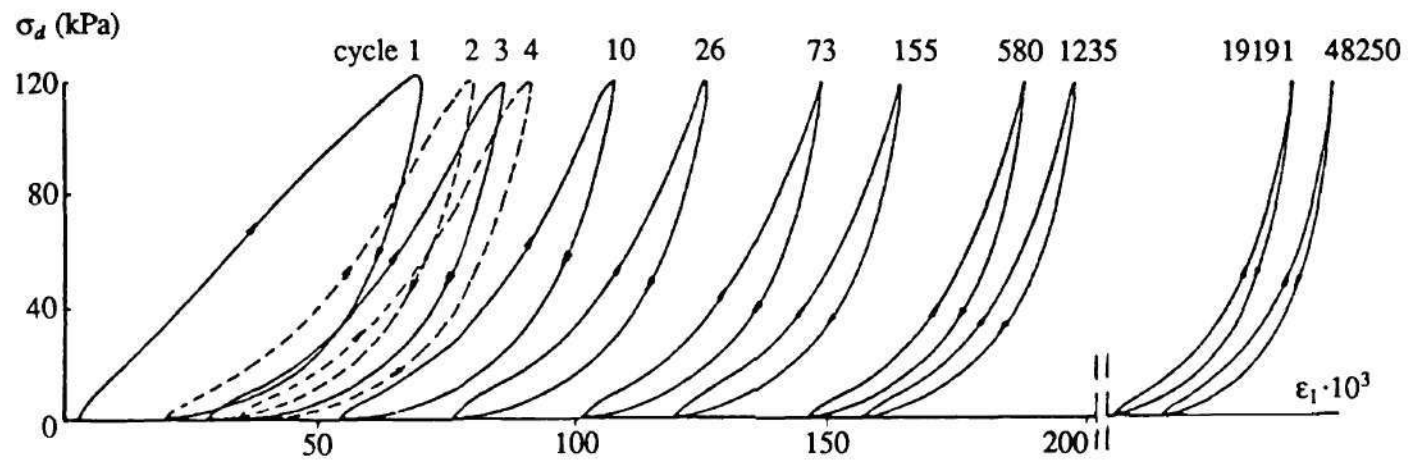
Introduction

To better understand the behavior of flexible pavements with granular bases, it is essential to correctly represent both the material response and geometry of unbound granular materials. Nonlinear material modeling can be achieved through the use of the resilient response models discussed in Chapter 2. Very few studies, however, have considered the material anisotropy which will be shown later to be necessary for predicting the unstabilized aggregate behavior in granular bases (Barksdale et al., 1989; Zeevaert, 1980; Crockford et al., 1990). The modeling of geometry and initial conditions, on the other hand, involve the consideration of several elements such as the: (1) correct representation of pavement geometry (including the allowance of any permanent deformations), (2) compaction and preloading induced residual stresses, (3) horizontal tensile stresses in the granular materials, (4) thermally induced stresses, and (5) ability of granular particles or groups of aggregates to freely move and transfer shear within the base. All of the above items can be considered when the finite element method

with an incremental loading scheme is applied using a nonlinear anisotropic material to model the behavior in the granular base.

The mechanical behavior of granular materials studied in this Chapter is limited to elastic response. Elastic response is realized in flexible pavements after a reasonably large number of the repeated applications of the moving traffic loads. Figure 3.1 shows a typical stress-strain diagram of a granular material tested over a number of load applications in a triaxial apparatus. The slopes of the loading-unloading curves (i.e., the resilient moduli) stay almost the same from 19,191 to 48,250 load cycles as shown in Figure 3.1. Furthermore, the permanent or plastic strain accumulation takes place at a decreasing rate as the number of load applications increases. After about several million repetitive wheel loads (not shown in Figure 3.1), most of the permanent deformation has already taken place in a representative flexible pavement. The remaining deformations are then almost all recoverable and can be considered elastic.

Throughout this chapter, some of the geometrical and material modeling aspects of flexible pavements with granular bases are explained. The importance of compaction-induced residual stresses, cross-anisotropic representation of granular material behavior are discussed. The “no tension” condition of granular bases is described and several analyses performed for correcting tensile stresses in the granular layers are summarized within the framework of axisymmetric continuum theory.



Note: 1 psi = 6.895 kPa

Figure 3.1. Typical Granular Material Behavior Under Repeated Applications of Axial Deviator Load (after Jouve et al., 1987).

Residual Stresses

During the initial construction stages of flexible pavements, large stresses are applied to granular layers by heavy compaction equipment. These layers are subjected to larger stresses during construction than they may ever experience during the service life of the pavement structure. The largest vertical and lateral stresses are caused in the uppermost lift as compaction progresses. After the compaction is completed, field measurements indicate compressive residual lateral stresses become locked in the granular bases (Barksdale and Alba, 1993). These residual stresses developed as a result of compaction of unbound aggregates must be included in determining the initial stress state of granular bases.

Thorough compaction of granular materials in pavements is required to provide increased strength and stability of the layer. The particles, when subjected to compaction, rearrange themselves by translating and rotating to become locked in a final position. After the externally applied compaction stress is removed, this final stage is not a stress free state, but rather a residual stress state. The residual stress state then involves both confinement and particle interlock affected by the highly nonlinear granular material behavior.

The initial stress state used in the analysis of pavements is usually determined only by geostatic stresses due to body weight and are ignored in most linear elastic pavement analyses. A correct modeling of granular bases, however, must include not only these overburden stresses, but also the horizontal residual stresses. Several researchers in the

past have experimentally analyzed the residual stresses produced in granular bases (Stewart et al., 1985; Uzan, 1985; Selig, 1987; Zeilmaker and Henny, 1989; Barksdale and Alba, 1993). According to the research performed by Uzan (1985) and Stewart et al. (1985) these horizontal residual stresses were found to be as high as 2 to 4 psi (14 to 28 kPa) in cohesionless granular materials. Barksdale and Alba (1993) also reported 3 psi (21 kPa) horizontal residual stresses in the upper 6 in. (152 mm) portion of a 12 in. (305 mm) thick granular base obtained from field measurements.

Based on experiments, Broms (1971), Ingold (1979) and Uzan (1985) employed a limit equilibrium approach to predict compaction induced lateral stresses. The vertical stress under the compaction equipment was determined assuming a line loading (Holl, 1941) and a semi-infinite homogeneous elastic halfspace (Boussinesq, 1885). The lateral stresses developed were limited to the maximum compaction loading and unloading conditions applied to a pavement in accordance with the classical earth pressure theory for frictional materials:

(1) Under the loading of compaction equipment, horizontal stresses start to increase according to the active state when the limit equilibrium is reached and horizontal compression develops in the granular layer:

$$\sigma_h = K_a \sigma_v \quad (3.1)$$

where σ_v and σ_h are the vertical and horizontal stresses, and K_a is the coefficient of active lateral earth pressure which is usually expressed in terms of the friction angle ϕ as:

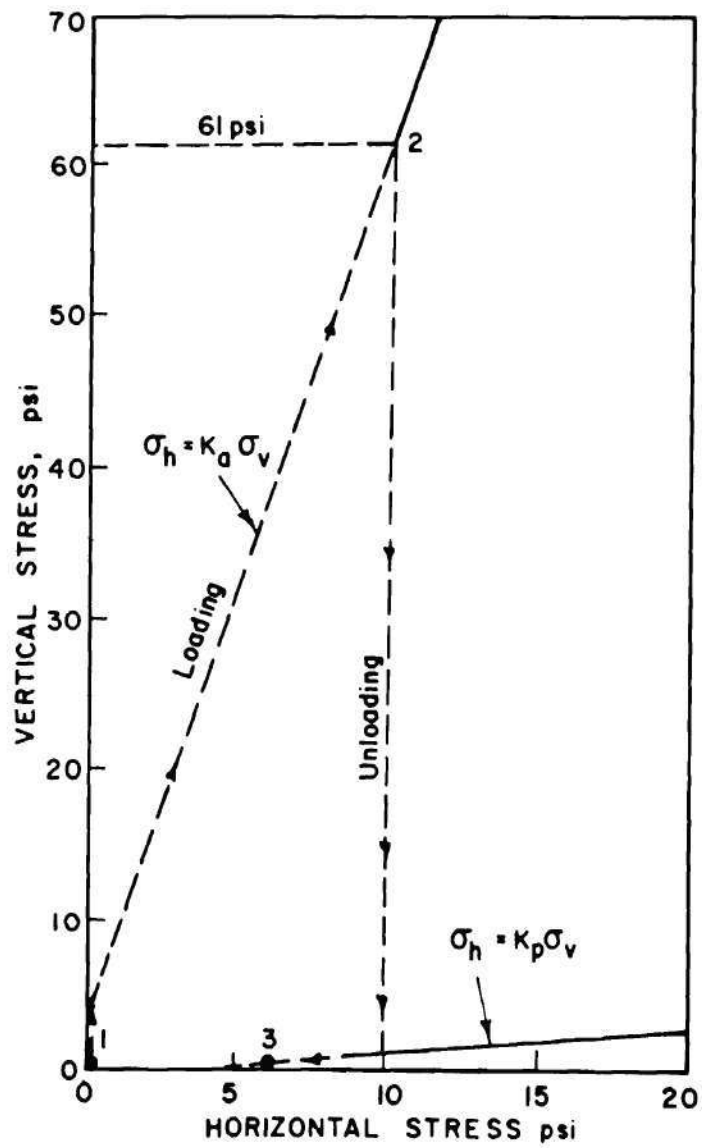
$$K_a = \tan^2 (45 - \phi / 2).$$

(2) After the compaction is completed, during unloading, the vertical stresses decrease. When the limit equilibrium is reached, horizontal stresses also decrease according to the passive state and vertical stresses finally reduce down to the overburden stresses:

$$\sigma_h = K_p \sigma_v \quad (3.2)$$

where K_p is the coefficient of passive lateral earth pressure which is usually expressed in terms of the friction angle ϕ as: $K_p = \tan^2 (45 + \phi / 2)$.

Figure 3.2 shows typical stress paths obtained by Uzan (1985) using the above described method of analysis for compacting a well-graded base material with a friction angle $\phi = 45$ degrees. The base was compacted by a vibratory compactor applying a 3 ton/ft (100 kN/m) line load to the granular layer. A maximum vertical stress of 61 psi (420 kPa) reached during compaction yields a horizontal residual stress of about 6 psi (40 kPa) (see Figure 3.2). Depending on the friction angle ϕ and load intensity (5 ton/ft., 7 ton/ft., etc.), a higher residual stress could be computed.



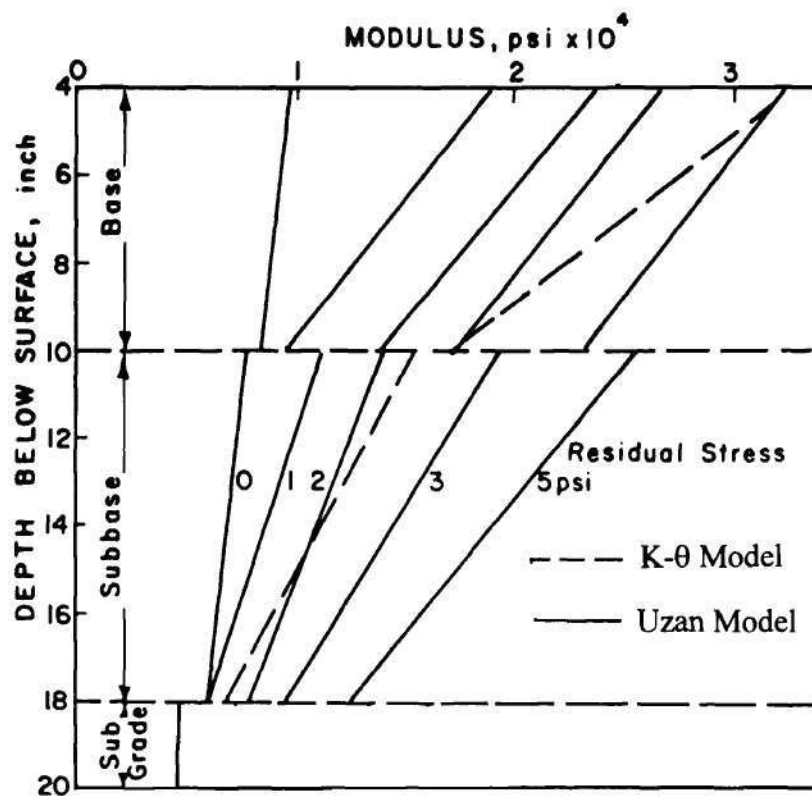
Note: 1 psi = 6.895 kPa

Figure 3.2. Schematic Representation of Stress Path During Compaction (after Uzan, 1985).

Uzan (1985) also investigated the effects of the in-situ compaction residual stresses on the performance of layered systems and granular material behavior. The nonlinear Uzan model was employed for characterization of the granular materials used in the analysis. For lateral residual stresses varying between 0 to 5 psi (0 to 34 kPa), the resilient modulus distribution under the load was plotted through the depth of granular bases and subbases (see Figure 3.3). The moduli, in all cases, were observed to increase with increasing residual stresses.

Duncan and Seed (1986) proposed a hysteretic model for the stresses generated by multiple cycles of loading and unloading. The model used incremental analytical methods for the evaluation of peak and residual earth pressures resulting from the placement and compaction of the soil. The predictions obtained using the model were in excellent agreement with observed laboratory test results. However, the model was complex and required 5 material property parameters including the coefficient of lateral earth pressure at rest K_0 . A simplified version of the model was later incorporated into the SSCOMPPC finite element program for evaluation of soil-structure interaction and compaction effects (Boulanger et al., 1991).

Selig (1987) studied in the laboratory the development of residual stresses in granular materials placed in soil tanks. In a two layer system consisting of sands and clays, horizontal plastic strains were developed in the bottom of the sand layer after the first loading cycle. Initially, horizontal stresses were bigger in the loaded state than in unloaded state. The lateral stresses in the bottom of the layer gradually increased in both



Note: 1 in. = 25.4 mm; 1 psi = 6.895 kPa

Figure 3.3. Distribution with Depth of Base and Subbase Moduli Under A Wheel Load (after Uzan, 1985).

the loading and unloading condition. After about 50 load cycles, the horizontal stress in the unloaded condition was observed to be larger than the stress existing in the loaded condition.

The existence of high horizontal compressive residual stresses in a base or subbase layer were proposed to offset the predicted incremental tensile strength at the bottom of the layer (Selig, 1987). These compressive stresses, if sufficiently large and properly accounted for in the pavement analysis, would reduce or eliminate the so-called "tensile zone" in the granular layers. Based on the results of a series of experiments using a compressometer, Zeilmaker and Henny (1989) found that the residual stresses are time-dependent. As time passes, relaxation of lateral compaction stresses primarily starts far away from the load and progresses towards the uppermost layer. The measured stresses were also found to be lower than predicted with the difference being mainly attributed to neglecting the elastic deformation in the unloading path.

Therefore, proper consideration of compaction-induced residual stresses in granular materials is required to correctly model the behavior of flexible pavements with granular bases. The stress path approach discussed above (Uzan, 1985) and experiments performed by Selig (1987) are useful to approximately estimate the magnitudes of residual stresses existing in the granular layers due to compaction or preloading of the pavement layers. Knowing these locked-in horizontal stresses are essential for determining the appropriate initial stress state to evaluate correctly the resilient modulus values used in the analysis.

Continuum Approach

The analysis of flexible pavements with granular bases commonly requires the solution of stress and strain distributions and load deformation characteristics in elastic layered continua. Although the pavement consists of both bound material such as asphalt concrete and unbound particulate media such as the granular base layers, it has been customary to model all layers including the granular bases using the continuum (see Figure 3.4). A special elastic solid continuum problem applicable to pavements under a circular uniform tire pressure is described under the axisymmetric stress conditions discussed in this section.

In a general three-dimensional continuum, the equilibrium equations of an elementary volume (see Figure 3.4) can be written as follows (Timoshenko and Goodier, 1970):

$$\begin{aligned}
 \frac{\partial \sigma_{xx}}{\partial x} + \frac{\partial \tau_{xy}}{\partial y} + \frac{\partial \tau_{xz}}{\partial z} &= 0 \\
 \frac{\partial \tau_{yx}}{\partial x} + \frac{\partial \sigma_{yy}}{\partial y} + \frac{\partial \tau_{yz}}{\partial z} &= 0 \\
 \frac{\partial \tau_{zx}}{\partial x} + \frac{\partial \tau_{zy}}{\partial y} + \frac{\partial \sigma_{zz}}{\partial z} &= 0
 \end{aligned}
 \tag{3.3}$$

The six constitutive equations for an isotropic continuum are also given as:

$$\sigma = \mathbf{D} \varepsilon \quad \text{with} \quad \sigma = \begin{bmatrix} \sigma_{xx} \\ \sigma_{yy} \\ \sigma_{zz} \\ \tau_{xy} \\ \tau_{xz} \\ \tau_{yz} \end{bmatrix} \quad \text{and} \quad \varepsilon = \begin{bmatrix} \varepsilon_{xx} \\ \varepsilon_{yy} \\ \varepsilon_{zz} \\ \gamma_{xy} \\ \gamma_{xz} \\ \gamma_{yz} \end{bmatrix} \quad (3.4)$$

in which the constitutive relation matrix \mathbf{D} is written in terms of elastic modulus E and Poisson's ratio ν as:

$$\mathbf{D} = \frac{(1-\nu)E}{(1+\nu)(1-2\nu)} \begin{bmatrix} 1 & \frac{\nu}{(1-\nu)} & \frac{\nu}{(1-\nu)} & 0 & 0 & 0 \\ \frac{\nu}{(1-\nu)} & 1 & \frac{\nu}{(1-\nu)} & 0 & 0 & 0 \\ \frac{\nu}{(1-\nu)} & \frac{\nu}{(1-\nu)} & 1 & 0 & 0 & 0 \\ 0 & 0 & 0 & \frac{(1-2\nu)}{2(1-\nu)} & 0 & 0 \\ 0 & 0 & 0 & 0 & \frac{(1-2\nu)}{2(1-\nu)} & 0 \\ 0 & 0 & 0 & 0 & 0 & \frac{(1-2\nu)}{2(1-\nu)} \end{bmatrix}$$

An equivalent formulation of the **D** matrix can be obtained in terms of the secant shear modulus G and the bulk modulus K once the following substitutions are made in the general matrix above:

$$G = \frac{E}{2(1 + \nu)} \quad \text{and} \quad K = \frac{E}{3(1 - 2\nu)} \quad (3.5)$$

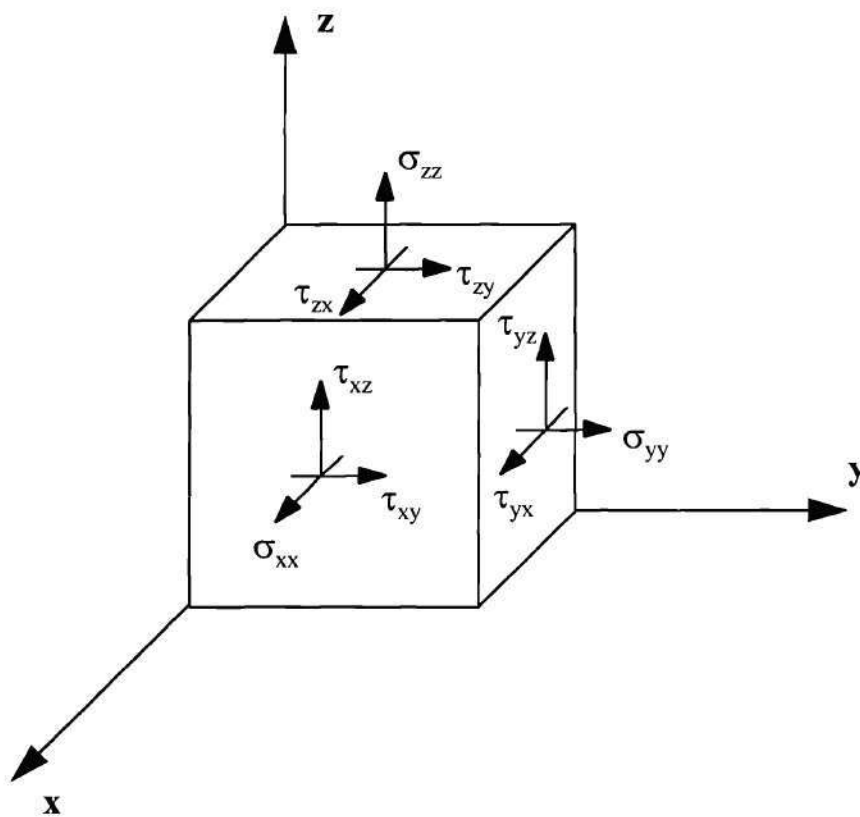


Figure 3.4. The Three-Dimensional Continuum Model.

The stress strain relation therefore can be expressed through the volumetric and deviatoric components using Equation 3.5 as follows:

$$p = K \epsilon_v \quad \text{and} \quad S_{ij} = 2G e_{ij} \quad (3.6)$$

where p is the mean stress, ϵ_v is the volumetric strain, and S_{ij} and e_{ij} are the deviatoric stress and strain components, respectively. Equation 3.6, therefore, enables solution of the continuum problem expressed in terms of isotropic volume change and pure shear deformations. The material models such as the K-G or the contour models discussed previously in Chapter 2 both employ such solutions in which constitutive material behavior is defined through the secant shear and bulk moduli.

In an elastic process, no strain energy disappears. Then, Maxwell's reciprocity theorem for the second order mixed partial derivatives requires that the following relationship must be satisfied at all states of stress (Love, 1944; Allaart, 1992)

$$\frac{\partial p}{\partial e_{ij}} = \frac{\partial S_{ij}}{\partial \epsilon_v} \quad (3.7)$$

where all terms are as defined in Equation 3.6. For triaxial stress conditions, the above equation takes the form:

$$\frac{\partial p}{\partial \epsilon_q} = \frac{\partial q}{\partial \epsilon_v} \quad (3.8)$$

where $q = \sigma_1 - \sigma_3$ is the shear stress, $\epsilon_v = \epsilon_1 + 2\epsilon_3$ is the volumetric strain, and $\epsilon_q = 2/3 (\epsilon_1 - \epsilon_3)$ is the shear strain.

In addition to the constitutive equations, a three-dimensional continuum solution also requires the following six compatibility equations (Timoshenko and Goodier, 1970):

$$\begin{aligned} \epsilon_{xx} &= \frac{\partial u}{\partial x}, & \epsilon_{yy} &= \frac{\partial v}{\partial y}, & \epsilon_{zz} &= \frac{\partial w}{\partial z} \\ \gamma_{xy} &= \frac{\partial u}{\partial y} + \frac{\partial v}{\partial x}, & \gamma_{xz} &= \frac{\partial u}{\partial z} + \frac{\partial w}{\partial x}, & \gamma_{yz} &= \frac{\partial v}{\partial z} + \frac{\partial w}{\partial y} \end{aligned} \quad (3.9)$$

in which u , v , and w are the displacement components in x , y , and z directions, respectively. Boundary conditions with regard to geometry and loading on the pavement complete the continuum model.

A common assumption of the continuum approach of modeling flexible pavements is that the interfaces between the asphalt concrete and the granular base layer and between the base layer and the subgrade have full bonding. The interlocking grains in the lower and upper boundaries of the base layer and the immovable asphalt concrete usually

prevent any slip at the interfaces. It is generally more likely to exceed the shear strength between the grains within the base before slip can occur in any horizontal or inclined grain to grain load transfer direction. Nevertheless, the assumed perfect bonding may be unrealistic in some cases although in practice slip between layers has not been identified as a widespread problem.

Micromechanics Based Continuum Solutions

In the micromechanics approach, the deformation behavior of a granular assembly is described by the above summarized concepts of stresses and strains. The constitutive relationships are derived considering particle interaction and structure of the material. A number of studies have been attempted to model the granular material behavior from micromechanical particle interactions for regular packings (Duffy and Mindlin, 1957; Deresiewicz, 1958; and Makhlof and Stewart, 1967) and for random packings (Digby, 1981; Walton, 1987; Jenkins, 1987; Chang, 1988; and Chang et al. 1992). Recently, with the help of the knowledge gained in heterogeneous and composite materials, the micromechanics approach has been advancing rapidly. However, most of the problems which can be solved by using the approach still do not go beyond idealized materials represented by several thousands of randomly generated microelements. Therefore, it is currently not practical to predict the full response of flexible pavements with granular bases using micromechanics based constitutive stress-strain models.

No Tension Analysis

Burmister's linear elastic layered theory (1945) has been the primary basis of most of the analysis methods commonly used in mechanistic flexible pavement design. When analyzing the case of a stiff layer (i.e., the AC layer) overlying less stiff granular layers, the linear elastic methods indicate a high horizontal tensile stress zone in the unbound granular layer. Even though the granular layer behaves elastically under repeated surface loading from vehicle traffic, a failure would be caused by this large horizontal stress. These horizontal tensile stresses usually occur in the lower portion of the granular base or subbase which is called a "tension zone". Moreover, since the granular materials are not, in general, capable of taking any tension (due to separation), a correcting type of analysis which deals with the reduction or elimination of these tensile stresses is sometimes undertaken. This type of analysis is described as a "no tension" analysis.

Several researchers in the past have investigated the tensile stresses predicted in the granular layers starting from late 1960's when the finite element method first emerged as a powerful tool to be used in pavement analysis. Duncan et al. (1968) indicated the potential for tensile stresses to develop in a granular base layer. Hicks (1970) later concluded from a finite element analysis that the occurrence of tensile stresses in a granular layer is a function of the moduli ratio of the AC to base and also base to subgrade. This finding was in good agreement with what Heukelom and Klomp (1962) found from field vibratory tests.

Using the layered theory, Heukelom and Klomp (1962) studied experimental evidence which indicated that the ratio of the modulus of an untreated granular base to that of the subgrade was not much higher than 2.5 (see Figure 3.5). The tensile stresses were hypothesized to give way to a tendency for decompaction, causing the modulus of the base layer to stabilize at the state where the radial stresses equaled zero (at a modular ratio of 1). Their design criterion for unbound bases was set not to permit horizontal stresses exceeding 0.5 times the vertical stresses plus the horizontal overburden pressure. Heukelom and Klomp (1962) concluded that unbound granular materials were capable of taking limited tensile stresses due to interlocking of the granules caused by forces perpendicular to the radial bending stresses.

Zienkiewicz et al. (1968) were among the first to offer a solution to the problem of rock and unbound aggregate not being able to take the tension predicted by the finite element method. They proposed an iterative tension correction procedure called the "stress transfer method". The horizontal tensile stresses predicted in the granular layer after a linear elastic analysis were counteracted by applying compressive forces equal in magnitude but opposite in direction in the base to maintain equilibrium. If the counteracting force was incremented such that the tensile straining was monotonically increasing, then a unique solution is obtained. In the final iteration, no tension is present and the statics are satisfied.

Using the SENOL nonlinear finite element program, Brown and Pappin (1981) predicted horizontal stress response of granular layers from instrumented pavement test

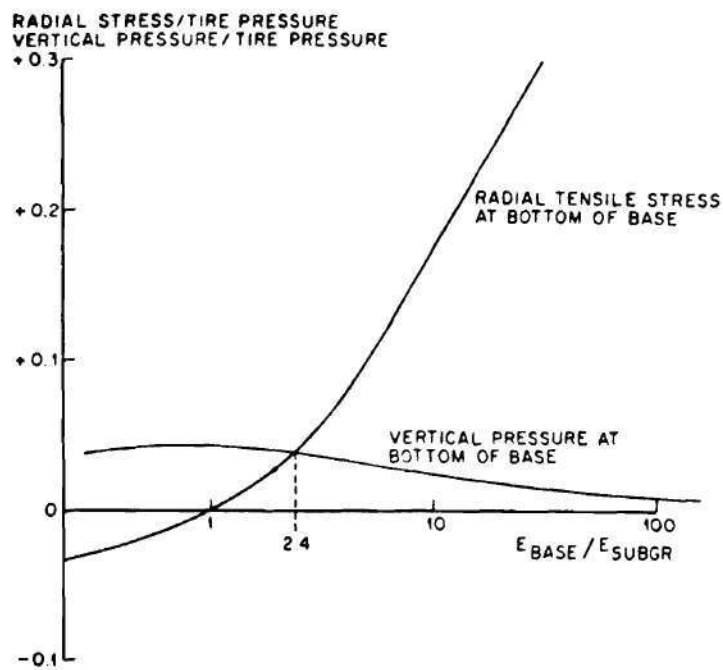


Figure 3.5. Radial Tensile Stress and Vertical Pressure at the Bottom of Base As A Function of Modular Ratio (after Heukelom and Klomp, 1962).

sections. As discussed in Chapter 2, the SENOL program uses for granular materials the contour model which consists of families of experimentally determined resilient strain contours on a q - p stress plot. These contours are used to obtain elastic constants for any calculated stress state changes. During the computation procedure if a tensile value of mean normal stress p was obtained, then *a very low vertical modulus* was assigned to that element. The use of the contour model and the computation procedure seemed to eliminate the tension zone in the base since SENOL did not predict any tensile stresses at the bottom of the granular layer. However, the approach is not realistic and large discrepancies were reported between the predicted and measured stresses and strains. In one instance, the measured radial and tangential strains were lower than the predicted ones by a factor of two.

Raad and Figueroa (1980) presented a method of analysis for granular materials based on incorporating Mohr-Coulomb theory into the finite element method. Principal stresses calculated in the granular base were not allowed to exceed the strength of the material as defined by the Mohr-Coulomb envelope. Using this very approximate method, the horizontal tensile stresses predicted in the granular layer by linear elastic or nonlinear, incremental methods were completely pulled into the compressive zone under the Mohr-Coulomb envelope (see Figure 3.6). This method is currently used by several nonlinear finite element programs routinely used in design, such as Illi-Pave and Mich-Pave, to eliminate horizontal tensile stresses in the unbound base layer. However,

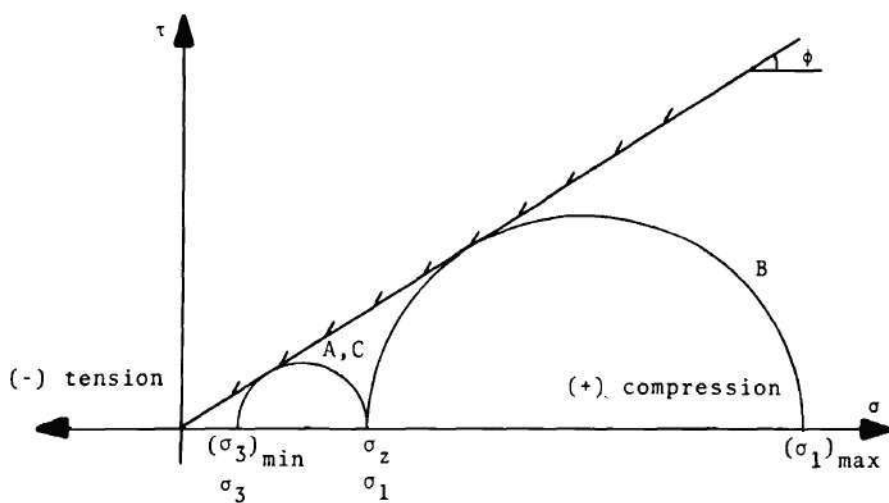
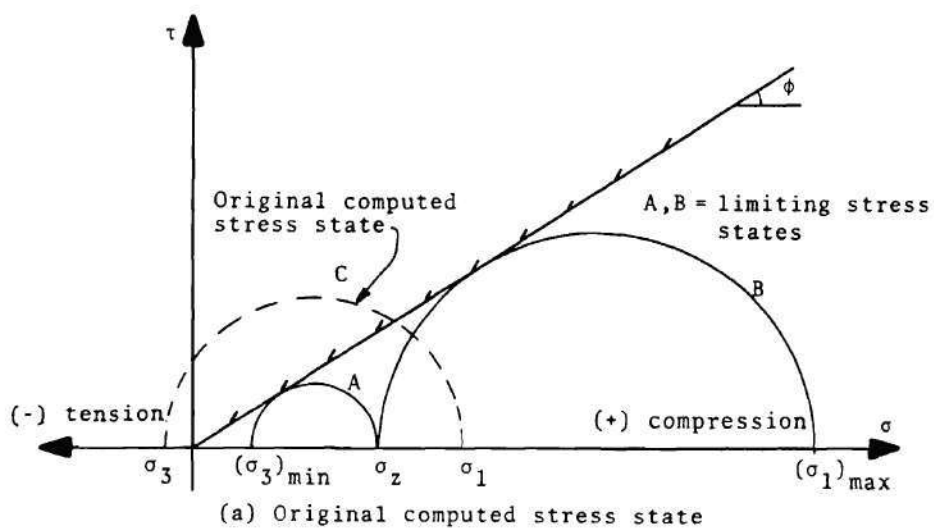


Figure 3.6. Mohr-Coulomb Stress Modification For A No Tension Failure Condition (after Zeevaert, 1980).

arbitrarily changing the stresses in each element without considering overall equilibrium does not appear to be theoretically correct.

Doddihal and Pandey (1984) modified for pavements the originally proposed no tension stress transfer approach by Zienkiewicz et al. (1968). A modification was required since the original version was not intended for granular bases in roadways and had serious convergence problems. In this modified approach, the tensile stresses are also counteracted by compressive nodal loads with the overall equilibrium insured after each iteration. Iterations are continued until tension is eliminated. The modified no tension analysis method achieves much faster convergence (typically in 3 to 4 iterations) than the original method (Zienkiewicz et al., 1968) for the elimination of the mainly horizontal tensile stresses encountered in the lower portion of the granular base.

To investigate the effects of residual stresses on the horizontal stresses in granular bases, Selig (1987) performed tank model experiments where an upper stiff layer was overlying a less stiff layer. Large horizontal compressive residual stresses were shown to develop after compaction in the granular layer. The residual stresses were believed to be the key factor limiting permanent deformation by offsetting the incremental horizontal tensile stresses associated with the loading. The explanation of how pavements with granular bases can carry many load cycles without failure was therefore attributed to the horizontal compressive residual stresses due to initial compaction counteracting the effects of horizontal tensile stresses caused by the wheel loading.

The no tension condition in granular bases is one of the main areas of interest in this study to be investigated in the light of theoretical and analytical work. The question raised by Selig (1987) and given below is a good starting point to initiate further research in the subject which has been almost abandoned since the late 1960's: "How can pavements carry many load cycles without failure under the high horizontal tensile stresses predicted in the granular layer?" Some possible explanations are given as follows:

- The mathematical models and layered theory incorrectly predict horizontal tensile stress. If this is true, improvement in both material and geometrical modeling will be able to offer satisfactory solution.
- Unbound granular materials are indeed capable of taking limited tensile stresses due to confinement, friction forces between granules and interlocking of aggregates (Heukelom and Klomp, 1962).
- The initial state before wheel loading corresponds to a state of both horizontal compressive overburden and residual compaction stresses. Any incremental tensile stresses are counteracted at least partly by the initial residual compressive stresses and hence local failure is prevented.

Probably all the explanations offered above are at least partly valid. No doubt that a better modeling of granular bases is needed especially in the areas of the cross-

anisotropic and particulate nature of the granular material behavior. Emphasis must be given to the load transfer mechanisms in shear and the effects of overburden and residual compaction stresses must also be included in the analysis. And finally, unlike the general assumption that granular materials not take any tension, both Heukelom and Klomp (1962) and Brown and Pell (1967) observed from pavement tests that some magnitude of radial tensile stresses existed in granular bases.

The horizontal stress measurements in soil and also stress measurements in the major principal stress directions are very difficult to make. Additionally, most stress gages are generally unsuitable and not accurate enough to measure tensile stresses. Therefore, experimental stress measurements have considerable uncertainty associated with them. This thesis has been undertaken to investigate the existence of horizontal tensile stresses in the unbound granular layer. In the next sections, some of the essential ingredients for better modeling granular bases are discussed including the cross-anisotropic and block movement approaches of the particulate media.

Cross-Anisotropy Under Axial Symmetry

A cross-anisotropic material representation has different resilient material properties (i.e., resilient modulus and resilient Poisson's ratio) in the horizontal and vertical directions. The usually used isotropic model has the same resilient properties in all directions. Figure 3.7 shows the stratified cross-anisotropic material properties needed

to define an anisotropic material under conditions of axial symmetry. In this case, σ_t is the hoop stress. From symmetry, movements in the θ direction are zero, thus making the shearing strains $\gamma_{r\theta}$ and $\gamma_{z\theta}$ also zero. The general axisymmetric elasticity strain-stress relations for an anisotropic stratified layered system in terms of the in plane and normal to the strata resilient moduli (M_R) and Poisson's ratio (ν) have been given by Zienkiewicz and Taylor (1989) as follows:

$$\begin{aligned}
 \epsilon_r &= \frac{\sigma_r}{M_R^r} - \nu_r \frac{\sigma_t}{M_R^r} - \nu_z \frac{\sigma_z}{M_R^z} \\
 \epsilon_\theta &= -\nu_r \frac{\sigma_r}{M_R^r} + \frac{\sigma_t}{M_R^r} - \nu_z \frac{\sigma_z}{M_R^z} \\
 \epsilon_z &= -\nu_z \frac{\sigma_r}{M_R^z} - \nu_z \frac{\sigma_t}{M_R^z} + \frac{\sigma_z}{M_R^z} \\
 \gamma_{rz} &= \frac{\tau_{rz}}{G_R^z}
 \end{aligned} \tag{3.10}$$

where M_R^r, ν_r = Resilient modulus and Poisson's ratio that correspond to the in-plane behavior in r - direction.

M_R^z, ν_z, G_R^z = Resilient modulus, Poisson's ratio, and shear modulus respectively, that correspond to the behavior normal to the strata in z - direction.

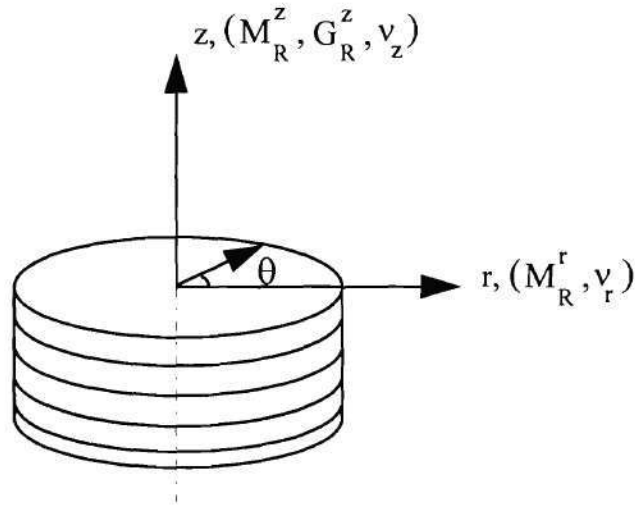


Figure 3.7. Stratified Anisotropic Material Under Axial Symmetry.

The constitutive axisymmetric anisotropic stress-strain relation matrix \mathbf{D} for Equation 3.4 then also takes the form:

$$\mathbf{D} = A \begin{bmatrix} n(1 - nv_z^2) & n(v_r + nv_z^2) & nv_z(1 + v_r) & 0 \\ n(v_r + nv_z^2) & n(1 - nv_z^2) & nv_z(1 + v_r) & 0 \\ nv_z(1 + v_r) & nv_z(1 + v_r) & (1 - v_r^2) & 0 \\ 0 & 0 & 0 & m(1 + v_r)(1 - v_r - 2nv_z^2) \end{bmatrix} \quad (3.11)$$

where $A = M_R^z / [(1 + v_r)(1 - v_r - 2nv_z^2)]$

$$n = M_R^r / M_R^z$$

$$m = G_R^z / M_R^z$$

The variables n and m represent the ratios of horizontal modulus to vertical modulus and vertical shear modulus to vertical resilient modulus, respectively. They are commonly used in the formulation replacing horizontal modulus (M_R^r) and vertical shear modulus (G_R^z). As observed in this study, the use of anisotropic material properties usually results in more accurate modeling and faster convergence when the initial stresses and wheel load are applied incrementally.

The elasticity Equations 3.4 to 3.6 previously summarized in the continuum approach section are valid for an isotropic material behavior. The behavior of a granular medium, however, depends at any point on the particle orientation which is usually determined by the loading conditions in vertical direction. In the case of granular bases in flexible pavements, an apparent anisotropy is induced in the fabric during construction by aggregate placement and then loading from the compaction equipment. The granular layer, therefore, becomes stiffer in the vertical direction than in the horizontal direction even before the wheel load on the pavement imposes further anisotropic loading.

The effects of anisotropic behavior of cohesionless soils have been reported by several researchers to influence the computed stress-strain response. Borowicka (1943) indicated an increase in the calculated vertical stresses near the load when overburden stresses were considered to cause an initial anisotropic material behavior. Similar results were obtained by Barden (1963), and Gerrard and Mulholland (1966) when anisotropy

was taken into account. Zienkiewicz et al. (1966) incorporated anisotropic material formulation into the finite element method to compute stresses particularly in rock mechanics problems. He found that an anisotropic representation was capable of giving good modeling accuracy.

Recently, Barksdale et al. (1989) observed from instrumented test sections that a linear cross-anisotropic model of an unstabilized aggregate base is at least equal to, and perhaps better for predicting general pavement response than the simplified contour model (Brown and Pappin, 1981). In this study, a cross-anisotropic model of the base was used along with an isotropic, homogeneous subgrade. The 8 measured response variables were predicted within a 20% accuracy and gave a better estimate of the vertical subgrade stress and the vertical surface deflection than did the nonlinear isotropic model. The anisotropic characterization was also found to more accurately model the tension effect in unbound granular bases.

Cross-anisotropy or transverse isotropy is often suitable for the special type of anisotropy observed in geomaterials which have been stratified as a result of one-dimensional vertical loading. By assuming different stiffnesses in vertical and horizontal directions, a better estimate can be obtained of the stress state in the system where no tension develops in the granular layer. For example, consider a conventional flexible pavement consisting of unbound base placed over a soil subgrade. The resilient modulus assigned to the elements in the horizontal direction can be easily set equal to zero or a

small value in areas of horizontal tension. The computed lateral stresses using the anisotropic idealization then more correctly depict the “no tension” condition.

Summary

Some of the most important modeling considerations of flexible pavements with granular bases were discussed in this chapter. Among these are the compaction-induced residual stresses, cross-anisotropic granular material properties, and horizontal tension predicted in granular bases. The effects of both residual stresses and cross-anisotropic formulation on the final stress state were described in the unstabilized aggregate base. The classical continuum approach was summarized for the analysis of pavement systems. Several methods proposed for the solution of the “no tension” problem were also presented.

CHAPTER IV

NEURAL NETWORK MODELING OF RESILIENT MODULUS

Introduction

The resilient behavior of granular materials has been well documented over the years to depend primarily on the applied stress state. The nonlinear material models presented in Chapter 2 all use the stress and strain levels as the main response predictors. Several other factors, however, also influence the resilient modulus of aggregates typically obtained from repeated load triaxial tests (Barksdale and Itani, 1989). The following secondary variables have been found to influence resilient modulus: gradation, dry density, degree of saturation, moisture content, compaction level, aggregate size, fines content, and load duration and frequency. A direct inclusion of these variables will not be considered herein. Instead, a new method of modeling resilient response behavior using artificial neural networks will be presented that uses these aggregate properties.

Computation by artificial neural networks (ANNs) has emerged in the last decade as a powerful paradigm which has found applications in almost all engineering branches. Neural networks were inspired by the mechanisms by which real biological neurons work

in the human brain. A neural network model, composed of highly interconnected processing units called artificial neurons (or nodes), manipulates the given input data and reaches decisions. The main advantage of using neural computations is in the area of intuitive types of problems. Such problems require the integration of experience to make decisions which cannot be clearly defined in mathematical terms. The process of learning by a neural network, using the existing available information, is achieved through training in a similar manner as the human brain processes data. A trained network can then predict output response to a high degree of accuracy much faster than sophisticated conventional models.

A new approach of modeling the resilient response behavior of granular materials is given in this Chapter through the use of artificial neural networks. The relative contribution is investigated of aggregate properties on the influence of the resilient modulus (M_R). The experimental resilient moduli obtained from a series of laboratory repeated load triaxial tests on different types of aggregates are used to train an artificial neural network (ANN) material model. The model captures the knowledge of the material behavior within the connections of a self organizing ANN. The ultimate goals in this study are: (1) to show the feasibility of using neural computations as an alternative to conventional stress state dependent resilient response modeling, and (2) to more correctly model the resilient modulus behavior incorporating granular material properties including gradation, dry density, degree of saturation, moisture content, compaction level, aggregate size, fines content.

Background on Neural Networks

A neural network, although being a novel form of artificial intelligence (AI), takes a different approach to AI by not using traditional techniques such as expert systems. Instead, a network of artificial neurons or nodes comprise the ANN geometry which closely resembles the arrangement of biological neurons in the human brain. The decision making process of the brain is simulated by an artificial network of neurons manipulating data among the many nonlinear nodes operating in parallel. Rumelhart et al. (1986) states that the multitasking ability of the human brain to simultaneously *consider a large number of pieces of information and constraints* is actually due to this powerful neuronal architecture of connectionism or parallel distributed processing.

Biological neurons are the basic computing units in the human brain. Each neuron is capable of receiving a number of analog input signals at once and output an analog signal. The strength of this output is determined by the input signals and the processing logic of the neuron. The biological neuron is replaced in artificial neural networks by the processing element called the artificial neuron or node. The artificial neuron also has many input paths and can output a signal, usually binary, to a single or several other processing elements.

The main type of ANN used in this Chapter is referred to as a multilayer, feed-forward neural network which was also called a perceptron by Rosenblatt (1958). The

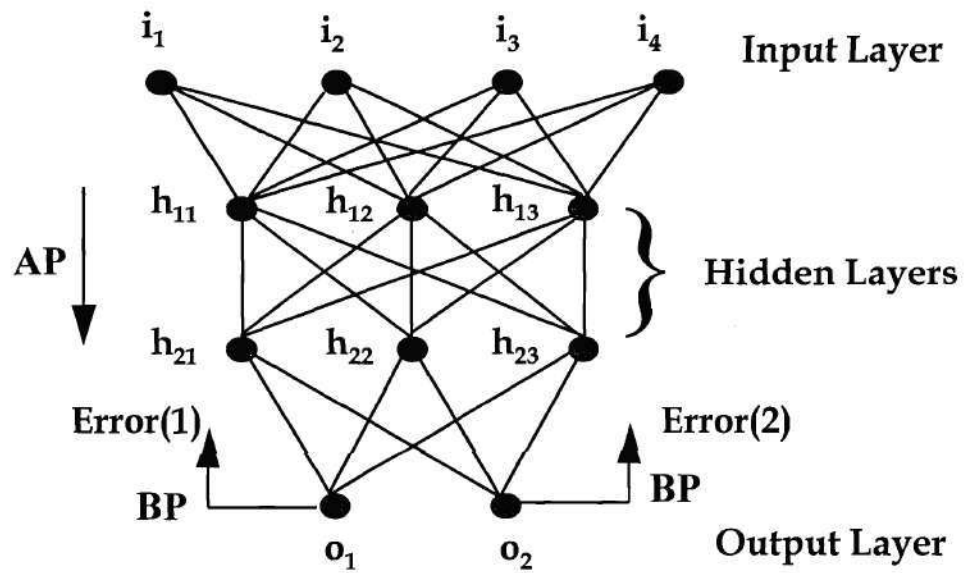
following are essential to perceptrons: (1) A feed-forward propagation rule, (2) a network topology (i.e., the number of nodes, layers, and their connectivity), and (3) a learning rule. The error back-propagation algorithm (also known as the generalized delta rule) is the most commonly used learning rule (Rumelhart et al., 1986). The feed-forward neural networks which use the error back-propagation learning rule is generally referred to as back-propagation neural networks. A typical back-propagation neural network used in this study is sketched in Figure 4.1.

The multilayered back-propagation ANN has usually one input layer, one output layer, and the constructed processing elements (artificial neurons) named as hidden layers. The hidden layers are sandwiched between the input and output layers. The network operation consists of a highly nonlinear functional mapping of the neurons in hidden layers between the input and output variables.

In perceptrons, each artificial neuron or processing element receives several input signals X_j originating from previous nodes and then processes each signal considering its connection weight W_{ij} (see Figure 4.2). The relationship between the input signals and the level of internal activity of the processing element is given by:

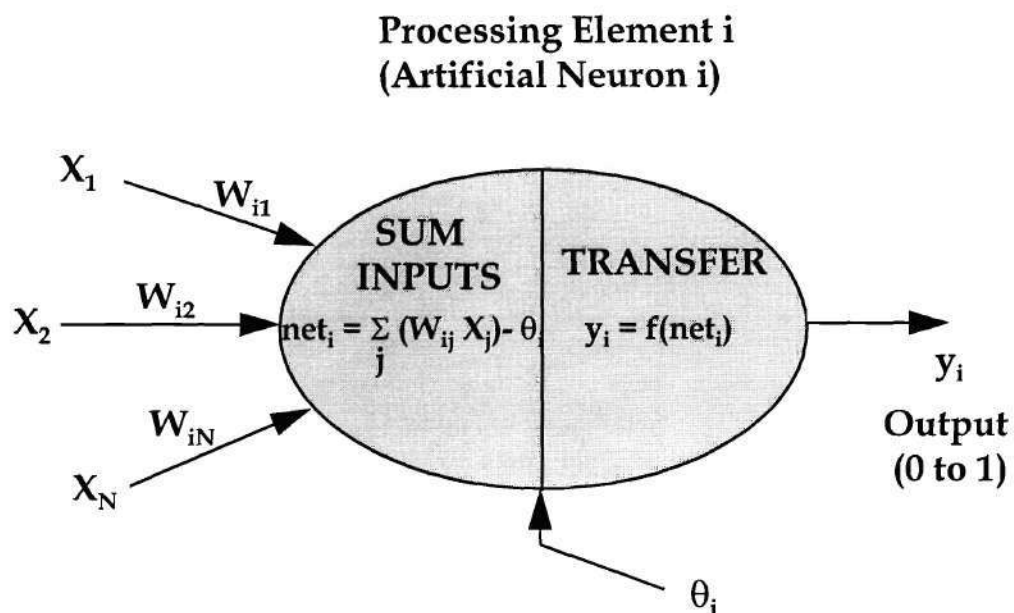
$$\text{net}_i = \sum_{j=1}^N (W_{ij} X_j) - \theta_i \quad (4.1)$$

where net_i = Net input signal (level of internal activity),



AP : Direction of Activation Propagation,
BP : Direction of Error Back-Propagation,
 i_1 to i_4 : Input variables,
 h_{11} to h_{23} : Artificial neurons (processing elements),
 o_1 to o_2 : Output variables.

Figure 4.1. A Typical Back-Propagation Neural Network.



x_1, x_2, \dots, x_N : Set of Inputs,

w_{ij} : Connection Weights (Strength of a Single Biological Synaptic Connection),

θ_i : Bias Term (Corresponds to an Activation Threshold),

net_i : Net Input Signal (Level of Internal Activity),

Transfer Function : $f(x) = 1/(1+e^{-x})$, Sigmoidal Function.

Figure 4.2. Summation and Transfer Functions of a Typical Artificial Neuron.

W_{ij} = Connection weight between artificial neurons i and j ,

X_j = Value of signal coming from previous node j ,

θ_i = Bias term of node i (corresponds to an activation threshold),

N = Number of input signals from previous nodes.

When the weighted sum of the input signals exceeds the activation threshold θ_i , the artificial neuron outputs a signal y_i dictated by a transfer function $f(x)$. The output signal is then expressed as a function of the net input signal by:

$$y_i = f(\text{net}_i) \quad (4.2)$$

where $f(x) = 1 / (1 + e^{-x})$, is a sigmoidal function which gives a value between 0 or 1 for the output y_i .

The neural network modifies the connection weights between the layers and the node biases in ensuing iterations to allow a type of learning for the network. The weights and node biases are shifted until the error between the desired output and the actual output is minimized. Wasserman (1989) describes the learning process as follows: "Learning (or training) is the process whose objective is to adjust the link weights and node biases so that when presented with a set of inputs, ANN produces the desired outputs."

After each feed-forward sweep of the ANN is completed in the direction of activation, the squared error terms E^k between the outputs y_i and the target values t_i (actual values in the output layer) are computed from the following:

$$E^k = \frac{1}{2} \sum_i [t_i^k - y_i^k]^2 \quad (4.3)$$

where i denotes the individual neurons, and superscript k represents the individual data values from the training data set. Note that the output y_i in the above equation is actually a function of the sigmoidal function given in Equation 4.2.

The change in the connection weights (ΔW_{ij}) between the nodes to be adjusted during the learning process is related to the minimization of the average squared error E . To minimize the squared error E^k , the derivative of the error with respect to the connection weight W_{ij} between nodes i and j is required as follows:

$$\Delta W_{ij} = -\eta \frac{\partial E}{\partial W_{ij}} = -\eta \sum_k \left(\frac{\partial E^k}{\partial W_{ij}} \right) \quad (4.4)$$

where η is a learning coefficient > 0 . Using the chain rule of differentiation, the derivative term $\partial E^k / \partial W_{ij}$ can now be written as:

$$-\frac{\partial E^k}{\partial W_{ij}} = -\frac{\partial E^k}{\partial y_i} \frac{\partial y_i}{\partial \text{net}_i} \frac{\partial \text{net}_i}{\partial W_{ij}} = -\delta_i^k \frac{\partial \text{net}_i}{\partial W_{ij}} = -\delta_i^k X_j \quad (4.5)$$

in which $\delta_i^k = (\partial y_i / \partial \text{net}_i) * (\partial \text{net}_i / \partial W_{ij})$ is defined as “delta” term of the generalized delta rule and is given by:

$$\delta_i^k = \begin{cases} (t_i^k - y_i^k) f'(\text{net}_i^k) & \text{for output layers} \\ \sum_m \delta_m^k W_{im} f'(\text{net}_i^k) & \text{for hidden layers} \end{cases} \quad (4.6)$$

where the letter “m” represents the nodes in the network below the current i’th layer in towards the output layer (see Figure 4.1). Since the back-propagation algorithm starts from the output layer, the calculations progress implicitly in the direction towards the input layer. The derivative of the sigmoidal function $f'(x)$ to be used in the above equation can be given in terms of the function:

$$f'(x) = f(x) \{1 - f(x)\} \quad (4.7)$$

now substitute Equation 4.7 in Equation 4.6 for easy computation of deltas.

During each iteration (it), the connection weights from node j to i are updated as follows:

$$W_{ij}(it+1) = W_{ij}(it) + \eta \sum_k \delta_i^k X_j^k + \alpha [W_{ij}(it) - W_{ij}(it-1)] \quad (4.8)$$

where α is called the momentum (or acceleration) term added to stabilize the training process. The summation is done over all individual data in the training set. The inputs to the nodes in the back-propagation direction are taken from the outputs of the nodes in the preceding layer, i.e., $X_j^k = y_j^k = o_j^k$ (for the first hidden layer). Similarly, the bias term θ_i is also updated at each iteration by an equation of the form:

$$\theta_i(it+1) = \theta_i(it) + \eta \sum_k \delta_i^k + \alpha [\theta_i(it) - \theta_i(it-1)] \quad (4.9)$$

As the iterations progress, the network repeatedly cycles through the training set. The parameters α and η in Equations 4.8 and 4.9 help provide an accurate approximation of the unknown mean squared error (MSE) minimum. Iterations must be continued until an apparent decrease in the maximum MSE to an acceptable level is observed. By using

the momentum term α in the search, settling into a local minimum or oscillating endlessly about the global minimum can be prevented (Hertz et al., 1991; Meier, 1995). In this study, a constant value of 0.5 has been used for both the training rate and the momentum term. Both parameters have also been kept constant throughout the training process.

Literature Review: Material Modeling Using Neural Networks

Very little material modeling has been carried out using neural networks since the pioneering work of Ghaboussi et al. (1991). Ghaboussi used back-propagation neural networks to model the behavior of plain concrete under monotonic biaxial loading and compressive uniaxial cyclic loading. He concluded that neural networks to model materials is very promising.

Ellis et al. (1992) trained an ANN which accurately modeled the mechanical behavior of medium to fine sand from a set of triaxial test data. The trained network was able to predict the results of other experiments. The influences of relative density and confining pressure on mechanical behavior were successfully simulated including the effects of strain softening and dilatancy. Pidaparti and Palakal (1993) described the behavior of composites using two different back-propagation ANNs. Experimentally determined nonlinear stress-strain curves for graphite-epoxy laminates were accurately modeled under monotonic and cyclic loadings. The networks developed in this study

helped identify important engineering behavior aspects of composites, such as breaking and fracture stress.

Penumadu (1993) employed neural networks for modeling the anisotropic rate dependent behavior of clays. The training set consisted of stress-strain data obtained for a kaolin-silica mix under a pressuremeter stress path. The measured strains in the testing set were accurately predicted using stress level and strain rate as the input variables. Okuda et al. (1994) reported the results of a viscoplastic material modeling study using the ANNs. Two three layer, back-propagation neural networks were trained with the input data calculated from existing constitutive equations. The neural networks were successfully trained to describe the fatigue-creep interactions, especially the transient behavior.

Little work in this area, therefore, has been done up to now in the development of neural network-based models to define the constitutive behavior of engineering materials. The approach in most of these studies has been to incorporate the results obtained from a series of experiments on selected materials to train a back-propagation neural network. The prediction capability of such a network is then limited to how comprehensive the information used in the training set is. With a relatively large set of available input data over wide ranges of values, a well-trained network not only can reproduce the experimental results, but also predict the results of other experiments yet to be performed. In a way, the neural-network based solutions approximates the laws of classical

mechanics to define the material behavior using vast knowledge gained through experience.

Modeling Resilient Modulus of Granular Materials

The current use of neural networks in this study has been focused on modeling the resilient modulus of granular materials as obtained from laboratory repeated load triaxial tests. The different stress levels used during testing together with the aggregate properties of the triaxial specimens constitute the input information needed in an ANN model for predicting the resilient modulus as the output. The measured moduli are then used to train the ANN with the error back-propagation algorithm. A well trained network can hopefully predict not only the resilient response for different stress states but also consider the effect of the physical characteristics of the material. The comprehensive resilient modulus tests performed on granular base materials at Georgia Tech (Alba, 1993) were used for training the back-propagation neural network.

Repeated Load Triaxial Tests

Alba (1993) performed a series of repeated load triaxial tests on granular base materials to develop a prototype resilient modulus test and to evaluate testing details that influence resilient modulus. Different materials were tested ranging from clean crushed stone to gravels with high fine contents. The tests were performed on 6.0 in. (152 mm)

diameter by 12 in. (305 mm) height triaxial specimens. The same specimen preparation and testing procedure were used for each material tested. Several experiments were conducted taking into account the effects of preconditioning, loading pulse shapes and different gradations. The extensive database obtained were used in statistical analyses to evaluate reliability, variability, and repeatability of the experimental procedures. Various resilient modulus models, such as those of Uzan (1985) and UT-Austin (Pezo, 1993), were fitted with the experimental data using multiple regression analysis.

Three sets of granular materials were tested following the Strategic Highway Research Program P-46 testing procedure (SHRP P-46) for Type I materials. These material sets comprised materials described as: (1) Georgia Tech (GT) bases, (2) SHRP bases, and (3) North Carolina (NC) bases. Each set of material consisted of specimens with different aggregate properties: gradation, dry unit weight, water content, percent fines content, percent compaction of AASHTO T-180 (1990), and plasticity index.

Tables A.1 through A.3 in Appendix A summarize the detailed input data used in the ANN study obtained from the laboratory testing of the three sets of materials, i.e. GT, SHRP, and NC bases. The aggregate properties for each specimen are given together with the measured resilient moduli obtained from testing at 15 different stress states (i.e., different cyclic axial stress and confining pressure). A total of 540 individual tests performed on 36 materials. Different aggregate properties comprise the data set used in the present study for both training and testing of the back-propagation ANN model.

ANN Model

Before training a back-propagation ANN, the network architecture must be established (see Figure 4.1). The input and output variables define the number of neurons needed in the first (input) and the last (output) layers of the network. The number of hidden layers and the number of neurons used in each hidden layer can not, however, be easily determined since well-established rules do not exist (Hertz et al., 1991; Meier and Rix, 1994). Therefore, in most ANN applications, a trial and error method must be employed among different network architectures to find the optimum network architecture which results in the lowest mean squared error (MSE).

Stress state is known to be the primary variable (Barksdale and Itani, 1989) that is used in all training. A preliminary study was undertaken to determine the relative contributions of the secondary input variables (i.e., the aggregate properties shown in Tables A.1 to A.3) to resilient response modeling. A commercially available software program called "AIM" (AbTech Corporation, 1992) was used as a first step to fit several input data sets with polynomial networks for predicting the resilient modulus. The AIM program automatically discovers the best polynomial network architecture to approximate the output response. The program also provides a complete environment to synthesize, analyze, and encode polynomial networks.

A thorough research using the AIM program found different combinations of the secondary variables (aggregate properties) with stress levels had relatively different influence in obtaining better fits of the resilient moduli. Some of the aggregate properties

which have more variation among different material types were observed to have greater influence on the resilient response predictions than the others. These properties were the coefficient of uniformity (C_u), average aggregate size (D_{50}), dry unit weight (γ_d), and percent fines content which were then chosen for use in the ANN model as secondary input variables. The six input variables to the model then consisted of the deviator stress (σ_d) and the confining pressure (σ_3) as the primary variables, and C_u , D_{50} , γ_d , and the percent fines content of the aggregates as the secondary ones.

With the number of neurons required for the input and output layers determined, the optimum network architecture was investigated by trial and error for a two-hidden layer network. Any functional mapping between the input and the output can be approximated with a neural network consisting of one hidden layer (Hornik et al., 1989). However, the use of two hidden layers drastically reduce the number of neurons in each layer. The prediction capacity of the network is also directly proportional to the number of hidden layers and the number of processing elements in each layer.

Six two-hidden layer network architectures were trained with 6 input nodes and 1 output node. The back-propagation ANN program developed by Meier (1995) was used for the training process which consisted of iteratively presenting training examples to the network. The 540 individual examples used were first normalized between the values 0 and 1, completely shuffled, and then split into 405 training sets and 135 testing sets. One training epoch was completed after each pass over the 405 training examples. The 135

testing examples were then used to monitor the training progress. Table 4.1 presents a summary of the training and testing mean squared errors (MSEs) obtained after 10,000 training epochs for different network architectures. A 6-4-4-1 architecture, for example, stands for 6 input nodes, 4 processing nodes in both hidden layers, and one output node.

Table 4.1. Mean Squared Errors Calculated Using Different Network Architectures after 10,000 Training Epochs.

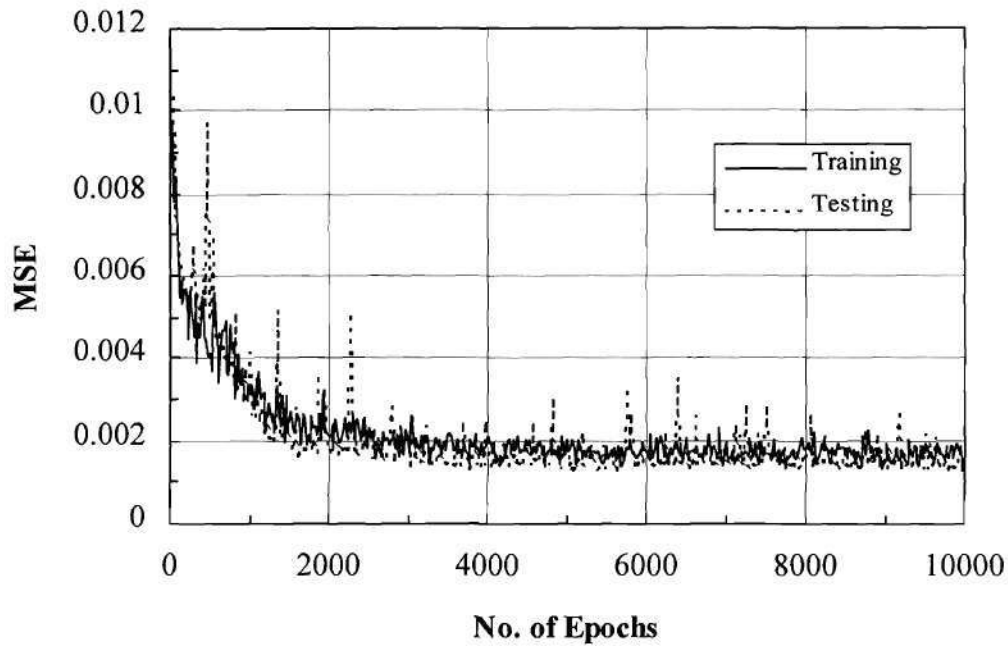
Trial No.	Network Architecture	MSE (Training)	MSE (Testing)
1	6-3-3-1	0.0027	0.0028
2	6-4-4-1	0.0020	0.0018
3	6-5-5-1	0.0018	0.0017
4	6-6-6-1	0.0019	0.0020
5	6-7-7-1	0.0017	0.0019
6	6-8-8-1	0.0013	0.0020

The optimum network architecture for resilient modulus modeling was found to be the 6-5-5-1 network (see Table 4.1). Several factors considered in reaching this decision are summarized as follows: (a) The lower capacity networks (6-3-3-1 and 6-4-4-1) gave higher MSEs after 10,000 epochs than the 6-5-5-1 network. (b) The higher capacity

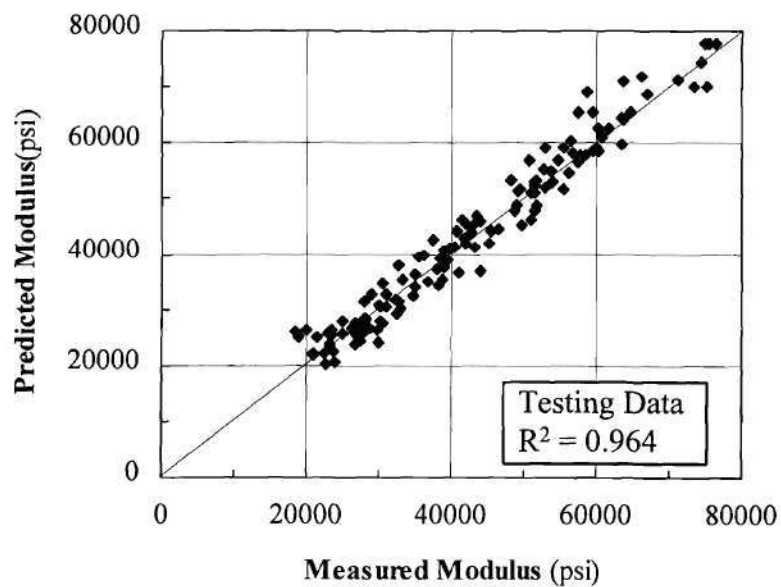
networks (6-7-7-1 and 6-8-8-1), on the other hand, resulted in considerably greater testing MSEs than the training ones. This is a clear indication of overtraining caused by the excessive capacity. (c) The 6-5-5-1 network architecture gave the lowest average MSEs after 10,000 epochs with no overtraining observed.

Figure 4.3 shows, for the optimum 6-5-5-1 network, the training progress and comparisons of the predicted with the measured moduli using the testing data. The MSEs of both the training and testing sets rapidly drop as the training epochs are completed. Both curves asymptotically approach a similar minimum level. Some high variations of the MSE (bumps) are observed at several epochs in the testing data compared to the smoother curve of the training progress. These variations, however, also decrease to negligible amounts as 10,000 epochs are reached. A plot of predicted resilient modulus as a function of the measured value is given in Figure 4.3b. The nonlinear function mapping ability of the neural networks is demonstrated by the reasonably good agreement of the predicted with the measured.

Figure 4.4 presents for two materials the ANN model resilient modulus predictions as a function of stress levels and measured vertical strains. For both materials, plotted randomly among the 36 aggregate types, predicted resilient moduli match very closely with the measured data points. The increase in deviator stress at a constant confining pressure generally results in an increased modulus which is correctly predicted by the ANN model. The good agreement observed between the measured and computed moduli, shown for two materials in Figure 4.4, is actually observed for all the materials

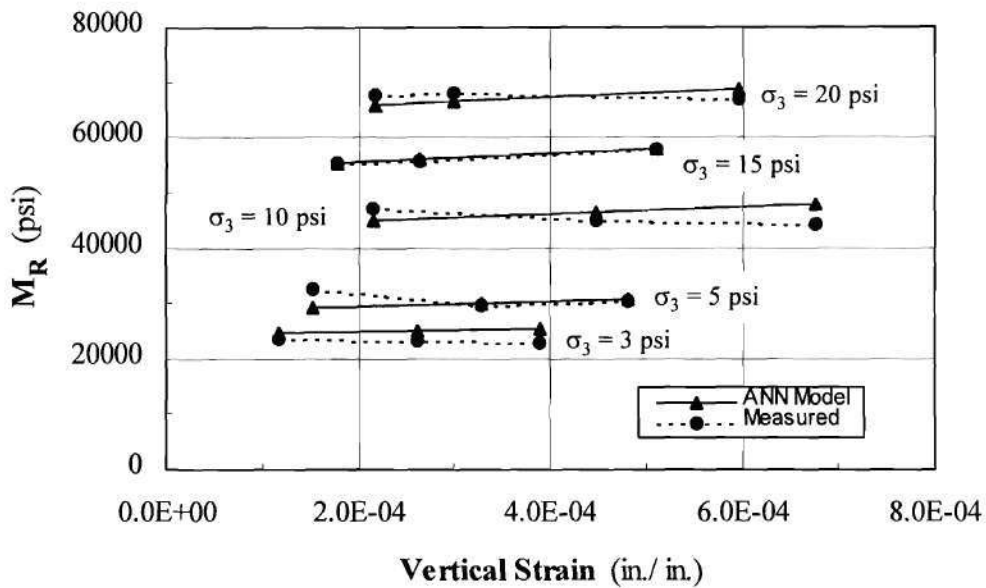


(a) Mean Squared Error Variation with Training Epochs

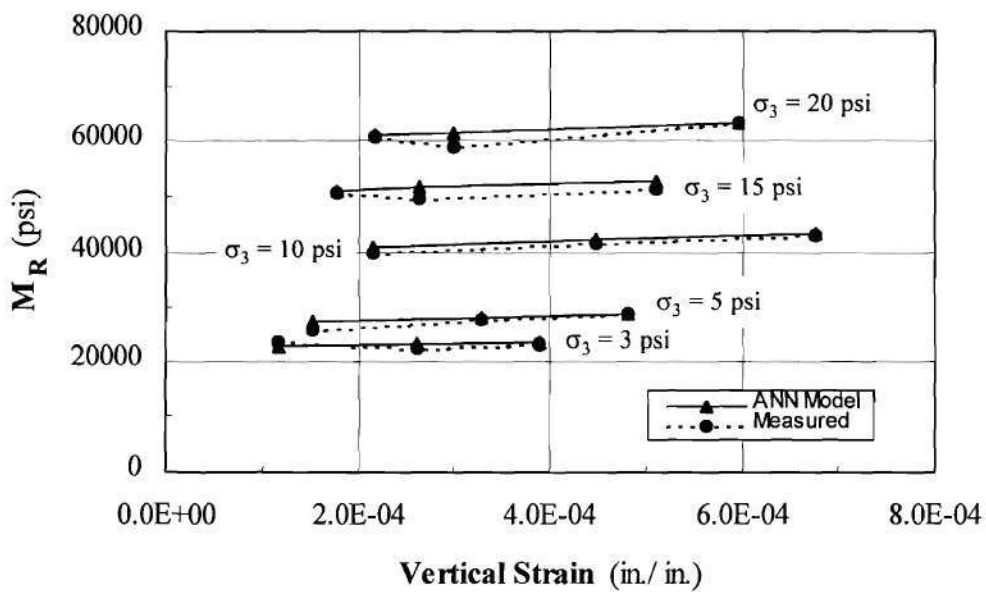


(b) Computed Moduli Compared With Measured Values
(1 psi = 6.895 kPa)

Figure 4.3. Training Progress and Predicted Results for 6-5-5-1 Network.



(a) GT Base B4S5



(b) NC Base 10F3S2B

Note: 1 in. = 25.4 mm; 1 psi = 6.895 kPa

Figure 4.4. ANN Predictions of Resilient Modulus for Materials with Varying Stress Levels.

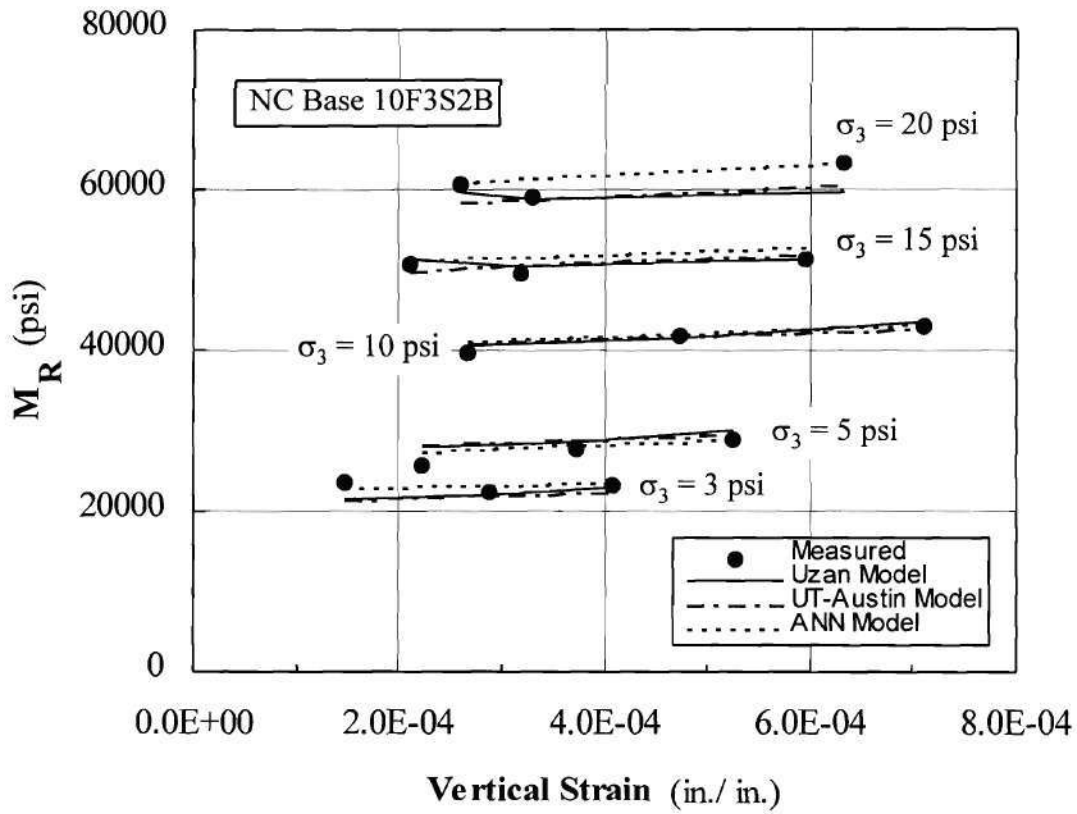
tested. Therefore, the secondary input variables which are not shown on the figure but were used in the analysis, have definitely contributed to the accuracy of the 6-5-5-1 ANN model.

Further comparisons of the ANN model predictions with the popular Uzan and UT-Austin models are shown in Figure 4.5 for the NC Base designated as 10F3S2B. For all different confining pressures considered, the ANN model gives good agreement with the measured values and similar results to the Uzan and UT-Austin models. For the lowest confining pressure $\sigma_3 = 3$ psi (20.7 kPa) and highest $\sigma_3 = 20$ psi (137.9 kPa), neural network gives even better results than the two conventional models.

Several other attempts were also made to train different networks with various combinations of deviator stress σ_d , confining pressure σ_3 , vertical stress σ_1 , and bulk stress σ_θ used for the primary stress variables. Different ANN models were developed using all two variable combinations of these stresses together with the 4 aggregate properties. Similar results, however, were obtained in terms of training progress and model predictions, and hence only the 6-5-5-1 ANN model with σ_d and σ_3 was studied further.

Validation Analysis

A validation study was undertaken for investigating the functional relations captured within the connections of the trained 6-5-5-1 neural network. It was hoped that



Note: 1 in. = 25.4 mm; 1 psi = 6.895 kPa

Figure 4.5. Comparison of ANN Model Predictions with Uzan and UT-Austin Models.

using this ANN model, resilient modulus predictions could be obtained for material types that were not considered among the 540 data sets used in the training and testing of the model. The nonlinear functional mapping adapted by the ANN model would then be used to compute moduli from any input variables given within the ranges of the training input data.

Figure 4.6 shows poor agreement between the measured and computed moduli for a sample having newly introduced material properties. The ANN model, in this case, predicted resilient moduli much higher than the actual values at high confining pressures. Only two of the aggregate properties, percent fines content and dry unit weight, were entered as numbers different than used in the training data set (see Figure 4.6). The combination, however, constituted a new aggregate property set unfamiliar to the 6-5-5-1 ANN model.

Two special neural network architectures were then constructed to conceive the influence of aggregate properties in the 6-5-5-1 ANN model. The first network considered only the two stress state variables in the input layer, whereas the second one had only the 4 aggregate properties as the input variables. Using the same 540 training and testing data sets, no training at all was achieved this time for either of the two neural network architectures. The discrepancy between the measured and predicted results observed in Figure 4.6 was then explained by the 6-5-5-1 ANN model's not finding any functional mapping between the aggregate properties and the computed resilient moduli.

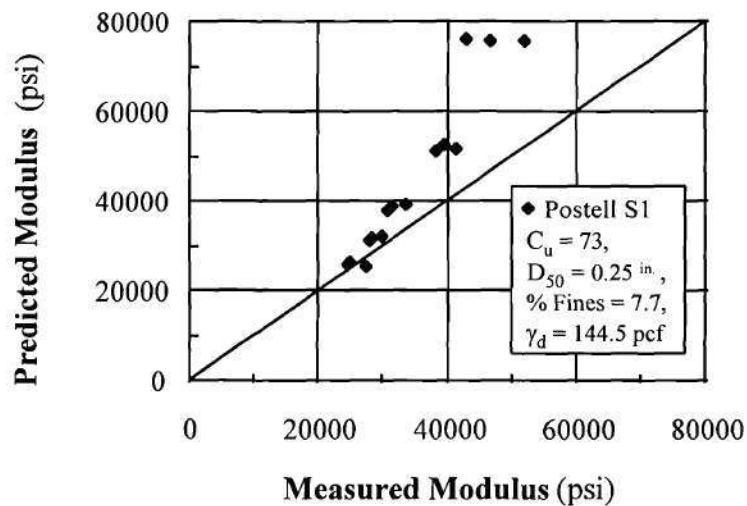


Figure 4.6. Computed Moduli Compared with Measured Values for A Sample Having Newly Introduced Material Property Set to the ANN Model.

The 6-5-5-1 ANN model had in essence memorized the 36 material types used to train the back-propagation neural network as a result of its excessive learning capacity. For each material type (represented by the 4 aggregate properties), the network had correlated the resilient moduli to the applied stress states similar to performing a multiple regression analysis to obtain the material constants for the Uzan or UT-Austin models. When tested with the new material properties, the 6-5-5-1 ANN model was then incapable of accomplishing mappings for material types that it did not memorize.

Summary

The 6-5-5-1 ANN model indeed proved itself for individual material types to accurately model the resilient modulus variation with stress state as shown by the good agreement in Figures 4.4 and 4.5. The developed back-propagation neural network was able to distinguish between 36 material types and perform different nonlinear functional mappings to define the resilient behavior of each material at the same time. The increase in deviator stresses at one constant confining pressure was correctly predicted by the ANN model to cause increase in the resilient modulus.

No functional relations were, however, discovered between the aggregate properties (as the secondary input variables) and resilient moduli by the 6-5-5-1 ANN model. The learning achieved by training of the model can be evaluated more in the area of pattern recognition and classification use of neural networks than actually the material modeling of the resilient response for various aggregate types. The model simply memorized the material types using the 4 aggregate properties and performed a functional mapping of the stress state to predict the resilient modulus for each material.

The future use of neural networks in the area of resilient response modeling can best be achieved by training the network with large and accurate experimental databases. *The limited number of examples in the training data set provided in this study could have made it difficult for the ANN model to find any functional relations between the aggregate properties and the moduli.* Accuracy and the repeatability of the laboratory data may have also influenced the model performance since the variation between the

moduli obtained from two experiments could be up to 7-8% (Alba, 1993). It is the author's opinion that the development of a general ANN model for directly predicting the resilient response of any granular material is quite feasible provided that an extensive and comprehensive training data set exist.

CHAPTER V

FINITE ELEMENT FORMULATIONS

Introduction

The finite element method has proved to be a very versatile and reliable method for modeling flexible pavements since late 1960's (Duncan et al., 1968; Hicks, 1970; Brown and Pappin, 1981; Harichandran et al., 1989). The finite element method simply approximates the behavior of a continuum (i.e., the flexible pavement geometry) by a model composed of an assemblage of a finite number of elements. These individual elements are interconnected at nodal points where force and displacement compatibility is maintained. In displacement-based finite element formulations, the displacements at the nodal points are treated as the primary unknowns solved using the elasticity equations. Stresses and strains in the elements are then calculated from these known displacements. The versatility of the method comes from discretization of the pavement structure into smaller elements which makes possible the realistic variation of material properties in the elements as determined by constitutive material laws. Any discontinuity or irregularity in

pavement geometry can also be accounted for through the utilization of different types of elements in the geometric model.

The finite element model developed in this study investigates the behavior of flexible pavements with granular bases subjected to static, monotonically increasing vertical loads. Dynamic loading and inertia effects are neglected. Special considerations are given in the model to incorporate: (1) residual compaction stresses, (2) material nonlinearity through the use of proper characterization models, (3) cross-anisotropic material behavior, (4) reduction and elimination of the tensile stresses encountered in the unbound base layer. A new concept is introduced to model the granular base as blocks separated by interface elements.

The pavement problem is approximated as one of axial symmetry of load, geometry and stiffness. A cylindrical coordinate system represented by r , θ , and z will be used throughout the analysis (see Figure 2.1). The positive displacements u , v , and w are in positive r , θ , and z directions, respectively. The wheel load is also taken as circular and uniformly distributed with the intensity q . The continuum elements needed to discretize the pavement structure are then circular solid rings with initially rectangular cross-sections in the r - z plane.

The axisymmetric pavement system problem is represented in the finite element model developed by two types of elements: (1) isoparametric eight node, and (2) interface elements. An isoparametric eight node quadrilateral element is used for

modeling the continuum in all layers of the flexible pavement (see Figure 5.1a). The node numbering of the element is as shown in Figure 5.1a.

The interface elements consist of six node spring elements placed between the eight node isoparametric continuum elements in the granular base for the block model representation of the particulate medium introduced in Chapter 8. To be compatible with the neighboring eight node elements, the interface elements, which have negligible thickness, can deform quadratically since they have three nodes on each side (see Figure 5.1b). Three normal and three shear springs are present in each interface element permitting the computation of normal and shear stresses between the continuous blocks.

Isoparametric Eight Node Quadrilateral Element

The axisymmetric, isoparametric eight node quadrilateral element is used in the finite element model for the continuum representation of the pavement. This element has quadratic interpolation functions which allow for a quadratic variation of displacements within the element. The quadrilateral can easily model curved boundaries and deformed geometry of the pavement. The stresses and strains between the neighboring elements also vary smoothly even in a high stress gradient area with fewer number of elements than the linear quadrilateral or linear strain triangle elements.

Under axial symmetry, the quadrilateral cross section of the element is rotated about the z -axis thus forming a solid circular ring (solid of revolution) in the $r - \theta$ plane.

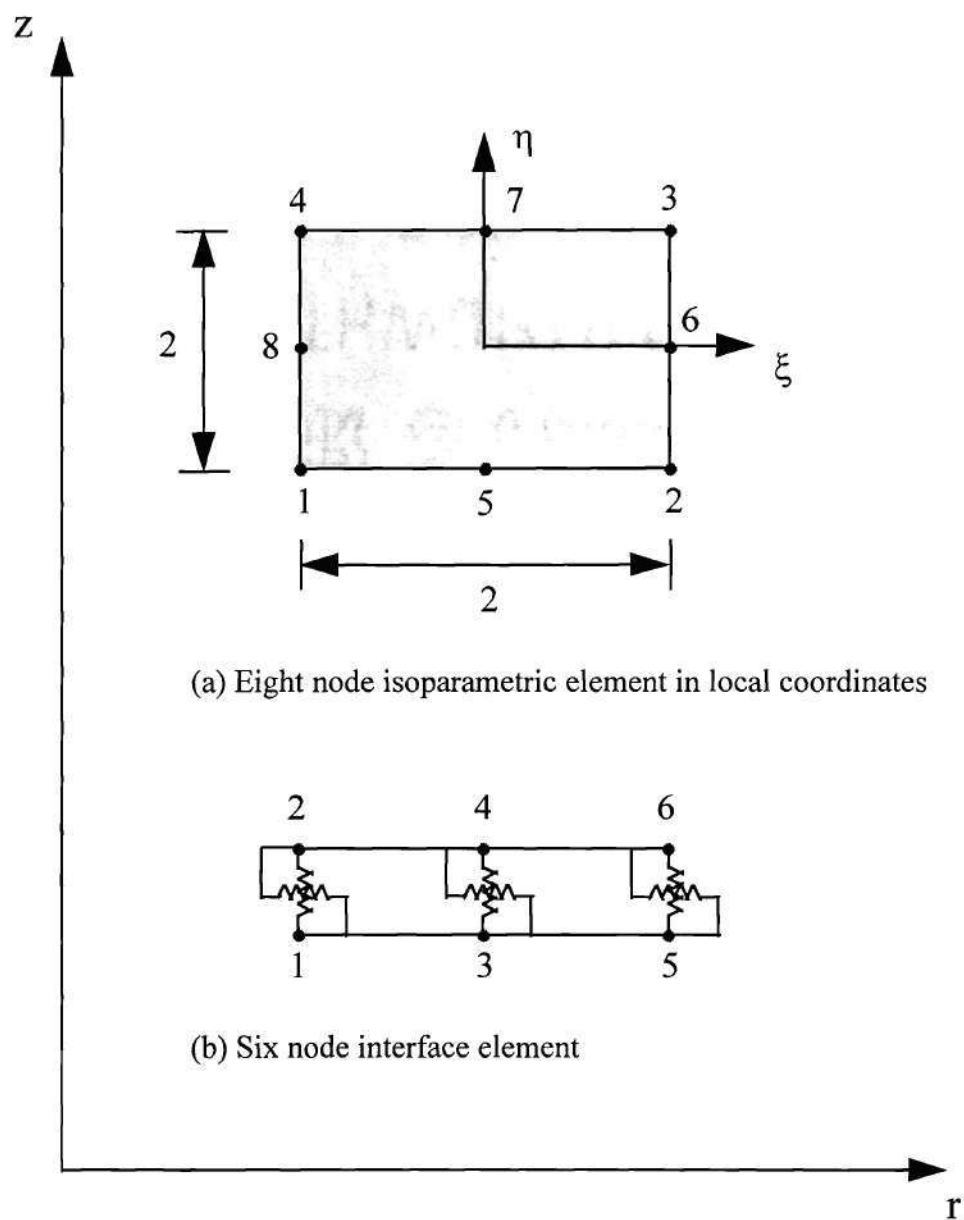


Figure 5.1. Finite Elements Used In the Model In Global Coordinates.

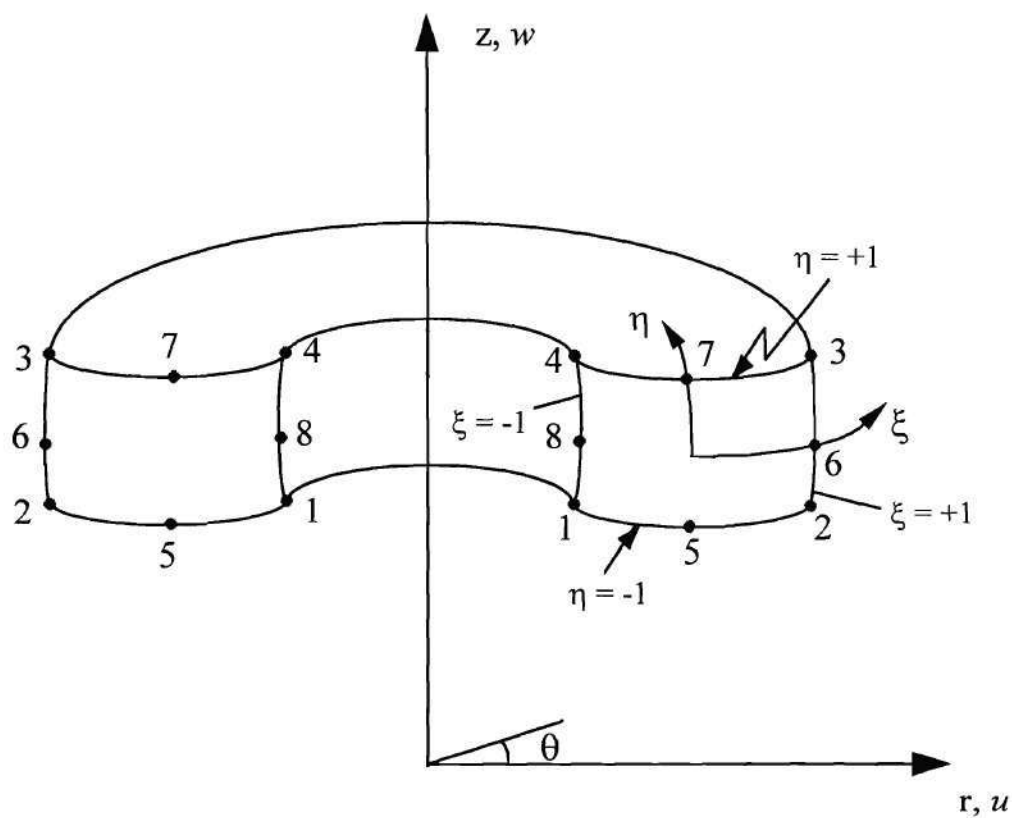
Figure 5.2 shows an eight node isoparametric quadrilateral element represented as an axisymmetric solid in cylindrical coordinates. The wheel loading is applied as a uniformly distributed line load in global coordinates in the r - z plane, and both the material properties and the boundary conditions are considered as independent of the rotation angle θ . The pavement problem then becomes essentially a two-dimensional one that can be analyzed in the r - z plane with the corresponding u and w degrees of freedom at nodal points.

For any point on the cross-section of an axisymmetrically loaded ring element, the generic displacements \mathbf{u} in the r - z plane are (Zienkiewicz and Taylor, 1989):

$$\mathbf{u} = \{u, w\} \quad (5.1)$$

Translations u and w occur in the r and z directions, respectively. Since the translation v in the θ direction is zero, the shearing strains $\gamma_{r\theta}$ and $\gamma_{z\theta}$ are also zero. Then, the strain displacement (compatibility) relation is given by:

$$\boldsymbol{\varepsilon} = \begin{Bmatrix} \varepsilon_r \\ \varepsilon_\theta \\ \varepsilon_z \\ \gamma_{rz} \end{Bmatrix} = \begin{bmatrix} \partial/\partial r & 0 \\ 1/r & 0 \\ 0 & \partial/\partial z \\ \partial/\partial z & \partial/\partial r \end{bmatrix} \begin{Bmatrix} u \\ w \end{Bmatrix} \quad (5.2)$$



Note: ξ and η represent curvilinear natural coordinates

Figure 5.2. Eight Node Isoparametric Quadrilateral Ring Element With Quadratic Displacements of Boundaries.

where the nonzero term $1/r$ in the second row of the above matrix is a multiplier of u , not a derivative.

For the axisymmetric stress problem, the stress-strain constitutive relation for an isotropic material is given as follows (Zienkiewicz and Taylor, 1989):

$$\sigma = \begin{Bmatrix} \sigma_r \\ \sigma_t \\ \sigma_z \\ \tau_{rz} \end{Bmatrix} = \mathbf{D} \varepsilon = \frac{M_R}{(1+\nu)(1-2\nu)} \begin{bmatrix} 1-\nu & \nu & \nu & 0 \\ \nu & 1-\nu & \nu & 0 \\ \nu & \nu & 1-\nu & 0 \\ 0 & 0 & 0 & \frac{(1-2\nu)}{2} \end{bmatrix} \begin{Bmatrix} \varepsilon_r \\ \varepsilon_\theta \\ \varepsilon_z \\ \gamma_{rz} \end{Bmatrix} \quad (5.3)$$

in which M_R is the resilient modulus, ν is the Poisson's ratio, σ_t is the hoop stress in the θ direction, and τ_{rz} is the only shear stress. In case of a cross-anisotropic material, the constitutive relation matrix \mathbf{D} in the above equation is replaced by Equation 3.11.

The isoparametric formulation makes it possible to generate elements that have curved sides. Both displacements and coordinates of a point in the element are defined through the same interpolation or shape functions. The relations between the nodal coordinates and coordinates of a point and nodal displacements and displacements of a point are then given by the following equations, respectively:

$$r = \sum_{i=1}^n N_i r_i \quad \text{and} \quad z = \sum_{i=1}^n N_i z_i \quad (5.4)$$

$$u = \sum_{i=1}^n N_i u_i \quad \text{and} \quad w = \sum_{i=1}^n N_i w_i \quad (5.5)$$

where r and z = global coordinates of the axisymmetric system,
 r_i and z_i = the coordinates of the nodes of the element,
 u and w = global displacements of the axisymmetric system,
 u_i and w_i = the displacements of the nodes of the element,
 N_i = the interpolation or shape function.
 n = number of nodes in the element (which equals 8).

Using Equations 5.4 and 5.5, the coordinates or displacements of a point within the element can be calculated from the known nodal coordinates (r_i and z_i) or the known nodal displacements (u_i and w_i) of the element.

The shape functions N_i and their partial derivatives in natural curvilinear coordinates with respect to ξ and η are tabulated in Table 5.1 for the eight node axisymmetric isoparametric element. Figure 5.2 shows the local coordinates ξ and η varying from -1 to +1 within the element boundaries. At each node, the corresponding shape function takes a zero value to satisfy the compatibility conditions.

For any point within the element, strain is related to the nodal displacements through the strain-displacement transformation matrix **B** as follows:

$$\varepsilon = \mathbf{B} \mathbf{u} \quad (5.6)$$

where \mathbf{B} is a 4×16 matrix having the shape functions and their derivatives with respect to global coordinates as follows (Cook et al., 1989):

$$\mathbf{B} = \begin{bmatrix} N_{i,r} & 0 \\ N_i / r & 0 \\ 0 & N_{i,z} \\ N_{i,z} & N_{i,r} \end{bmatrix}_{4 \times 16} \quad (i = 1, 2, \dots, 8) \quad (5.7)$$

Table 5.1. Shape Functions and Their Derivatives For The Eight Node Element.

Node	N_i	$N_{i,\xi}$	$N_{i,\eta}$
1	$1/4 (1-\xi) (1-\eta) (-\xi-\eta-1)$	$1/4 (2\xi+\eta) (1-\eta)$	$1/4 (1-\xi) (2\eta+\xi)$
2	$1/4 (1+\xi) (1-\eta) (\xi-\eta-1)$	$1/4 (2\xi-\eta) (1-\eta)$	$1/4 (1+\xi) (2\eta-\xi)$
3	$1/4 (1+\xi) (1+\eta) (\xi+\eta-1)$	$1/4 (2\xi+\eta) (1+\eta)$	$1/4 (1+\xi) (2\eta+\xi)$
4	$1/4 (1-\xi) (1+\eta) (-\xi+\eta-1)$	$1/4 (2\xi-\eta) (1+\eta)$	$1/4 (1-\xi) (2\eta-\xi)$
5	$1/2 (1-\xi^2) (1-\eta)$	$-\xi (1-\eta)$	$-1/2 (1-\xi^2)$
6	$1/2 (1+\xi) (1-\eta^2)$	$1/2 (1-\eta^2)$	$-\eta (1+\xi)$
7	$1/2 (1-\xi^2) (1+\eta)$	$-\xi (1+\eta)$	$1/2 (1-\xi^2)$
8	$1/2 (1-\xi) (1-\eta^2)$	$-1/2 (1-\eta^2)$	$-\eta (1-\xi)$

The problem encountered here is that the shape functions for the eight node isoparametric quadrilateral element presented in Table 5.2 are explicit functions of the natural coordinates ξ and η . Therefore, to perform the differentiation with respect to r and z , the chain rule must be used. The derivatives of the shape functions with respect to ξ and η can be written in terms of r and z using the Jacobian matrix \mathbf{J} as follows:

$$\begin{Bmatrix} \frac{\partial N}{\partial \xi} \\ \frac{\partial N}{\partial \eta} \end{Bmatrix} = \mathbf{J} \begin{Bmatrix} \frac{\partial N}{\partial r} \\ \frac{\partial N}{\partial z} \end{Bmatrix} = \begin{bmatrix} \frac{\partial r}{\partial \xi} & \frac{\partial z}{\partial \xi} \\ \frac{\partial r}{\partial \eta} & \frac{\partial z}{\partial \eta} \end{bmatrix} \begin{Bmatrix} \frac{\partial N}{\partial r} \\ \frac{\partial N}{\partial z} \end{Bmatrix} \quad (5.8)$$

where the components of \mathbf{J} are computed from shape functions and nodal coordinates as,

$$J_{11} = \frac{\partial r}{\partial \xi} = \sum_{i=1}^8 N_{i,\xi} r_i$$

$$J_{12} = \frac{\partial z}{\partial \xi} = \sum_{i=1}^8 N_{i,\xi} z_i$$

$$J_{21} = \frac{\partial r}{\partial \eta} = \sum_{i=1}^8 N_{i,\eta} r_i$$

$$J_{22} = \frac{\partial z}{\partial \eta} = \sum_{i=1}^8 N_{i,\eta} z_i$$

The strain displacement matrix **B** of Equation 5.7 then can be formed explicitly in terms of natural coordinates with the following substitutions made into Equation 5.7:

$$\begin{aligned}
 N_{i,r} &= \frac{1}{|J|} [J_{22} N_{i,\xi} - J_{12} N_{i,\eta}] \\
 N_{i,z} &= \frac{1}{|J|} [-J_{21} N_{i,\xi} + J_{11} N_{i,\eta}] \quad (i = 1, 2, \dots, 8) \\
 \frac{N_i}{r} &= \frac{N_i}{\sum_{j=1}^8 N_j r_j}
 \end{aligned} \tag{5.9}$$

where $|J| = J_{11} J_{22} - J_{12} J_{21}$ is the determinant of the Jacobian matrix and r is the average radius.

The stiffness matrix (**S**) of the element relates the applied nodal forces (**P**) and displacements (**u**) in global coordinates as follows:

$$\mathbf{P} = \mathbf{S} \mathbf{u} \tag{5.10}$$

To calculate coefficients of the stiffness matrix, the expression is used for the internal potential energy U (strain energy due to deformation of the element). The strain energy is given by

$$U = \frac{1}{2} \int_{Vol} \boldsymbol{\sigma}^T \boldsymbol{\varepsilon} dV \quad (5.11)$$

in which $dV = r dr d\theta dz$ is the volume element. Now, substituting the constitutive stress strain relation of Equation 5.3 and the strain displacement relation of Equation 5.6 into the above integral equation, one obtains:

$$U = \frac{1}{2} \int_{Vol} \boldsymbol{\varepsilon}^T \mathbf{D} \boldsymbol{\varepsilon} dV = \frac{1}{2} \int_{Vol} \mathbf{u}^T \mathbf{B}^T \mathbf{D} \mathbf{B} \mathbf{u} dV \quad (5.12)$$

The second derivative of the strain energy with respect to the displacement field \mathbf{u} then results in the 16x16 element stiffness matrix \mathbf{S} :

$$\mathbf{S} = \int_{Vol} \mathbf{B}^T \mathbf{D} \mathbf{B} dV \quad (5.13)$$

where \mathbf{B} and \mathbf{D} are the strain displacement and the constitutive relation matrices, respectively.

For the axisymmetric problem, the eight node quadrilateral element makes a 2π revolution around the z axis which makes the matrices \mathbf{B} and \mathbf{D} independent of θ . Equation 5.13 then takes the following form:

$$\mathbf{S} = 2\pi \int \int \mathbf{B}^T \mathbf{D} \mathbf{B} r dr dz \quad (5.14)$$

where $dr dz = d\xi d\eta | \mathbf{J} |$, and in local coordinates, the stiffness matrix is expressed as follows:

$$\mathbf{S} = 2\pi \int_{-1}^1 \int_{-1}^1 \mathbf{B}^T(\xi, \eta) \mathbf{D} \mathbf{B}(\xi, \eta) r(\xi, \eta) | \mathbf{J}(\xi, \eta) | d\xi d\eta \quad (5.15)$$

in which $r(\xi, \eta) = \sum_{j=1}^8 N_j r_j$.

The stiffness matrix \mathbf{S} can be evaluated by numerical integration using two-dimensional Gaussian quadrature. A Gaussian quadrature of order 3, which was used in this study, exactly integrates the stiffness matrices of 8 node rectangular elements. The axisymmetric eight node isoparametric quadrilateral element derived here can be sufficiently approximated by the 3th order quadrature with 9 integration points within the element located as shown in Figure 5.3. Instead of having a large number of low accuracy elements, this study uses a small number of high accuracy eight node elements with a higher order Gaussian quadrature rule.

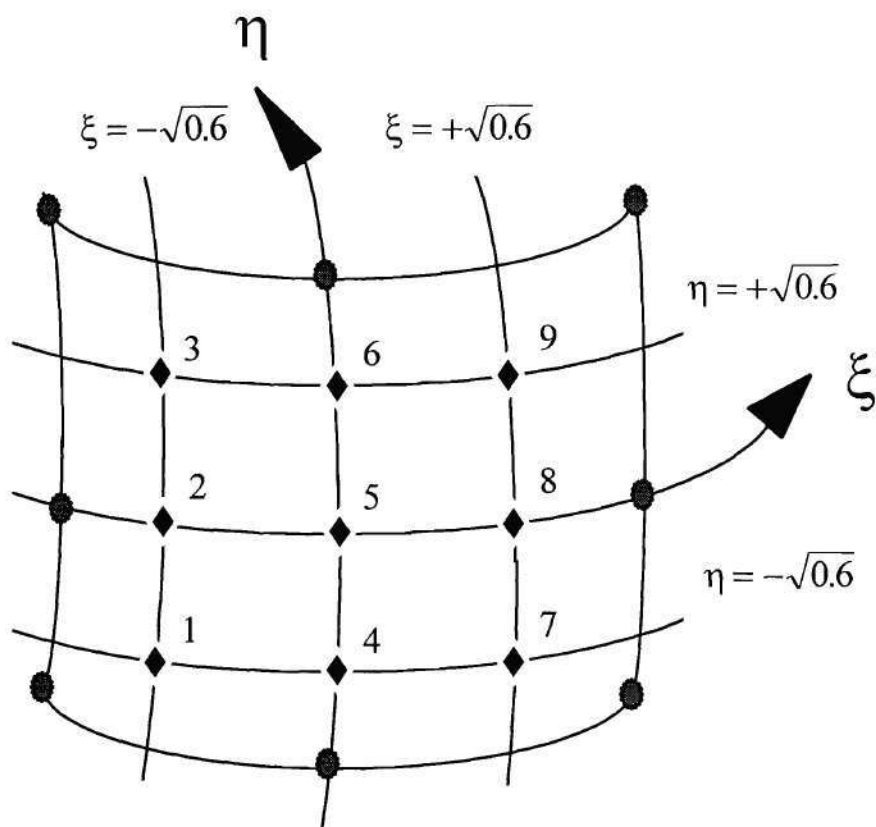


Figure 5.3. Third Order Gauss Integration Point Locations In the Eight Node Quadrilateral Element.

The integrals of the stiffness matrix \mathbf{S} (Equation 5.15) can then be approximated as the weighted summation of the values at the 9 Gauss sampling points within the element by:

$$\mathbf{S} = 2\pi \sum_{i=1}^3 \sum_{j=1}^3 \mathbf{B}^T(\xi_i, \eta_j) \mathbf{D} \mathbf{B}(\xi_i, \eta_j) |\mathbf{J}(\xi_i, \eta_j)| r(\xi_i, \eta_j) w_i w_j \quad (5.16)$$

where ξ_i and η_i are the local coordinates of the sampling points, and w_i and w_j are the weight factors given as:

For $i = 1, 3$ and $j = 1, 3$: $w_i = w_j = 5/9$ (Gauss points 1, 3, 7, 9).

For $i = 2$, and $j = 2$: $w_i = w_j = 8/9$ (Gauss points 2, 4, 5, 6, and 8).

Loading:

The shape factors \mathbf{N} and the strain displacement matrix \mathbf{B} derived in the stiffness formulation are used to evaluate the loads acting on the eight node quadrilateral element. The types of loads considered in this study are body (gravity) forces, initial residual stresses, nodal concentrated loads, temperature loads, and uniformly distributed edge loads. All loadings are axisymmetrical and applied with θ varying from 0 (r-z plane) to 2π .

For body forces, the gravity loading is considered through the unit weight γ in the load matrix $\mathbf{F}_B^T = \{0, \gamma\}$ only in the z direction. The nodal loads due to body forces \mathbf{q}_B are computed from:

$$\mathbf{q}_B = 2\pi \int_{-1}^1 \int_{-1}^1 \mathbf{N}^T(\xi, \eta) \mathbf{F}_B |\mathbf{J}(\xi, \eta)| r(\xi, \eta) d\xi d\eta \quad (5.17)$$

where \mathbf{N}^T is the transpose of the shape function, $|\mathbf{J}|$ is the determinant of Jacobian, and r is the average radius defined in Equation 5.15.

The horizontal residual stresses locked in the pavements are considered as initial stresses, and can be included in the formulation as follows:

$$\mathbf{q}_I = 2\pi \int_{-1}^1 \int_{-1}^1 \mathbf{B}^T(\xi, \eta) \sigma_0 |\mathbf{J}(\xi, \eta)| r(\xi, \eta) d\xi d\eta \quad (5.18)$$

where \mathbf{q}_I is the nodal loads due to the initial stresses in the element, and σ_0 is the initial stress matrix.

Temperature changes, which were not considered in this study, can also impose loading in the pavements. Temperature changes are especially important in cold climates and in milder regions when an excessively hard asphalt is used. The initial thermal strain matrix ϵ_0 can be written in terms of the coefficient of thermal expansion α and the constant change in temperature ΔT as:

$$\epsilon_0 = \begin{Bmatrix} \epsilon_{r_0} \\ \epsilon_{\theta_0} \\ \epsilon_{z_0} \\ \gamma_{rz_0} \end{Bmatrix} = \begin{Bmatrix} \alpha \Delta T \\ \alpha \Delta T \\ \alpha \Delta T \\ 0 \end{Bmatrix} \quad (5.19)$$

where $\Delta T = T_f - T_i$ with T_i being a starting temperature at which the body is free of stress and T_f is the final temperature. The nodal loads due to the thermal strains then are given by

$$\mathbf{q}_T = 2\pi \int_{-1}^1 \int_{-1}^1 \mathbf{B}^T(\xi, \eta) \mathbf{D} \epsilon_0 |\mathbf{J}(\xi, \eta)| r(\xi, \eta) d\xi d\eta \quad (5.20)$$

For edge loads, a uniformly distributed line load is considered in the r - z plane with the load intensity vector $\Phi^T = \{\phi_r, \phi_z\}$. The nodal load vector due to the edge loads \mathbf{q}_S is written as a surface integral:

$$\mathbf{q}_S = 2\pi \int_{-1}^1 \mathbf{N}_S^T(\xi, \eta) \Phi |\mathbf{J}_S(\xi, \eta)| r(\xi, \eta) d\xi \quad (5.21)$$

where \mathbf{N}_S and \mathbf{J}_S are the surface shape function and surface Jacobian matrix modified in the above equation for the lower or upper edges of the element (see Figure 5.2) where $\eta = -1$ or $\eta = +1$.

Stress Computations

The stresses σ are calculated from the computed strains ϵ , the initial thermal strains ϵ_0 , and the initial residual stresses σ_0 in the general form as follows:

$$\sigma = \mathbf{D} \{ \epsilon - \epsilon_0 \} + \sigma_0 \quad (5.22)$$

The strains are first produced by the displacements of the nodes, and then the stresses are calculated in the above equation from the strains. Therefore, the stresses are less accurate than the displacements. However, higher order elements, such as the one formulated here, usually display good accuracy for stresses computed at the Gaussian integration points. The axisymmetric eight node quadrilateral element performs very well in overall efficiency and accuracy as compared with simpler elements (Bathe and Wilson, 1976).

Due to the formulation of the axisymmetric problem, it is unavoidable to obtain a division by zero error when $r = 0$ because of the u/r term in the strain displacement relation of Equation 5.2. This difficulty, however, is easily solved in the computer program by substituting the tangential strain ϵ_θ with the radial strain ϵ_r at the centerline ($r = 0$) where the radial and tangential components of the strains are equal.

Six Node Interface Element

Conventional finite element analyses employ the continuum requirement of nodal point displacement compatibility without considering any relative movements between neighboring elements. To model a particulate medium, interface elements are needed on each face of the element to provide for sliding and separation of blocks of aggregates. The block model, to be introduced in Chapter 8 for modeling granular base behavior, will be implemented in the finite element analysis using interface elements surrounding the continuum elements.

To allow for relative shear movements and separation between the adjacent two-dimensional elements, Goodman et al. (1968) developed a one-dimensional linear elastic interface element. This zero-thickness element was later modified by Clough and Duncan (1969) for the nonlinear hyperbolic shear stress - shear displacement behavior. Ghaboussi et al. (1973) and Desai (1974) formulated and applied the interface element for the axisymmetric stress problems. Several researchers have used an isoparametric formulation of the interface element (Zienkiewicz, 1970; Katona, 1983; Beer, 1985) to model contact problems in soil and rock mechanics.

Desai et al. (1984) proposed a thin layer, solid element to be used in the interfaces which involves a small but finite thinness rather than a zero thickness. Satisfactory simulation of the interface was obtained when the thickness was 0.1 to 0.01 times the length of the interface element. More recently, Snyman and Martin (1992) developed an

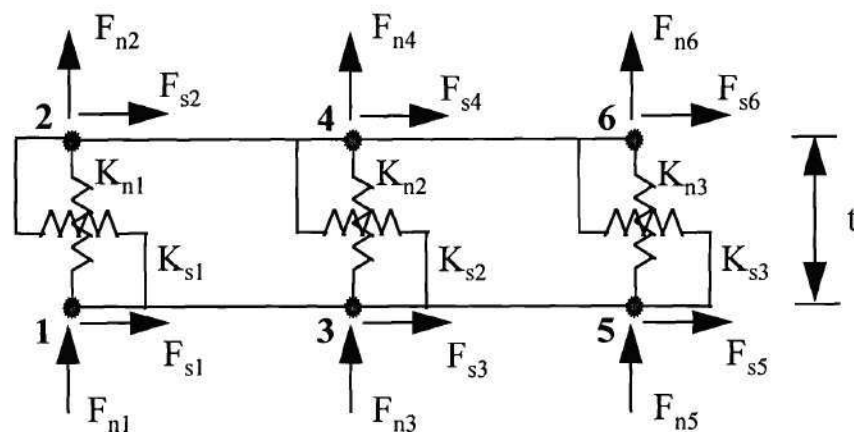
element to model the dilatant behavior of discontinuities with rough contact surfaces. The element was successfully implemented into a standard nonlinear finite element code to realistically account for dilatancy.

The six node interface element selected in this study is compatible with the eight node isoparametric element previously described (see Figure 5.4). The element essentially has zero thickness and consists of three parallel nodal links (Zeevaert, 1980). Each nodal link is composed of a normal and a shear spring placed between nodes on each side. Similar to the eight node element, the element deforms quadratically thus creating shear and normal displacements in the springs. The spring coefficients (normal k_n and shear k_s) are calculated as a modulus of subgrade reaction (Force / Length³) from the normal σ_n and shear stresses τ_s by:

$$\begin{aligned}\sigma_n &= k_n \Delta_n \\ \tau_s &= k_s \Delta_s\end{aligned}\tag{5.23}$$

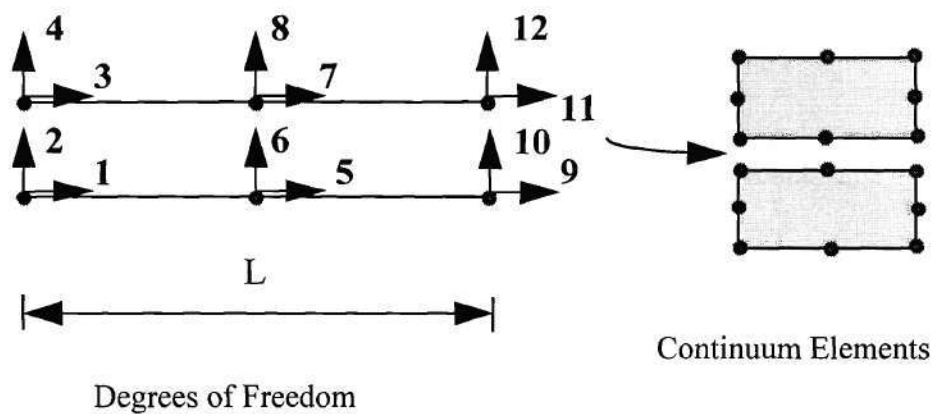
where Δ_n is the average relative normal displacement across the element, and Δ_s is the average relative shear displacement along the element.

The subgrade reaction type moduli k_s and k_n assigned to the element control the opening (separation) and relative movement of the interface (slip) between the adjacent two-dimensional elements. Computer analyses using interface elements have indicated that high values of the modulus of subgrade reaction k in the order of 10^6 to 10^8 pci



$t = \text{negligible thickness}$

- (a) Three nodal links with concentrated normal and shear spring constants, and nodal forces acting on the interface element



- (b) Compatibility of interface elements

Figure 5.4. Six Node Interface Element.

(2.7×10^8 to 2.7×10^{10} kN/m³) provide accurate results when modeling a continuum. Similar values were also obtained for k_n and k_s by Clough and Duncan (1969) and Zeevaert (1980). For a normal stiffness k_n of 10^6 pci (2.7×10^8 kN/m³), it would take a relative compressive displacement of 10^{-4} in. (2.54×10^{-6} m) across the element to develop a 100 psi (690 kPa) compressive stress which is usually higher than stresses generally encountered in pavement bases. In the normal direction, a high resistance to compression is achieved using these stiffnesses and the overlapping of the continuum elements are minimized. When tension is observed in the interface, both the normal stiffness k_n and the shear stiffness k_s is set to zero allowing separation to occur.

In the direction of shear, the shear stresses computed agree reasonably well with the stresses obtained in the continuum elements for the above given range of k_s values. The shear behavior at the interface is modeled at failure by the frictional shear strength using the Mohr-Coulomb failure envelope as follows:

$$\tau_{\max} = c + \sigma_n \tan \phi \quad (5.24)$$

where τ_{\max} is the shear strength, c is the cohesion intercept (usually taken as zero for the granular bases), and ϕ is the friction angle of the granular materials. When the interface shear is larger than the shear strength τ_{\max} , slip occurs, and only the maximum shear that

can be developed (τ_{\max}) is applied at the interface. Also, the shear stiffness k_s is reduced to a small residual value. For the current application of interface elements, a more sophisticated hyperbolic modeling of shear behavior is not used to avoid having to determine the additional model parameters needed in the analysis.

Stiffness Formulation

The interface is assumed to have a uniformly distributed modulus of subgrade reaction k [F/L^3] along its boundary (see Figure 5.5). The displacement function of the interface is quadratic between the nodes on each side and hence it is compatible with the adjacent eight node isoparametric elements. The concentrated springs K_n and K_s [F/L] shown in Figure 5.4a replace the foundation modulus k in the nodal links of the six node interface element.

The nodal load vector \mathbf{q}_s due to a uniformly distributed line load was given in local coordinates in Equation 5.21 for the axisymmetric eight node isoparametric element. Considering the compatibility requirements, the external loads F_{ni} and F_{si} (see Figure 5.4a) in the interface element are therefore equivalent to the computed nodal loads given a uniform load distribution on a boundary of the eight node isoparametric element. This uniform edge loading can be written as $\Phi^T = \{0, k\}$, where k is the magnitude of the uniformly distributed line load acting in local coordinates perpendicular to the boundary of the element.

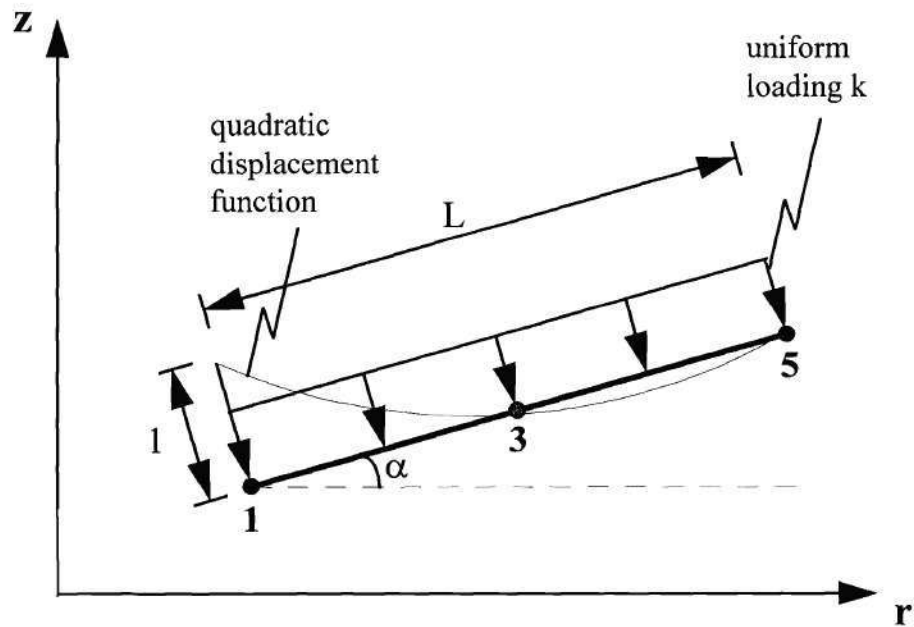


Figure 5.5. Uniform Load k Applied at the Boundary of An Eight Node

Isoparametric Element with Unit Displacement Shown at Node 1.

Assuming the nodes of the element boundary are 1, 3, and 5 (see Figure 5.5) and the interface is at angle α with the horizontal, the concentrated loads are then obtained by equating the work done on both systems as follows:

$$F_i \times 1 = 2\pi \int_{r_1}^{r_5} k N_i r \, dr \quad (5.25)$$

where F_i = equivalent concentrated nodal forces at 1, 3, or 5 (see Figure 5.5),
 k = uniform load acting normal to the member,
 N_i = shape functions of nodes for the eight node isoparametric element,
 r = horizontal coordinate.

In local coordinates, Equation 5.25 can be expressed as:

$$F_i \times 1 = 2\pi \int_{-1}^1 k N_i \left(r_{\text{avg}} + \xi \frac{L}{2} \cos\alpha \right) \frac{L}{2} d\xi \quad (5.26)$$

where $r_{\text{avg}} = (r_1 + r_3 + r_5) / 3$,
 L = Length of the boundary 1-3-5, and
 α = initial angle between global horizontal r axis and the 1-3-5 side.

Considering node 1 in Figure 5.5 to coincide with the top left corner of the eight node quadrilateral, $N_4 = 1/2 (\xi^2 - \xi)$ is obtained from Table 4.1 for $\eta = +1$. With substitution of N_4 into Equation 5.26, the integral is then solved for F_1 to give:

$$F_1 = \pi k \frac{L}{3} \left(r_{\text{avg}} - \frac{L}{2} \cos\alpha \right) \quad (5.27)$$

Similar shape function substitutions are made into Equation 5.26 for nodes 3 and 5 to obtain the concentrated forces F_3 and F_5 by:

$$F_3 = \frac{4}{3} \pi k L r_{\text{avg}} \quad (5.28)$$

and

$$F_5 = \pi k \frac{L}{3} \left(r_{\text{avg}} + \frac{L}{2} \cos \alpha \right) \quad (5.29)$$

Using the above equations, it is then possible to relate the nodal forces to the uniform edge loading k through the axisymmetric load factors, AL_i , as follows:

$$\begin{aligned} F_1 &= AL_1 \times k = \left\{ \pi \frac{L}{3} \left(r_{\text{avg}} - \frac{L}{2} \cos \alpha \right) \right\} \times k \\ F_3 &= AL_3 \times k = \left\{ \frac{4}{3} \pi L r_{\text{avg}} \right\} \times k \\ F_5 &= AL_5 \times k = \left\{ \pi \frac{L}{3} \left(r_{\text{avg}} + \frac{L}{2} \cos \alpha \right) \right\} \times k \end{aligned} \quad (5.30)$$

The axisymmetric load factors given above are used in the derivation of the interface element stiffness matrix.

Considering that the strain energy of the distributed foundation modulus k is equal to the strain energy of the concentrated spring stiffness K at nodes 1, 3, and 5 (see Figure 5.4a), k can be related to K in the energy equation by the following:

$$\frac{1}{2} 2\pi \int_{r_1}^{r_5} k \Delta u^2 r dr = \frac{1}{2} K \Delta u_i^2 \quad (5.31)$$

where Δu = is the relative displacement between the two sides of the interface at any point along the 1-3-5 element boundary, and

Δu_i = is the displacement at nodes 1, 3, or 5 relative to the nodes 2, 4, or 6 (see Figure 5.1b).

Using the definition of isoparametric element formulation (Equation 5.6), Δu can be written in terms of Δu_i as follows:

$$\Delta u = \sum_{i=1}^8 N_i \Delta u_i \quad (5.32)$$

Now, with the substitution of Equation 5.32 into Equation 5.31, the strain energies of both systems are differentiated and equated to zero to obtain the stiffnesses:

$$k \int_{r_1}^{r_5} 2\pi N_i \Delta u_i r dr = K \Delta u_i = 0 \quad (5.33)$$

in which the concentrated spring stiffness K is equivalent to:

$$K = 2\pi \int_{r_1}^{r_5} N_i r dr \times k \quad (5.34)$$

Equation 5.34 is similar to Equation 5.25 with the force term in Equation 5.25 replaced by the spring constant K . Then, the integral of Equation 5.34 results in the axisymmetric load factors AL_i as summarized in Equation 5.30. It is, therefore, possible to relate the concentrated spring stiffnesses to the foundation modulus (or subgrade modulus) in the normal and shear direction in the interface as follows:

$$\begin{aligned} K_{si} &= AL_i k_s \\ K_{ni} &= AL_i k_n \end{aligned} \quad (5.35)$$

where subscript i represents nodes 1, 3, and 5, as shown in Figure 5.1a.

The displacements of the nodes were previously denoted by u and w (Equation 5.1) in the r and z directions, respectively. A total of twelve degrees of freedom exist in

the six node interface element, as shown in Figure 5.4b. The transpose of the displacement vector \mathbf{u}^T for the interface element is then given by:

$$\mathbf{u}^T = \{u_1 \ w_1 \ u_2 \ w_2 \ u_3 \ w_3 \ u_4 \ w_4 \ u_5 \ w_5 \ u_6 \ w_6\} \quad (5.36)$$

Using the above displacements, one can calculate the relative displacements (Δu 's) by the following equations:

$$\begin{aligned} \Delta u_1 &= u_2 - u_1, & \Delta w_1 &= w_2 - w_1 \\ \Delta u_3 &= u_4 - u_3, & \Delta w_3 &= w_4 - w_3 \\ \Delta u_5 &= u_6 - u_5, & \Delta w_5 &= w_6 - w_5 \end{aligned} \quad (5.37)$$

The local stiffness matrix \mathbf{S}_{ier} of the six node interface element is then assembled in terms of the above summarized relative displacements between the nodal links as follows:

$$\mathbf{S}_{ier} = \begin{bmatrix} AL_1 k_s & & & & & \\ & AL_1 k_n & & & & \\ & & AL_3 k_s & & & \\ & & & AL_3 k_n & & \\ & & & & AL_5 k_s & \\ & 0 & & & & AL_5 k_n \end{bmatrix}_{6 \times 6} \quad (5.38)$$

The element stiffness matrix \mathbf{S}_{ie} (12x12) can now be formulated directly in terms of nodal displacements from the matrix multiplication:

$$\mathbf{S}_{ie} = \mathbf{B}_i^T \mathbf{S}_{ier} \mathbf{B}_i \quad (5.39)$$

in which \mathbf{B}_i is a transformation matrix relating relative displacements to nodal displacements in the following form:

$$\Delta \mathbf{u} = \mathbf{B}_i \mathbf{u} \quad (5.40)$$

where $\Delta \mathbf{u}^T = \{\Delta u_1 \Delta w_1 \Delta u_3 \Delta w_3 \Delta u_5 \Delta w_5\}$ and

$$\mathbf{B}_i = \begin{bmatrix} -1 & 0 & 1 & 0 & 0 & 0 & 0 & 0 & 0 & 0 & 0 & 0 \\ 0 & -1 & 0 & 1 & 0 & 0 & 0 & 0 & 0 & 0 & 0 & 0 \\ 0 & 0 & 0 & 0 & -1 & 0 & 1 & 0 & 0 & 0 & 0 & 0 \\ 0 & 0 & 0 & 0 & 0 & -1 & 0 & 1 & 0 & 0 & 0 & 0 \\ 0 & 0 & 0 & 0 & 0 & 0 & 0 & 0 & -1 & 0 & 1 & 0 \\ 0 & 0 & 0 & 0 & 0 & 0 & 0 & 0 & 0 & -1 & 0 & 1 \end{bmatrix}_{6 \times 12}$$

Since the complete derivation of the six node interface element can be achieved in closed form, numerical integration is not necessary. As shown in Equation 5.38, the two parameters needed to form the global stiffness matrix of an interface element are the subgrade reaction type moduli k_s and k_n in the shear and normal directions, respectively. The shear strength τ_{\max} that controls the slip condition in the interface is also determined by the cohesion intercept c , and friction angle ϕ of the granular material.

Summary

The formulations of the axisymmetric stiffness and load matrices were given in this chapter for two types of elements used in the finite element model developed for the analysis of the pavement system problem. The elements used consisted of an isoparametric eight node quadrilateral and a six node interface element. The formulation of the eight node quadrilateral element required a third order numerical integration. The eight node element is used in the model for the continuum representation of the pavement. The six node interface elements were formulated for the axisymmetric uniform loading conditions. The stiffness matrix for the six node interface element was obtained in closed form. The interface elements will be used in Chapter 8, in the block model representation of granular bases between the eight node isoparametric continuum elements.

CHAPTER VI

COMPUTER CODE ORGANIZATION AND CAPABILITIES

General Description

The theoretical development of the finite element formulation given in Chapter 5 is implemented into a nonlinear finite element computer code named GT-PAVE. To more correctly model the flexible pavement behavior, GT-PAVE program incorporates both the continuum model described in Chapter 3 and a new block model approach introduced in Chapter 8. Flexible pavements are modeled as axisymmetric solids consisting of either linear or nonlinear elastic layers. A dynamic analysis is not considered and hence inertia forces are neglected. The wheel load is then approximated by a circular uniform static load. The program employs the small-displacement theory and considers the cross-anisotropic behavior exhibited by unbound aggregates when used in a base. The program also permits incremental loading in the nonlinear analysis, handles residual compaction stresses, and eliminates, if necessary, horizontal tensile stresses developed in the lower part of the base.

The GT-PAVE computer program organization is summarized in this chapter. The important features of the program such as the pre- and post-processing, nonlinear analysis, incremental loading and no tension considerations for the continuum representation of the granular base are discussed in detail. The limitations of the program are also given. Analyses using the block model approach are presented in Chapter 8.

Overview

Written in Fortran 77, the GT-PAVE nonlinear finite element program runs on a personal computer with the requirements of a minimum 8 megabyte RAM and a DOS memory extender. Watcom Fortran 77 compiler and tools (Waterloo, Ontario, Canada) were used in creating the executable program. Pre-processing capabilities include automatic rectangular mesh generation and simple data input. Post-processing uses Tecplot software (Amtec Engineering Inc., Bellevue, WA, 1993) for full output data visualization capability. The program uses up to 400 axisymmetric 8-node isoparametric quadrilateral elements and 200 6-node interface elements to discretize the pavement structure. Approximate run times on a 66 MHz, 486DX2 computer with 16 megabyte RAM is less than 30 minutes for a nonlinear analysis using about 400 8-node elements, with the wheel load applied in 10 increments and tension correction modifications. Gravity loading due to self weight and initial lateral stresses locked in the granular base

due to compaction are also considered initially for a more realistic representation of the pavement problem.

As presently dimensioned, the GT-PAVE program solves problems up to 1400 nodal points, 400 8-node quadrilateral elements, and 200 6-node interface elements in the granular base. Ten different material types can be used with material properties entered for either isotropic (M_R , ν) or cross-anisotropic (M_R^r , ν_r , M_R^z , ν_z , G_R^z) analysis. Loading types consist of nodal point loads, uniform pressure (edge) loads, gravity loads, and temperature loads. Maximum half-bandwidth of the banded global stiffness matrix is set at 200 for 1400 nodal points.

Emphasis in program development has been given to realistic nonlinear material modeling using routine laboratory tests. Simplified resilient modulus models (i.e., Uzan, 1985; Pezo, 1993), which consider both confinement and shear stress effects for the nonlinear behavior of base and subgrade layers were carefully chosen to be suitable for practical design use. The inclusion of the neural network model developed in Chapter 4 was considered although not implemented in the program due to modulus modeling of just the data points for the different aggregate types (refer to Chapter 4). Material nonlinearity is handled by using a secant chord modulus which was found to be the most effective method of analysis when used with the simplified material models described in Chapter 2. In addition to the material models presently employed, the program is designed for the easy insertion of new material models for both the base and subgrade.

The unbound granular base in flexible pavements can be modeled by using GT-PAVE program either as a continuum or as blocks of aggregates capable of undergoing sliding and reorientation under the applied wheel load. The continuum representation is realized by using the 8-node quadrilateral elements. In the block movement approach, the 6-node interface elements are added in between the continuum elements. When the granular base goes into horizontal tension, GT-PAVE program employs the following “no tension” or equilibrium analyses depending on the type of model used in the base:

(1) Continuum Model. The continuum model incorporates the “no tension” stress transfer approach which was originally proposed by Zienkiewicz et al. (1968) and later modified for flexible pavements following the recommendations of Doddihal and Pandey (1984). In this approach, the tensile stresses are counteracted by compressive nodal loads always maintaining the overall equilibrium after each iteration until tension is eliminated.

(2) Block Model. The block model employs an iterative procedure, different than the stress transfer algorithm, to maintain equilibrium in the granular base. The aggregate blocks separate and the horizontal tension is balanced by the counteracting friction forces in the horizontal interfaces between continuum elements permitting the blocks to rearrange until equilibrium is achieved.

The overall nonlinear analysis performed for both the continuum and block models consists of two major parts: (1) first the computation of initial stresses due to overburden including the effects of horizontal residual compaction stresses and then (2) the application of the uniform circular wheel loading at the centerline in the axisymmetric mesh. The gravity and the wheel loadings are, unless specified otherwise, applied in 5 and 10 increments, respectively, until the full load for each is applied in the last increment. The first load increment of the gravity loading is solved assuming linear elastic response. To obtain convergence for nonlinear problems, the number of load increments can be varied to suit the requirements of the problem. The gravity loading including the effects of initial compaction stresses provides a correct starting point with appropriate stress state determined before superposition of the wheel loading.

During each load increment, GT-PAVE computes the resilient response through two sets of iterations: (1) first correct nonlinear material modeling is achieved and then (2) corrections are made for horizontal tension. New values of resilient moduli are calculated from the previously computed principal stresses using the simplified models (i.e., Uzan, 1985; or Pezo, 1993). The new and the old moduli are compared for convergence of the nonlinear iterations using both a cumulative and an individual error criterion. Then, the horizontal tension predicted in the granular base at the end of each nonlinear iteration is reduced or eliminated (only in the continuum representation of the base) by performing no tension modifications in which the overall equilibrium of the pavement system is always maintained.

GT-PAVE Program Organization

GT-PAVE finite element program consists basically of a main program which controls the flow by handling the input data, calling the several subroutines, and outputting the results for the visualization option. A total of 16 subroutines are used for the required computations. Figure 6.1 shows the general flow diagram of the GT-PAVE program which employs incremental loading with iterations performed for nonlinear analysis and tension or equilibrium modifications.

The input of the program consists of geometry (i.e., mesh layout and element connectivities), initial material properties, residual compaction stresses, boundary conditions and the loading. Nonlinear material model parameters and tension modification parameters must also be specified together with the number of load increments to be used for both gravity and surface wheel loads. The basic input and output of these properties are processed in the INOUT subroutine. This routine also calls the mesh generator subroutine MESHGR and the residual stress computation subroutine RESIDUE.

The pre-processing abilities of the program include a rectangular mesh generator using 8-node quadrilateral elements. Six-node interface elements can also be used in the granular base layer when block movements are considered. After the general mesh generation is completed, any irregular zone in the mesh can be assigned different material types by modifying the element properties. The horizontal stresses due to self weight are

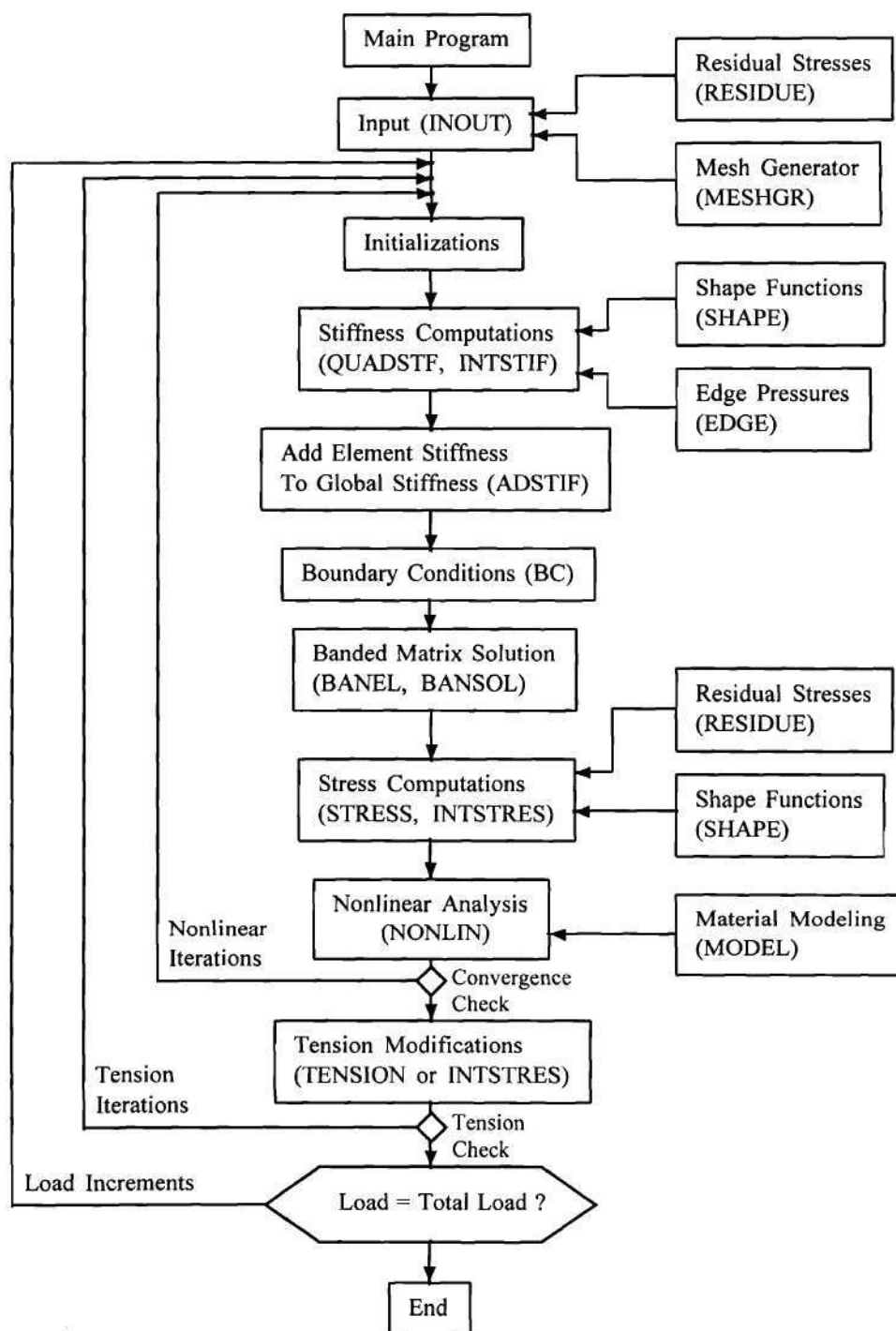


Figure 6.1. Flow Diagram of GT-PAVE Finite Element Program.

computed in the granular layer in the RESIDUE subroutine which shares the geometry and the material property information with INOUT and MESHGR subroutines.

The formulations given in Chapter 5 for the element stiffnesses of the 8-node quadrilateral and the 6-node interface elements are implemented in QUADSTF and INTSTIF subroutines, respectively. QUADSTF calls SHAPE and EDGE subroutines. The SHAPE subroutine forms the strain-displacement matrix and calculates the initial strain values. The EDGE subroutine modifies the shape functions for 4 edges of the 8-node quadrilateral element, computes the arc lengths on those 4 sides, and forms uniformly distributed edge load vectors. Residual stress, body force, and temperature load vectors are formed in the QUADSTF subroutine. The flowcharts of QUADSTF, SHAPE, and EDGE subroutines are presented in Figures 6.2 and 6.3.

The element stiffness matrices are assembled into proper locations of the global banded stiffness matrix in the ADSTIF subroutine. The BC subroutine imposes boundary conditions relevant to the problem geometry on the banded stiffness matrix and the load vector for the specified displacements. The symmetric system stiffness matrix then takes the form:

$$S_{\text{Global}} = \begin{bmatrix} s_{11} & s_{12} & 0 & 0 \\ & s_{22} & s_{23} & 0 \\ & & s_{33} & s_{34} \\ & & & s_{44} \end{bmatrix}_{4 \times 4} \quad (6.1)$$

maximum
half-bandwidth

symmetric

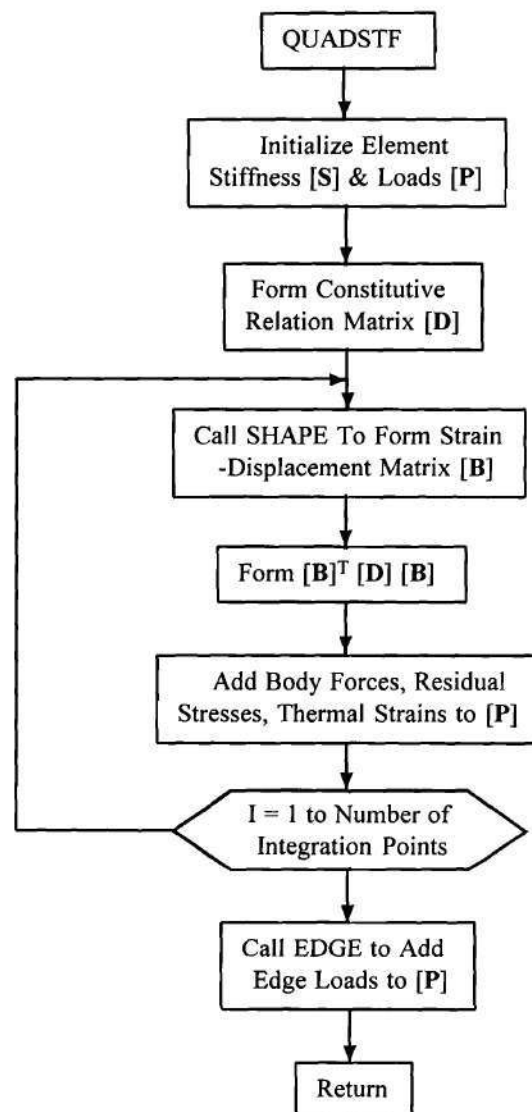
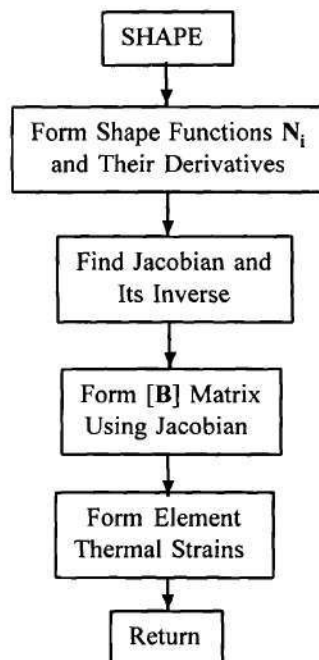
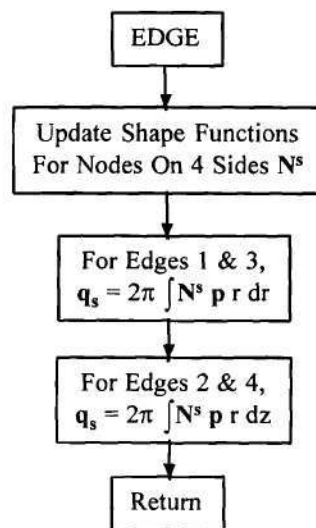


Figure 6.2. Flow Diagram of QUADSTF Element Stiffness Subroutine.



(a) SHAPE Subroutine



(b) EDGE Subroutine

Figure 6.3. Flow Diagrams of SHAPE and EDGE Subroutines.

where the maximum half-bandwidth is shown for a 4x4 symmetric matrix and the stiffness terms in the half-bandwidth can be stored in one array in the direction of the arrows. The maximum half-bandwidth of the global stiffness matrix is determined by the maximum difference between node numbers of the element (max. diff.) as follows:

$$\text{Maximum half-bandwidth} = 2 * (\text{max. diff.} + 1) \quad (6.2)$$

Two subroutines, BANEL and BANSOL, are employed to solve the system of simultaneous equations using the global banded stiffness matrix and the load vectors. BANEL triangularizes the banded and symmetric coefficient matrix by storing only the upper portion in a rectangular array as shown in Equation 6.1. BANSOL multiplies the inverse of left triangular form with the right hand side vector and then using double precision solves for the unknown displacements by the back substitution process (Golub and Van Loan, 1989).

The strains and stresses are calculated from nodal displacements in STRESS and INTSTRES subroutines. STRESS calls the SHAPE subroutine which forms the strain displacement matrix for the 8-node quadrilateral element to calculate first strains and then stresses from Equation 5.2. The normal stresses in the r , θ , z directions and the shear stress in r - z plane are computed directly at the integration points for the nonlinear analysis. The principal stresses used to determine the material properties in a nonlinear

analysis are then calculated using Equation 2.7. GT-PAVE also includes options to print the final results of the analysis at both the integration points and the nodal points. The nodal values calculated are averaged depending upon the number of elements neighboring at that node.

INTSTRES calls for the stiffness matrix of the interface elements (INTSTIF) to compute interface stresses in the granular base from average relative displacements between the nodes of two neighboring continuum elements. Equilibrium iterations related to the slippage and separation of the individual blocks are also performed in INTSTRES. Both the INTSTIF and INTSTRES subroutines, which are used in the new block movement modeling of granular bases, are discussed in more detail in Chapter 8.

Nonlinear Analysis

The material nonlinearity observed in both the granular base and subgrade is considered in the GT-PAVE finite element program for both the continuum and block model approaches through the use of the resilient models summarized in Chapter 2. Specifically, the Uzan (1985) and the UT-Austin (Pezo, 1993) models given by Equations 2.20 and 2.30, respectively, have been included in the MODEL subroutine. This subroutine calculates the vertical resilient modulus of granular bases from the stress state at each integration point in each element. For the subgrade, the resilient modulus of a subgrade can be obtained by using the bilinear approximation (Equation 2.31) defined by

the repeated load triaxial test results. The Loach model, given by Equation 2.33, has also been included as an alternative for representation of the subgrade resilient response.

Both the Uzan (1985) and UT-Austin (Pezo, 1993) models consider the effects of confinement and shear stress in granular materials. The constants used in these models can be readily determined from routine resilient modulus tests. When compared, for example, to the more complicated, but admittedly more accurate shear and volumetric stress-strain contour model (Brown and Pappin, 1981), this type model gives reasonably good agreement (Uzan, 1985). These simplified models are therefore used in the GT-PAVE program as a practical expedient to encourage the routine use of improved nonlinear models attractive to state transportation agencies. Although included in the MODEL subroutine, the use of the $K-\theta$ model is not recommended because of its limited ability to account for the shear stress effects.

Nonlinear Solution Technique

Several nonlinear solution techniques have been investigated for use in GT-PAVE finite element program. Due to the nature of the material models used, which are all functions of the total stresses (and not defined through incremental constitutive relations), an incremental tangent stiffness type of nonlinear analysis could not be successfully adapted of the form:

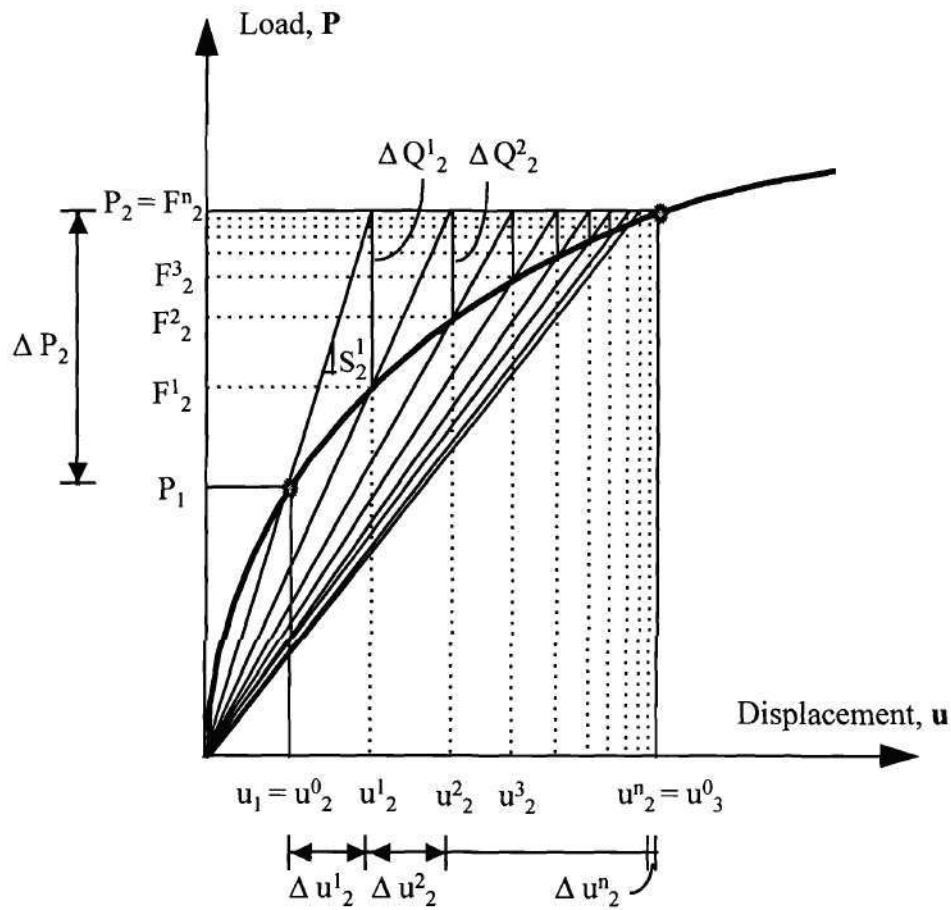
$$[S_{\text{Global}}] \{d\mathbf{u}\} = \{d\mathbf{P}\} \quad (6.3)$$

where S_{Global} is a tangent stiffness and the displacement increments $d\mathbf{u}$ are added from each load increment $d\mathbf{P}$ to calculate the stress-strain response.

An iterative procedure which considers a secant stiffness approach, was found to be necessary in the analysis with an incremental loading scheme. In each load increment, the nonlinear iterations are performed using the appropriate resilient modulus models to calculate the correct vertical resilient modulus corresponding to the total stress state.

The two nonlinear solution techniques suitable for the above discussed material models were then chosen to be: (1) the direct secant method and (2) the Newton-Raphson scheme with the secant modulus approach (Chen and Lui, 1987). The direct secant method involves the solution of the nonlinear load-displacement behavior by updating the secant stiffness in each iteration until convergence is reached for the load increment. For subsequent load increments, the procedure is followed using the previously calculated secant stiffnesses.

The second method involves for each iteration the solution of the updated secant chord stiffness matrix \mathbf{S} with the load imbalance vector $\Delta\mathbf{Q}$ until the convergence for the load increment is reached (see Figure 6.4). A rapid convergence was expected using this Newton-Raphson scheme modified for the secant stiffnesses as compared to the direct secant stiffness method. As shown in Figure 6.4, the Newton-Raphson method using the



P_1 = Load increment 1,

F_2^1 = Calculated internal load after 1st iteration at load increment 2,

u_2^1 = Total displacement after 1st iteration at load increment 2,

S_2^1 = Secant stiffness at the beginning of load increment 2,

$\Delta Q_2^1 = P_2 - F_2^1$; load imbalance after 1st iteration,

n = number of iterations for convergence.

Figure 6.4. Secant Modulus Approach For Newton-Raphson Scheme.

secant stiffnesses is summarized for the second load increment through the following steps:

1. Solve for incremental displacements $\Delta \mathbf{u}_2^1 = [\mathbf{S}_2^1]^{-1} \Delta \mathbf{P}_2$

2. Update displacements $\mathbf{u}_2^1 = \mathbf{u}_2^0 + \Delta \mathbf{u}_2^1$

Calculate stresses $\boldsymbol{\sigma}_2^1 = \mathbf{D} \boldsymbol{\varepsilon}_2^1$ where $\boldsymbol{\varepsilon}_2^1 = \mathbf{B} \mathbf{u}_2^1$

3. Using the material model, compute $\mathbf{D}(\mathbf{M}_R) = f(\boldsymbol{\sigma}_2^1)$

Compose $\mathbf{S}_2^2 = \int_V \mathbf{B}^T \mathbf{D} \mathbf{B} dV$

4. Find internal forces at nodes $\mathbf{F}_2^1 = \int_V \mathbf{B}^T \boldsymbol{\sigma}_2^1 dV$

5. Calculate load imbalance $\Delta \mathbf{Q}_2^1 = \mathbf{P}_2 - \mathbf{F}_2^1$

6. Solve for $\Delta \mathbf{u}_2^2 = [\mathbf{S}_2^2]^{-1} \Delta \mathbf{Q}_2^1$ and update $\mathbf{u}_2^2 = \mathbf{u}_2^1 + \Delta \mathbf{u}_2^2$

7. Repeat n times until convergence when $\mathbf{u}_3^0 = \mathbf{u}_2^n$.

Preliminary studies using the secant modulus approach with the Newton Raphson iteration scheme, however, indicated convergence problems to exist. The load imbalance $\Delta \mathbf{Q}$ was observed to increase after the third or fourth iteration thus causing the nonlinear iterations to diverge. The reason for this is believed to be the hardening nature of the

resilient behavior of granular materials used in the nonlinear base layer. Hardening behavior is shown in an example problem solved in Chapter 7.

Unlike many other type of engineering materials such as steel or concrete, granular materials exhibit increased resilient stiffness at higher stress levels. The hardening shape of the nonlinear stress-strain relationship can be visualized, for example, when two elastic spheres are pressed against each other. When the applied pressure is small, the contact surface is also small and an increase in pressure results in a large displacement between the centers of the spheres. When the applied pressure is high, the contact surface becomes large and the same amount of increase in pressure causes relatively smaller displacement between the centers of the spheres but higher stiffness (Timoshenko and Goodier, 1970; Seridi and Dobry, 1984).

An example of the Newton-Raphson method for the secant modulus approach is given in Figure 6.5 illustrating the resilient hardening behavior of granular materials. Following the Newton-Raphson procedure, the load imbalance obtained after the first iteration ΔQ_2^1 becomes greater than the load increment ΔP_2 . Furthermore, the secant chord drawn to this last point comes down on the first load increment point on the curve at the P_2 level thus making the second load imbalance $\Delta Q_2^2 = \Delta P_2$. According to this sample illustration, convergence is never achieved since the second iteration returns back to the starting point of the second load increment. Similar unsatisfactory results were obtained in a preliminary study using GT-PAVE and the Newton-Raphson scheme for the secant modulus.

A direct secant stiffness approach was then developed for the nonlinear analysis of granular base and subgrade layers and included in the GT-PAVE finite element program. The direct secant method, in general, is less complicated than the Newton-Raphson scheme. Yet it is sophisticated enough to give good convergence of the iterations (see Figure 6.6). The nonlinear analysis is performed using both an incremental loading scheme and an iterative solution technique for each load increment as follows:

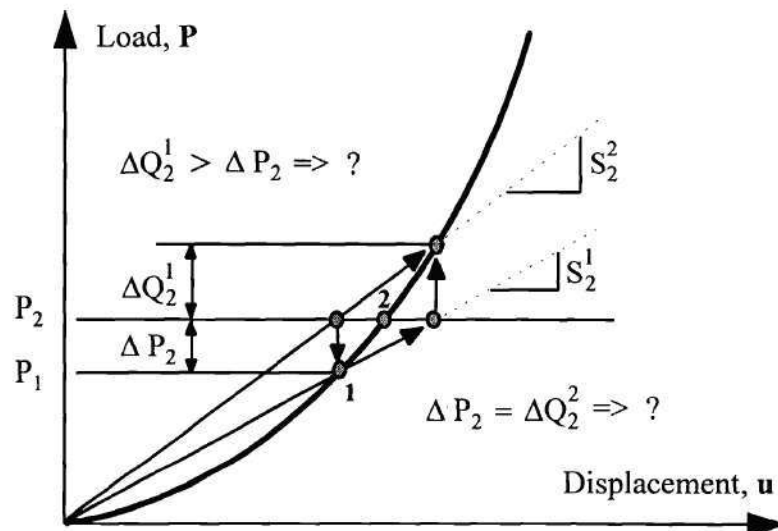
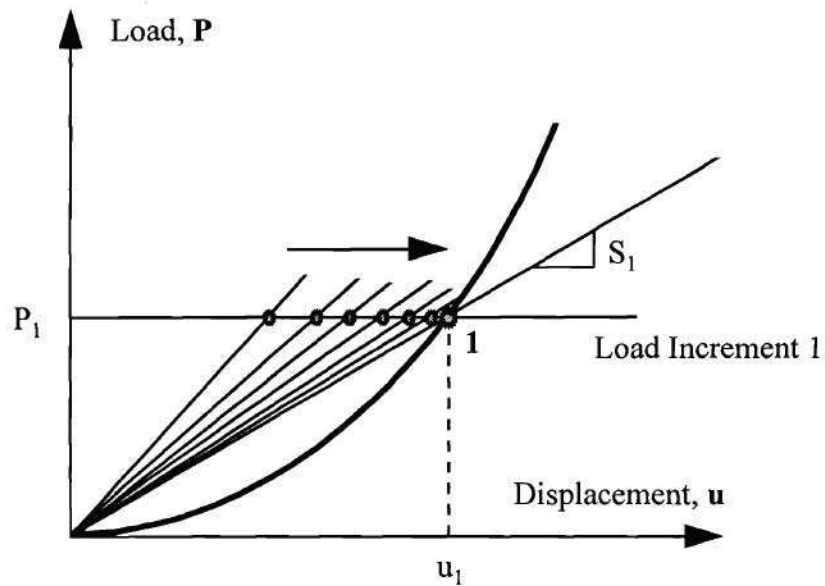
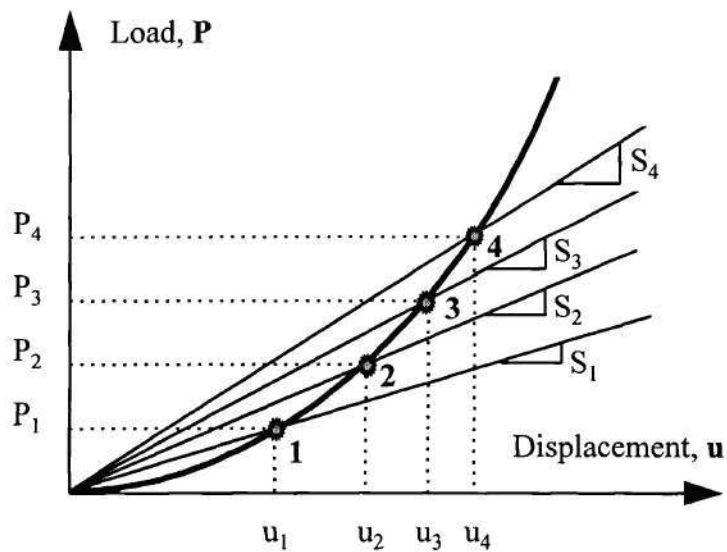


Figure 6.5. Secant Newton-Raphson Scheme for the Hardening Granular Material Behavior.

1. First the finite element mesh is generated to give the desired pavement geometry. Necessary material property constants, number of load increments, and



(a) Nonlinear iterations for convergence during load increment 1.



(b) Secant stiffnesses after 4 load increments.

Figure 6.6. Resilient Modulus Search Technique Using Secant Stiffnesses For Flexible Pavements.

convergence criteria are input along with initially assumed material properties and the wheel loading.

2. The nonlinear analysis is begun by applying in typically five load increments just the gravity (body weight) loads and the initial residual compaction stresses. For each increment of body loading, principal stresses are calculated at the nine integration points in each element. New values of the secant resilient modulus are computed at each integration point using the material model and the latest principal stresses.

3. To converge smoothly for each load increment as shown in Figure 6.6a, a damping factor λ (which has values between 0 and 1) was developed to obtain an improved estimate of the resilient modulus for the next iteration in the form:

$$M_R^j = (1 - \lambda) M_R^{j-1} + \lambda M_{R_{\text{Model}}}^j \quad (6.4)$$

where M_R^j = actual M_R to be used at the end of iteration number j ,

M_R^{j-1} = M_R used at the end of iteration number $(j-1)$,

$M_{R_{\text{Model}}}^j$ = M_R computed from the model at the end of iteration number j .

Typically, λ has no major effect on the gravity loading and the residual compaction stress computations and is therefore taken to be 1.0. For the wheel

load, however, the values needed for quick convergence were found to be between $\lambda = 0.3$ and 0.4 .

4. The convergence criteria used in this study consist of (i) a maximum of a 5% difference between the old and new values of resilient modulus at each integration point in each element and (ii) a 0.2% maximum cumulative error (E_c) criterion which is similar to the one used in the Senol program (Brown and Pappin, 1981):

$$E_c = \frac{\sum_{i=1}^n \left(M_R^j - M_R^{j-1} \right)^2}{\sum_{i=1}^n \left(M_R^j \right)^2} \quad (6.5)$$

where n = total number of integration points in the mesh,

j = the last iteration number for each load increment.

5. After the full body weight and residual stresses have been applied and convergence achieved, the wheel load is added in increments permitting the resilient modulus to gradually change as the stresses increase. Typically 10 load increments are used. For each load increment, new values of the secant moduli are computed at each integration point using the most recently calculated stresses in the elements. Once again the moduli for the next iteration are computed using the damping factor λ and checked for convergence.

In general, the cumulative error limit of 0.2% is quite easily satisfied within two iterations. The 5% individual error criterion usually controls convergence with up to 7 or 8 iterations being necessary as the wheel loading is gradually increased to the full value.

6. At the end of each increment of wheel loading, principal stresses at each integration point within the granular base are checked to see if tension exists. If tension is found, the stress transfer algorithm of Doddihall and Pandey (1984) is employed only in the continuum approach until the solution converges.

Figure 6.7 presents a flow diagram of the NONLIN subroutine summarizing the above described steps followed in the nonlinear analysis. The convergence of the direct secant stiffness approach can usually be controlled by assigning low values to the damping factor λ on the order of 0.3 to 0.4. Large changes in material properties are therefore avoided, and the oscillations of the resilient moduli which can cause divergence of the solution are prevented. The use of low λ values, however, generally results in an increased number of iterations needed for convergence. Therefore, λ should be varied to optimize the solution process. In case of an increase in the individual or cumulative errors, iterations for continuum model tension modifications or nonlinear iterations for the next load increment are initiated and a warning statement is printed.

The NONLIN subroutine calls the MODEL subroutine for the computation of the new moduli from the previous stress state. Principal stresses computed at each

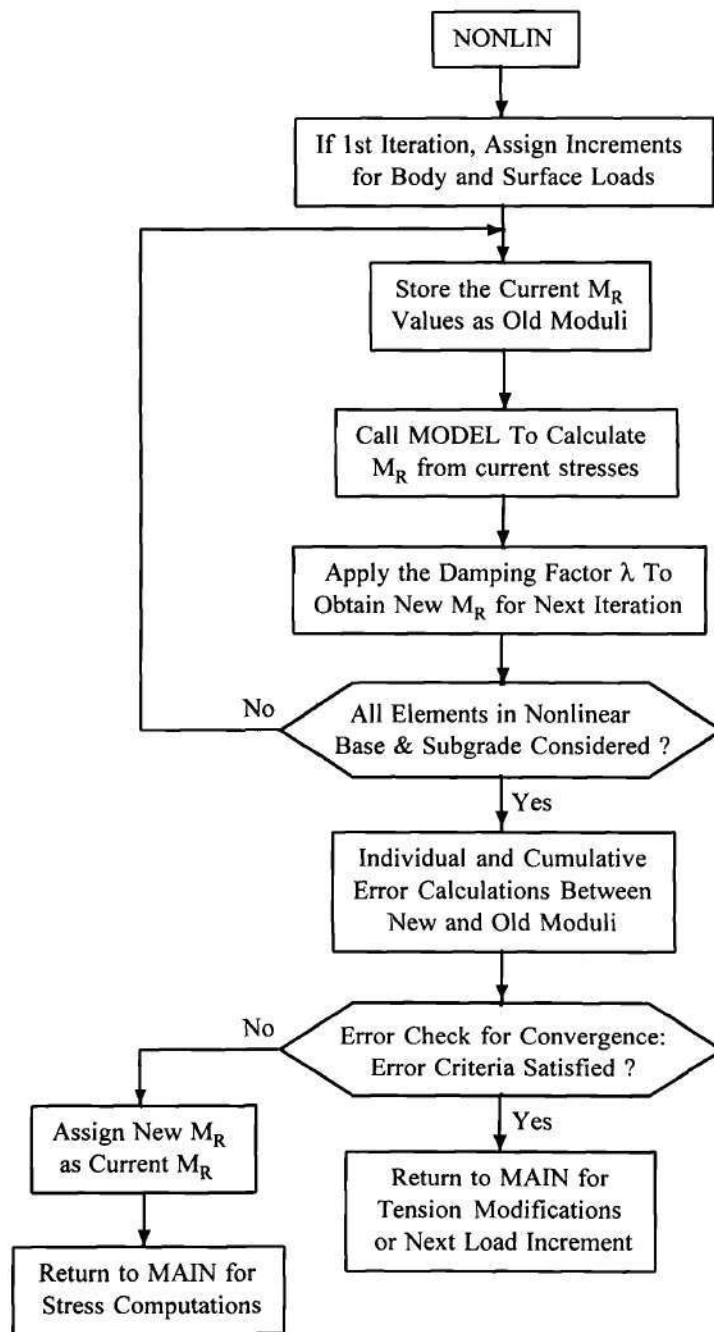


Figure 6.7. Flow Diagram of NONLIN Nonlinear Analysis Subroutine.

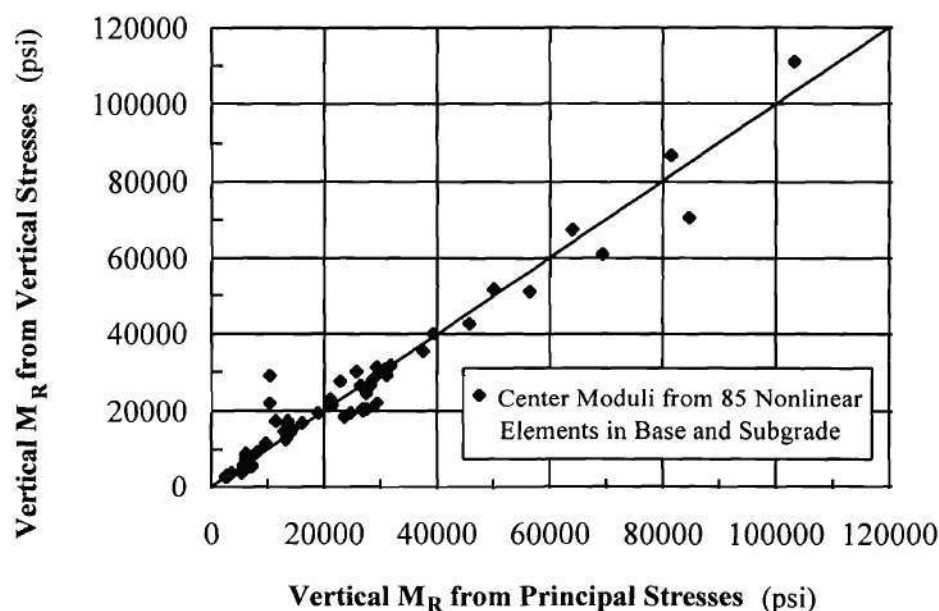
integration point are used to determine the material properties at that point. This approach eliminates the need to interpolate stresses and strains at element edges and layer boundaries, and therefore is more accurate than using stresses at the nodes.

Due to the rotation of the principal stress axes, the use of principal stresses for calculating the vertical resilient moduli can, however, introduce error for the elements located away from the centerline of loading. On the other hand, using principal stresses also eliminates the effect of any shear stresses included in the stiffness computations. Figure 6.8 shows the effect of principal stress rotation on the vertical resilient modulus computed using the simplified models. The vertical moduli obtained at the center of 85 elements used in the nonlinear base and subgrade layers are plotted in Figure 6.8. The moduli plotted on the horizontal axis were calculated using principal stresses and those on the vertical axis using vertical stresses. Some differences in vertical moduli were observed mostly at the higher stiffnesses encountered in the top portion of the granular base layer. In general, however, the rotation of principal stress axes was found to have negligible effect on the flexible pavement response predictions when compared to the results obtained using vertical stresses in the models.

No Tension Modifications

The horizontal tension in a granular base layer, as obtained from the elastic layered solutions, is reduced or eliminated in the GT-PAVE finite element program using the

following approaches: (1) assignment of cross-anisotropic material properties to the unbound aggregates, (2) reducing the horizontal stiffness in the elements that go under tension, (3) applying the no tension stress transfer approach of Doddihal and Pandey (1984) in the continuum model, and (4) applying equilibrium iterations in the block model in which no tension is allowed to develop between the blocks of aggregates. The fourth method is described in detail in Chapter 8.



$$1 \text{ psi} = 6.895 \text{ kPa}$$

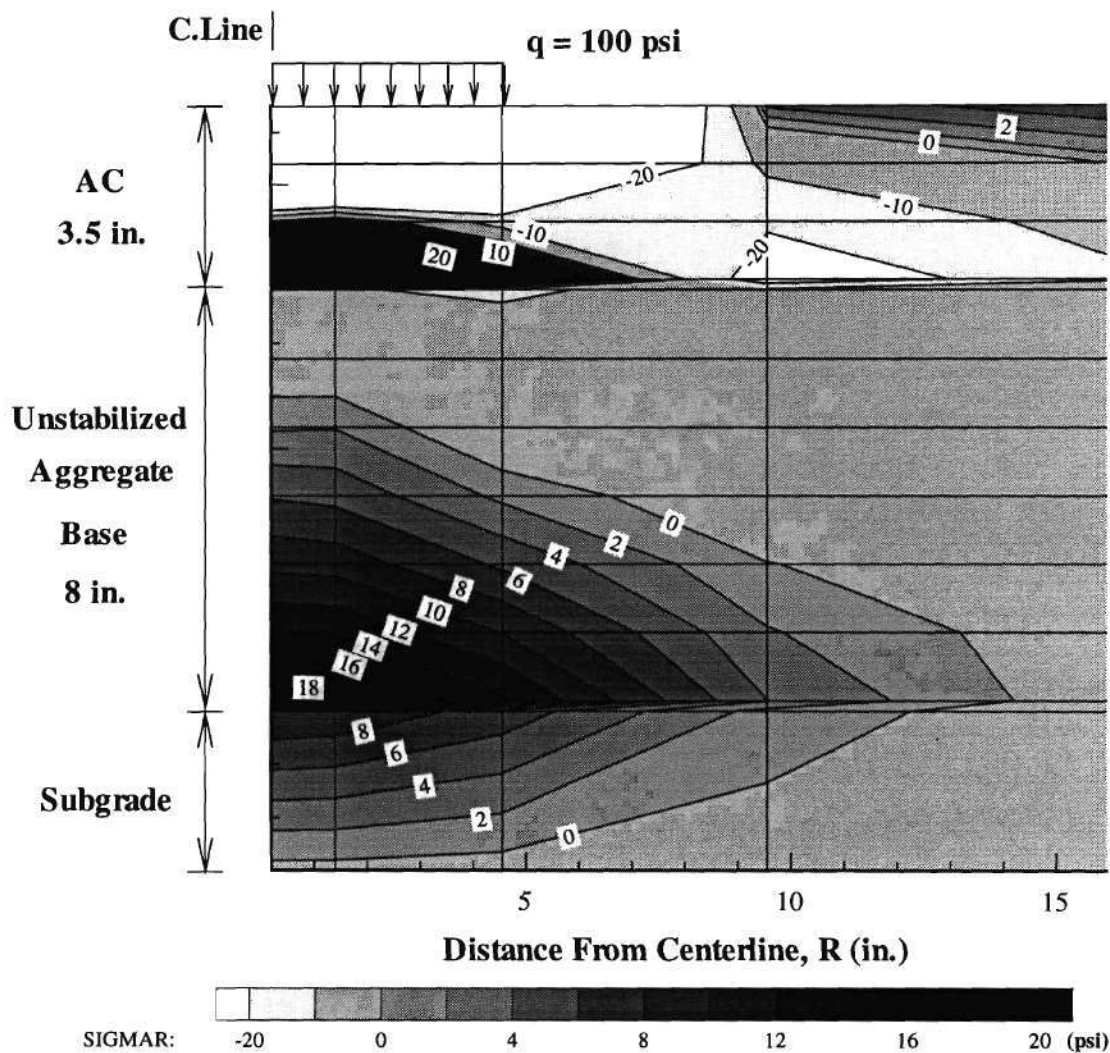
Figure 6.8. Effect of Principal Stress Rotation on the Computed Vertical Modulus.

The first two approaches mentioned above are closely related and applied to both the continuum and block models. A realistic representation of the base is achieved when

cross-anisotropy enables the assignment of different stiffnesses in vertical and horizontal directions. Horizontal tensile stresses calculated in the nonlinear analysis are eliminated by applying compressive nodal loads in the granular base. Overall equilibrium after each iteration until the tension is eliminated.

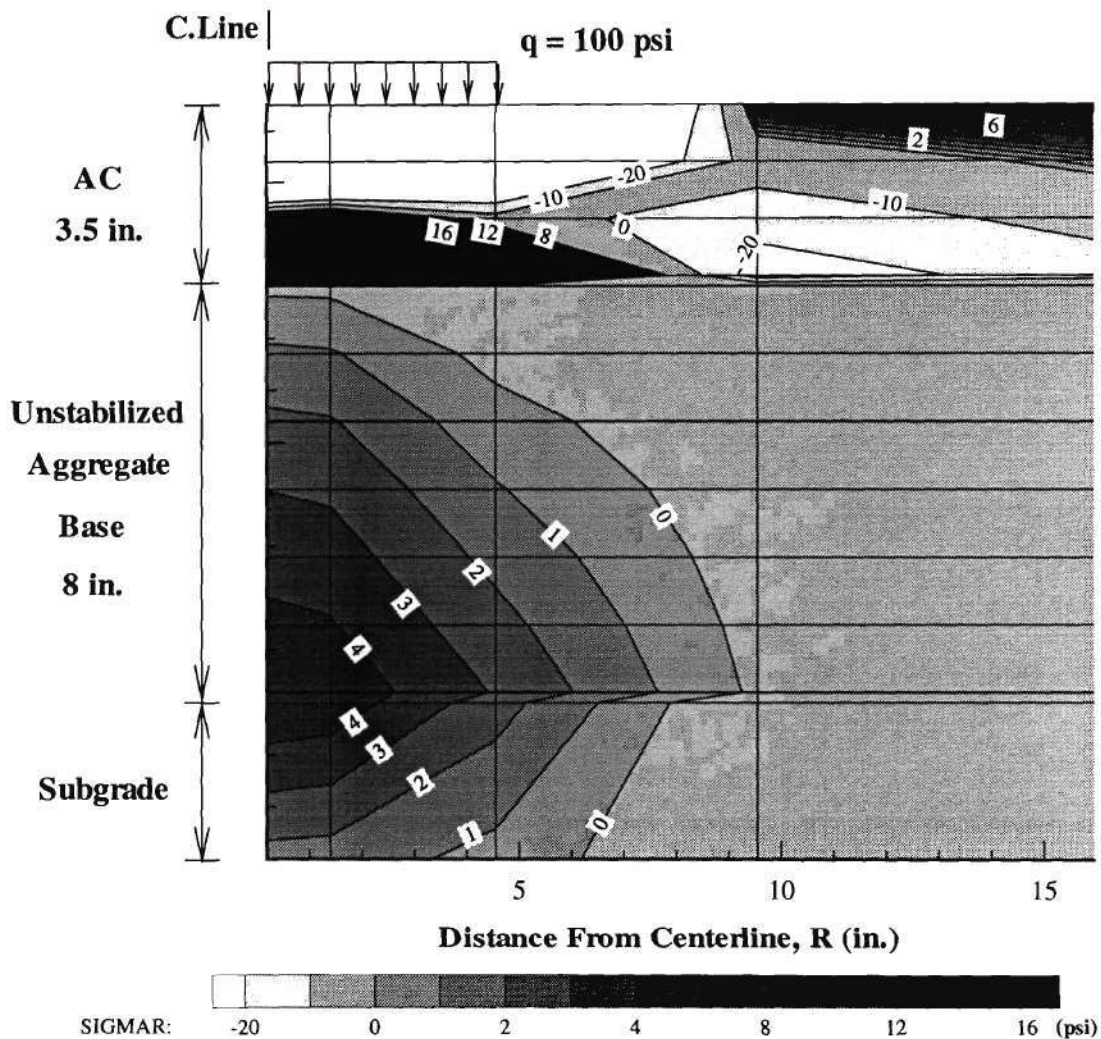
To demonstrate the effects of how cross-anisotropic representation alone can change the horizontal stress state in granular bases, a three layer flexible pavement test section problem was analyzed. The section consisted of: (1) a 3.5 in. (89 mm) thick asphalt concrete (AC) surfacing, (2) an 8 in. (203 mm) thick unbound aggregate base, and (3) a 50 in. (1270 mm) thick subgrade. A 100 psi (689 kPa) uniform wheel load was applied over a circular area of radius 4.55 in. (116 mm). Two linear elastic runs were performed using the GT-PAVE program with isotropic and cross-anisotropic material properties assigned in the base layer.

Figures 6.9 and 6.10 show the contour plots of the radial stresses in the section as obtained using the linear elastic solutions for isotropic and cross-anisotropic bases, respectively. In both cases, the same 34,925 psi (240.8 MPa) value of the vertical resilient modulus was used in the base while the horizontal stiffness in the cross-anisotropic base was decreased to 15% of the vertical. The Poisson's ratio in the horizontal direction was taken to be 0.15 in the cross-anisotropic representation. As a result, the magnitudes of the calculated horizontal tensile stresses in the cross-anisotropic base were only about 1/4 of the isotropic values (Figure 6.10). The assignment of realistic cross-anisotropic material properties to unbound bases, therefore, helps



- Notes: 1. Isotropic Linear Elastic Properties in Base:
 $M_R = 34925 \text{ psi}$, $\nu = 0.45$
 2. Tension is positive
 3. 1 in. = 25.4 mm, 1 psi = 6.895 kPa

Figure 6.9. Horizontal Tension Zone in the Base As Predicted By Isotropic Linear Elastic Solution.



- Notes: 1. Cross-Anisotropic Linear Elastic Properties in Base:
 $M_R^z = 34925 \text{ psi}$, $n = 0.15$, $m = 0.34965$, $\nu_z = 0.45$, $\nu_r = 0.15$
 2. Tension is positive
 3. 1 in. = 25.4 mm, 1 psi = 6.895 kPa

Figure 6.10. Horizontal Tension Zone in the Base As Predicted By Cross-Anisotropic Linear Elastic Solution.

significantly reduce the horizontal tensile stresses calculated in the granular bases using isotropic, linear elastic theory.

A simple method to handle tension which usually works is to set the horizontal resilient modulus equal to zero or a small value in the elements where horizontal tension is observed. To do this, a tension reduction factor n has been adapted in the GT-PAVE program which specifies the percent reduction of the vertical modulus to be assigned in the horizontal direction as follows:

$$n = M_R^r / M_R^z \quad (6.6)$$

where M_R^r is the resilient modulus in horizontal direction and M_R^z is the modulus in vertical direction. After the new resilient moduli are computed in the MODEL subroutine from the most recently calculated principal stresses, the radial and tangential stresses (σ_r , and σ_θ) are checked to see if horizontal tension exists (radial tensile stresses greater than 0.1 psi, 0.69 kPa) in the element. In case of tension, the horizontal modulus is calculated from Equation 6.6. The appropriate values assigned to the tension reduction factor n has been found from modeling of full-scale pavement tests to be in the order of 10 to 20% which is in agreement with the values reported by Chan et al. (1989). In contrast to recommendations of others (Zienkiewicz et al., 1968), a zero stiffness in the horizontal

direction does not result in the best agreement between the predicted and measured response variables in flexible pavements.

The GT-PAVE program also employs for the continuum approach a “no tension” analysis to modify the calculated stresses when the granular base does go into tension. The “no tension” stress transfer approach, originally proposed by Zienkiewicz et al. (1968), has been modified following the recommendations of Doddihal and Pandey (1984). In this approach, the tensile stresses are counteracted by compressive nodal loads always maintaining the overall equilibrium after each iteration until tension is eliminated. The modified “no tension” analysis method achieves faster convergence than the original one (Zienkiewicz et al., 1968) for the elimination of mainly the horizontal tensile stresses encountered in the lower portion of the granular base.

The modified “no tension” method (Doddihal and Pandey, 1984) has been implemented in TENSION subroutine with its flowchart also given in Figure 6.11. After the nonlinear iterations converge for one load increment, the horizontal stresses in the unbound aggregates are checked for tension. An iterative tension modification procedure is then applied to the granular base as follows:

1. The total strain, total stress, and global restraining load vectors related to the tension analysis are initialized in the TENSION subroutine.
2. The strains and stresses calculated at the integration points in the nonlinear analysis (if 2nd tension iteration, these are the stresses and strains obtained from

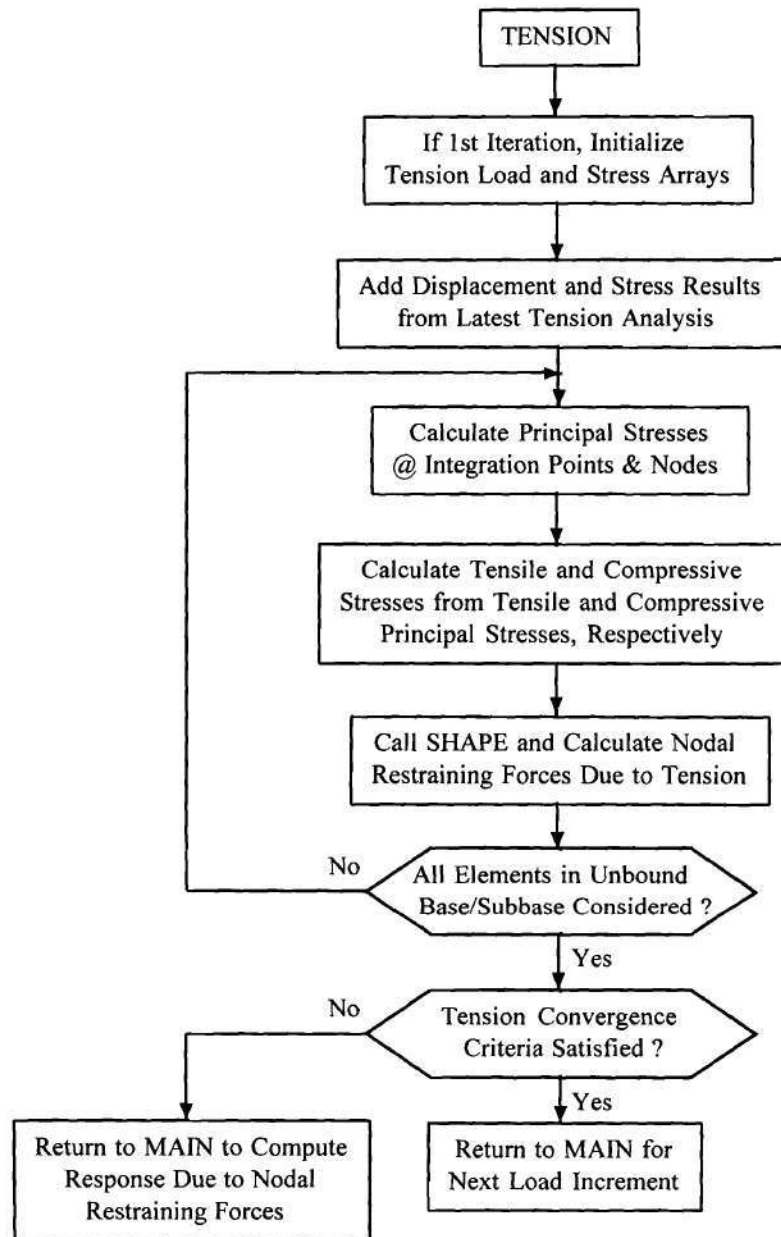


Figure 6.11. Flow Diagram of TENSION Tension Modification Subroutine.

the first tension iteration) are added to the total strain and stress arrays and the principal stresses are calculated using Equation 2.7.

3. The principal stresses calculated at the integration points in the elements are separated into tensile and compressive components. A principal stress of 0.1 psi (0.69 kPa) has been considered in the TENSION subroutine to be the limiting tensile strength of granular materials above which the principal tensile stresses can not exist.

4. The tensile stresses necessary on the elements to cause only principal tensile stresses, if exist, are computed from the following equations:

$$\sigma_r = [(\sigma_1 + \sigma_3) / 2] + [(\sigma_1 - \sigma_3) / 2] \cos 2\theta \quad (6.7)$$

$$\sigma_t = \sigma_2 \quad (6.8)$$

$$\sigma_z = [(\sigma_1 + \sigma_3) / 2] - [(\sigma_1 - \sigma_3) / 2] \cos 2\theta \quad (6.9)$$

$$\tau_{rz} = [(\sigma_1 - \sigma_3) / 2] \sin 2\theta \quad (6.10)$$

5. The nodal restraining forces needed to counteract the tensile stresses obtained from Equations 6.7 to 6.10 are found for each element as follows:

$$\mathbf{F} = - \int_V \mathbf{B}^T \boldsymbol{\sigma} dV \quad (6.11)$$

where \mathbf{B}^T is the strain-displacement matrix for each element and σ is the tensile stress vector obtained from Equations 6.7 to 6.10.

6. The nodal forces obtained in step 5 for each element are assembled to obtain a global load vector.

7. The compressive stresses which were applied to the elements to cause only principal compressive stresses this time are also computed using Equations 6.7 to 6.10.

8. Elastic analysis is then carried out using the material properties obtained from the previous nonlinear analysis. The response variables are computed under the application of the global load vector assembled in step 6.

9. The stresses calculated in step 8 are added to the compressive stresses found in step 7. The strains obtained as the response variables in step 8 are added to the strains computed at the end of the nonlinear iterations.

10. If the stresses in step 9 are tensile and greater than the 0.1 psi (0.69 kPa) limiting tensile strength, steps 2 to 9 are repeated until convergence is reached.

Using this tension modification procedure, most of the horizontal tension is generally reduced down to negligible amounts after about 2 to 3 iterations. For the tension modifications between any two load increments (before the full wheel load is applied), the maximum number of iterations has been specified to be 4 in the tension convergence criteria. Four iterations are often required due to the small, negligible

amounts of tension remaining in a few elements. The number of tension iterations for the last load increment, however, has not been restricted and usually takes about 8 to 9 iterations until no horizontal tensile stresses greater than the assigned tensile strength of the granular materials exist in the base layer.

The modified stress transfer approach used in the GT-PAVE finite element program, therefore, enables the complete elimination of any horizontal tensile stresses in the granular layer. This procedure, which uses an incremental iterative procedure, can be applied to either the linear or nonlinear analyses of a layered pavement system. The method, however, is considered to be another “band-aid” type approach, such as the ones given by Zienkiewicz et al. (1968) and Raad and Figueroa (1980), for the approximate solution of the continuum modeling of particulate media. By eliminating completely the horizontal tensile stresses, no consideration is given to the ability of aggregate particles to resist an apparent tension due to particle interlock and frictional resistance. The new block movement approach is described as an alternative method of handling the “no tension” problem in Chapter 8.

Limitations of the Computer Code

One potential major limitation of the GT-PAVE finite element program is that a static analysis is employed to model resilient response behavior of flexible pavements due to the moving vehicle loads. Foinquinos et al. (1994) recently showed that the

dynamic amplification of the computed response variables could possibly occur in the case of a shallow subgrade depth to bedrock where resonance exists. Other limitations of the program include: (1) modeling of the viscoelastic AC layer using linear elastic material properties; this approach should be reasonably valid since the loading time is relatively short and the stress levels on the pavement are small, (2) consideration for only axisymmetric stress analysis in the program, (3) employing small-displacement theory in the analytical models, and finally (4) no consideration has yet been given to elastic dilation of granular particles at block interfaces used in the block model described in Chapter 8.

Mamlouk and Davies (1984) developed a computer program for the analysis of flexible pavements considering the inertial effects due to dynamic loads. A damping ratio was assigned for each layer and the program was limited to the analysis of linear elastic materials. Mamlouk (1987) later indicated that the inertia effects are most pronounced when shallow bedrock or frozen subgrade is encountered and is more important for vibratory than for impulse loading. Monismith et al. (1988) also found that a complete dynamic analysis is not usually needed. The local dynamic response can thus be determined by an essentially static method using material properties compatible with the rate of loading for usually encountered pavement conditions.

Recently, Foinquinos et al. (1994) analyzed the dynamic response of pavement systems to dynamic loads imposed by nondestructive pavement testing techniques such as the falling weight deflectometer test (FWD). Analytical studies of the dynamic response

of a flexible pavement system to an FWD load indicated that at low frequencies of less than 10 Hz., the response is frequency independent and the system behaves as if the load was applied statically. When the frequency increased, the displacements also increased until they reached a peak characteristic frequency usually referred to as the resonance frequency. With further increase in frequency, the displacements, however, rapidly declined as the inertial effects damped out the response.

The static displacements decreased significantly at low frequencies, less than about 10 Hz., as the depth to bedrock decreased. The dynamic displacements were influenced very little by depth to bedrock for depths in excess of 20 ft. (6.1 m). The ratio of dynamic (peak) displacements to the static displacements (the so-called dynamic amplification) was also found to be a function of the depth to bedrock, peaking at a depth of about 7 to 10 ft. (2.1 to 3.1 m). The ratio was greater at radial distances away from the load application and was reduced down to less than 1 for a subgrade depth to bedrock of about 50 ft. (15.2 m). Therefore, for subgrade depths to bedrock less than about 50 ft. (15.2 m), a dynamic analysis is more critical and special care should be taken when interpreting the results of any static pavement analysis such as the analyses performed using the nonlinear GT-PAVE program.

Summary

The organization and capabilities of the nonlinear finite element program GT-PAVE was described in detail for the analysis of flexible pavements with granular bases.

The program is capable of modeling the granular base using both the continuum and block model approaches. The flow diagrams of the main program and several of the subroutines called from the general algorithm were presented. The essential features of the program were discussed such as the nonlinear analysis, residual compaction stresses, pre- and post-processing, incremental loading, and horizontal tension corrections in the unbound aggregate base.

The nonlinear analysis procedure adapted in the program employs a direct secant stiffness approach using a damping factor to iteratively calculate for each load increment the new resilient moduli from the stress state. The "no tension" modification procedure, which is only applicable to the continuum approach, eliminates any inadmissible horizontal tension in the granular base by using the stress transfer approach modified for use in flexible pavements. The static analysis performed in the GT-PAVE program is usually recognized as adequate for the analysis of flexible pavements except in cases of shallow subgrade depths to bedrock of less than 50 ft. (15.2 m).

CHAPTER VII

APPLICATIONS OF THE COMPUTER CODE

Introduction

The GT-PAVE finite element program is verified in this chapter using several example problems involving both the linear and nonlinear analyses. The results of these problems, which can usually be solved using closed form solutions, or results from laboratory measured data are compared with the GT-PAVE predictions. The effects of the compaction induced residual stresses on the horizontal tension zone in granular bases are also demonstrated in one example problem. The applications presented here model the AC layer as linearly elastic instead of viscoelastic since the loading time due to wheel load is relatively short and the stress levels on the pavement are rather small.

The resilient response of five well instrumented full-scale test sections is calculated in this chapter using the GT-PAVE program to determine if the nonlinear material models are practical for routine use give good results. These test sections were a part of an earlier study to evaluate factors affecting crushed stone base performance (Barksdale and Todres, 1983). They consist of 3 conventional sections with granular bases and two

inverted sections with cement stabilized subbases. An inverted section is constructed by placing in a flexible pavement an unbound aggregate base sandwiched between an upper asphalt concrete surfacing and a lower cement stabilized subbase. Eight measured response variables are predicted at different locations in the test sections. A sensitivity analysis of inverted sections is also performed to find optimum design geometries for the inverted sections. The potential performance of the selected inverted pavement sections are then compared with the conventional ones and practical conclusions are made.

Verification of the Computer Code

The linear elastic verification of the program mainly consists of solving 3 example problems using the GT-PAVE finite element program and then comparing the predictions with the closed form solutions. These example problems are: (1) a circular uniformly distributed load applied on a semi-infinite Boussinesq half-space, (2) a three layer system under the circular uniform load, and (3) the same three layer system used in the second problem but having cross-anisotropic properties in the granular base. In cases where the closed form solutions are not available, the predictions are then compared with the results obtained from the widely used, and commercially available, computer codes such as Kenlayer (Huang, 1993) and GT-STRUDL¹. For the nonlinear verification of the GT-

¹ Computer Aided Structural Engineering Center, Atlanta, GA 30332-0355 USA.

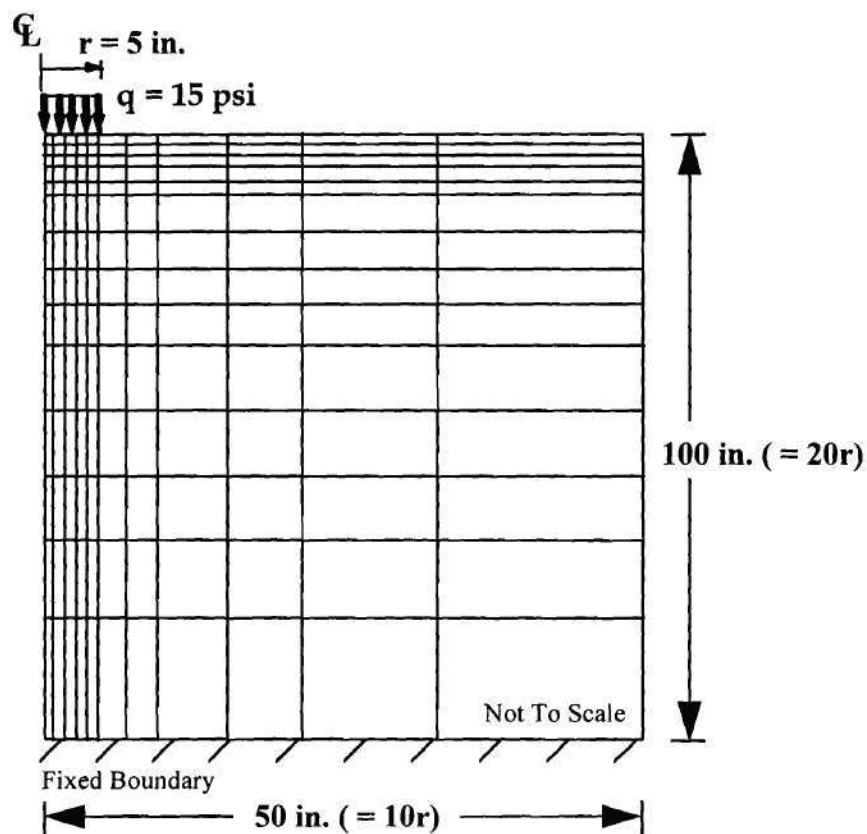
PAVE program, the measured resilient load-deformation response from one of the triaxial repeated load tests is used to compare with the finite element model predictions for the nonlinear granular material behavior. Verifications of the gravity loading, initial compaction stresses, temperature loading, and displacement loading in the form of support settlements were performed by comparing the predicted results with the GT-STRUDL results. These verifications are further checks of the GT-PAVE program but are not described here.

Example 1: Stress Distribution Boussinesq Type Problem

In this example a uniform circular load is applied over a semi-infinite elastic halfspace. The problem was originally solved by Boussinesq (1885) and the closed form solutions for the centerline stresses, strains, and surface deflection are given in Equations 2.2 through 2.6. This example problem then verifies the program for an isotropic, linear elastic condition by comparing the GT-PAVE finite element predictions with the closed form solutions.

A 154 element, 513 node axisymmetric finite element mesh was used to analyze stress distribution in the Boussinesq problem (see Figure 7.1). The load was applied as a uniform pressure of 15 psi (103.4 kPa) over a circular area of radius 5 in. (127 mm). To model the infinite depth and the horizontal direction of the Boussinesq problem where all stresses and displacements diminish, the finite element mesh was taken to be approximately 100 in. (2.54 m) deep (i.e., 20 times the load radius) and 50 in. (1.27 m)

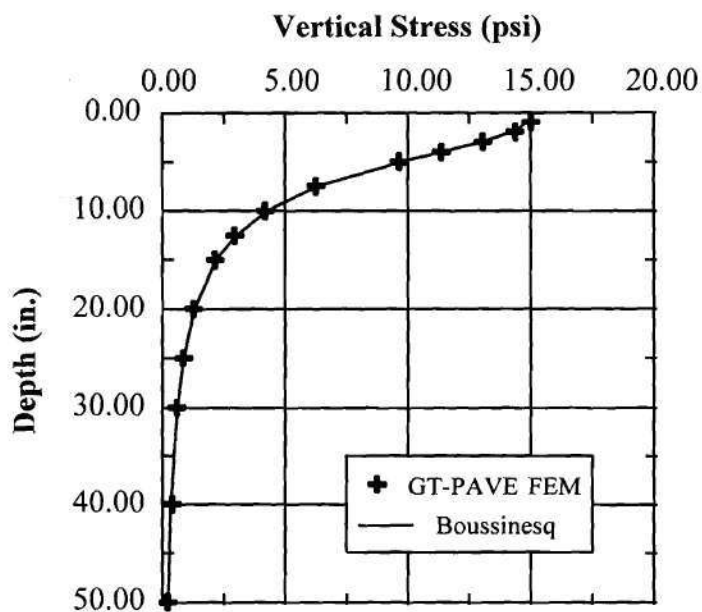
wide (i.e., 10 radii). The isotropic material properties assigned to the layer consisted of an elastic modulus of 30,000 psi (206.85 MPa) and a Poisson's ratio of 0.3.



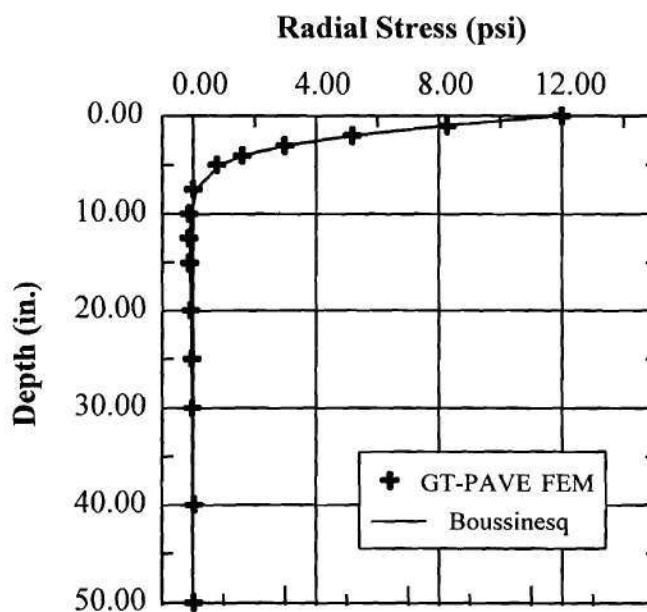
- Notes: 1. 1 in. = 25.4mm, 1 psi = 6.895 kPa.
2. Nodes on vertical boundaries restrained horizontally.

Figure 7.1. Finite Element Mesh for the Boussinesq Type Problem.

The closed-form Boussinesq solution for radial and vertical stresses at the centerline of loading calculated using Equations 2.2 and 2.3, respectively, are plotted in Figure 7.2 together with the GT-PAVE FEM predictions. For a depth of 50 in. (1270



(a) Vertical stress @ centerline, (compression is positive)



(b) Radial stress @ centerline, (compression is positive)

(Note: 1 in. = 25.4 mm, 1 psi = 6.895 kPa)

Figure 7.2. GT-PAVE FEM Stress Predictions for the Boussinesq Type Problem.

mm) shown, the finite element results are in good agreement with the stress distribution curves obtained from the equations. The maximum error between the predicted stresses and closed-form solutions is about 3.3% which was obtained for the low values of the radial stresses less than 1 psi (6.895 kPa). The predicted surface deflection of 0.00442 in. (0.112 mm) also compares very well with the theoretical value of 0.00455 in. (0.116 mm) resulting in a 2.9% error.

Previous experience has shown that stresses based on quadrilateral elements are accurate provided that the length to width ratio does not exceed five to one (Cook et al., 1989). In the present analysis, however, good predictions have been obtained although many elements used in the mesh did not satisfy the above stated aspect ratio criterion. The use of elongated elements, with an aspect ratio of up to 40 to 1 at the bottom of the mesh, has been found not to change the accuracy of the computed response values since the stresses, strains, and deflections and their gradients become small at a depth of about three to four times the diameter of the loading.

Example 2: Isotropic Three Layer System

The elastic multi-layered theory, discussed in Chapter 2, is applied in this example for the solution of an isotropic three-layer problem on a semi-infinite halfspace (see Figure 7.3). The three-layered system used consists of a 4 in. (102 mm) top layer (asphalt concrete, AC), an 11 in. (279 mm) middle layer (base), and a bottom layer (subgrade) of infinite in thickness. All layers are homogeneous, isotropic and linearly elastic with

stiffnesses of each layer decreasing with depth. The three-layered problem, therefore, represents a flexible pavement where the stresses caused by a 15 psi uniformly distributed circular wheel load are spread out with increasing depth. The three layer pavement having the isotropic material properties are shown in Figure 7.3.

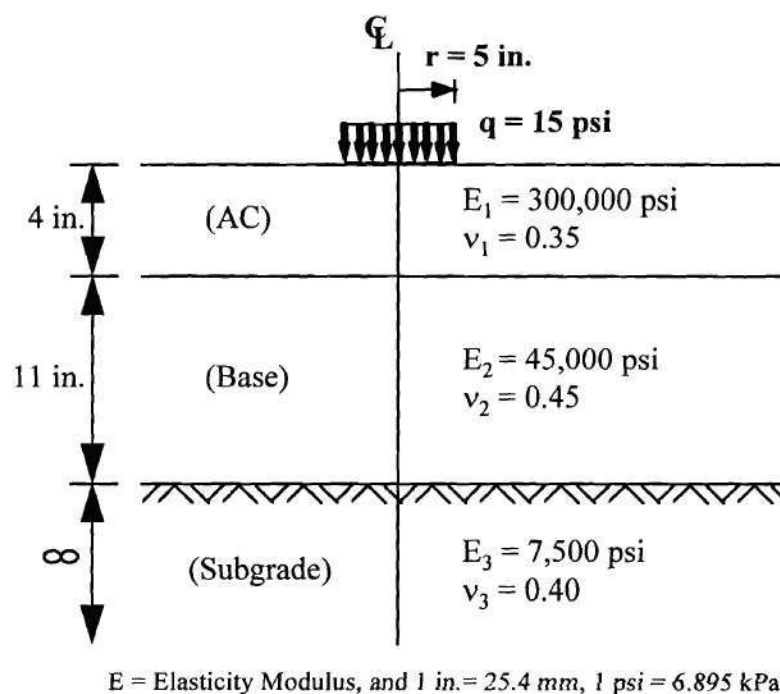


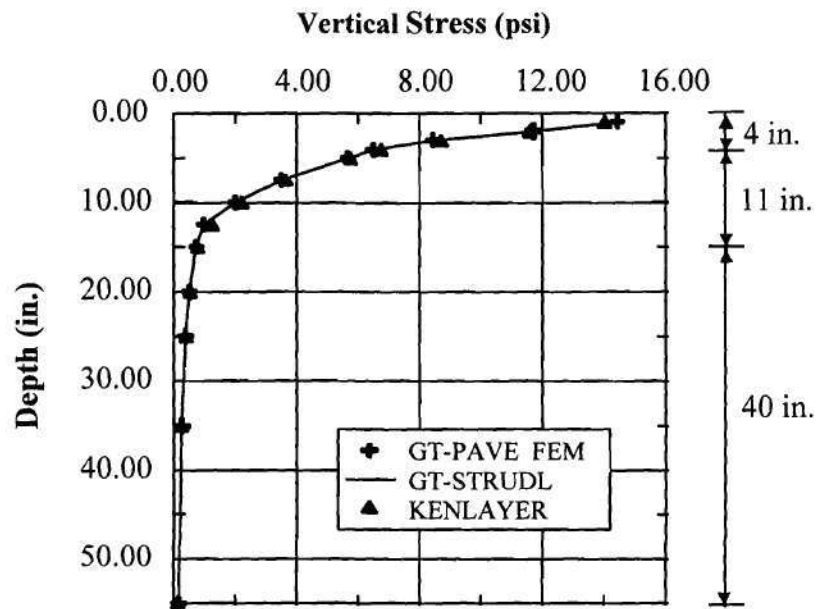
Figure 7.3. Three-Layer Elastic Isotropic System Problem on Semi-Infinite Halfspace.

The same 154 element, 513 node axisymmetric finite element mesh (see Figure 7.1) used for the one layer Boussinesq problem is employed again to analyze the stress distribution in the isotropic three-layered problem. The load was applied as a uniform pressure of 15 psi (103.4 kPa) over a circular area of radius 5 in. (127 mm). The elastic

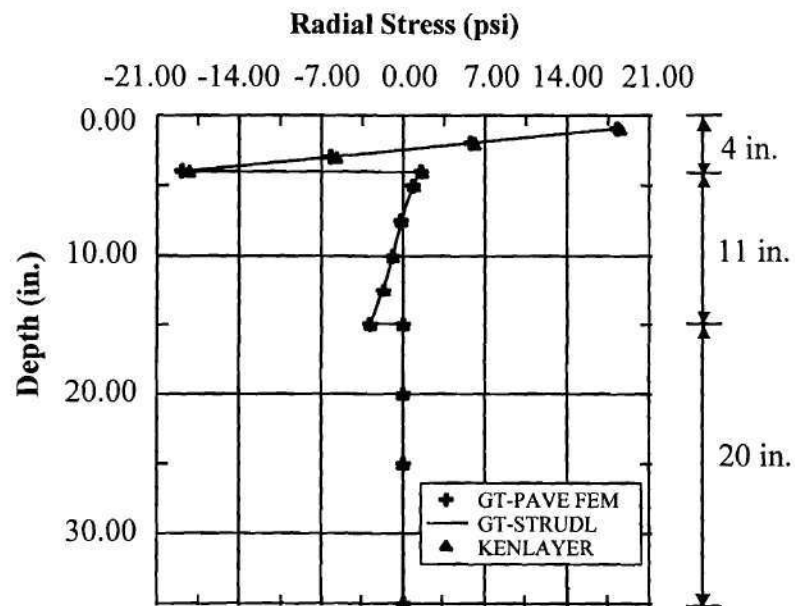
solution was then obtained using both the GT-PAVE program and the two commercially available computer codes. The Kenlayer (Huang, 1993) program gave closed form integral solutions. The GT-STRUDL program is a finite element program and was also employed to solve the three layer problem using the same mesh shown in Figure 7.1.

Figures 7.4 and 7.5 show the vertical and radial stresses computed by the GT-PAVE program and the other codes both at the centerline of loading and also at a 5 in. (127 mm) radial distance from the centerline. The results obtained for the same mesh from the two finite element programs, GT-PAVE and GT-STRUDL, were found to be essentially identical for up to six significant figures. The GT-STRUDL results are presented as a solid line in Figures 7.4 and 7.5 whereas the GT-PAVE predictions are shown as data points. Very good agreement was obtained between the GT-PAVE finite element program and the Kenlayer closed form solutions (see Figures 7.4 and 7.5) with typical errors in the order of 4% observed at the bottom of the top layer for the radial stresses.

The predicted GT-PAVE surface deflection of 0.00284 in. (0.072 mm) at centerline, differed from the 0.00299 in. (0.076 mm) Kenlayer closed form value of about 5.0%. The theoretical 0.00299 in. (0.076 mm) surface deflection was corrected for the 100 in. (2.54 m) depth considered in the finite element analysis. According to Duncan et al. (1968), a reasonable comparison between the finite element model and the integral solution can be made for a three-layered system if the bottom boundary in the mesh is moved to a depth of about 50 radii. This implies that an extra 150 in. (3.81 m) depth



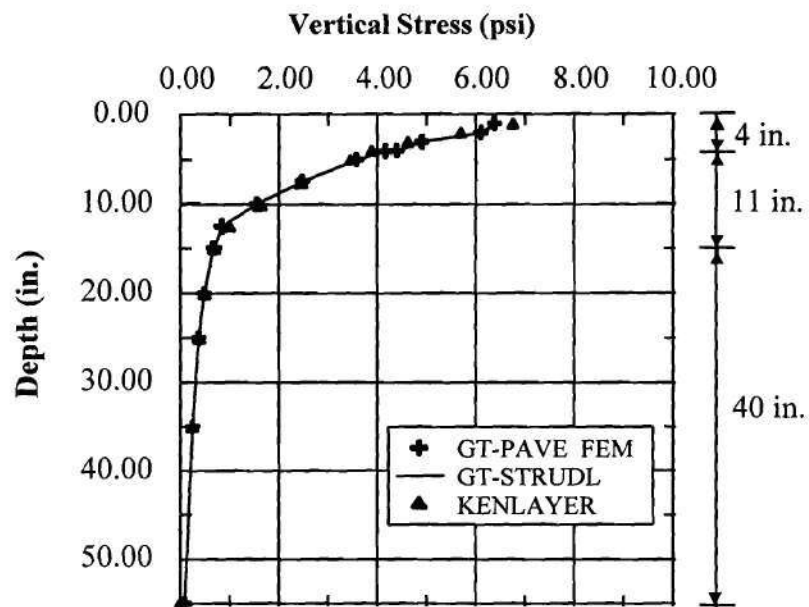
(a) Vertical stress, (compression is positive)



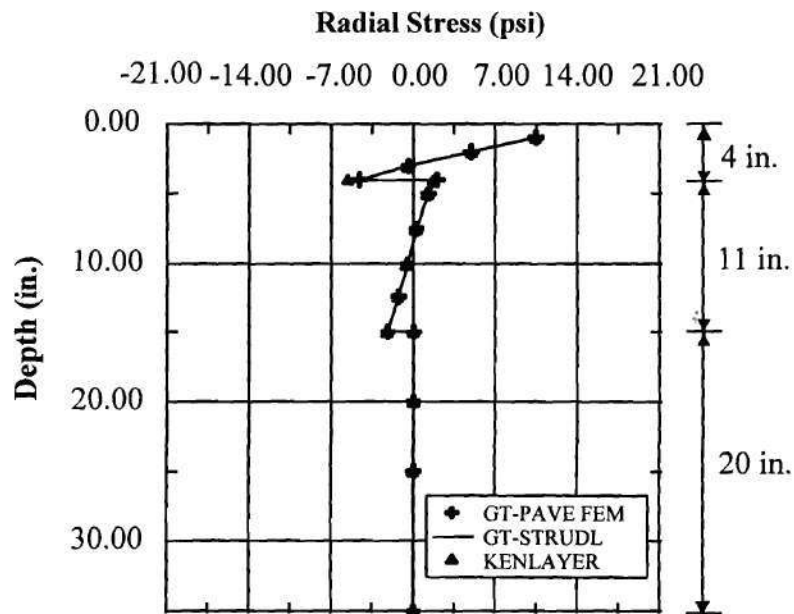
(b) Radial stress, (compression is positive)

(Note: 1 in. = 25.4 mm, 1 psi = 6.895 kPa)

Figure 7.4. GT-PAVE FEM Stress Predictions at Centerline for the Isotropic 3-Layer Problem.



(a) Vertical stress, (compression is positive)



(b) Radial stress, (compression is positive)

(Note: 1 in. = 25.4 mm, 1 psi = 6.895 kPa)

Figure 7.5. GT-PAVE FEM Stress Predictions at 5 in. Radial Distance for the Isotropic 3-Layer Problem.

added to the finite element model would then result in similar surface deflections without having to do any corrections on the theoretical surface deflections.

Example 3: Cross-Anisotropic Three Layer System

A three-layered linear elastic system similar to the previous isotropic example problem is considered now with cross-anisotropy assumed in the middle (base) layer. Everything else is the same as shown in Figure 7.3. The cross-anisotropic material properties assigned to the middle layer are as follows:

Elastic modulus in vertical direction: 45,000 psi (310.28 MPa),

Elastic modulus in horizontal direction: 6,750 psi (46.54 MPa),

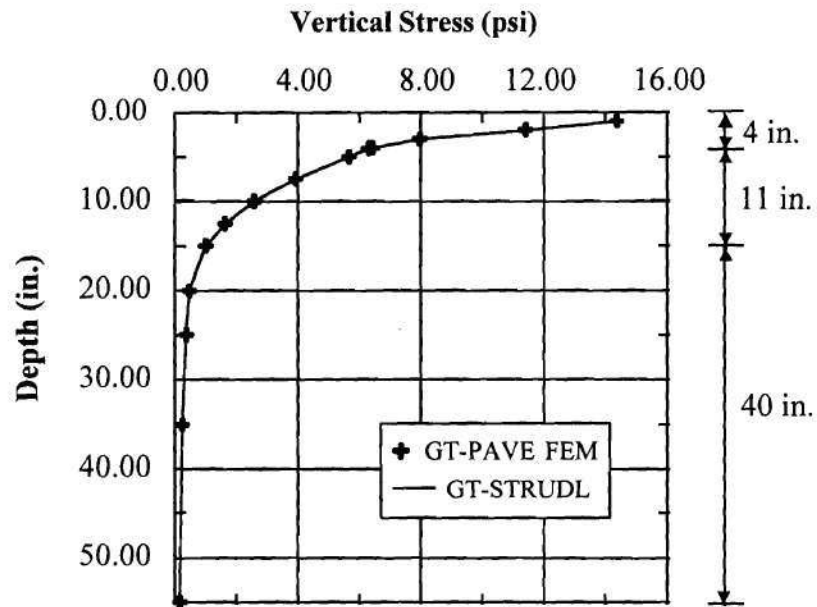
Shear modulus in vertical direction: 15734 psi (108.49 MPa),

Poisson's ratio in vertical direction: 0.45,

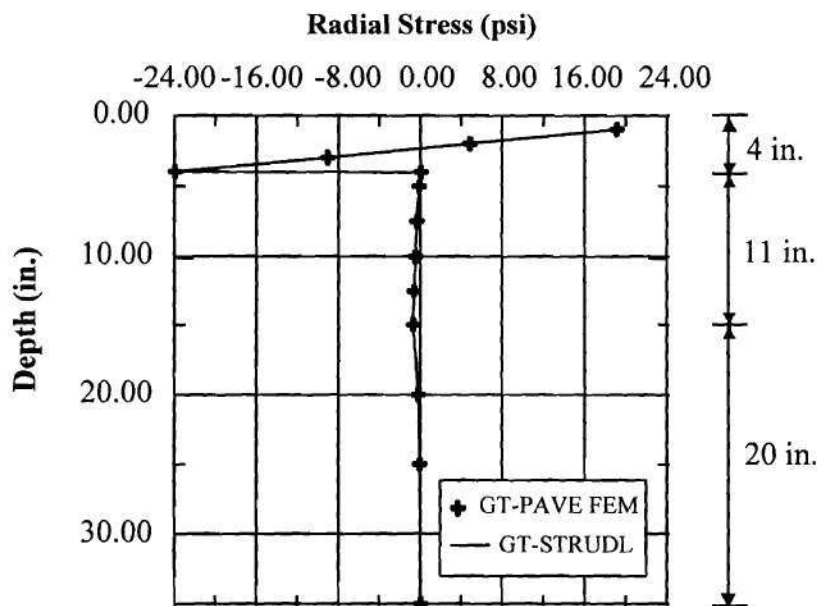
Poisson's ratio in horizontal direction: 0.15.

The same finite element mesh as shown in Figure 7.1 is again used in this example to achieve the following: (1) to compare both the isotropic and anisotropic solutions and also (2) to verify the GT-PAVE program by comparing the anisotropic predictions with the anisotropic GT-STRUDL results. No comparison for this example could be made with the closed form solutions since cross-anisotropic solutions were not available.

Figure 7.6 compares at the centerline of loading the vertical and radial stresses computed by using the GT-PAVE and GT-STRUDL finite element programs. As in the isotropic case, the vertical and radial stress predictions obtained using both computer



(a) Vertical stress, (compression is positive)



(b) Radial stress, (compression is positive)

(Note: 1 in. = 25.4 mm, 1 psi = 6.895 kPa)

Figure 7.6. GT-PAVE FEM Stress Predictions at Centerline for the Cross-Anisotropic 3-Layer Problem.

programs exactly match up to five significant figures for the anisotropic representation of the middle (base) layer. Therefore, the cross-anisotropic GT-PAVE program formulation is verified as shown in Figure 7.6. The GT-STRUDL results are shown with solid lines and the GT-PAVE predictions are plotted as data points.

The surface deflection at the centerline was found to be greater, 0.00329 in. (0.084 mm), in the anisotropic problem than the 0.00284 in. (0.072 mm) value obtained in the isotropic analysis. This 15.8% increase in surface deflection is computed mainly due to larger vertical deformations within the anisotropic base. Moreover, by comparing Figures 7.4 and 7.6, the magnitude of radial stresses computed in the base are significantly reduced in the anisotropic representation compared to the isotropic one because of the assignment of the low modulus in the horizontal direction.

Example 4: Modeling of Repeated Load Triaxial Tests

The results of the repeated load triaxial tests performed on granular materials (Alba, 1993), given in Appendix A, are used in this example to verify the GT-PAVE finite element model predictions for nonlinear incremental loading. As discussed in more detail in Chapter 4, the resilient modulus tests used in this example were performed on 6 in. (152 mm) diameter by 12 in. (305 mm) height cylindrical specimens. These specimens can be easily modeled using an axisymmetric finite element mesh (see Figure 7.7). The loading in the laboratory consisted of repeatedly applying 3 increasing levels of deviator stress, σ_d , on the triaxial samples at confining pressures σ_3 of 3, 5, 10, 15, and

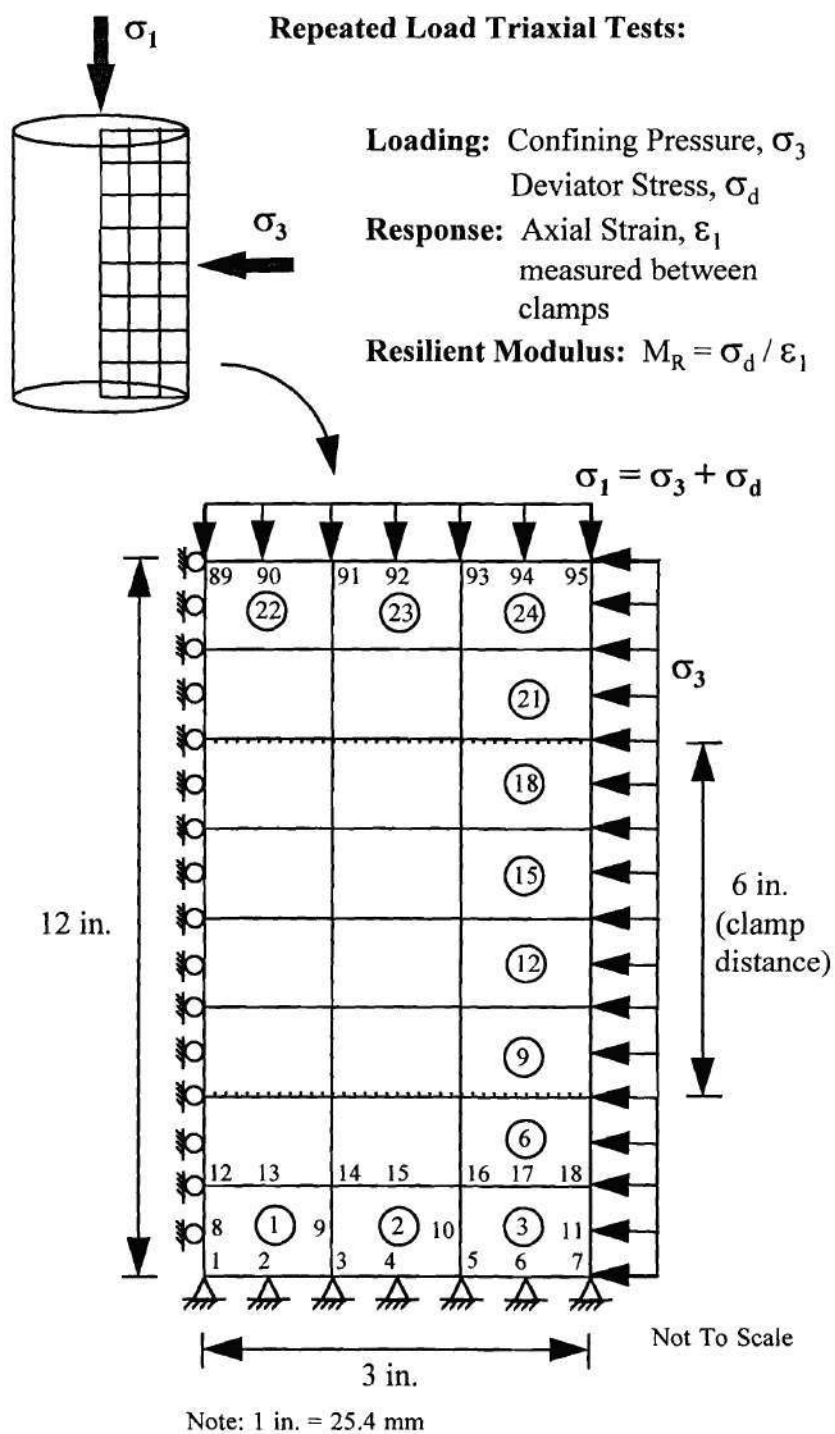


Figure 7.7. Axisymmetric Finite Element Mesh Used to Model Repeated Load Triaxial Tests on Granular Materials.

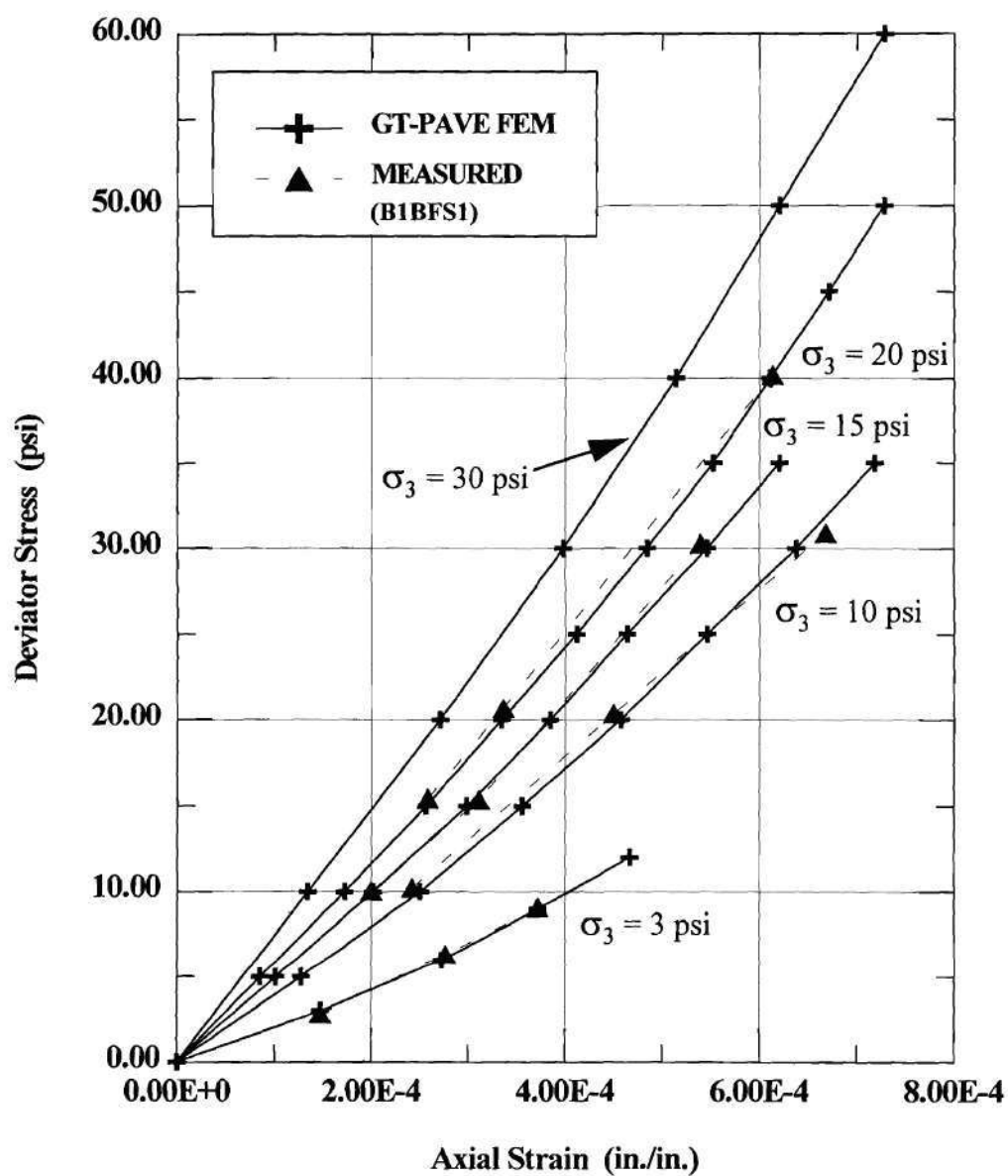
20 psi (20.7, 34.5, 68.9, 103.4, and 137.9 kPa). The tests were analytically modeled by statically loading the triaxial specimens at each confining pressure.

The measured resilient response was obtained from the tests after about 100 load repetitions of the 0.1 second duration haversine load pulse applied once in every second vertically on the specimen. The axial strain due to the applied deviator stress was measured from the LVDTs between clamps which were positioned at approximately one quarter distance from the top and bottom of the specimen height (see Figure 7.7). The load sequence was applied following the Strategic Highway Research Program P-46 (SHRP P-46) procedure. The resilient modulus of the granular material is calculated by dividing the applied deviator stress by axial resilient strain measured between the clamps.

Figure 7.7 shows the finite element idealization of the triaxial tests using a 24 element 95 node axisymmetric mesh. The granular material selected for this example is B1BFS1 which is one of the Georgia Tech bases with the properties given in Appendix A. The material is assigned isotropic properties with initial guesses of 45,000 psi (310.275 MPa) for the resilient modulus and 0.45 for Poisson's ratio. The nonlinear analysis consists of first applying the gravity loading due to its own weight [dry unit weight = 142.5 pcf (22.4 kN/m³)] and then applying the deviator stress in several increments at each confining pressure. For the material characterization, the Uzan (1985) model given in Equation 2.20 is used with the following parameters obtained from the multiple regression analysis of the measured response (Alba, 1993): $K_3 = 4231$ psi (SI equivalent of 521.92 MPa), $K_4 = 0.645$, and $K_5 = -0.056$.

Figure 7.8 compares the GT-PAVE predictions obtained using the nonlinear incremental loading analysis with the measured experimental results. The load increments used in the analysis were 3 psi (20.69 kPa) for the confining pressure $\sigma_3 = 3$ psi (20.69 kPa); 5 psi (34.48 kPa) for $\sigma_3 = 10, 15$, and 20 psi (68.95, 103.43, and 137.90 kPa); and 10 psi (68.95 kPa) for $\sigma_3 = 30$ psi (206.85 kPa). All measured data were predicted reasonably accurately by the stress-strain curves generated using the GT-PAVE program from $\sigma_3 = 3$ psi (20.69 kPa) to 20 psi (137.90 kPa). The maximum error between the predicted and measured values was 4.1% computed at the confining pressure of 10 psi (68.9 kPa). The maximum 4.1% error includes any inaccuracy in fitting the Uzan model to the experimental results. Although no experimental data exist, the predictions for $\sigma_3 = 30$ psi (206.85 kPa) are also plotted to present a realistic range for the resilient response of the granular material for confining pressures varying between 3 to 30 psi (20.69 to 206.85 kPa).

The good agreement between the measured data points and the predicted response curves, therefore, verifies the convergence of the nonlinear iterations at each load increment. The shapes of the curves shown in Figure 7.8 also justify the hardening type of the granular material resilient response behavior as characterized by the Uzan (1985) model. In addition, two potential sources of errors which could affect the results in the finite element model were not important in predicting vertical displacements. These are: (1) the shear loading on the top and bottom of the specimen due to the placement of a



Note: 1 in. = 25.4 mm, 1 psi = 6.895 kPa

Figure 7.8. Comparisons of the GT-PAVE Nonlinear Resilient Response Predictions with the Measured Experimental Results.

rigid cap on the specimen, and (2) the assumption in developing Uzan model constants that the radial stress is equal to the tangential hoop stress ($\sigma_r = \sigma_t$) for the triaxial conditions which is only true at the centerline in the model.

Effects of Compaction Induced Residual Stresses

The influence of the compaction induced residual stresses on the horizontal tension zone in granular bases has been investigated by several researchers as discussed in Chapter 3 (Uzan, 1985; Selig, 1987). Selig (1987) proposed one possible explanation to the no tension problem stating that the existence of high horizontal compressive residual stresses in a base layer offsets the incremental tensile stresses predicted by the elastic solution. The magnitudes of these horizontal residual stresses were recently measured in the field to be as high as 3 psi (21 kPa) in the unbound aggregate due to the application of a 10 ton (8,896 kN) vibratory compactor (Barksdale and Alba, 1993).

To demonstrate the offsetting effects of the compaction induced residual stresses on the horizontal tension in granular bases, an example problem involving a three layer conventional flexible pavement was analyzed using the GT-PAVE program. The pavement section had the same geometry of the three layer system shown in Figure 7.3. The section consisted of a 4 in. (102 mm) thick asphalt concrete surfacing (AC) and an 11 in. (279 mm) thick unbound aggregate base underlain by the subgrade layer. A 3 psi (20.7 kPa) horizontal compressive residual stress was assumed to exist in the granular

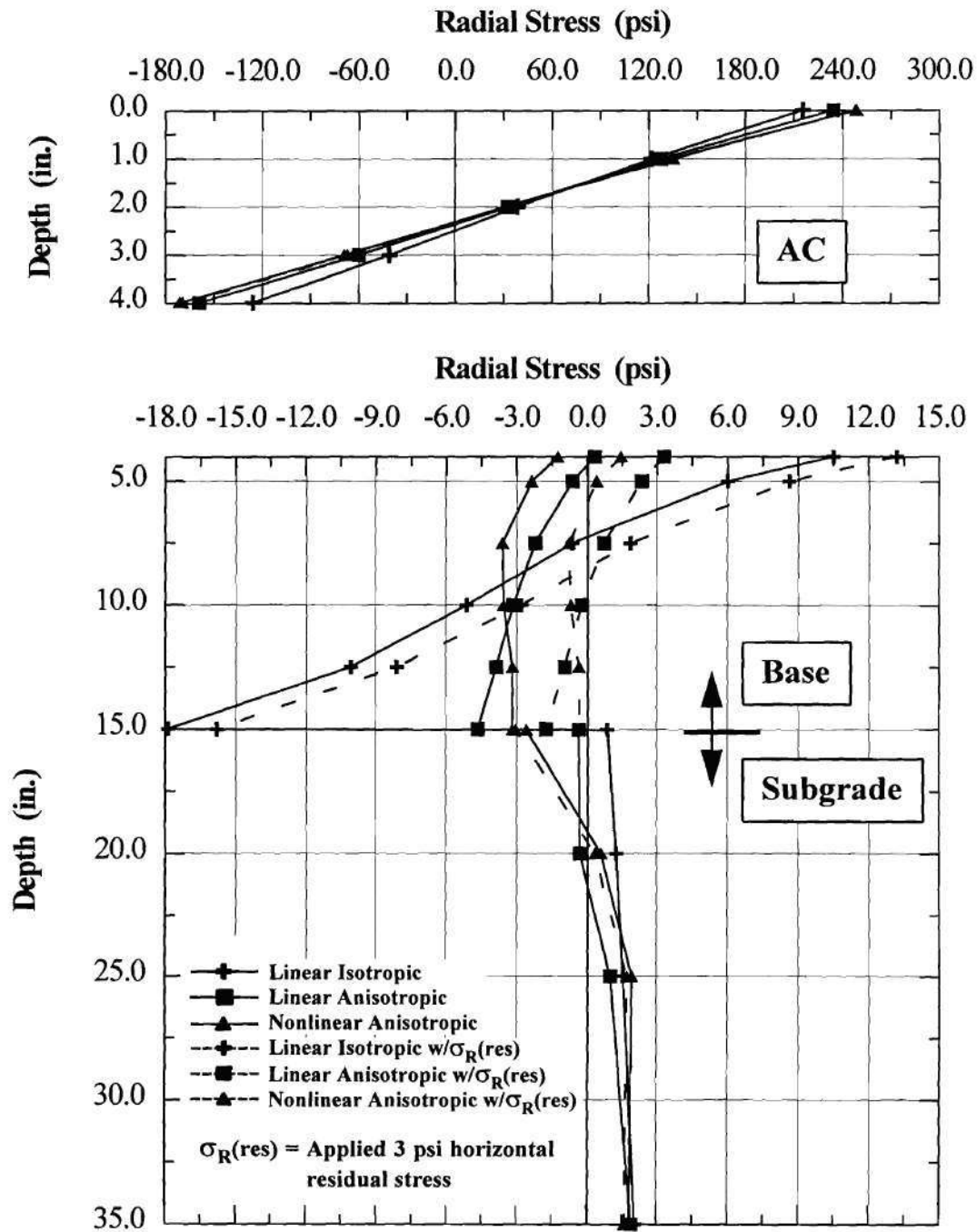
base before the 100 psi (689 kPa) uniform tire pressure was applied on the surface over a circular area of diameter 10 in. (254 mm).

The 154 element 513 node finite element mesh given in Figure 7.1 was used to model the conventional pavement section with the subgrade thickness taken as approximately 85 in. (2159 mm). The isotropic material properties assigned to the top AC layer, middle aggregate base, and the bottom subgrade are shown in Figure 7.3. The unit weights used were 147 pcf (23.1 kN/m³) for the AC, 137 pcf (21.5 kN/m³) for base, and 105 pcf (16.5 kN/m³) for the subgrade. The anisotropic representation of the granular base was also achieved by using the same anisotropic properties as in the program verification Example No. 3 for the cross-anisotropic three layer system.

For the nonlinear analysis, the model parameters used were selected such that the average stiffnesses obtained in base and subgrade layers after the nonlinear analysis were approximately equal to the linear elastic initial guesses. The Uzan (1985) M_R model given in Equation 2.20 was used in base with the following parameters: $K_3 = 5367$ psi (SI equivalent of 1091.6 MPa), $K_4 = 0.75$, and $K_5 = -0.07$. For the subgrade, the resilient response was modeled using the bilinear approximation given in Equation 2.31 with the parameters: $K_{19} = 4900$ psi (33.79 MPa), $K_{20} = 2.5$ psi (0.017 MPa), $K_{21} = 8040$, $K_{22} = 26.67$. A tension modification factor n of 15% was also employed in the granular base for determining the horizontal moduli as percentage of the vertical moduli when horizontal tension was encountered in the base.

Figure 7.9 shows the radial stresses predicted on the centerline of loading from the linear isotropic, linear anisotropic, and nonlinear anisotropic analyses. For comparison purposes, radial stresses, in all cases, have been calculated both in the presence (dashed lines) and absence (solid lines) of the 3 psi (20.7 kPa) initial horizontal residual stress in the granular base. Neither in the subgrade, nor in the AC layer, the 3 psi (20.7 kPa) residual stress included in the analysis resulted in an apparent change in the predictions.

In the granular base, however, predictions obtained in the presence of residual stress from all three analyses clearly indicate reductions in horizontal tension. The larger reductions of up to 3 psi (20.7 kPa) in radial stress were observed mainly in the anisotropic analyses (see Figure 7.9). The nonlinear anisotropic analysis with the applied 3 psi (20.7 kPa) residual stress predicts a maximum tensile stress of 0.74 psi (5.1 kPa) in the base. The 3 psi residual stress thus almost eliminates the maximum 16 psi (110.3 kPa) tension predicted by the linear isotropic analysis. Even though the stress predictions by both linear and nonlinear anisotropic analyses are reasonably close in magnitude (see Figure 7.9), the main differences between the two analyses are generally found in the predicted strains. Nonlinear anisotropic analysis tends to predict more accurate vertical and horizontal strains in the granular layer as shown in the next section.



Notes: 1. Compression is positive
 2. 1 in. = 25.4 mm; 1 psi = 6.895 kPa

Figure 7.9. The Effect of Compaction Induced Residual Stresses on the Predicted Centerline Radial Stresses.

Full-Scale Pavement Resilient Response Predictions

The GT-PAVE nonlinear finite element program is used in this section to calculate the resilient pavement response of five well instrumented full-scale test sections. These sections were a part of an earlier study at Georgia Tech to evaluate factors affecting crushed stone base performance (Barksdale and Todres, 1983). Mainly two types of flexible pavement sections are considered here for analysis. These are conventional sections with a granular base but no subbase and the inverted sections having an unstabilized crushed stone base sandwiched between a lower cement stabilized subbase and the upper asphalt concrete surfacing. A 140 element, 475 node axisymmetric mesh is used to analyze both the conventional and inverted sections as nonlinear elastic layered systems.

Georgia Tech Full-Scale Pavement Test Study

A total of twelve large scale pavement test sections were tested to evaluate pavement performance (Barksdale and Todres, 1983). Pavement testing was conducted in a facility consisting of a test pit 8 ft. (2.4 m) by 12 ft. (36.6 m) in plan and 5 ft. (1.5 m) deep. A heavy steel reaction frame was constructed over the test pit and an air over oil pneumatic loading system was attached to the load frame. Pavements tested in this facility consisted of two inverted sections, five conventional sections having crushed stone bases and five full depth asphalt concrete sections (see Table 7.1). The pavement test sections were fully instrumented with pressure cells and bison type strain coils. The

Table 7.1. The Geometry and Performance Summary of Georgia Tech Pavement Test Sections (after Barksdale and Todres, 1983).

Section No.	Asphalt Concrete Thickness (in.)	Crushed Stone Thickness (in.)	Repetitions to Failure	Failure Mode	Comments
CRUSHED STONE BASE					
1	3.5	12.0	3,000,000 3,500,000	Fatigue/ Rutting	Tested to 2.4 million repetitions Failure Extrapolated
2	3.5	8.0	1,000,000	Rutting	
FULL DEPTH ASPHALT					
3	9.0	None	10,000,000	Rutting (1 in.)	Bad Asphalt: AC Content: 5.9 % Flow: 15.4 (1/100 in.) Stability: 1870 lb. Dry Density: 145.1 pcf
4	6.5	None	10,000	Rutting (1 in.)	
5	9.0	None	130,000	Rutting	Rutting Primarily in AC
6	6.5	None	440,000	Rutting	Rutting Primarily in AC
7	7.0	None	150,000	Rutting	
CRUSHED STONE BASE					
8	3.5	8.0	550,000	Rutting	Permanent Deformation: 0.28 in. Permanent Deformation: 0.34 in.
9	3.5	8.0	2,400,000	Fatigue	
10	3.5	8.0	2,900,000	Fatigue	
INVERTED SECTIONS					
11	3.5	8.0	3,600,000	Fatigue/ Rutting	6.0 in. Soil Cement Subbase
12	3.5	8.0	4,400,000	Fatigue/ Rutting	6.0 in. Cement Stabilized Subbase

Note: 1 in. = 25.4 mm; 1 psi = 6.895 kPa; 1 lb. = 4.448 kN

instrumented sections were then tested to either a rutting or fatigue type failure under a repetitively applied, 6,500 lb. (28.9 kN) uniform circular load having a diameter of 9.1 in. (231 mm).

The aggregate gradations and the material properties used in the full-scale test sections are summarized in Table 7.2. A Georgia DOT B-binder asphalt concrete was employed for the AC surfacing with an AC-20 viscosity grade asphalt cement used in the mix. The unstabilized aggregate base course consisted of crushed granitic gneiss prepared by blending in a small 0.125 yd³ (0.096 m³) Barber-Greene pugmill 20% by weight of No. 5 size aggregate, 25% of No. 57, and 55% of No. 810 stone sizes. A low to moderate strength micaceous nonplastic silty sand subgrade, classified as an AASHTO A-4 soil, was used beneath the test sections.

Test Section Construction. The silty sand subgrade was placed in the pit in 2 in. (51 mm) lifts up to a total thickness of 50 in. (1270 mm) in the conventional sections and 44 in. (1118 mm) in the inverted sections. Each lift was compacted using a Wacker or a Jay compactor to 98% of AASHTO T-99 (1990) standard proctor maximum dry density at a moisture content of 20.5%. A spring loaded static penetrometer was used to insure the uniformity of the subgrade during construction. The as constructed density was determined using a thin wall, drive tube sampler.

The 6 in. (152 mm) thick cement stabilized subbase used only in the inverted sections was constructed on top of the subgrade followed by the placement of the crushed

Table 7.2. Aggregate Gradations and Material Properties Used In Flexible Pavement Test Sections.⁽¹⁾

SIEVES	Cumulative % Passing By Weight										Maximum Density (pcf)	Opt. Water Content (%)
	1.5 in. (38 mm)	1 in. (25 mm)	3/4 in. (19 mm)	1/2 in. (13 mm)	3/8 in. (10 mm)	No. 4 (4.75 mm)	No. 10 (2.00 mm)	No.40 (.425 mm)	No. 60 (0.25 mm)	No. 200 (.075 mm)		
AC Aggregate Gradation: ⁽²⁾	100	100	100	86	75	51	36	18	14	7	147	-
Base Aggregate Gradations:												
No. 5	100	96	37	5	2	-	-	-	-	-	-	-
No. 57	100	98	82	43	20	3	-	-	-	-	-	-
No. 810	100	100	100	100	100	77	56	27	19	8	-	-
Combined	100	99	83	67	61	43	31	15	10	4	137 ⁽⁵⁾	5.7
Subgrade Gradation: ⁽³⁾	100	100	100	100	100	100	99	85	70	39	105 ⁽⁴⁾	18.5
CEMENT STABILIZED SUBBASE PROPERTIES :												
A. Soil - Cement Subbase: 5% by weight of Type I Portland cement added to the silty sand subgrade. (Section 11) Average 28-day unconfined compressive strength = 214 psi.											107 ⁽⁵⁾	18.0
B. Aggregate - Cement Subbase: 4.5% by weight of Type I Portland cement added to the Combined base. (Section 12) Average 28-day unconfined compressive strength = 1146 psi.											138 ⁽⁵⁾	6.0

- Notes:
- 1 in. = 25.4 mm; 1 psi = 6.895 kPa; 1 lb = 4.448 kN; 1 pcf = 0.157 kN/m³
 - The B-binder AC had a 5.2% optimum asphalt content, 4 % voids in the total mix, Marshall mix stability of 2300 lb. (10.2 kN), and a flow value of 9.0/100.0 in. (2.3 mm).
 - Maximum aggregate size = 1.5 in. (38 mm)
 - Determined by AASHTO T-99 test method
 - Determined by AASHTO T-180 test method

stone base. All base and subbase layers were placed in approximately 2 in. (51 mm) lifts. Compaction of the subbase and base was achieved using 5 to 7 passes of the Jay 12 vibrating plate compactor. The unstabilized aggregate bases were compacted to 100% of the AASHTO T-180 (1990) modified proctor maximum dry density. Nuclear density measurements revealed that due to the presence of the underlying rigid cement stabilized subbase, the compaction density in the unstabilized aggregate base of the inverted sections was 105% of the T-180 maximum dry density.

The cement stabilized layers used in the inverted sections were allowed to cure for 28 days before loading the test sections. The B-binder asphalt concrete mix was placed over the unstabilized base. This mixture was used to give a strong asphalt concrete surface course so as to resist rutting in that layer under the heavy applied loading.

Performance of the Test Sections. The full-scale laboratory tests conducted to failure permitted comparing the performance of the conventional sections with both the inverted sections and the full depth asphalt concrete sections (see Tables 7.1 and 7.3). A maximum rut depth of 0.5 in. (13 mm) was considered to constitute a rutting failure. A fatigue failure of the sections was also considered to occur when the surface cracks became connected together to form a grid type pattern usually over the loaded area. Only hairline cracks were allowed to develop. Before wider cracks formed, testing was terminated because of the large number of load repetitions required to reach this state of deterioration.

Table 7.3. Detailed Summary of Resilient Test Section Response.⁽¹⁾

Section	Horizontal Tensile Strain (micro in./in.)		Vertical Stress (psi)		Vertical Strain (micro in. /in.)				Surface Deflection (in.)	
	Bottom AC	Bottom Base	Top Base	Top Subgrade	AC	Top Base	Bottom Base	Top Subgrade	10 in. from Centerline	14.5 in. from Centerline
CRUSHED STONE BASE										
1	465	597	-	3.4	-	-	-	1700	0.03	0.015
2	674	754	-	-	11000	21300	-	13100	0.019	0.01
FULL DEPTH ASPHALT										
3	Premature Failure - Excessive Asphalt Content									
4	Premature Failure - Excessive Asphalt Content									
5	319	-	-	8.7	850	-	-	1380	0.012	0.007
6	460	-	-	12.6	-	-	-	1500	0.02	0.012
7	410	-	-	12.9	650	-	-	2200	0.019	0.013
CRUSHED STONE BASE										
8	300	375	-	11.9	-	560	110	1850	0.02	0.013
9	280	1080	62	11.1	-	560	340	1750	0.022	0.013
10	400	1025	54	6.8	-	620	400	2500	0.017	0.01
INVERTED SECTION										
11	340	54	-	3.3	-	730	370	390	0.007	0.003
12	260	22	-	3.4	-	760	420	340	0.006	0.003

Note: 1. A "-" in a data field indicates data was not taken.

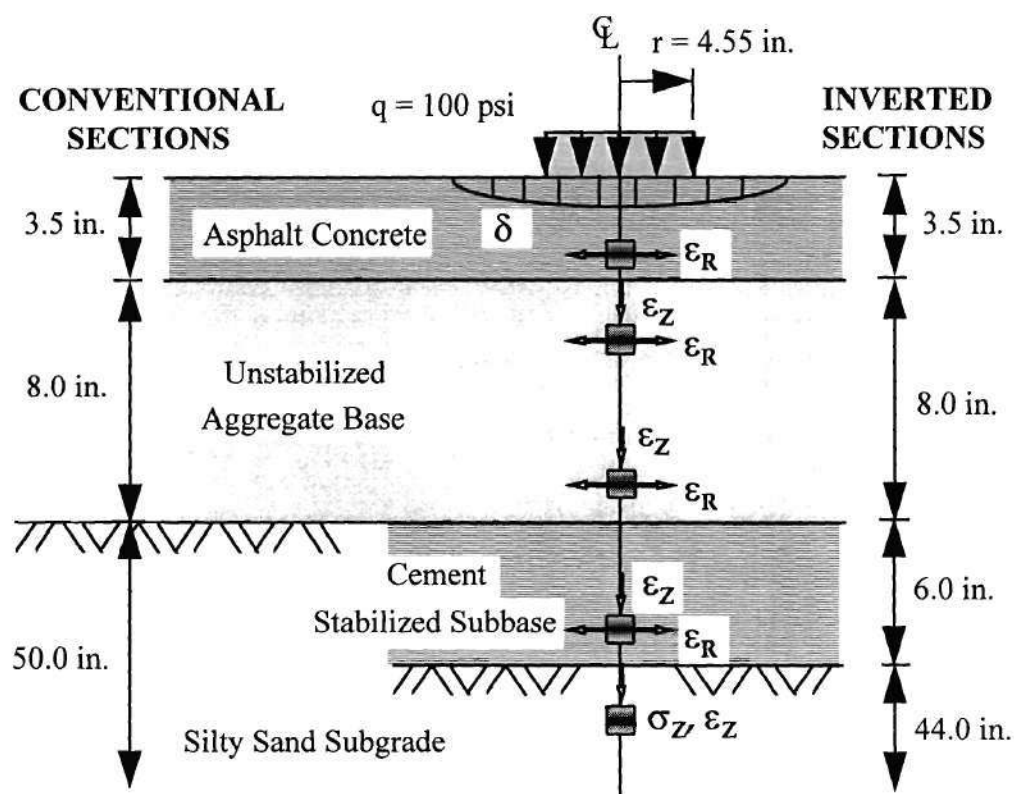
1 in = 25.4 mm; 1 psi = 6.895 kPa; (Compression is positive)

Overall, the two inverted sections performed the best of all the sections studied (see Table 7.1). Both inverted sections (Section 11 and 12) failed in combined rutting and fatigue with the strongest cement stabilized crushed stone subbase (Section 12) withstanding up to a maximum of 4.4 million load repetitions. The two inverted sections also exhibited lower vertical stresses on the subgrade and lower resilient surface displacements than the others (see Table 7.3).

Table 7.3 presents a detailed summary of the observed resilient response of the pavement test sections as obtained at different locations in the sections. In addition to the critical response values such as the vertical stress on the subgrade and the horizontal tensile strain at the bottom of the AC, up to 7 more response variables (stresses, strains and displacements) were measured in the sections using the bison type strain coils and pressure cells. These results are used in this study to compare the predicted with the observed resilient response of the test sections using the GT-PAVE nonlinear finite element program. The accuracy of the overall modeling of resilient behavior of both the conventional and inverted sections is related to how well the measured response variables are predicted at the same time.

Modeling of the Pavement Test Sections

Figure 7.10 shows the typical cross sections used for the conventional (Sections 8, 9, and 10) and inverted sections (Sections 11 and 12) along with the locations of the measured and predicted response variables. In both the conventional and the inverted



Note: 1 in. = 25.4 mm, 1 psi = 6.895 kPa.

Figure 7.10. Typical Cross Sections of Pavement Test Sections.

sections, a 3.5 in. (89 mm) asphalt concrete (AC) binder was employed for the surfacing. The unstabilized aggregate base course consisted of crushed granitic gneiss 8 in. (203 mm) in thickness. Section 11 and 12, the inverted sections, had an additional 6 in. (152 mm) subbase consisting of a cement stabilized subgrade and a stronger cement treated aggregate base, respectively. The thickness of the micaceous silty sand subgrade was 44 in. (1118 mm) in the inverted sections and 50 in. (1270 mm) in the conventional sections. A 6 in. (152 mm) thick concrete slab was located at the bottom of the subgrade.

A 140 element, 475 node axisymmetric finite element mesh was used to analyze both the conventional and inverted sections as nonlinear elastic layered systems. The subgrade and the unstabilized aggregate base were treated as nonlinear elastic materials while the AC surfacing and cement stabilized subbase were modeled as linear elastic materials. In addition, the base was also given cross-anisotropic material properties. Use of an anisotropic characterization, compared to isotropic characterization, has been found to be necessary to better model the tension effect in the unstabilized granular bases (Barksdale et al., 1989). To model the test sections, the wheel load was applied as a uniform pressure of 100 psi (689 kPa) over a circular area of radius 4.55 in. (116 mm) (see Figure 7.10). A fixed boundary was assumed at the bottom of the subgrade where the concrete slab was placed.

Table 7.4 summarizes the material properties used in the pavement test sections including initial guesses and the model parameters needed for the nonlinear analysis. The initial guesses consist of the vertical and horizontal values of resilient modulus and

Table 7.4. Material Properties and Model Parameters Used In Modeling Pavement Test Section Response.

Layer Type	Thickness (in.)	Vertical Modulus (psi)	Vertical Poisson's Ratio	Horizontal Modulus (psi)	Horizontal Poisson's Ratio	Shear Modulus (psi)	Model Parameters ^(3/4)				Density (pcf)
							K3/K19 (psi)	K4/K20	K5/K21	K22	
Asphalt Concrete ⁽¹⁾	3.5	250,000	0.35	-	-	-	-	-	-	-	147
Crushed Stone Base: ⁽³⁾											
Conventional Sections: Top	2.6	53,960	0.43	42,940	0.15	18,867	4,867	0.80	-0.05	-	137
Middle	2.6	38,000	0.43	3,234	0.15	13,287	4,867	0.80	-0.05	-	137
Bottom	2.8	31,084	0.45	863	0.10	10,719	4,867	0.80	-0.05	-	137
Inverted Sections: Top	2.6	53,960	0.43	42,940	0.15	18,867	5,367	0.61	-0.07	-	144
Middle	2.6	38,000	0.43	30,239	0.15	13,287	5,367	0.61	-0.07	-	144
Bottom	2.8	31,084	0.45	24,736	0.10	10,719	5,367	0.61	-0.07	-	144
Cement Stabilized Subbase: ⁽¹⁾											
Soil-Cement (Sect. 11)	6.0	600,000	0.2	-	-	-	-	-	-	-	107
Stone-Cement (Sect. 12)	6.0	1,500,000	0.2	-	-	-	-	-	-	-	138
Silty Sand Subgrade: ⁽⁴⁾											
Top	3.0 (2.0 ²)	3,000	0.4	-	-	-	5,900	2.5	11640	26.67	105
Middle	27.0 (22.0 ²)	6,000	0.4	-	-	-	5,900	2.5	11640	26.67	105
Bottom	20.0	15,000	0.4	-	-	-	5,900	2.5	11640	26.67	105

- Notes: 1. Isotropic linear elastic analysis
2. Inverted sections only
3. Cross-anisotropic nonlinear analysis using Uzan's model
4. Isotropic nonlinear analysis using bilinear representation
5. 1 in. = 25.4 mm; 1 psi = 6.895 kPa; 1 pcf = 0.157 kN/m³

Poisson's ratio, vertical shear modulus and material densities. Model parameters K_i are given for the Uzan model (1985) used in the granular base (see Equation 2.20) and for the bilinear approximation used in the subgrade (see Equation 2.31). The nonlinear model parameters used in the crushed stone base differed between the conventional and the inverted sections since a higher percentage compaction was achieved in the inverted sections due to the presence of the underlying stiff cement stabilized subbase.

When modeling the pavement sections, both the nonlinear aggregate base and the subgrade were divided into sublayers, thus enabling a more realistic assignment of initial material properties (see Table 7.4). The unstabilized crushed stone bases were initially assigned vertical resilient moduli varying from 30 ksi (206.9 MPa) at the bottom to 60 ksi (413.7 MPa) at the top. The horizontal resilient moduli were initially assumed to be 80% of the vertical moduli at the top of the anisotropic base. In the conventional sections only, the horizontal moduli were initially 2% of the vertical moduli in the lower portion of the base to account for the horizontal tension. Similarly, an assumed Poisson's ratio of 0.43 in the vertical direction was reduced to 0.15 in the horizontal direction based on previous studies (Barksdale et al., 1989). The subgrade was also initially assigned nonlinear isotropic material properties with a Poisson's ratio of 0.40 and the resilient moduli varying from 3 ksi (20.7 MPa) at the top to 15 ksi (103.4 MPa) at the bottom.

The resilient modulus of the AC layer was taken based on previous studies (Barksdale et al., 1989) to be 250 ksi (1720 MPa) with a corresponding Poisson's ratio of 0.35. Linear elastic moduli used to model the cement treated subbase were estimated

from both charts and empirical correlations obtained from several sources (Felt and Abrams, 1957; Jones, 1966; Williams, 1972; FHWA, 1979; and Hadley, 1991). Resilient moduli in these correlations were related to the unconfined compressive strength of laboratory specimens prepared from cement treated materials used in the Georgia Tech study (Barksdale and Todres, 1983).

For the soil-cement subbase of Section 11, the estimated elastic moduli ranged from 507 to 1,300 ksi (3,500 to 8,900 MPa). Similarly, for the crushed stone cement subbase of Section 12, the estimated moduli ranged from 1,200 to 2,000 ksi (8,300 to 14,800 MPa). After reviewing the variations in the moduli, a modulus of 600 ksi (4,140 MPa) was assumed in the cement treated silty sand subbase of Section 11, and a modulus of 1,500 ksi (10,340 MPa) was used for the cement stabilized crushed stone subbase of Section 12. The Poisson's ratio was assumed to be 0.2 for both sections (FHWA, 1979).

Test Section Resilient Response Predictions

Table 7.5 compares the eight measured resilient response variables with the predicted ones. The average values of the measured resilient response of the conventional sections, Sections 8, 9, and 10, have been used in the comparisons. In general, finite element predictions are in reasonably good agreement with the observed behavior of both the conventional and inverted sections. The predicted values of surface deflections, vertical strain and stress on the subgrade, and radial strains at the bottom of base and AC are essentially the same as the measured ones in the conventional sections. In the

TABLE 7.5. Comparison of Predicted and Measured Response Variables.⁽¹⁾

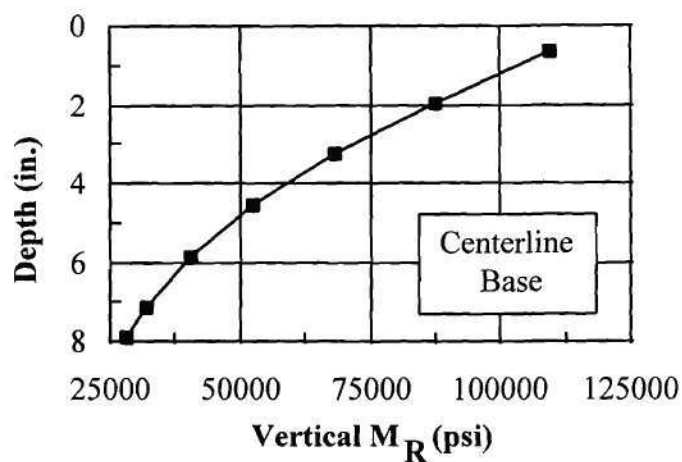
RESPONSE	TOP SUBGRADE		BOTTOM SUBBASE		BOTTOM BASE		TOP BASE	BOTTOM AC		SURFACE DEFLECTION		
	σ_z (psi)	ϵ_z (10^{-6})	ϵ_R (10^{-6})	ϵ_z (10^{-6})	ϵ_R (10^{-6})	ϵ_z (10^{-6})	ϵ_z (10^{-6})	ϵ_R (10^{-6})	ϵ_z (10^{-6})	$\delta_{C.L.}^{(2)}$ (in.)	$\delta_{10"}^{(3)}$ (in.)	$\delta_{14.5"}^{(3)}$ (in.)
MEASURED (Conventional ⁴)	9.9	2000	-	-	-936	280	580	-330	-	0.028	0.017	0.013
PREDICTED (Conventional)	9.5	2080	-	-	-985	478	626	-384	553	0.026	0.017	0.013
MEASURED (Inverted 11)	3.3	390	-	-	54	370	730	-340	-	0.019	0.007	0.003
PREDICTED (Inverted 11)	4.0	390	-79	45	51	317	1050	-348	536	0.016	0.009	0.006
MEASURED (Inverted 12)	3.4	340	-	-	22	420	760	-260	-	0.016	0.006	0.003
PREDICTED (Inverted 12)	3.5	236	-46	25	35	362	1047	-341	532	0.015	0.008	0.006

- Notes: 1. A "-" in data field indicates not applicable or no data was taken
2. Measured deflections at centerline $\delta_{C.L.}$ are extrapolated
3. Deflections measured at 10 in. and 14.5 in. radial distances away from centerline
4. Measured values are averaged from response of Sections 8, 9, and 10
5. 1 in. = 25.4 mm; 1 psi = 6.895 kPa; (Compression is positive)

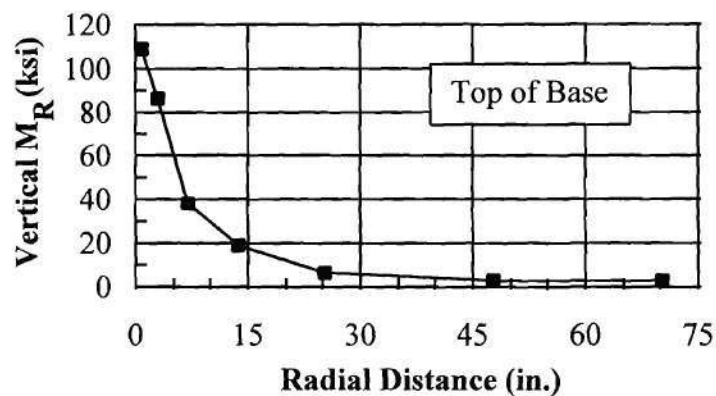
inverted sections, predicted vertical and radial strains in different layers were in better agreement with observed response for Section 11 than for Section 12. The vertical stress on top of subgrade was, however, predicted better in Section 12 than in Section 11. The resilient surface deflections and vertical strains on top of the base were not predicted to a high degree of accuracy.

The predictions summarized in Table 7.5 tend to verify the ability of nonlinear, anisotropic finite element models such as GT-PAVE, to reasonably accurately predict **at the same time** a large number of measured stress, strain, and deflection response variables. Although room for improvement still exists, such predictions are hard to achieve and indicate that the model used is reasonably valid. This, however, can not be said for models that are verified by predicting only one or perhaps two measured response variables.

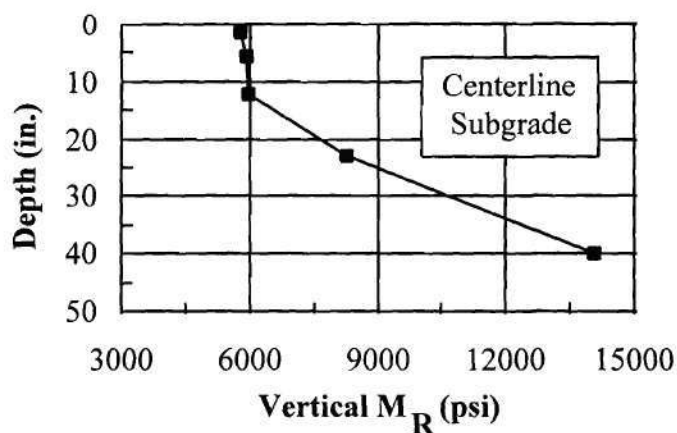
For the conventional three layer pavement, the variation of vertical resilient modulus within the nonlinear unstabilized aggregate base and the silty sand subgrade are shown in Figure 7.11. The values plotted are at the middle of elements both at the centerline of loading and at the top of the granular base layer. The variations with increasing depth in both layers, are nonlinear. The moduli decrease with depth in the base, as shown in Figure 7.11a, due to the decreasing bulk stress term in Equation 2.20. And as indicated in Figure 7.11c, the moduli increase with depth in the subgrade due to the decrease in deviatoric stress in Equation 2.31. Figure 7.11b also shows an expected



(a) Vertical resilient modulus variation with depth within the base



(b) Vertical resilient modulus variation with radial distance at top of base



(c) Vertical resilient modulus variation with depth within the subgrade

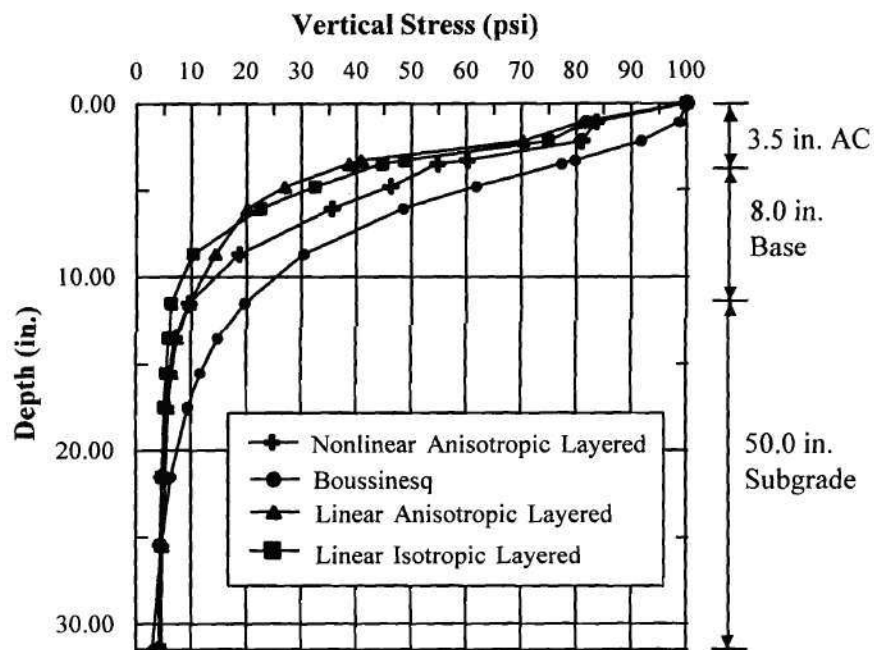
Note: 1 in. = 25.4 mm; 1 psi = 6.895 kPa

Figure 7.11. Vertical Stiffnesses Predicted for the Conventional Sections.

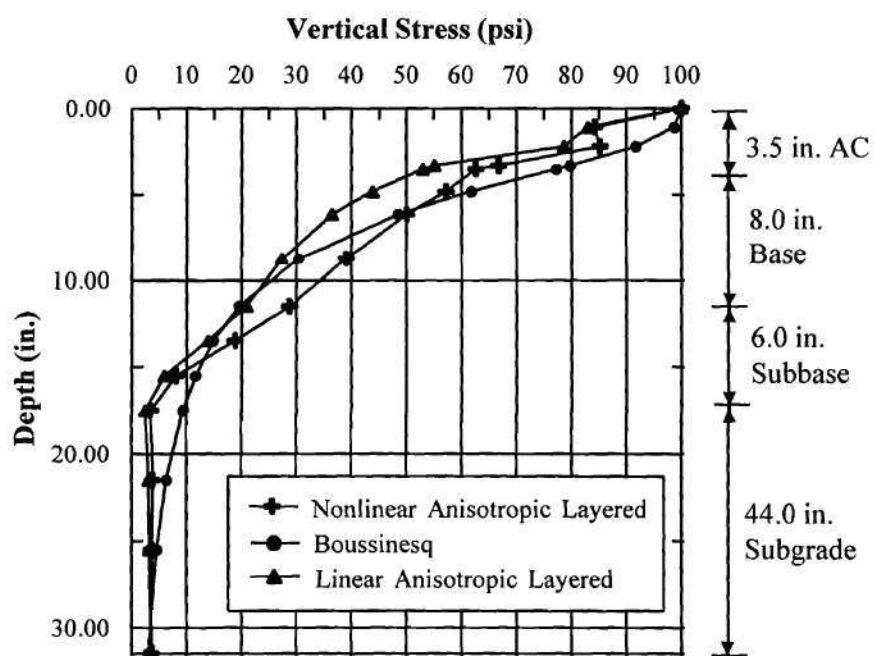
decrease in stiffness with radial distance due to the lower vertical confinement encountered radially away from the wheel load.

A 15% tension modification factor n , which was empirically obtained in the nonlinear analysis by trial and error, was needed in the bottom portion of the base to obtain good radial strain prediction compared to measured values in the conventional sections. The 15% corresponds to the percentage of the vertical moduli assigned to the horizontal moduli where horizontal tension was observed in the base. Similarly, a 10 to 20% reduction in vertical moduli were also reported by others assigned in horizontal direction in their analyses of cross-anisotropic bases (Chan et al., 1989 and Barksdale et al., 1989). In addition, the stress transfer method (Doddihal and Pandey, 1984) was also applied at the end of the nonlinear iterations to eliminate any horizontal tension in the unstabilized aggregate base.

Figure 7.12 shows the vertical stress distribution on the centerline of loading predicted in the conventional sections and inverted Section 12. The results of the different analysis types used (Boussinesq halfspace approach, linear elastic layered with isotropic and anisotropic base, and the nonlinear anisotropic layered analysis) are presented for comparison. The linear elastic analyses were performed by using the initial guesses of material properties assigned in the nonlinear analysis. For both conventional and inverted sections, the good vertical stress predictions shown in Table 7.5 have been found to generally fall in between the linear elastic layered and Boussinesq halfspace solutions. This is indeed in accordance with the earlier experience of linear elastic



(a) Conventional sections



(b) Inverted Section 12

Note: 1 in. = 25.4 mm; 1 psi = 6.895 kPa

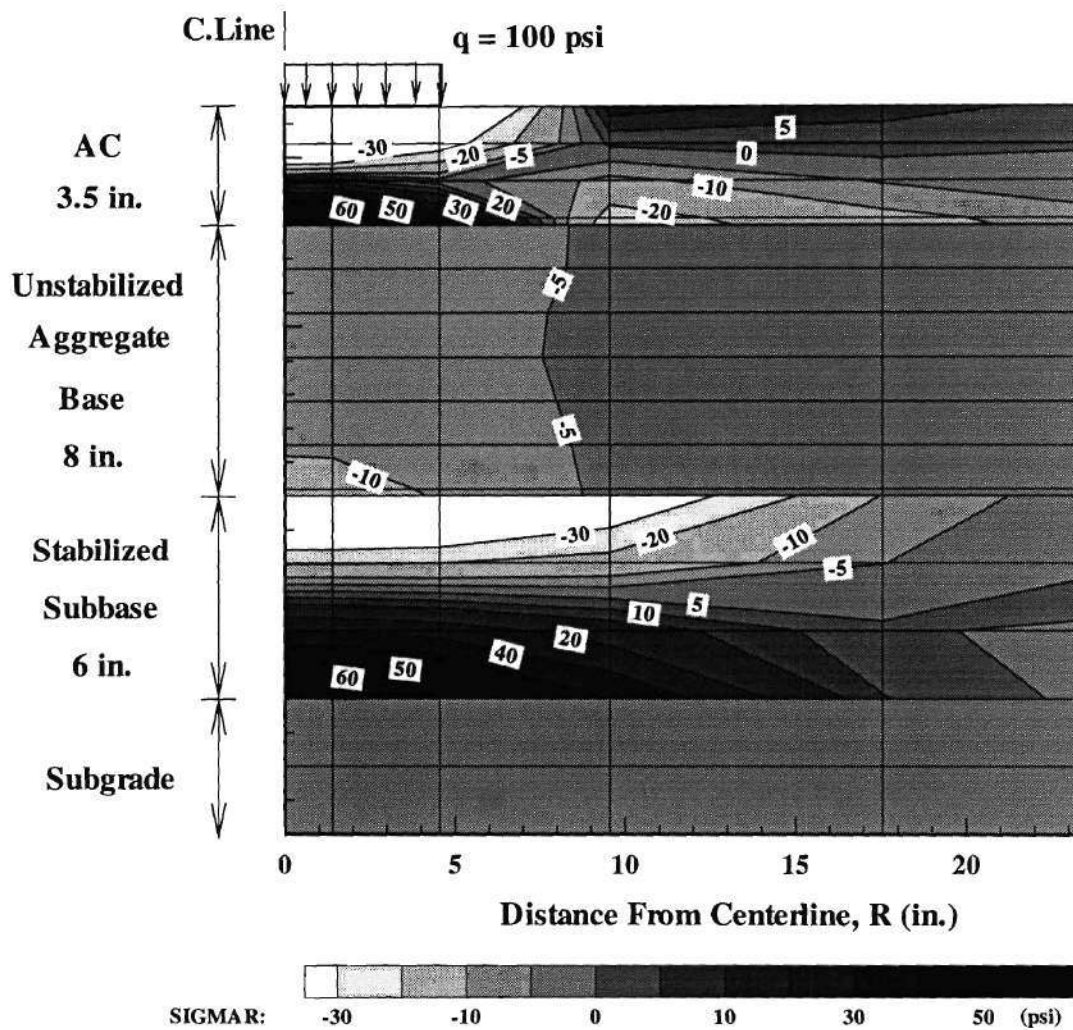
Figure 7.12. Predicted Vertical Stress Distribution on the Centerline of Loading.

layered solution's usually underestimating the measured vertical stresses in the field. Moreover, the decrease of vertical stresses throughout the cement stabilized subbase in inverted Section 12 is greater for the nonlinear analysis than the other methods (see Figure 7.12b).

Figure 7.13 shows for the inverted Section 12 contours of horizontal radial stresses plotted for the top portion of the finite element mesh. The contours in Figure 7.13 show that the upper portion of the cement treated subbase and all of the unstabilized crushed stone base near the load are in horizontal compression. The bottom half of the subbase is in horizontal tension. As a result of placing the cement stabilized layer beneath the unstabilized crushed stone base, primarily horizontal compressive stresses of magnitudes ranging from 0 to 16 psi (0 to 110 kPa) are developed in the base. The aggregate base performed very well with the high calculated values of vertical resilient moduli varying from 35 ksi (241 MPa) at the bottom to 80 ksi (552 MPa) at the top. Relatively high horizontal tensile stresses (up to 85 psi; 586 kPa on the centerline of loading) were predicted at the bottom of stabilized subbase in Sections 11 and 12.

Practical Design Considerations of Inverted Sections

A sensitivity analysis of inverted sections was performed using the GT-PAVE program for four different unstabilized aggregate base thicknesses varying from 3 to 16 in. (76 to 406 mm) in thickness and three different cement treated subbase thicknesses varying from 4 to 10 in. (102 to 254 mm). The purpose of the sensitivity analysis was to

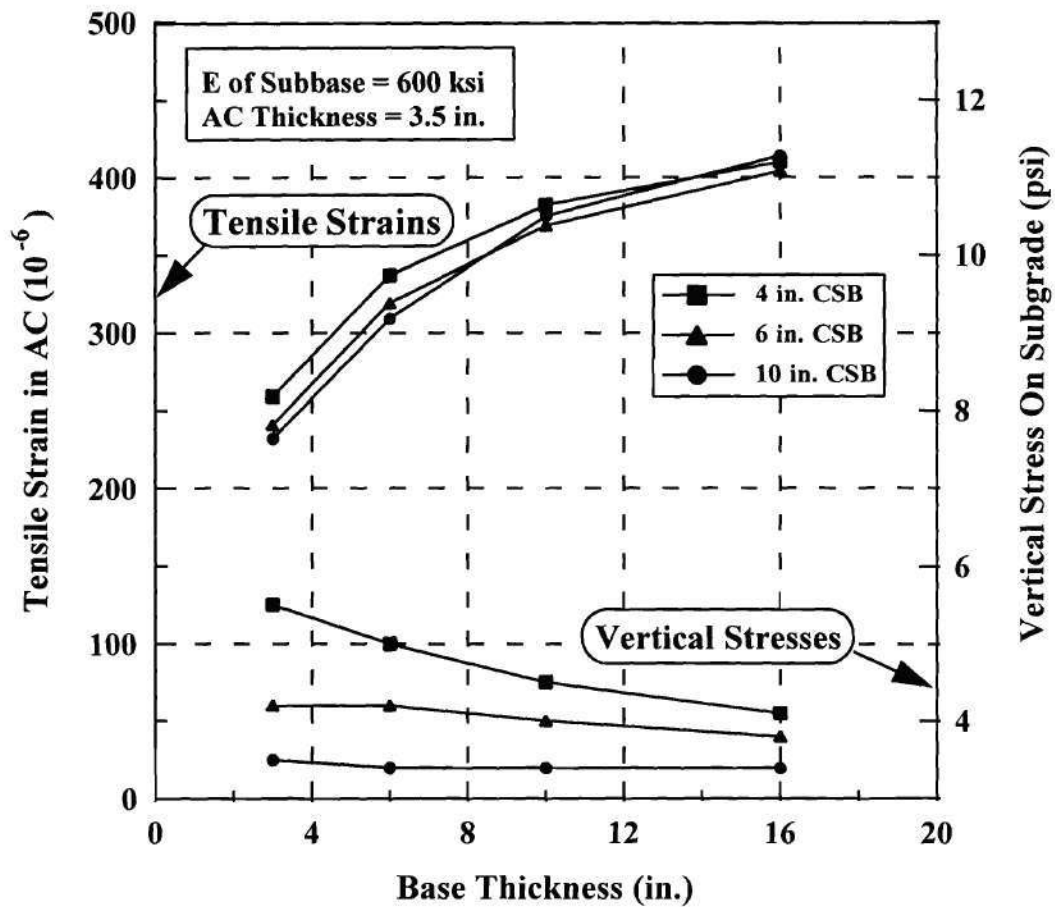


Notes: 1. 1 in. = 25.4 mm; 1 psi = 6.895 kPa
2. Tension is positive

Figure 7.13. The Variation of Radial Tensile Stresses Throughout the Unstabilized Aggregate Base and Cement Stabilized Subbase in Section 12.

find optimum design geometries for the inverted sections as defined by horizontal tensile strain in the bottom of the AC, vertical stress on the subgrade, and the tensile stress in the cement stabilized subbase. Levels of subbase stabilization comparable to Section 11 and 12 were used corresponding to resilient moduli of 600 ksi (4,140 MPa) and 1,500 ksi (10,340 MPa), respectively. An important factor in achieving good performance of an inverted section is to provide a stabilized subbase having sufficient strength to prevent fatigue and durability related failures.

The sensitivity analysis (see Figure 7.14) indicates that increasing the thickness of the unstabilized aggregate base in the inverted sections causes an important increase in the horizontal tensile strains at the bottom of the AC for stabilized subbase thicknesses of 4 in., 6 in., and 10 in. (102 mm, 152 mm and 254 mm). Resilient surface deflections also increase with increasing base thickness although these results are not presented. For a base thickness equal to or greater than about 6 in. (152 mm), only a very small reduction occurs in the vertical subgrade stress with increasing base thickness (see Figure 7.14). Therefore, inverted pavements having a 6 to 8 in. (152 mm to 203 mm) thick unstabilized crushed stone base and also a similar thickness of cement stabilized subbase appear to be a practical, economical design which minimizes tensile strain in the AC and vertical stress on the subgrade. Base or subbase thicknesses less than 6 in. (152 mm) are not considered to be practical to construct. This finding is in general agreement with the full-scale field tests recently conducted by the North Carolina DOT.



Note: 1. CSB: Cement Stabilized Subbase

1 in. = 25.4 mm; 1 psi = 6.895 kPa

Figure 7.14. The Variations of Horizontal Tensile Strain in AC and Vertical Stress on Subgrade with Base Thickness in Section 11.

Figure 7.15 shows the variation of horizontal radial tensile strain at the bottom of AC with increasing AC thicknesses for both inverted and conventional sections. The lower curve, which is for inverted Section 12 having a 6 in. (152 mm) thick base and subbase, shows significant reductions in tensile strain compared to the conventional sections. For both type sections, the horizontal radial tensile strain at the bottom of the AC decreases significantly with increasing AC thickness suggesting the potential for improved fatigue life of the AC.

The variation of the horizontal radial tensile stress at the bottom of the stabilized subbase beneath the center of the load is shown in Figure 7.16 as a function of subbase thicknesses. In both the low and high moduli subbase inverted sections, an important decrease in tensile stress occurs with increasing subbase thickness. Fatigue life of the cement stabilized subbase can therefore be improved by increasing subbase thickness.

Cost Comparison Analysis

A 6 in. (152 mm) unbound aggregate base and a 6 to 8 in. (152 to 203 mm) thick cement stabilized subbase has been found in the sensitivity analysis to be a practical inverted section which minimizes tensile strain in AC and vertical stress on the subgrade. Using this finding, a cost analysis was undertaken comparing the potential performance of inverted and conventional sections having equal initial construction cost. Three inverted field sections were compared with 3 conventional unbound base sections of approximately the same cost. The inverted sections consist of a 6 in. (152 mm)

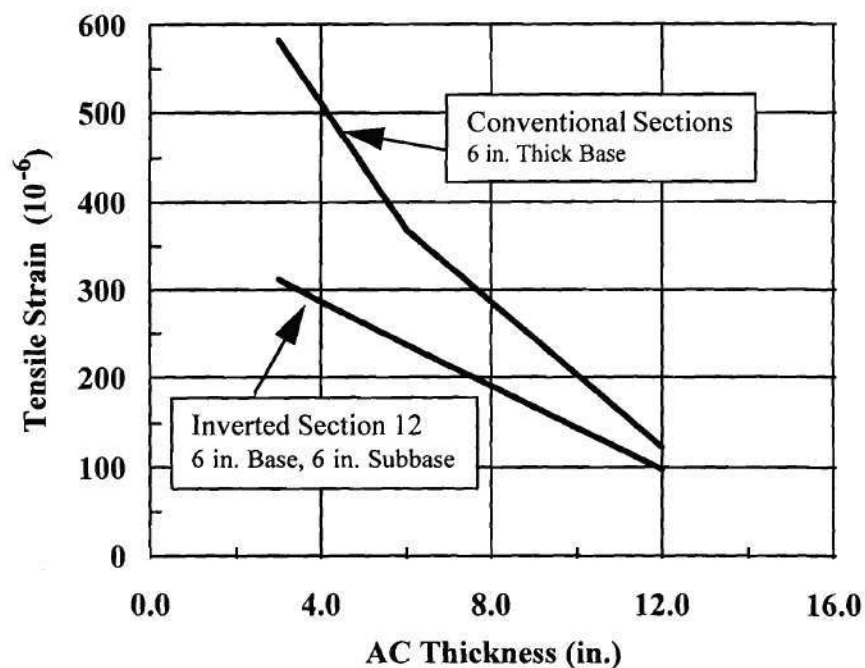


Figure 7.15. The Variation of Horizontal Tensile Strain at the Bottom of AC with AC Thickness (Note: 1 in. = 25.4 mm, 1 psi = 6.895 kPa).

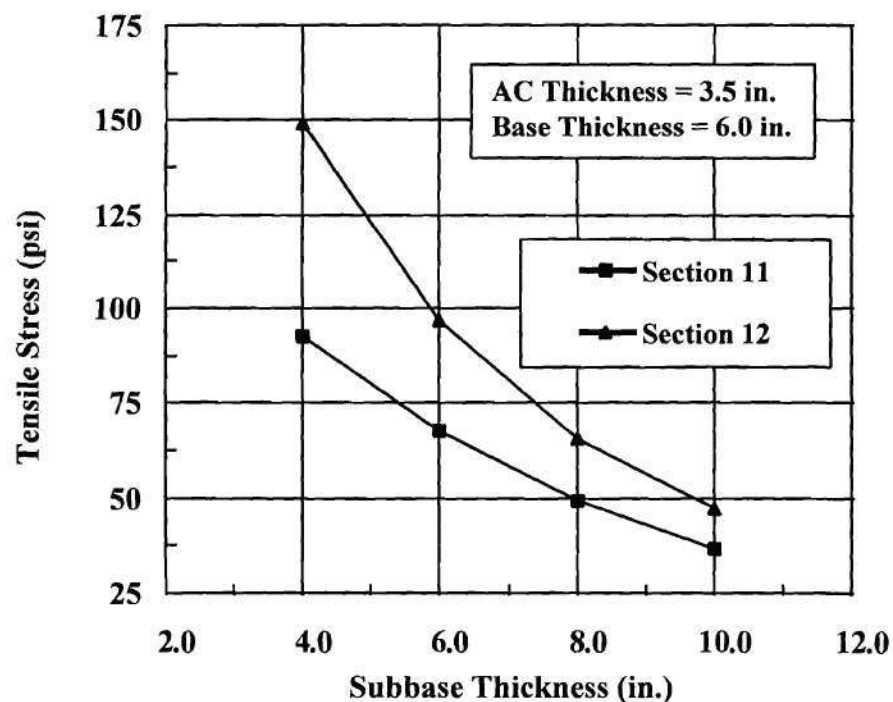


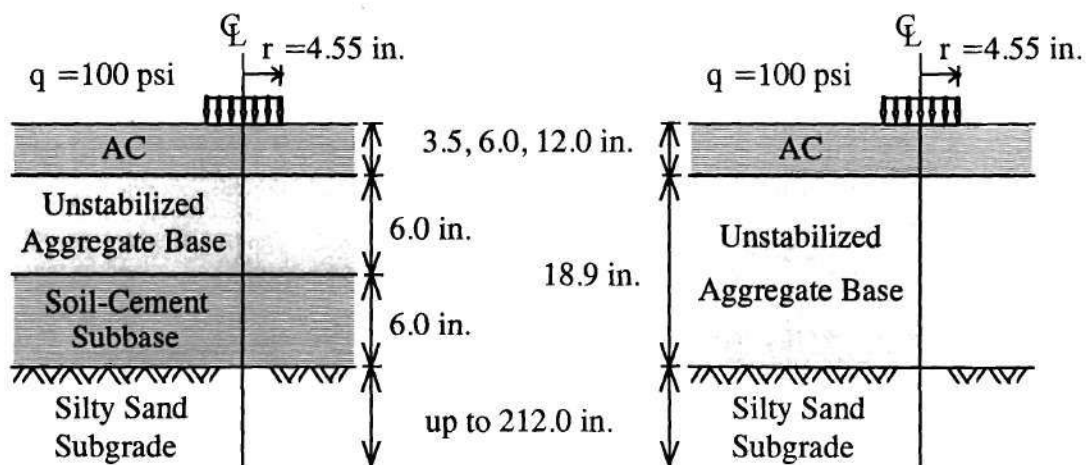
Figure 7.16. The Variation of Horizontal Tensile Stress Beneath the Centerline at the Bottom of Cement Stabilized Subbase with Subbase Thickness.

unstabilized aggregate base and a 6 in. (152 mm) cement stabilized silty sand subbase having the same properties as used in test Section 11 (see Table 7.4). Asphalt concrete (AC) thicknesses were 3.5 in. (89 mm), 6 in. (152 mm) and 12 in. (305 mm).

The same AC thicknesses were used for the conventional sections with the thickness of the base being varied to give the same total cost as for the inverted sections. Sections having approximately the same total cost were determined using the following prices reported by the Georgia Department of Transportation: AC mix, \$29.00/ton; unbound base, \$5.00/ton; cement stabilized subgrade, \$13.40/ton. The use of a cement stabilized natural subgrade for the subbase is about 23% cheaper than a cement stabilized aggregate subbase. To have similar total cost, 18.9 in. (480 mm) of unbound base in the conventional sections replaced 6 in. (152 mm) of unbound base and 6 in. (152 mm) of cement stabilized subgrade (see Figure 7.17). Using the GT-PAVE program, both the inverted and conventional sections were analyzed as actual field sections having a total depth of 227.6 in. (5780 mm) which corresponds to 50 radii of the wheel load (Duncan et al., 1968).

Figure 7.18 shows the variation of horizontal tensile strain (ϵ_t) at the bottom of the AC and the vertical stress on top of subgrade with increasing AC thickness. Both the equal cost inverted and conventional section results are shown. In general, an increase in AC thickness causes a reduction in both the horizontal tensile strain in AC and the vertical stress on subgrade. Predicted vertical subgrade stresses are lower in inverted sections than in conventional sections. Similarly, the horizontal predicted tensile strains

are slightly lower in the inverted sections than in the conventional sections for AC thicknesses greater than 5.1 in. (130 mm). However, for AC thicknesses smaller than 5.1 in. (130 mm), the horizontal tensile strain in the conventional section is less and becomes relatively small as AC thickness decreases below 3.5 in. (89 mm). This important finding helps to explain the excellent performance observed in conventional sections having thin AC thicknesses. This large reduction in strain is not observed in models that do not use a no tension, cross-anisotropic analysis.



Note: 1 in. = 25.4 mm; 1 psi = 6.895 kPa.

Figure 7.17. Equal Cost Inverted and Conventional Field Section Constructions.

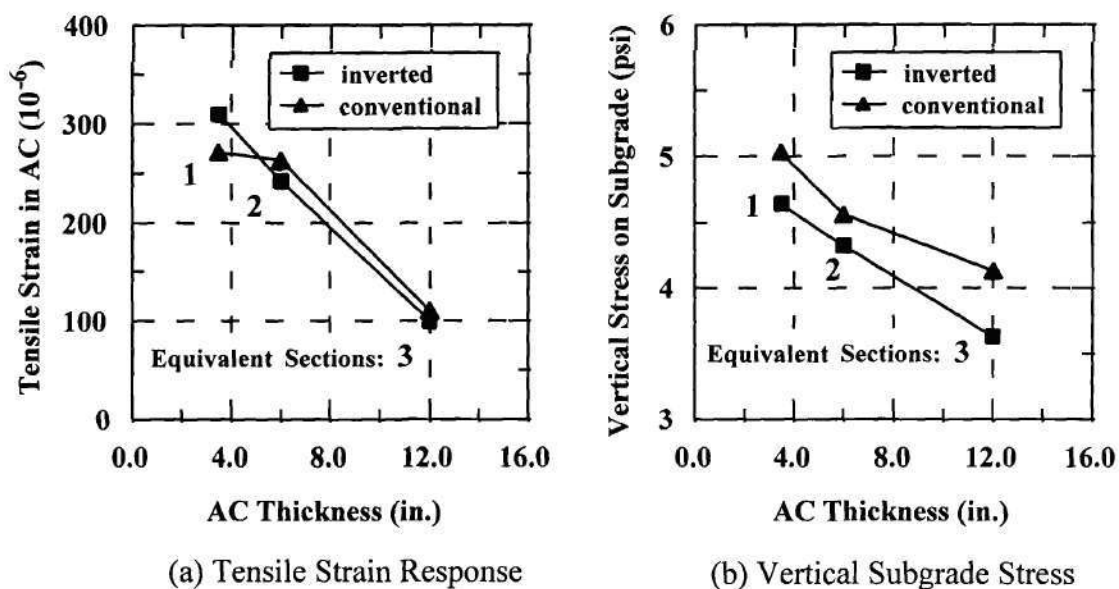


Figure 7.18. Predicted Performance of the Equal Cost Inverted and Conventional Field Sections (1 in. = 25.4 mm; 1 psi = 6.895 kPa).

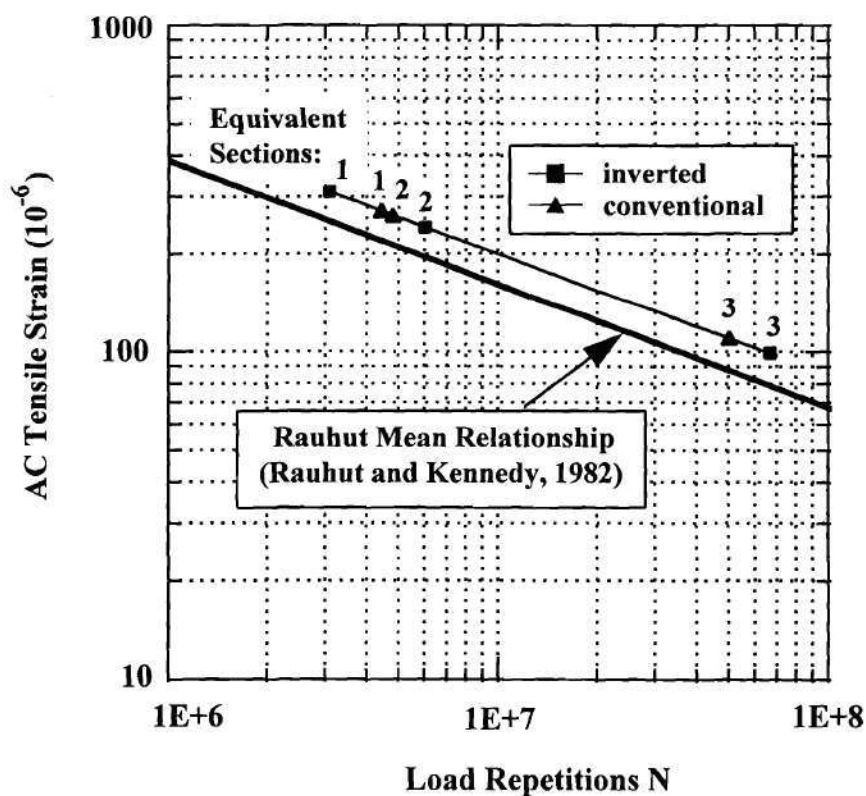


Figure 7.19. Predicted Fatigue Performance of the Equal Cost Inverted and Conventional Field Sections.

Fatigue Study. Full-scale test sections 9 through 12, including both the conventional and inverted sections, failed in fatigue or a combined fatigue-rutting failure (see Table 7.1). Assuming that each load application caused the same amount of damage, the following fatigue relationship was obtained from these data points for 26.1° C:

$$N_f = 0.00108 \epsilon_t^{-2.695} \quad (7.1)$$

where N_f is the number of repetitions to cause fatigue failure, and ϵ_t is the tensile strain in the bottom of AC layer.

The number of load repetitions calculated using Equation 7.1 for the equal cost inverted and conventional sections 1, 2 and 3 are plotted in Figure 7.19. The predicted fatigue performance of the inverted sections are better than the conventional ones except for Section 1 having the very thin AC surfacing. The fatigue curves of both inverted and conventional sections, represented on the same line, fall above the mean relationship given by Rauhut and Kennedy (1982). This may be due to use of a high quality unbound aggregate base in both sections and the absence of environmental effects in the test sections.

Summary

Reasonably good agreement with measured values was achieved of the resilient behavior of a number of response variables for five flexible pavements with unbound aggregate bases using the cross-anisotropic, nonlinear GT-PAVE program. Resilient modulus models which consider both confinement and shear stress effects in granular materials give good results and are also suitable for routine design use. Inverted flexible pavements with an unbound aggregate base sandwiched between lower cement stabilized subbase and an upper asphalt concrete surfacing have been observed to perform better than conventional ones.

Both measurements and theory show that inverted sections have lower subgrade vertical stresses and lower tensile strains in AC surfacing. The lower vertical stresses on the subgrade are primarily caused by the "beam" action of the stabilized subbase which spreads the stress out. The significant reduction of vertical stress on the subgrade make the use of an inverted section appealing for construction over a weak subgrade. The high quality, cement stabilized crushed stone subbase inverted section had the lowest tensile strain in the bottom of the AC of all twelve test sections studied. The low tensile strain in the AC and low vertical subgrade stress help explain why this section performed best.

Inverted sections also make optimum use of the excellent compressive characteristics of unstabilized aggregate by placing it above the cement stabilized layer where radial stresses are compressive. Better compaction of unstabilized materials placed over the stabilized layers is achieved. As a result of better confinement and a higher level

of compaction, permanent deformations in the base are small. Reflection cracking is significantly reduced or eliminated since the cement treated layer is placed deep in the section below the aggregate base.

The accuracy of the overall modeling of resilient behavior of both the conventional and inverted sections is related to how well the measured response variables are predicted at the same time. Pavement response predictions for the two inverted sections made at six locations were in reasonably good agreement with observed values. This finding indicates the GT-PAVE nonlinear, cross-anisotropic program and the material characterization models used is quite encouraging. The theoretical sensitivity analysis performed using these models indicate an optimum and economical inverted pavement design placed on a weak to moderately strong subgrade would have a 6 in. (152 mm) thick unstabilized aggregate base and a 6 to 8 in. (152 mm to 203 mm) thick cement stabilized subbase.

An inverted section and a conventional section having the same total cost give different performances as predicted by the GT-PAVE program. For equal AC thicknesses greater than about 5.1 in. (130 mm), the inverted sections should perform slightly better than the conventional sections. Fatigue life is about 30% greater and subgrade stress 10% less than the conventional sections of comparable cost. For AC thicknesses less than 5.1 in. (130 mm), however, conventional sections show increasingly better performance due to an important decrease in tensile strain in the bottom of the AC.

CHAPTER VIII

ANALYSIS OF GRANULAR BASES USING THE BLOCK MODEL

Introduction

Unlike a homogeneous continuum, granular bases are actually particulate media where individual particles are surrounded by other particles in contact with air voids in between. The granular medium also has the ability to increase or decrease its volume (dilate) under shear stresses. Therefore, when a granular base is strained, motion takes place that may involve one or all of the following modes: interparticle slippage, particle rotation, particle separation and even fracture at particle contacts. As a result of small rearrangements of particles, stresses are transmitted along different lines through the material. A new state of stress is then formed in the material where some contacts have opened up slightly, and some small gaps have closed to readjust for the equilibrium of the particles. In most micromechanics based continuum solutions discussed in Chapter 3, however, the constitutive relationships used for granular systems do not take into account the effects of separation and particle sliding at contacts.

A new block model approach is introduced in this chapter for modeling granular bases in flexible pavements. In this approach, blocks of aggregates are employed in the

base to approximately model the load transfer mechanisms of the real particulate nature of granular materials. The organizations are summarized of the block model INTSTIF and INTSTRES subroutines. The iterative procedure for equilibrium employed in the model is described in detail, and the criteria used in the analysis are listed for determining the behavior modes of the interface elements. The verification of the interface elements are first achieved by comparing the normal and shear interface stresses with the closed-form solutions of a one-layer continuum problem. The block model behavior is then demonstrated in a simple three-layered sliding block example problem. Finally, the model is applied to the granular base layer of the Georgia Tech conventional pavement test sections, and the results obtained are used to explain the "no tension" problem of the elastic continuum solutions.

Literature Review: Discrete Particle Approach

Several investigators in the past have described the behavior of granular media as well as that of discontinuous rocks using a discrete particle approach involving the equilibrium of particles and their compliance to external forces. The objective was, in general, to model a particulate material or a jointed rock system using certain strain discontinuities and volume change properties. Computer programs have been developed in which the behavior of an assembly of particles are calculated by considering the behavior and interrelation of individual contacts. Round (1976) developed a program

where particle movements were obtained from the solution of equilibrium equations. Cundall and Strack (1979) developed a similar program which uses a "Distinct Element Method" that considers particle dynamics. The program is able to handle a two-dimensional sample of disks or cylinders to calculate the forces and displacements at contacts. The average stresses and strains are then determined when the system stabilizes. The solution is time dependent and models the slow progressive movement of particles.

Goodman and Shi (1981) introduced a "key block method" which identifies potentially loose rocks as kinematically possible mechanisms in exposed rock faces and underground excavations. In any jointed rock mass, key blocks can be removed or fall from rock faces without breaking intact rock. Other blocks are locked in place until these key blocks are removed. Goodman and Shi developed a powerful approach that used analytical geometry to identify the key blocks considering the static equilibrium of joints.

Later, in 1985, Goodman and Shi proposed the block theory based on geometric information from structural geology and equilibrium equations using simple statics. By means of block theory, the system of joints and other rock discontinuities are analyzed to find the critical blocks of the rock mass when excavated along defined surfaces. Using a three-dimensional analysis, the key block types are determined, and the theory then provides a description of the locations around the excavation where the key block is a potential hazard.

Ghaboussi (1988) proposed a fully deformable discrete element analysis using a finite element approach for the deformation of individual blocks used in rock mechanics. The method of analysis, similar to the block model proposed in this chapter, considers blocks as single quadrilateral elements. A constitutive model is used for computing the contact forces. The importance of block deformations in the analysis is emphasized by comparing the two classes of problems involving both deformable and the rigid blocks.

Goodman and Shi (1989) formulated a generalized two-dimensional discontinuous deformation analysis for numerical modeling of rock block systems. The analysis computed stress, strain, sliding and opening of the rock blocks; considered rigid body movement and deformation to occur simultaneously. Input data consist of block geometry, loading forces, the deformability constants E and ν , and the restraint or boundary conditions of the block system. Output data give the movements, deformations, stresses and strains of each block, and the sliding and detachment or rejoining of blocks. The forces acting on each block, from external loading or contact with other blocks, satisfy the equilibrium equations. Equilibrium is also achieved between external forces and block stresses.

Wang and Garga (1991) proposed a block-spring model for analyzing discontinuous heavily jointed rocks. The jointed rock mass is simulated by an assemblage of rigid blocks interacting through particle contacts. Based on the equilibrium of all the blocks, the model evaluates the states of stress and deformation of the rock masses by solving a set of stiffness equations. The block-spring model was also

developed to simulate large scale sliding of the blocks and to predict unstable blocks. The model was used to analyze stability of the surrounding rock masses of either open pits or underground excavations in jointed rocks.

Very recently, Ullidtz (1995) performed calculations using the Distinct Element Method for a two-dimensional particulate material. A box containing about 3010 disks was loaded by a small plate at the surface, and the displacements and contact forces between the particles were calculated using the method for small increments of time. Normal stresses and strains were determined at different distances and depths. These results were compared to stresses and strains predicted using a linear elastic continuum model and a probabilistic stress distribution model. Even though the vertical stresses calculated by these two methods agreed reasonably well with the Distinct Element solutions, predicted horizontal stresses and strains were not in good agreement.

The distinct element approach solves for the assembly deformation based on governing equations for each particle interacting with its surrounding particles. The approach, however, can be cumbersome for systems composed of a large number of different size particles. For example, considering the work of Ullidtz (1995), approximately three thousand particles were used to model a one-layer particulate medium to compare with the Boussinesq solution. The simple problem modeled did not deal with real pavements as layered systems or even with real irregular shaped and sized pavement materials (friction and interlocking of particles). This approach still needs to be researched for a long time before any practical usage can be achieved in design.

Load Transfer in Granular Materials

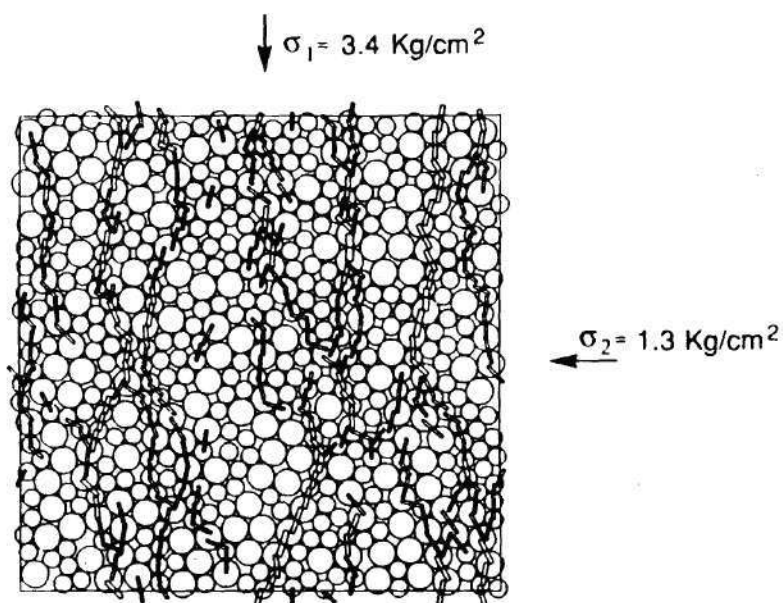
The mechanism of load transfer in granular materials was first experimentally studied by Dantu (1957) with the help of photoelastic models. From the experiments performed, it was concluded that the stresses in granular materials were not uniformly distributed but were concentrated along load carrying particle chains. Later Oda (1974) described other experiments in which photoelastic rods were loaded biaxially. Forces across individual particle contacts were monitored by counting the resulting interference fringes.

Based on experimental studies, the stresses in particulate media are not transferred in a uniform manner but are concentrated along continuous columns of particles. The particles in between the columns only provide lateral support but do not carry much load. At a critical load, a column will fail and the internal structure will be rearranged. Formation of a new column takes place if particles in that region are favorably orientated. The deformation of a particulate mass under increasing load is then mostly the continual collapse and generation of adjacent chains of load-carrying particles. And the predominant orientation of particle contacts are in the direction of the major principal stress.

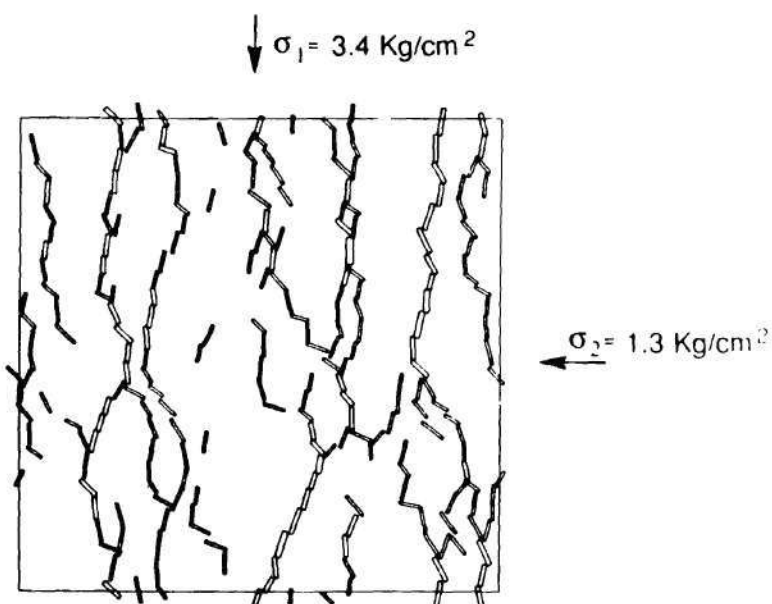
Similar results on the load transfer and deformation characteristics of granular materials were also obtained by Dobry et al. (1989). Using the discrete element approach

(Cundall and Strack, 1979), Dobry et al. modeled granular soil as random arrays of 531 elastic, rough spheres of two different sizes. Numerical simulations of these arrays under monotonic and cyclic loading were compared with typical experimental results from compression triaxial tests on a medium dense uniform quartz sand. The contact forces between spheres were computed using the Hertz-Mindlin force-displacement law (Seridi and Dobry, 1984). Figures 8.1a and 8.1b show the contact forces under anisotropic deviator loading, with and without spheres respectively, corresponding to the shearing part of the triaxial tests. A wider rectangle represents greater force at contact points. Contact forces smaller than 25% of the maximum contact force in the assembly are not included in the figures. The triaxial deviator stress is clearly transmitted by a limited number of "stiff chains" or irregular columns of grains aligned in generally the vertical direction.

According to the experimental and numerical findings, the deformation pattern of the base is directly related to load transfer by shear in the columns of particles (see Figure 8.2). The orientation of the columns are primarily in the direction of the principal stresses and are also affected by the assembly of the grains and their shape. In Figure 8.3, these load-bearing columns are shown to be originating from the applied load on the centerline of the pavement. Each column of grains is supported by the adjacent surrounding particles. The fixed support representation at the bottom of each column corresponds to shear and normal forces at the interface of base with the underlying subgrade layer.



(a) Contact forces with spheres



(b) Contact forces without spheres

$$1 \text{ kg/cm}^2 = 14.2 \text{ psi} = 98.1 \text{ kPa}$$

Figure 8.1. Contact Forces for Two-Dimensional Numerical Simulation - Anisotropic Loading (After Dobry et al., 1989).

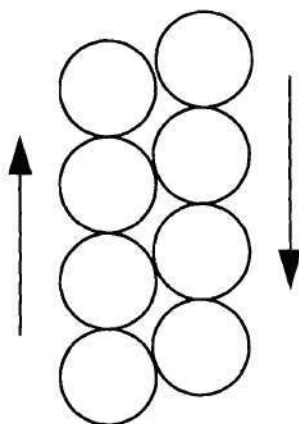


Figure 8.2. Deformation of The Base Layer.

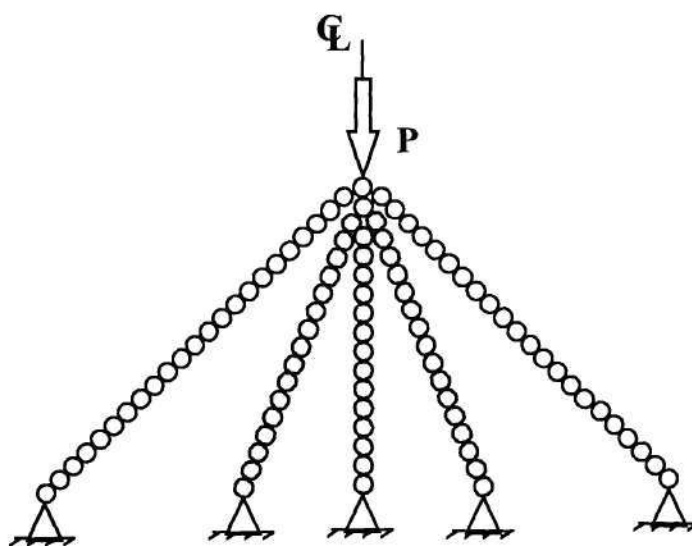


Figure 8.3. Load Transfer In the Base Layer.

A model of the base as a set of coupled springs was proposed by Galjaard and Allaart (1989) and Allaart (1992). This model considers the shear load transfer between the aggregates. In this model, vertical springs support the asphalt concrete (AC) surfacing while the coupling between them permit the shear load from vertical to horizontal directions in the base (see Figure 8.4). The existence of any horizontal tension in the base can then be realistically resisted by the shear load.

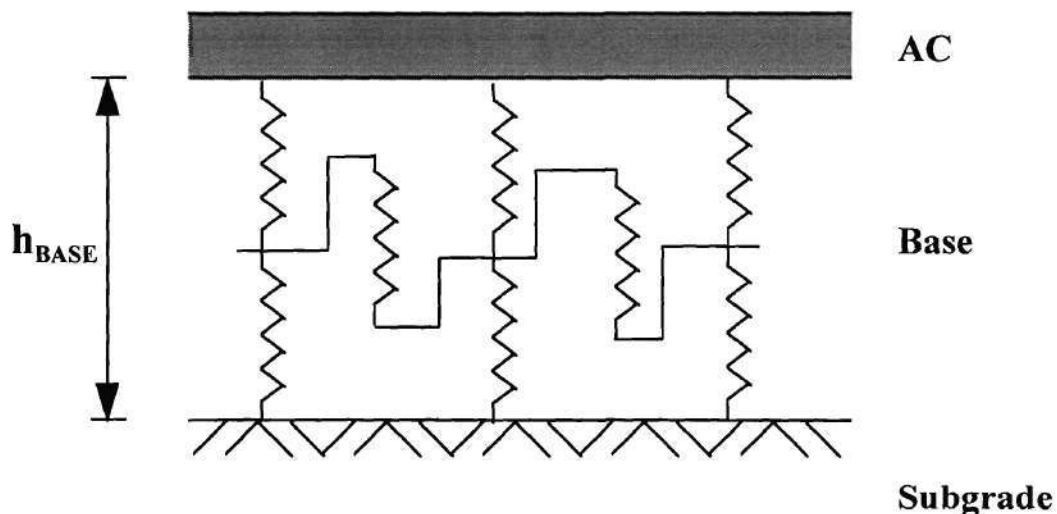


Figure 8.4. Base Layer As A Set of Coupled Springs (After Allaart, 1992).

Block Model

A new method of modeling particulate media is developed as a part of this thesis. The new model incorporates both the classical continuum constitutive relations and at the

same time handles the particulate material characteristics such as translation, sliding, and even separation. This technique is called the “Block Model”. In this approach, a granular base is modeled by discrete blocks with each block consisting of an assembly of granular particles that interact with each other through normal and shear springs (see Figure 8.5). Each block is considered to be a part of the continuum. When the block size becomes as small as the size of an aggregate, micromechanical particle interactions are achieved.

Conventional interface elements are used between the blocks of aggregates (Goodman et al., 1968; Clough and Duncan, 1969; Desai et al., 1984). Normal and shear springs placed between neighboring blocks provide for different behavior and relative movements depending upon the spring stiffnesses. When subjected to compressive forces at block interfaces, the normal interface springs are assigned high normal stiffnesses to maintain continuity and prevent overlapping of the two blocks. When a block is subjected to tension, the normal interface spring stiffnesses are set to zero to enable separation of the two blocks. A slip condition between any two blocks is reached when the applied shear force on the interface exceeds the shear strength of the granular material as defined by the Mohr-Coulomb failure envelope:

$$\tau_{\max} = c + \sigma_n \tan \phi \quad (3.12)$$

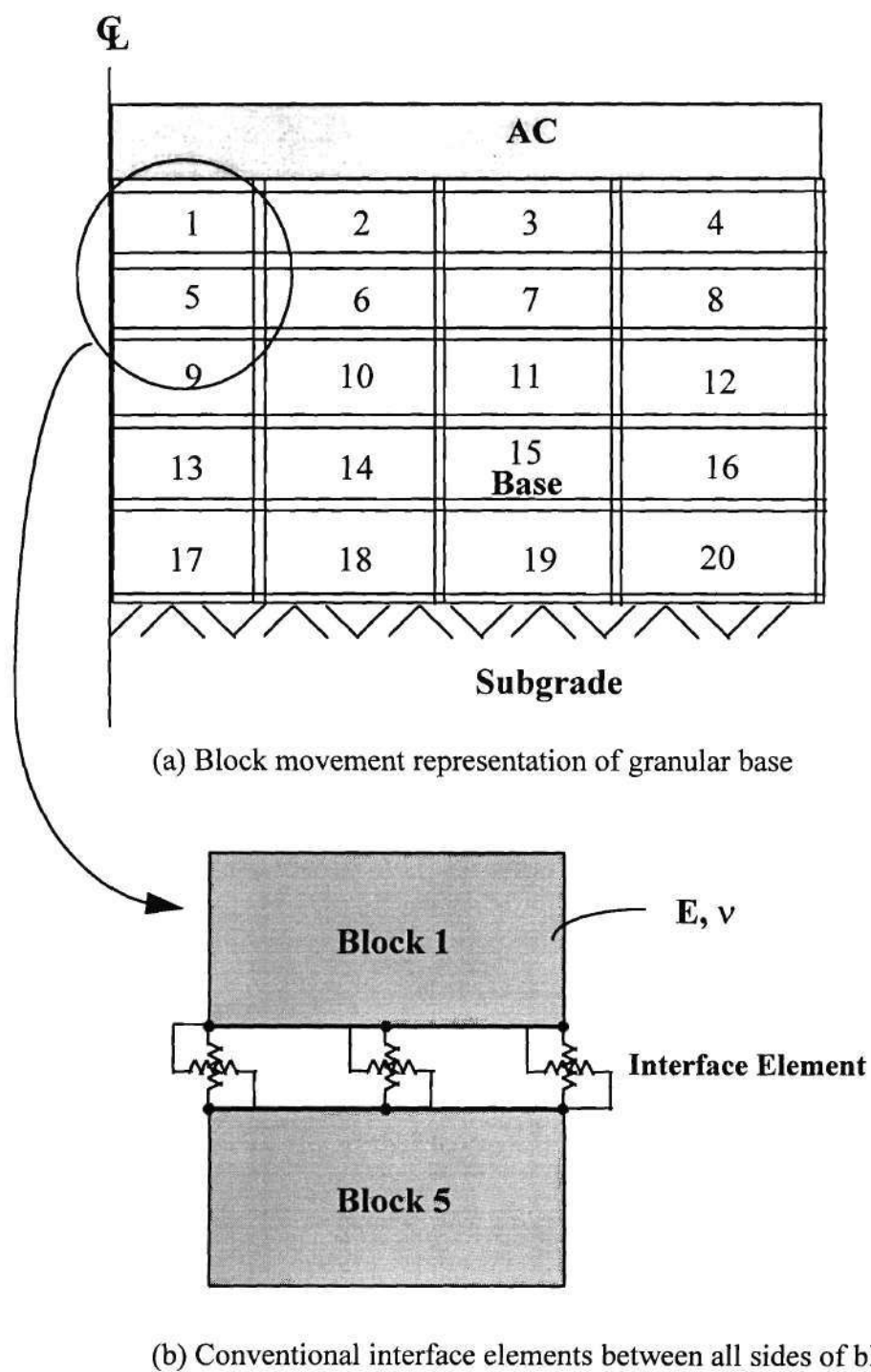


Figure 8.5. Granular Base Consisting of Blocks of Granular Particles Interacting Through Normal and Shear Springs.

where τ_{\max} is the shear stress at failure and, σ_n is the compressive normal stress acting on the interface; and c and ϕ are the cohesion (usually negligible for unbound aggregates) and friction angle of the granular material, respectively.

The model can be easily incorporated into the finite element method. In modeling the granular base, each aggregate block which is represented by a continuum element is surrounded by interface elements. The interface elements used are of negligible thickness. The use of no thickness interface elements between the continuum blocks of aggregates therefore helps to macroscopically model the behavior of the particulate medium.

The deformation pattern under the applied wheel load is directly related to load transfer between the blocks through compression and shear forces. When horizontal tension is encountered in unstabilized aggregate bases and subbases, the block representation models the particulate media as follows (see Figure 8.5): (1) the vertical interfaces separate since interface elements are not assigned stiffness in tension, and also (2) slip can occur in the horizontal interface elements when the maximum shear stress at failure (τ_{\max}) is exceeded by the calculated interface shear stress due to the external loading.

The main purpose of employing the block model in unbound aggregate bases is to approximately model the real particulate nature of these layers. This can best be achieved when response to a surface loading is calculated at the interfaces which allows

determination of the interaction between aggregate blocks. Realistic interface properties, preferably obtained from direct shear tests on each material, are used in the analysis.

Granular bases used in flexible pavements do not, in general, fail even though high horizontal tensile stresses are predicted by elastic continuum solutions. However, the interface elements, when assigned zero normal stiffness in tension and residual shear stiffness in slip, can cause the base layer to totally collapse under the wheel load. The interface elements, when in the slip and separation modes, must have balancing forces applied to them using an iterative procedure to maintain overall equilibrium. The proposed block analysis, therefore, calculates iteratively the final displacement and stress states which consider the limited amount of horizontal tension on the block taken by the shear resistance at the horizontal interfaces.

Using the block model approach, the so-called "no tension" condition of granular bases related to elastic continuum assumptions is investigated. The blocks of aggregates are best idealized when the block size approaches to the aggregate size used in the field. Whether or not the base is capable of taking apparent tension in the field depends then on the ability of granular particles taking shear stresses in the horizontal direction under normal confinement. Since pavements do not actually fail under the predicted tensile stresses, any explanation attempted will also have to consider the effects of residual compaction stresses and the cross-anisotropic material behavior. These important aspects of granular base behavior are discussed subsequently in more detail.

Organization of Interface Elements In the Computer Code

The GT-PAVE nonlinear finite element program includes as an option the block model analysis of unbound granular layers using six-node interface elements. When this option is selected, the block model is employed only in the unstabilized base and subbase. Asphalt concrete surfacing (AC) overlies the base and the subgrade is below it. To generate the rectangular finite element mesh, proper numbering of the elements and nodes are required in the granular layers with interface elements. Figure 8.6 shows the block model representation in a small, three layered rectangular axisymmetric finite element mesh. The mesh consists of top and bottom continuum layers, and a middle granular layer. The example mesh, which is used later in an example problem, permits the use of interface elements between the continuum elements in the granular layer. The node numbering starts first from the bottom left corner and proceeds horizontally to the right and then increases in the vertical direction. The last node and element numbers in the mesh are always assigned at the top right corner of the mesh.

The formulations given in Chapter 5 for the element stiffnesses of the 6-node interface elements are implemented in INTSTIF subroutine. Figure 8.7 shows the flow diagram in which the mathematical procedure is summarized. The interface element stiffness matrix is calculated in a closed form and then stored in the global stiffness matrix of the system with subroutine ADSTIF. Transformation of the local interface element stiffness into the global coordinate system is achieved by the following matrix multiplications:

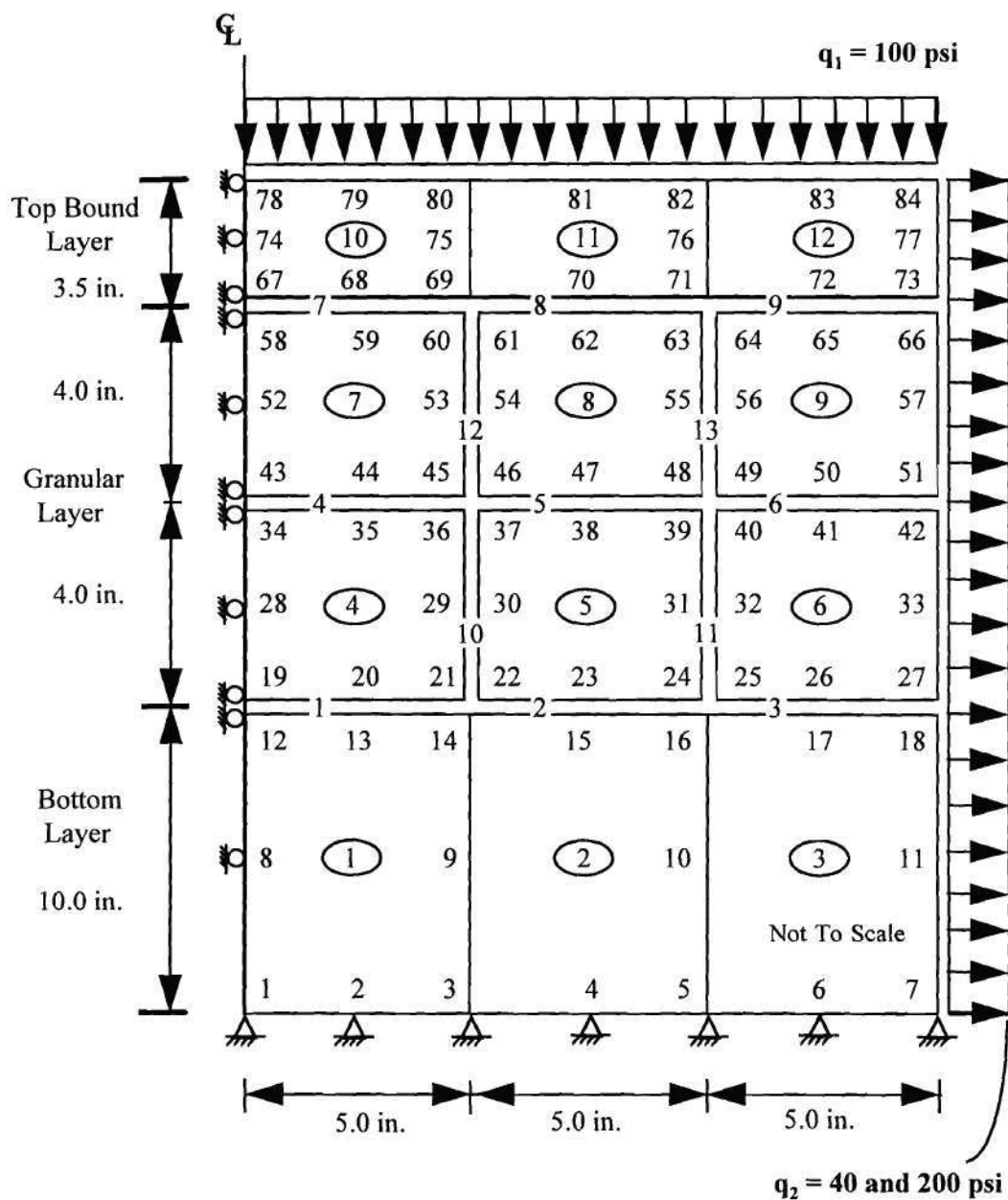


Figure 8.6. The Block Model Representation of the Granular Layers in the Finite Element Mesh: Example 2.

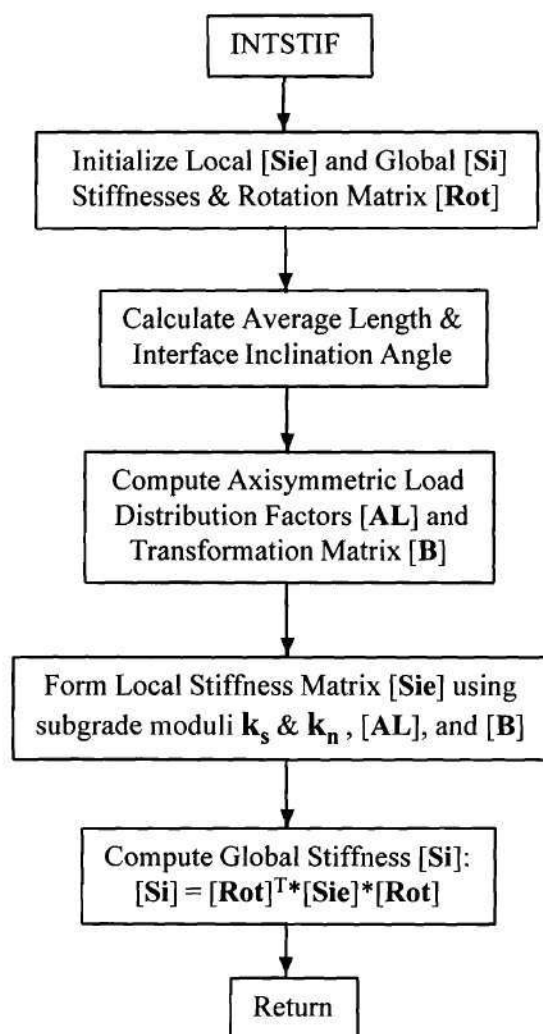


Figure 8.7. Flow Diagram of INTSTIF Element Stiffness Subroutine.

$$\mathbf{S}_i = \mathbf{Rot}^T * \mathbf{S}_{ie} * \mathbf{Rot} \quad (8.1)$$

where \mathbf{S}_{ie} = interface element stiffness matrix in local coordinates,
 \mathbf{S}_i = interface element stiffness matrix for the global system, and
 \mathbf{Rot} = rotation transformation matrix.

The rotation matrix \mathbf{Rot} performs coordinate transformation using the inclination angle α of the interface element. The inclination angle α , which is shown in Figure 5.5, indicates the orientation of the interface element measured counter-clockwise from the horizontal. The interface elements used in the block model are either assigned $\alpha = 0$ for the horizontal, or $\alpha = 90$ degrees for the vertical directions in the granular layer. The 12x12 rotation matrix \mathbf{Rot} is then formed by placing the following 2x2 \mathbf{Rot}_d matrix in the diagonal,

$$\mathbf{Rot}_d = \begin{bmatrix} \cos \alpha & \sin \alpha \\ -\sin \alpha & \cos \alpha \end{bmatrix} \quad (8.2)$$

where α is the inclination angle of the interface.

Interface element stresses are calculated in INTSTRES subroutine and the no tension analysis using interface elements are performed after each linear or nonlinear elastic analysis is completed. INTSTRES calls for the stiffness matrix to compute interface stresses in the granular base from average relative displacements between the nodes of two adjacent continuum elements. The flowchart of computations performed in the INTSTRES subroutine is shown in Figure 8.8.

For each interface element, normal (σ_n) and shear (τ_s) interface stresses are calculated in the normal and tangential directions to the interface, respectively. The maximum shear stress at failure (τ_{max}) is obtained from the Mohr-Coulomb envelope (Equation 5.24) using measured material properties c and ϕ , and the computed normal stress σ_n . The interface behavior mode is then determined through a series of computations as indicated in the elliptical block in the flow diagram of Figure 8.8 and is described in detail in the next section.

The three possible behavior modes that an interface can have are: no slip (0), slip (1), and separation (2). Interface elements in separation are assigned zero shear and normal subgrade reaction type moduli (i.e., $k_s = k_n = 0$) while the ones in the slip mode are given the residual value of shear stiffnesses. In both cases, required balancing forces on the blocks are applied in the next iteration. The analysis and special computations necessary for determining the interface behavior is described next and the iterative equilibrium procedure is summarized.

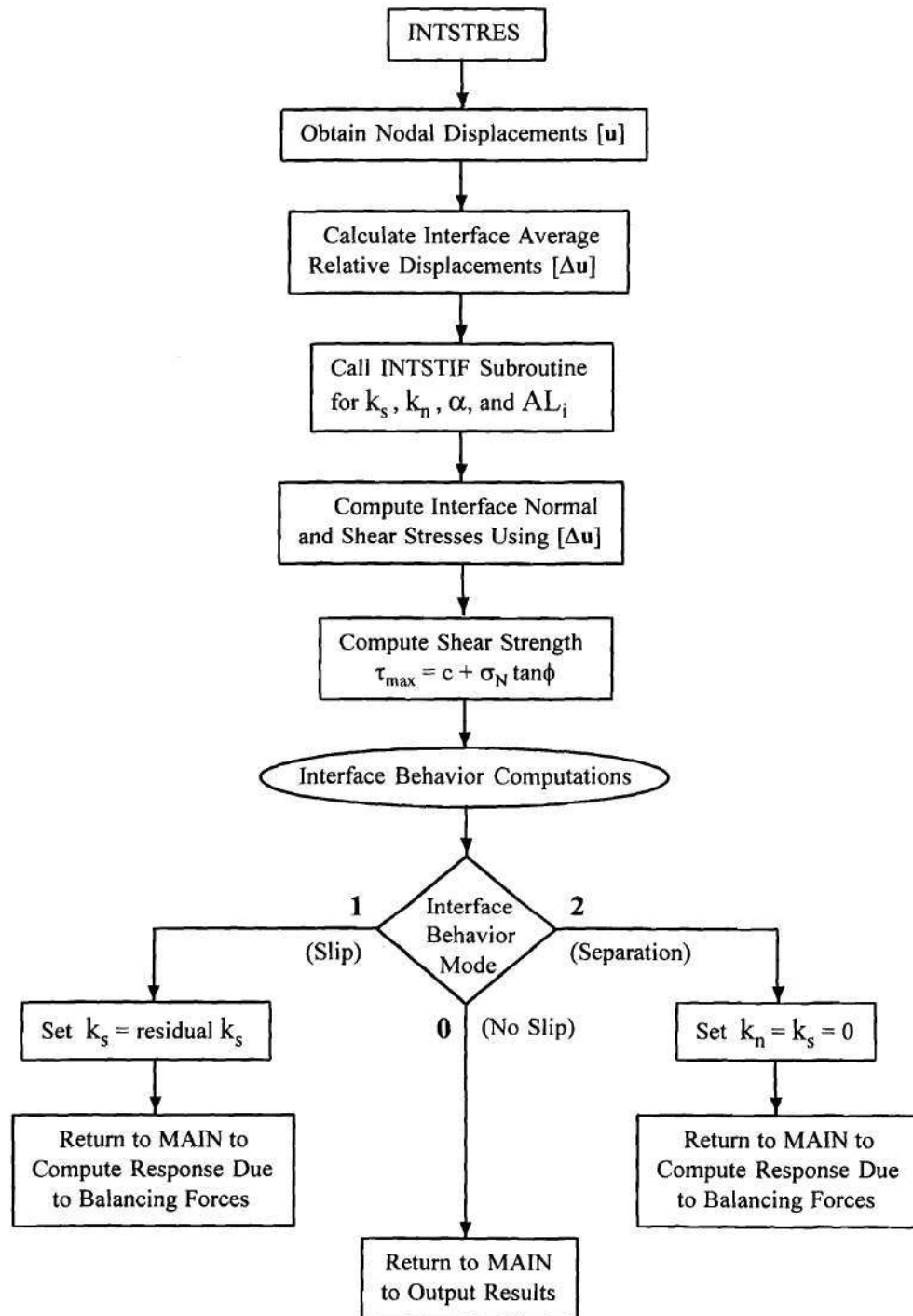


Figure 8.8. Flow Diagram of INTSTRES Interface Element Stress Subroutine.

Interface Behavior and Iterative Procedure For Equilibrium

The six node interface elements surrounding the continuum elements in a granular base deform quadratically due to load application in a similar manner as the eight node elements. Figure 8.9 illustrates both the undeformed and a deformed shape of an *initially* horizontal interface element. An average chord drawn at the interface determines direction of the contact plane. As indicated in Figure 8.9, the originally horizontal interface element deforms giving inclination α with the horizontal. In a typical flexible pavement problem, this angle, however, is very small and therefore neglected in the analysis since GT-PAVE program considers only small-displacements. The program does not update the coordinates of the nodes through iterations for different geometries since small-displacements are assumed.

Figure 8.9 also shows, for the originally horizontal interface element, the initial and final (deformed) positions of an interface element center point defined by the following average coordinates:

$$\begin{aligned} r_c &= (r_1 + r_2 + r_3 + r_4 + r_5 + r_6) / 6 \\ z_c &= (z_1 + z_2 + z_3 + z_4 + z_5 + z_6) / 6 \end{aligned} \tag{8.3}$$

where r_c and z_c = r and z coordinates of the interface element center point,

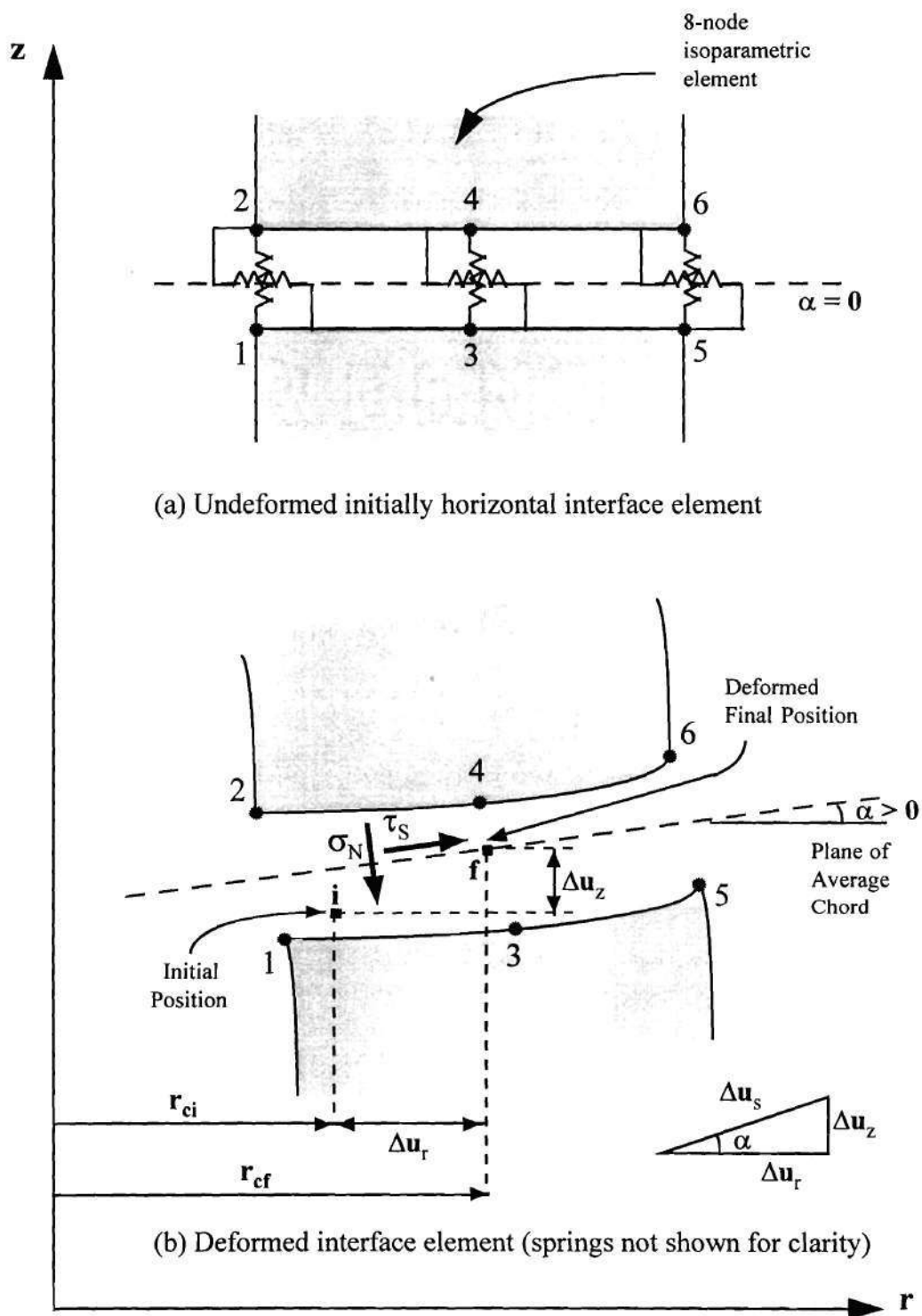


Figure 8.9. Interface Behavior with Relative Displacements and Stresses.

r_1 to r_6 = r coordinates of the six nodes of the interface element, and

z_1 to z_6 = z coordinates of the six nodes of the interface element.

Starting from an initially undeformed displacement state, the average relative displacements at the centerpoint $\Delta \mathbf{u}$ are obtained between the top and bottom nodes of the interface element as follows:

$$\begin{aligned}\Delta u_r &= (u_2 + u_4 + u_6 - u_1 - u_3 - u_5) / 3 \\ \Delta u_z &= (w_2 + w_4 + w_6 - w_1 - w_3 - w_5) / 3\end{aligned}\tag{8.4}$$

where u_1 to u_6 = nodal displacements in r direction and

w_1 to w_6 = nodal displacements in z direction.

Consider now the horizontal interface elements located at the centerline of the axisymmetric mesh. The average vertical relative displacement for these elements is approximated by the centroid value (see Figure 8.9):

$$\Delta u_z = (w_4 - w_3)\tag{8.5}$$

The normal and tangential average relative displacements, Δu_n and Δu_s , are computed in the direction of the interface using the average relative displacements in r and z directions and the inclination angle α as follows:

$$\begin{aligned}\Delta u_n &= \Delta u_z \cos \alpha - \Delta u_r \sin \alpha \\ \Delta u_s &= \Delta u_z \sin \alpha + \Delta u_r \cos \alpha\end{aligned}\tag{8.6}$$

The interface normal and shear stresses, σ_n and τ_s , are then calculated at the interface centerpoint by using the following equations:

$$\begin{aligned}\sigma_n &= k_n \Delta u_n \\ \tau_s &= k_s \Delta u_s\end{aligned}\tag{8.7}$$

where k_n and k_s are the normal and shear moduli of subgrade reaction (F/L^3), respectively. The centerpoint stresses are used to determine the behavior mode of the element. Additionally, the stresses calculated at the nodes of the interface elements are generally assigned as the interface final stress state.

Figure 8.10 summarizes the algorithm used for interface behavior computations in the INTSTRES subroutine. The algorithm consists of first selecting the behavior mode of the interface element, and then performing balancing force computations related to the behavior mode. Interface shear and normal stresses are used to define the mode of behavior of an element. The slip and separation modes, when encountered in the

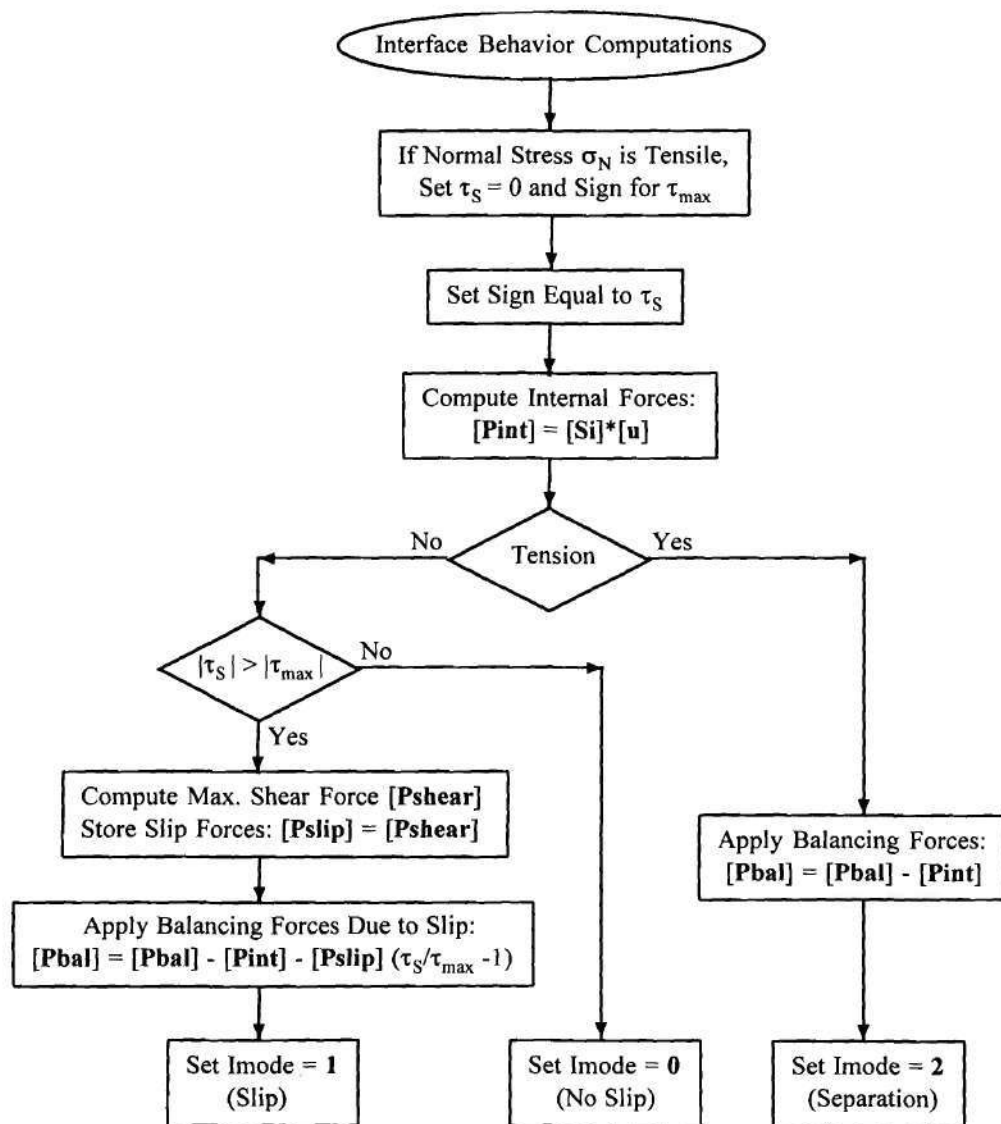


Figure 8.10. Algorithm for the Selection of Interface Behavior Mode and Computation of Balancing Forces.

interfaces, require special computations to obtain the unbalanced forces that must be applied to the system to maintain the overall equilibrium.

The algorithm begins by setting the direction of the maximum shear stress at failure (τ_{\max}) in the same direction with the calculated interface shear stress τ_s in case of a possible slip behavior. Next, internal spring forces at the interface are computed using the interface element stiffness matrix \mathbf{S}_i and the calculated nodal displacements \mathbf{u} . The forces are given by the following matrix equation:

$$\mathbf{P}_{\text{int}} = \mathbf{S}_i \mathbf{u} \quad (8.8)$$

where \mathbf{P}_{int} = internal spring forces at the interface.

When the calculated interface normal stress σ_n is tensile, tension is said to exist at the interface. Separation between the elements is then likely to occur. To maintain overall equilibrium, forces equal in magnitude but in the opposite direction are applied in the next iteration. These forces are the balancing forces computed in the internal springs ($-\mathbf{P}_{\text{int}}$). Both the normal and shear interface stiffnesses, k_n and k_s , are set to zero in the interface. These zero stiffnesses are also used in the next iteration in the formulation of the interface element stiffness matrix.

If tension does not exist in the interface element, the slip condition is checked next. Slip of an interface element means that the maximum allowable shear force due to one

block pushing against another has been exceeded by the applied force (i.e., by the calculated spring shear forces of the interface). The algorithm summarized in Figure 8.10 checks slip by comparing the magnitudes of the computed shear stress τ_s with the shear strength of the interface τ_{\max} . In case of slip, special computations are necessary.

The limiting slip force is defined as the maximum allowable shear force that can develop in the shear spring corresponding to the maximum shear stress τ_{\max} available in the interface. Consider the general case of an interface element having an inclination angle α with the horizontal. The nodal force components due to the maximum shear stress are given for the 12 degrees of freedom of the interface element (see Figure 5.4b) in the r, z coordinate axes as follows:

$$\mathbf{P}_{\text{slip}} = \begin{Bmatrix} \tau_{\max} AL_1 \cos\alpha \\ \tau_{\max} AL_1 \sin\alpha \\ -\tau_{\max} AL_1 \cos\alpha \\ -\tau_{\max} AL_1 \sin\alpha \\ \tau_{\max} AL_3 \cos\alpha \\ \tau_{\max} AL_3 \sin\alpha \\ -\tau_{\max} AL_3 \cos\alpha \\ -\tau_{\max} AL_3 \sin\alpha \\ \tau_{\max} AL_5 \cos\alpha \\ \tau_{\max} AL_5 \sin\alpha \\ -\tau_{\max} AL_5 \cos\alpha \\ -\tau_{\max} AL_5 \sin\alpha \end{Bmatrix}_{12 \times 1} \quad (8.9)$$

where τ_{\max} = maximum shear stress, α = the angle of inclination, and AL_1 , AL_3 , and AL_5 are the axisymmetric load distribution factors derived in Chapter 5 and given by Equation 5.30.

The correction forces that must be applied to the system for the slip condition are then the unbalanced slip forces which are not taken by the maximum shear stress at slip. These unbalanced forces are given by

$$\mathbf{P}_{\text{unbal}} = \mathbf{P}_{\text{spring}} - \mathbf{P}_{\text{slip}} = \mathbf{P}_{\text{slip}} \left(\frac{\tau_s}{\tau_{\max}} - 1 \right) \quad (8.10)$$

where $\mathbf{P}_{\text{unbal}}$ = unbalanced slip forces,

$\mathbf{P}_{\text{spring}}$ = forces created at the springs due to the calculated τ_s

$= (\tau_s / \tau_{\max}) * \mathbf{P}_{\text{slip}}$, and

\mathbf{P}_{slip} = slip forces given in Equation 8.9.

To maintain the general equilibrium of the system, the elements in the slip mode are acted upon by the balancing forces. The shear stiffnesses k_s of the elements in slip mode are assigned small residual values and iterations are performed with the following balancing forces \mathbf{P}_{bal} applied to the system:

$$\mathbf{P}_{\text{bal}} = -\mathbf{P}_{\text{int}} - \mathbf{P}_{\text{slip}} \left(\frac{\tau_s}{\tau_{\text{max}}} - 1 \right) \quad (8.11)$$

where \mathbf{P}_{int} = internal spring forces and the other terms are as defined above. The system becomes in equilibrium when no element exists in slip mode (but elements can be on the verge of slip). An unstable system may be encountered, when the interface elements are not able to take the total unbalanced shear force. This condition is usually followed by the separation of the interface element in the next iterations, sometimes resulting in dislocation of the neighboring continuum elements.

The Block Model Iterative Equilibrium Procedure:

The block model analysis using interface elements mainly involves: (1) the elimination of tension in the vertical interface elements and (2) balancing the slip condition which occurs when the computed interface shear stress exceeds the maximum shear stress at failure in the horizontal interfaces. The amount of apparent tension that can be taken in a granular layer depends on the material properties of the aggregates (especially the friction angle ϕ) and the shear stiffness k_s of the aggregates. These properties should preferably be obtained from direct shear testing of the material. The procedure outlined below is performed after the end of each linear or nonlinear elastic analysis until equilibrium of the system is achieved:

1. The iteration counter INTFLAG and the other counters showing the number of interface elements undergoing tension (ITEN) or slip (ISHEAR) failure are set to zero for the first iteration.
2. No slip is assumed in the interface (IMODE = 0). The average relative normal and shear displacements, Δu_n and Δu_s , are calculated at the centerpoint of each interface element.
3. The interface normal and shear stresses, σ_n and τ_s , are calculated using Δu_n and Δu_s , and interface normal and shear stiffnesses, k_n and k_s .
4. The maximum shear stress at failure, τ_{max} , is computed using the Mohr-Coulomb law: $\tau_{max} = c + \sigma_n \tan \phi$. The direction of τ_{max} is set in the direction of the calculated shear stress τ_s .
5. The interface behavior mode is determined. First, the interface is checked for tension and separation. If σ_n is tensile, IMODE is set to 2 and both the normal and shear stiffnesses at the interface are set to zero ($k_n = k_s = 0$). The balancing forces \mathbf{P}_{bal} are calculated from internal spring forces \mathbf{P}_{int} .
6. If σ_n is not tensile, the interface is checked for slip. In case of slip, the magnitude of the maximum shear stress is exceeded by the interface shear stress (i.e., $|\tau_s| > |\tau_{max}|$). IMODE is then set to 1 and the shear stiffness at the interface

k_s is set to a small residual value (typically 1% of the original). The balancing force vector \mathbf{P}_{bal} is computed from Equation 8.11.

7. Steps 2 to 6 are repeated for each interface element.
8. Print the total number of interface elements in tension (ITEN) and in slip (ISHEAR) failure. If both ITEN and ISHEAR are not equal to 0, balancing forces are added to the current external load to obtain the total global loading ($\mathbf{P}_{total} = \mathbf{P}_{external} + \mathbf{P}_{bal}$) which is applied to the system in the next iteration.
9. When both ITEN and ISHEAR are equal to 0, overall equilibrium exists and the no tension iterations have converged to the correct condition. The new stress state in the granular layer is obtained from the interface stresses which are obtained at the nodes. An unstable system, if encountered, results in an increase or fluctuation of the number of elements undergoing a tension or slip failure.

Verification of Interface Elements

Example 1: Boussinesq Type Problem

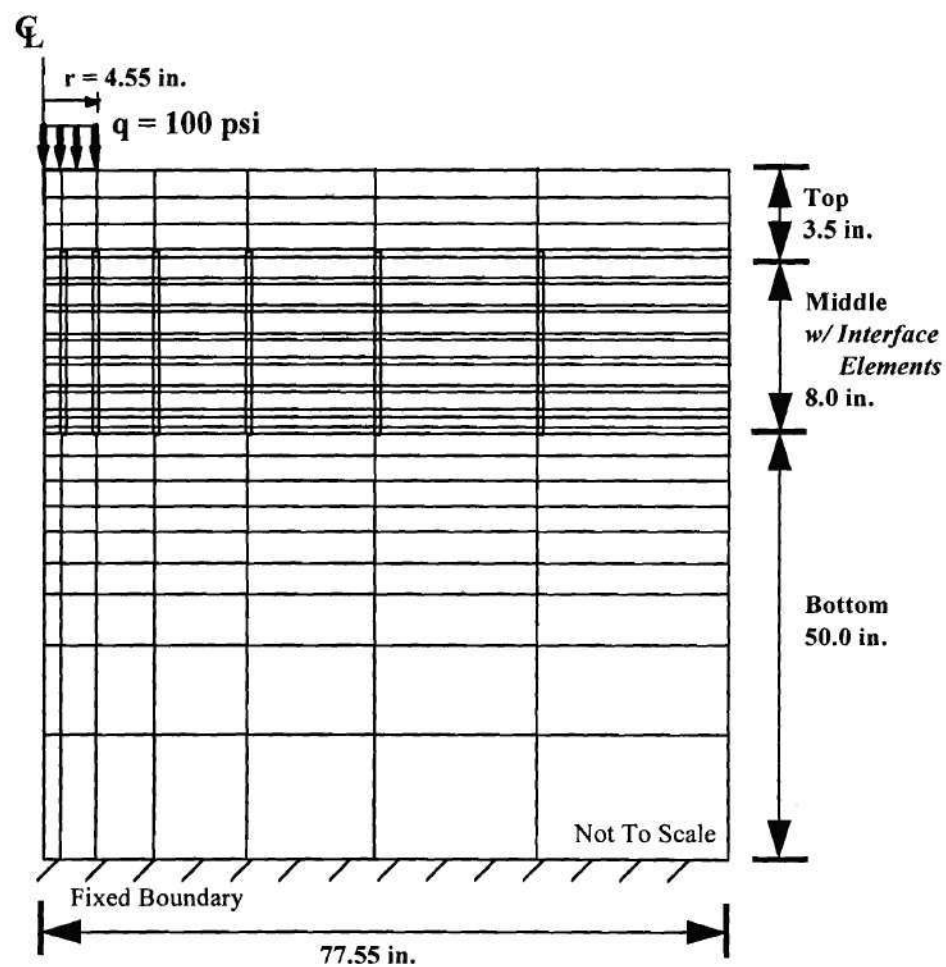
The accuracy of the interface elements is verified in this section by comparing the response predicted at the interfaces with the closed form solutions of an elastic halfspace Boussinesq type problem. A 100 psi (689 kPa) uniformly distributed circular load is

applied over a diameter of 9.1 in. (231 mm). Figure 8.11 shows the finite element mesh used to approximate the semi-infinite halfspace. The geometry and loading conditions of the mesh are similar to the one used in Chapter 7 for modeling the Georgia Tech pavement test sections. In addition to the 140 continuum elements, this new mesh contains 721 nodes and 98 interface elements located in a middle 8 in. (203 mm) zone (see Figure 8.11). Isotropic material properties consisting of a 250,000 psi (1723.8 MPa) modulus of elasticity and a Poisson's ratio of 0.35 are assigned for this example to the elastic Boussinesq halfspace.

The spring coefficients K_s and K_n of the interface elements (defined by Equation 5.35 in Chapter 5) are made as large as practical to give negligible fictitious deformation in the springs. Present and past computer analyses using interface elements have indicated that the following values for the normal and shear subgrade reaction type moduli give good accuracy when the variables are given double precision (Zeevaert, 1980): $k_n = 9.0 \times 10^6$ pci (2,442.6 GN/m³) and $k_s = 4.0 \times 10^6$ pci (1,085.6 GN/m³). The use of higher subgrade reaction type moduli do not result in any significant improvement in accuracy.

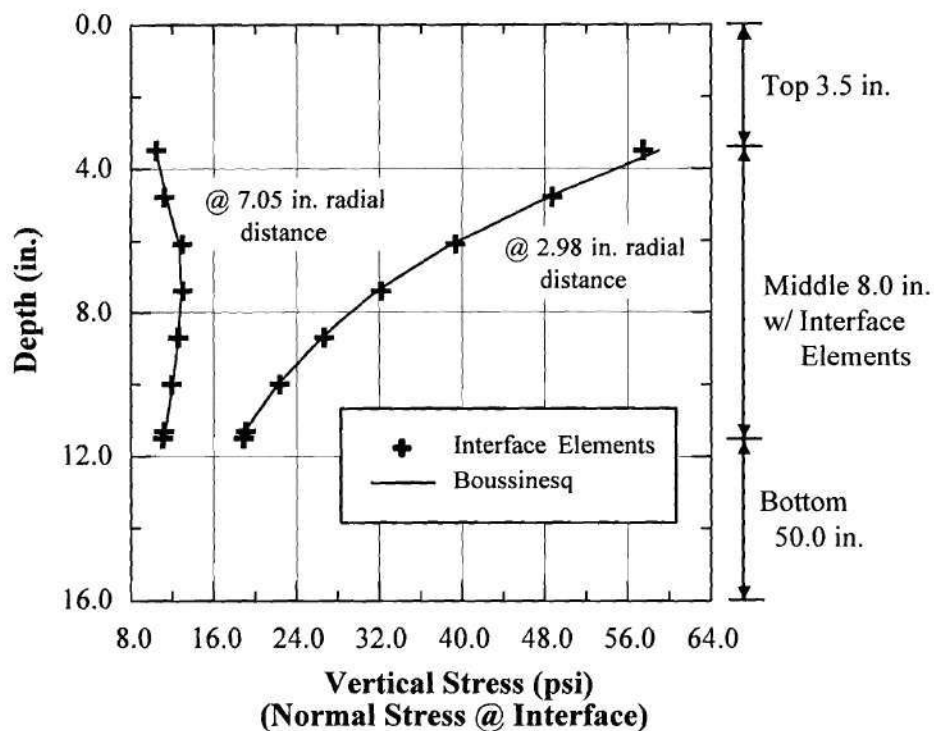
Figure 8.12 shows the interface element stress predictions in the middle 8.0 in. (203 mm) zone compared with the theoretical Boussinesq solution results. In Figure 8.12a, the average normal stresses in the interfaces are plotted with depth both at 2.98 in. (76 mm) and 7.05 in. (179 mm) radial distances from the centerline. A maximum error of

2.7% was found between the predicted normal interface stresses and the Boussinesq vertical stresses.

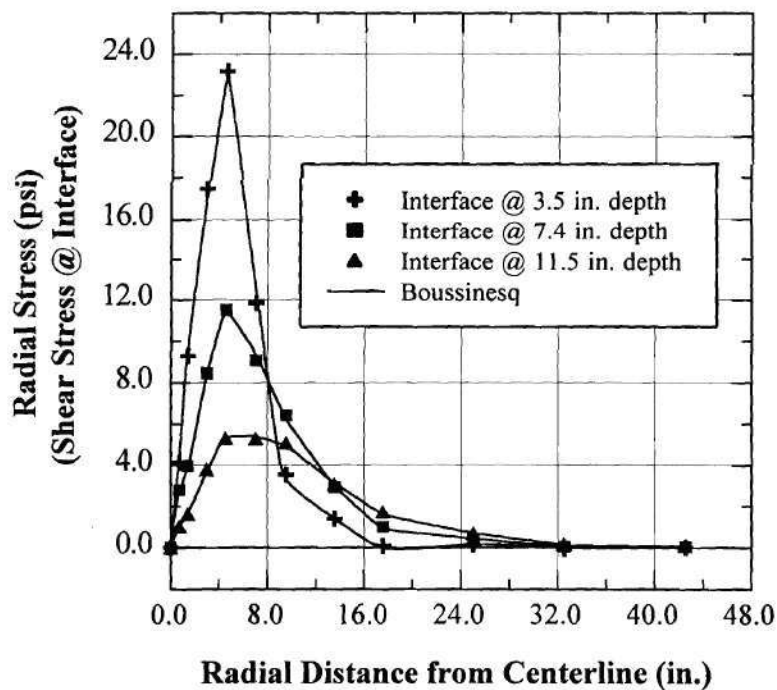


- Notes: 1. 1 in. = 25.4 mm; 1 psi = 6.895 kPa.
2. Nodes on vertical boundaries restrained horizontally.

Figure 8.11. Finite Element Mesh with Interface Elements Used in the Middle 8.0 in. (203 mm) Zone [Examples 1 and 3].



(a) Variation of interface element normal stresses with depth: Example 1



(b) Variation of interface element shear stresses with radial distance: Example 1

Note: 1 in. = 25.4 mm; 1 psi = 6.895 kPa

Figure 8.12. Interface Element Stress Predictions for the Boussinesq Type Problem.

The variation of the interface shear stresses are plotted with radial distance in Figure 8.12b at 3 different depths in the 8.0 in. (203 mm) middle zone. The stresses shown at depths 3.5 in. (89 mm) and 11.5 in. (292 mm) are from the interfaces located at the zone boundaries. The shear stresses at 7.4 in. (188 mm) are for the middle of the zone. The interface shear stress predictions, in general, are in good agreement with the Boussinesq shear stress solutions with a maximum error of 6.7% between the predicted and the theoretical values.

Applications of the Block Model

The block model analysis is first employed in this section using the simple finite element mesh shown in Figure 8.6. This mesh has an 8.0 in. (203 mm) thick granular layer in the middle of the mesh. The use of this simple mesh which has 6 aggregate blocks and 13 interface elements demonstrates how the block model works for layered systems under both normal and failure load conditions. Later, the block model is applied to the unbound aggregate bases used in the Georgia Tech full-scale conventional pavement test sections. The iterative procedure using the interface elements is then carried out in the granular base to solve for the final displacement, strain and stress states obtained at the block interfaces.

Interface Properties

The particulate media modeled using the block model in the applications section consists of the crushed granitic gneiss used in the Georgia Tech conventional pavement test sections (Barksdale and Todres, 1983). The combined aggregate gradations of the unstabilized crushed granitic gneiss base course are listed in Table 7.2. Table 7.2 also gives the properties of the base which include a density of 137 pcf (21.5 kN/m³) corresponding to 100% of AASHTO T-180 (1990) modified proctor maximum dry density and 5.7% optimum moisture content.

The interface properties required for the model are the cohesion c , friction angle ϕ , and the subgrade reaction type modulus in shear k_s . These properties were obtained from direct shear tests performed on several granitic gneisses in an earlier study undertaken at Georgia Tech to determine the shear strength of rock discontinuities in Georgia (Syriopoulos and Barksdale, 1985). In this study, the angle of internal friction of rock discontinuities was measured using a multi-stage, direct shear test. The rock surfaces tested were fractures found in 2 in. (51 mm) cored rock specimens. Rock samples varying in surface roughness from very smooth to very rough were tested at 3 different normal stresses changing from 63 to 191 psi (434.4 to 1316.9 kPa). Relationships between peak shear strength and normal stress were established.

Among the 7 granitic gneiss rock samples tested, only the one with the very rough surface resulted in a maximum peak friction angle of 46°. The others with smooth to

rough surfaces gave friction angles ranging between 19 to 36 degrees. The subgrade reaction type modulus in shear k_s was also obtained from the plots of shear stress as a function of horizontal displacement. The values for k_s ranged between 8,800 to 29,900 pci (2,388.3 to 8,114.9 MN/m³) with a representative value for the very rough sample of approximately $k_s = 15,000$ pci (4071 MN/m³) obtained at a normal stress of 63 psi (434.4 kPa).

Based on the shear strength study results for granitic gneiss (Syriopoulos and Barksdale, 1985), the following properties are assigned to the interface elements in the block model examples examined in this Chapter: **1.** cohesion $c = 0$; **2.** friction angle $\phi = 46$ degrees, and **3.** subgrade reaction type shear modulus $k_s = 15,000$ pci (4071 MN/m³) with the assignment of a 1% residual value (i.e., 150 pci; 40.7 MN/m³) when slip is encountered at the interface. A large vertical subgrade reaction type modulus of $k_n = 9.0 \times 10^6$ pci (2,442.6 GN/m³), which was also used in Example 1, was used again for the crushed granitic gneiss layer since overlapping of the blocks of aggregates are not permitted in the block model.

Example 2: Sliding Block Example

The block model approach is employed here for the simple layered system problem shown in Figure 8.6. The 8 in. (203 mm) thick middle granular layer, which is similar to a base course in a flexible pavement, is sandwiched between the top AC and bottom

subgrade layers modeled using continuum elements. The block model representation of the middle granular layer simply consists of using 6 blocks of aggregates as continuum elements surrounded by a total of 13 interface elements. Unlike a conventional flexible pavement, however, the vertical nodes on the right side of the finite element mesh are not restrained in the horizontal direction. As shown in Figure 8.6, the loading on the system includes both a uniform vertical compressive load $q_1 = 100$ psi (689 kPa) on the top of the mesh and a uniform tensile load q_2 applied on the right side of the mesh. The problem is solved for magnitudes of q_2 equal to 40 and 200 psi (276 and 1379 kPa).

The top and bottom layers were assigned isotropic properties for this illustrative example. The middle granular layer was considered to be cross-anisotropic inside the blocks for the continuum to model the assembly of particles. The material properties (inside the blocks in the base layer) used in the analysis are as follows:

Top (AC) layer: $M_R = 250,000$ psi, $\nu = 0.35$, unit weight $\gamma = 148$ pcf,

Middle (base) layer: $M_R^v = 38,000$ psi, $M_R^h = 5700$ psi, $G_R^v = 13287$ psi,

$\nu_v = 0.43$, $\nu_h = 0.15$, unit weight $\gamma = 139$ pcf,

Bottom (subgrade) layer: $M_R = 6,000$ psi, $\nu = 0.40$, unit weight $\gamma = 105$ pcf,

where 1 in. = 25.4 mm, 1 psi = 6.895 kPa, 1 pcf = 0.157 kN/m³.

The simple layered system problem was analyzed using the linear elastic option of the GT-PAVE finite element program under the following two loading conditions: 1. q_1

= 100 psi (689 kPa) compression and $q_2 = 40$ psi (276 kPa) tension, and 2. $q_1 = 100$ psi (689 kPa) compression and $q_2 = 200$ psi (1379 kPa) tension. For both loading conditions, the applied tensile load q_2 initially caused the vertical interface elements in the granular layer to separate. Failure due to slip at the horizontal interfaces, however, occurred only for the second loading condition where the horizontal interface shear stresses τ_s exceeded the maximum shear stress τ_{\max} due to the application of the large 200 psi tensile stress on the boundary.

To visualize the variation of the interface normal and shear stresses obtained at the end of the iterations, contour plots of interface vertical, radial, and shear stresses are drawn on the finite element mesh in the r - z plane. Figure 8.13 illustrates in the r - z plane the equivalent vertical, radial, and shear stresses on the sides of one continuum element. The stresses are obtained from the relative displacements between the top and bottom nodes in vertical and horizontal interface elements. Assume that the displacements calculated are small, and the interface elements have negligible change in inclination at the end of the analysis. Then, (1) the normal stress in the vertical interface element can be considered to be equivalent to the radial stress and (2) the normal stress in the horizontal interface element is considered to be equivalent to the vertical stress in the r - z plane. Since the interface stresses calculated are not valid within an element, the contour plots, strictly interpreted, are not valid. They do, however, nicely show general trends of stresses acting within the interfaces.

Loading Condition 1 ($q_2 = 40$ psi): For the horizontal tensile load $q_2 = 40$ psi (276 kPa), the 4 vertical interfaces in the granular layer went into the separation mode. This resulted in the assignment of zero normal and shear stiffnesses in the second iteration. At the end of two iterations, however, equilibrium was achieved without any horizontal interface going into the slip mode. The shear stresses created at the horizontal interfaces due to $q_2 = 40$ psi (276 kPa), therefore, were not exceeded by the maximum shear stresses calculated from the Mohr-Coulomb envelope using Equation 5.24.

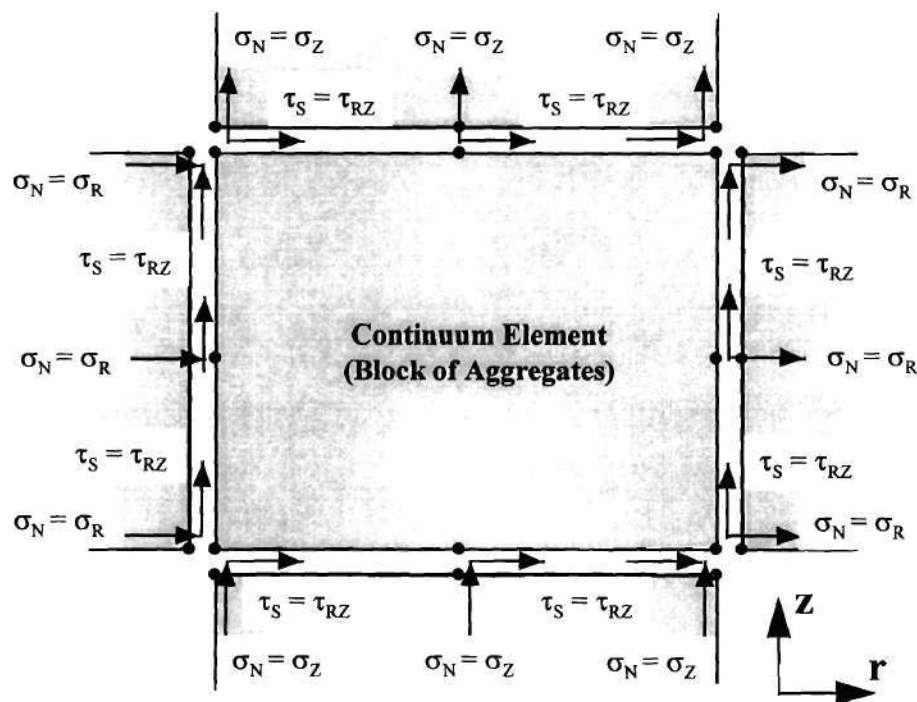
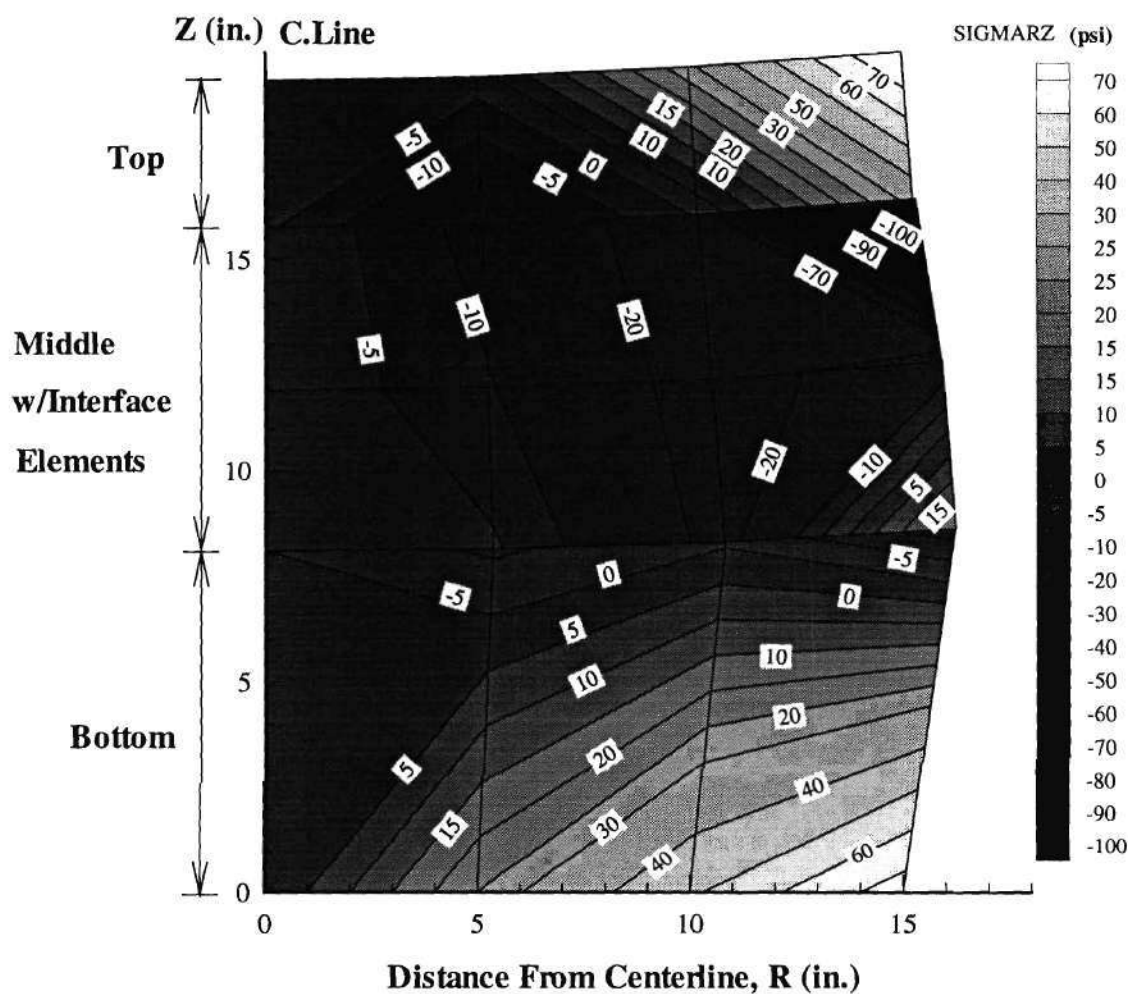


Figure 8.13. Interpretation of Interface Element Normal and Shear Stresses in r - z plane.

Figure 8.14 shows contours of interface shear stresses predicted in the deformed mesh at the end of the no tension analysis. The deformed mesh was plotted using an exaggeration factor of 10. The calculated displacements were multiplied by 10 and added to the original coordinates. The granular layer shear stress distribution shown in the plot was obtained by interpreting stress at the nodes of the interface elements (see Figure 8.13). The negative shear stresses mainly computed in the horizontal interfaces prevent slip failure and help maintain the equilibrium of the continuum elements. The stresses in the top and bottom layers are the calculated stresses at the 9 integration points in the eight-node quadrilateral elements.

Loading Condition 2 ($q_2 = 200$ psi): For the applied large horizontal tensile load $q_2 = 200$ psi (276 kPa), the 4 vertical interfaces in the granular layer again went into the separation mode in the first iteration. In addition, the three horizontal interface elements, elements 3, 6, and 9, went into the slip mode. After the first iteration, vertical elements were assigned zero normal and shear stiffnesses, and the shear stiffness in the sliding horizontal elements was reduced to a residual value of 1% of the peak value. The calculated balancing forces for separation and slip were then applied in the subsequent iterations. At the end of 4 iterations, equilibrium was never achieved, and elements 3, 6, and 9 were in a condition of total slip failure. The shear stresses applied to these



- Notes:**
1. Displacements are exaggerated by a factor of 10
 2. Tension is positive
 3. 1 in. = 25.4 mm, 1 psi = 6.85 kPa

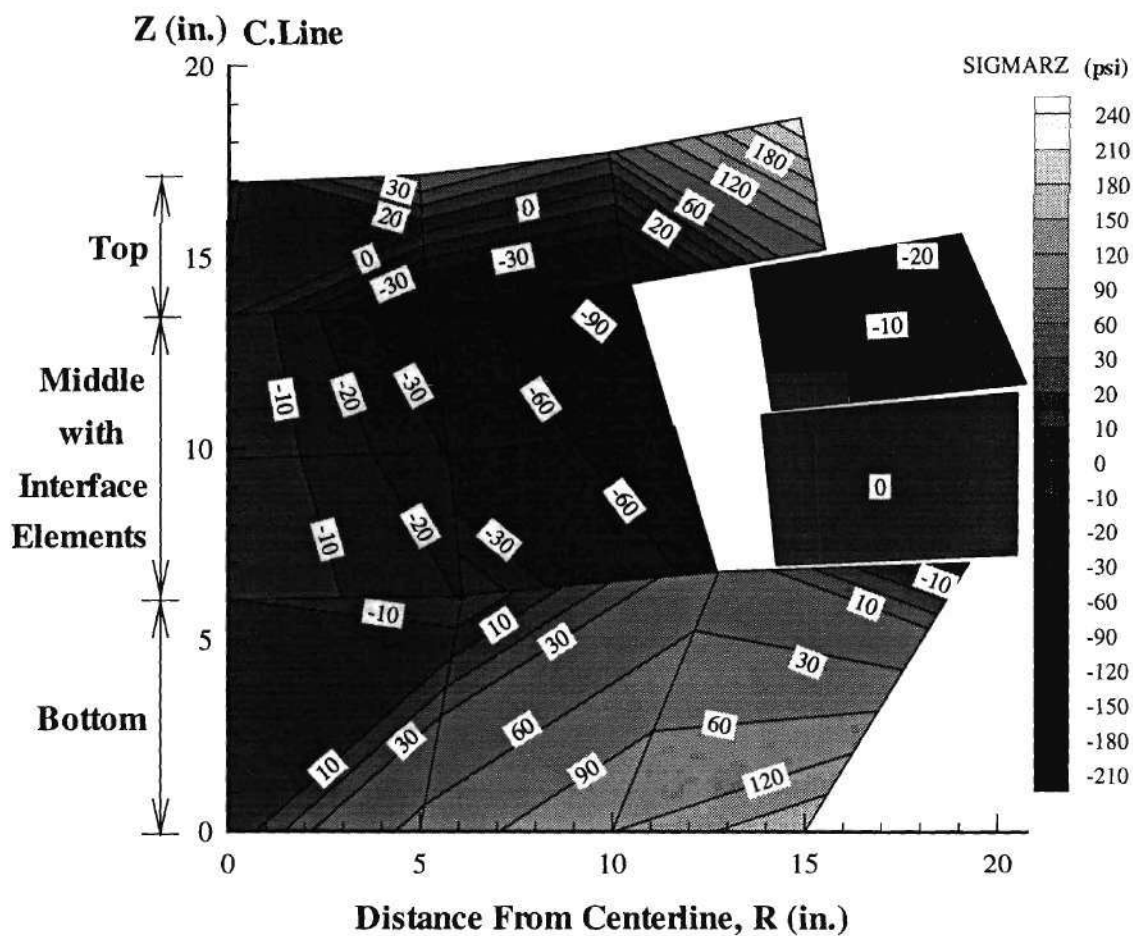
Figure 8.14. Example 2: The Deformed Mesh and the Variation of Interface Shear Stresses Throughout the Middle (Base) Layer for Loading Condition 1.

horizontal interfaces due to $q_2 = 200$ psi (1379 kPa) therefore exceeded the maximum possible shear stresses calculated from the Mohr-Coulomb envelope (Equation 5.24).

Figure 8.15 illustrates how the block model works in the granular layer when failure is encountered due to slip and separation. Blocks with element numbers 6 and 9 were both pulled out in the deformed mesh showing no shear resistance to the high 200 psi (1379 kPa) horizontal tensile load. The interface shear stress distribution predicted for the failure condition, however, still indicates stresses less than required for failure at the horizontal interfaces of the other 4 non-failing blocks (see Figure 8.15). The shear resistance observed at these non-failing horizontal block interfaces demonstrates the load transfer ability of the granular particles in shear when subjected to normal stress.

Example 3: Georgia Tech Conventional Test Sections

The block model is applied in this example to the crushed granitic gneiss base course used in the Georgia Tech full-scale conventional pavement test sections. First, the cross-anisotropic nonlinear analysis described in Chapter 7 is performed on the sections. Next, the block model is used with the iterative equilibrium procedure employed in the base. The stress state determined at the interfaces between the neighboring blocks is proposed as a practical method for calculating the tensile stress actually developed in the granular base. Thus, a solution is presented to the long neglected “no tension” granular base problem of the elastic continuum approach discussed in Chapter 3.



- Notes:**
1. Displacements are exaggerated by a factor of 10
 2. Tension is positive
 3. 1 in. = 25.4 mm, 1 psi = 6.85 kPa

Figure 8.15. Example 2: The Deformed Mesh and the Variation of Interface Shear Stresses Throughout the Middle (Base) Layer for Loading Condition 2.

Stress State at the End of the Nonlinear Continuum Solution: The conventional test sections (Sections 8, 9, and 10) were modeled earlier in Chapter 7 using the continuum representation for the granular layers. The geometry and the material properties used in the analysis are summarized in Figure 7.10 and Table 7.4. The results of the cross-anisotropic nonlinear analysis performed using the GT-PAVE program were given previously in Table 7.5 and in Figure 7.12. In these solutions, the horizontal tensile stresses in base were artificially eliminated using the stress transfer algorithm for no tension modifications. Figure 8.16 presents a contour plot of the horizontal stresses in the base. These stresses were obtained from the nonlinear analysis presented in Chapter 7 before the stress transfer algorithm for “no tension” modifications were applied. The complete granular base was found to be in radial tension with horizontal tensile stresses as large as 5 psi predicted in the middle section using the continuum approach. After the tension modifications were applied, the radial tensile stresses were completely eliminated in the base.

The Block Model Iterative Equilibrium Analysis: The nonlinear block model analysis of the Georgia Tech conventional test sections was carried out using the same initial material properties of the base (within the blocks) and subgrade layers as used in Chapter 7 (see Table 7.4). Figure 8.11 shows the 140 continuum element, 921 node finite element mesh used in the block analysis with 98 interface elements employed in the 8.0

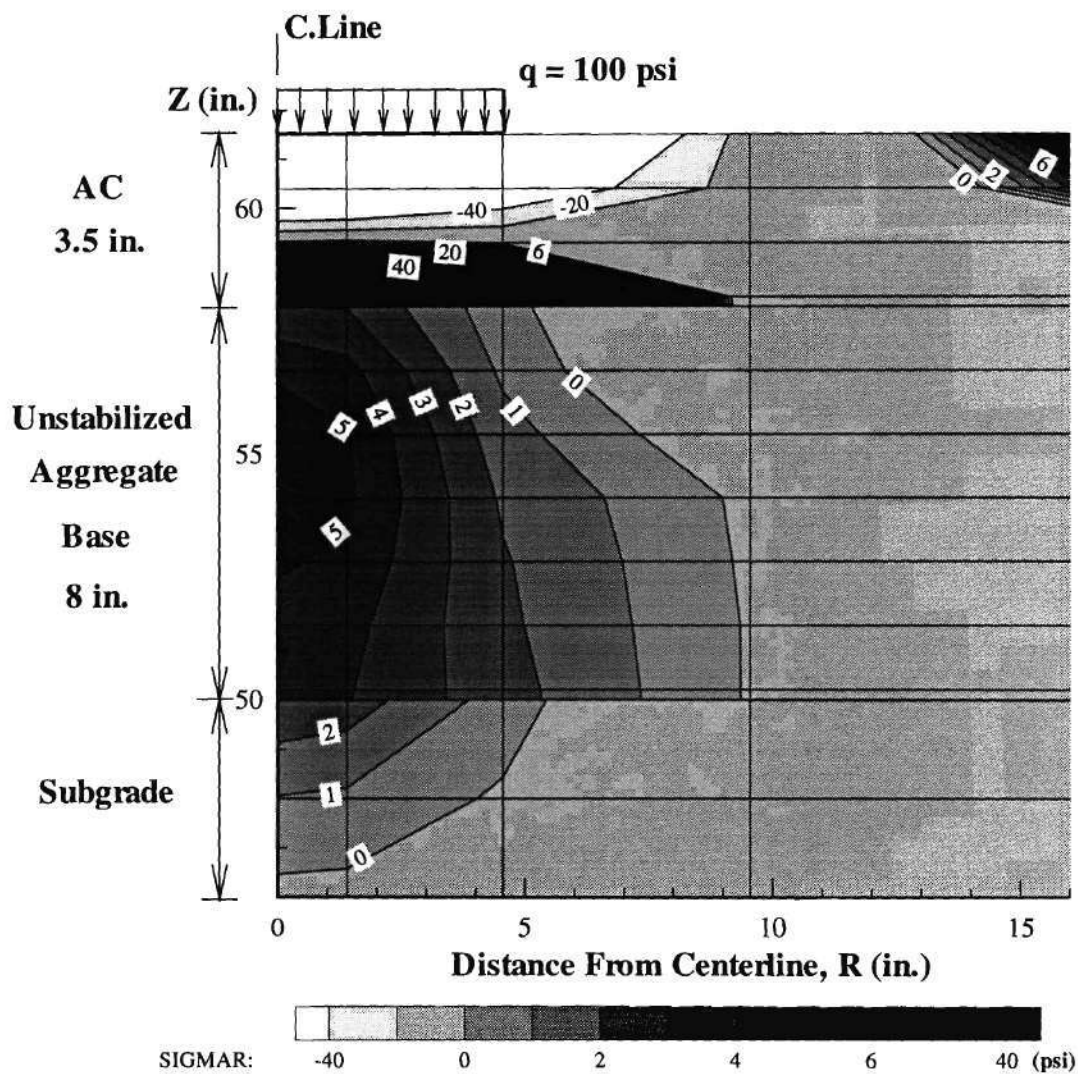


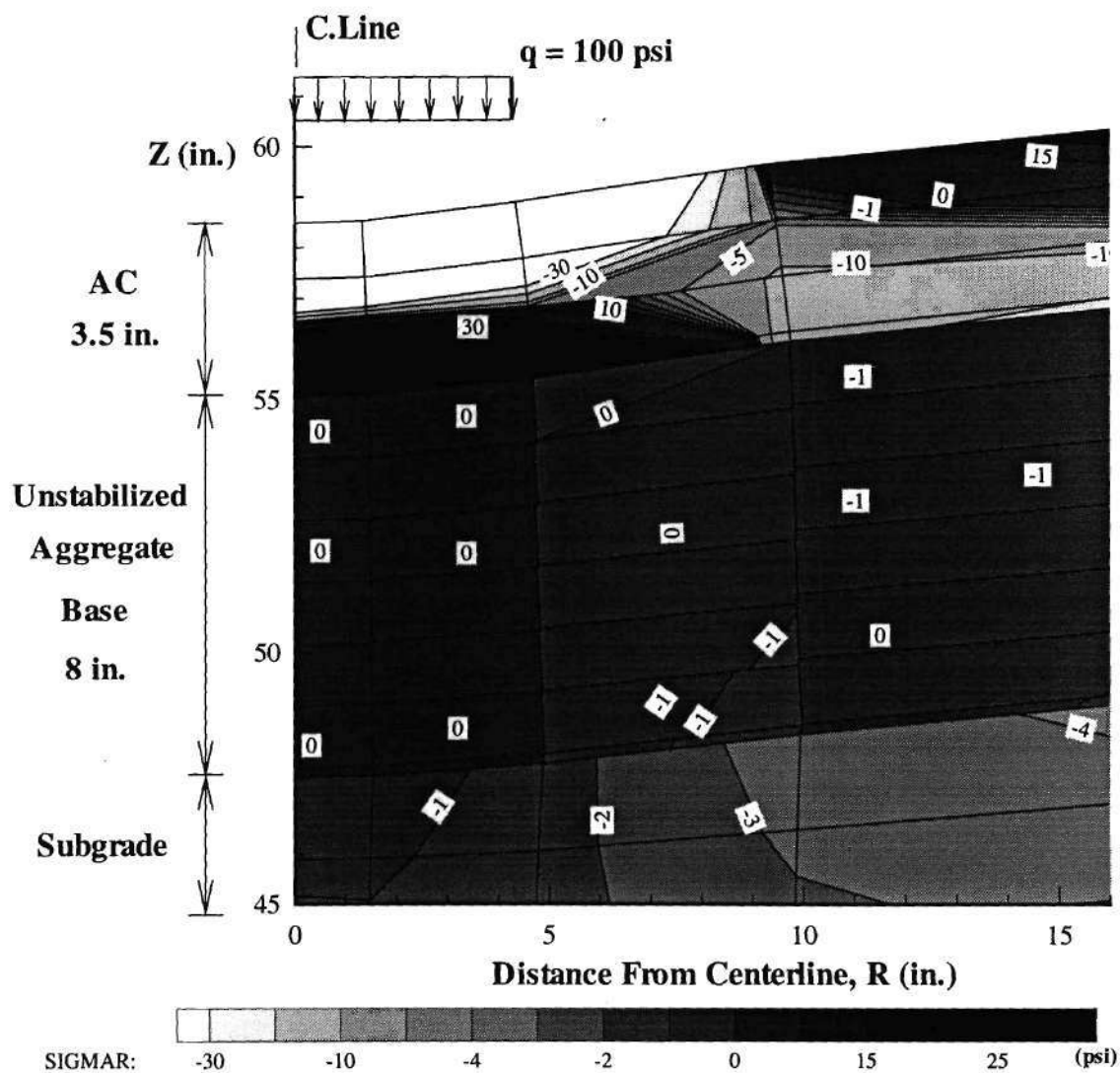
Figure 8.16. Example 3: The Variation of Radial Stresses In the Crushed Stone Base - Nonlinear Analysis Using Elastic Continuum Approach.

in. (230 mm) thick middle base layer. The iterative procedure for the block model described earlier is applied after convergence is reached for the nonlinear analysis.

In the first iteration of the block model analysis, 15 vertical interface elements were found to be in the separation mode while 15 horizontal interface elements were in slip mode. The vertical interfaces in the separation mode were assigned zero normal and shear stiffnesses and the horizontal ones in the slip mode were given 1% residual shear stiffness. The second and subsequent iterations were performed with the calculated balancing forces applied to the system as nodal loads together with the external wheel load of 100 psi (689 kPa). At the end of 5 iterations, no interface element was found to be in either the slip or separation mode and the overall equilibrium was maintained.

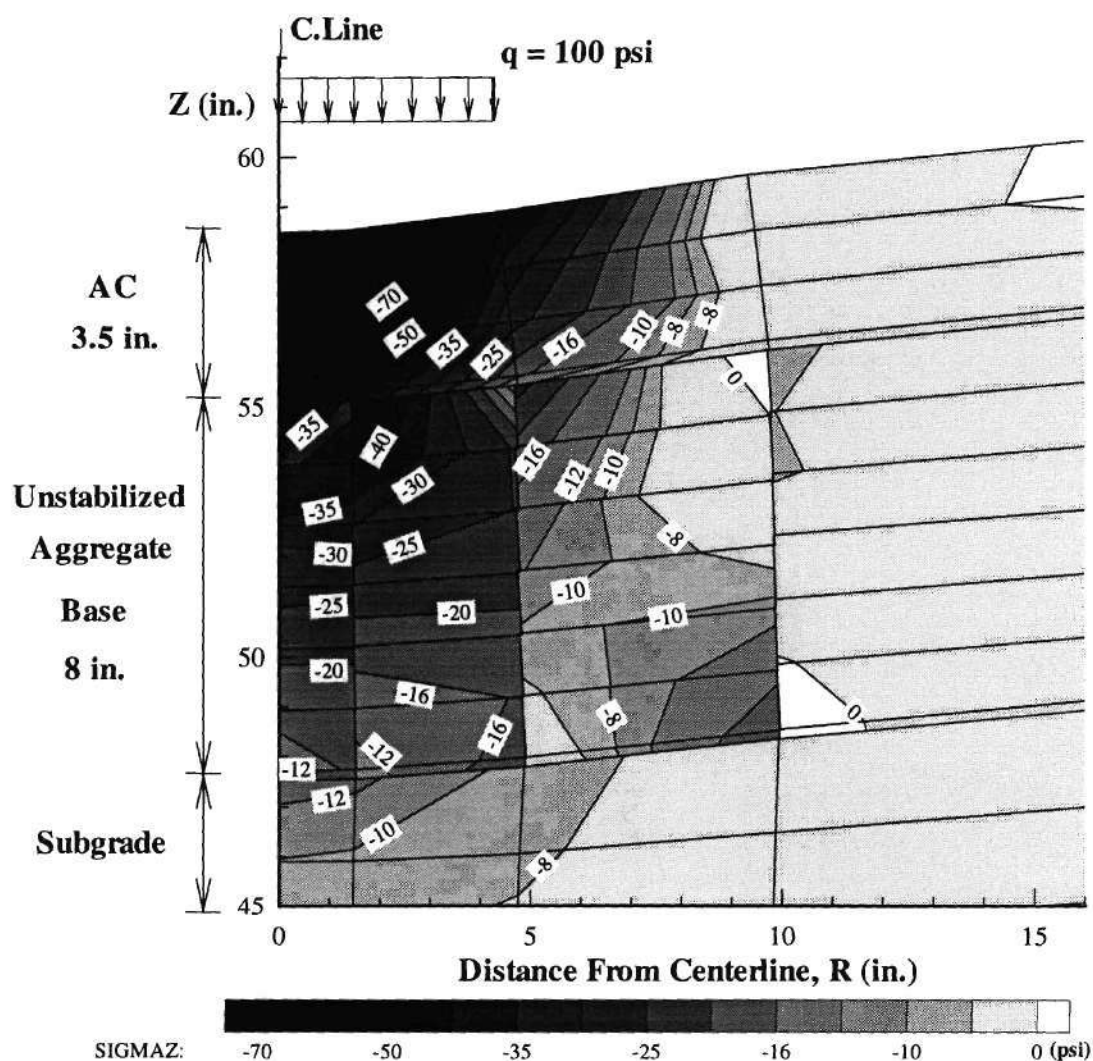
Figure 8.17 shows the contour plots of radial stresses in the top portion of the finite element mesh. The deformed mesh is plotted this time using an exaggeration factor of 100. The radial stresses shown in Figure 8.17 in the AC and subgrade were calculated at the nodes using the continuum approach. The radial stresses shown in the granular base layer were obtained from the normal stresses in the vertical interface elements. A total of 25 vertical interfaces that went into the separation mode resulted in zero radial stresses in the r - direction.

Figure 8.18 presents contours of the vertical stresses in the top portion of the mesh. The vertical stresses in the granular base were extrapolated from the interface normal stresses calculated in the horizontal interface elements. The equal stress contours are,



- Notes:** 1. Displacements are exaggerated by a factor of 100
 2. Tension is positive
 3. 1 in. = 25.4 mm, 1 psi = 6.85 kPa

Figure 8.17. Example 3: The Variation of Radial Stresses Obtained from the Vertical Interface Elements In the Crushed Stone Base.



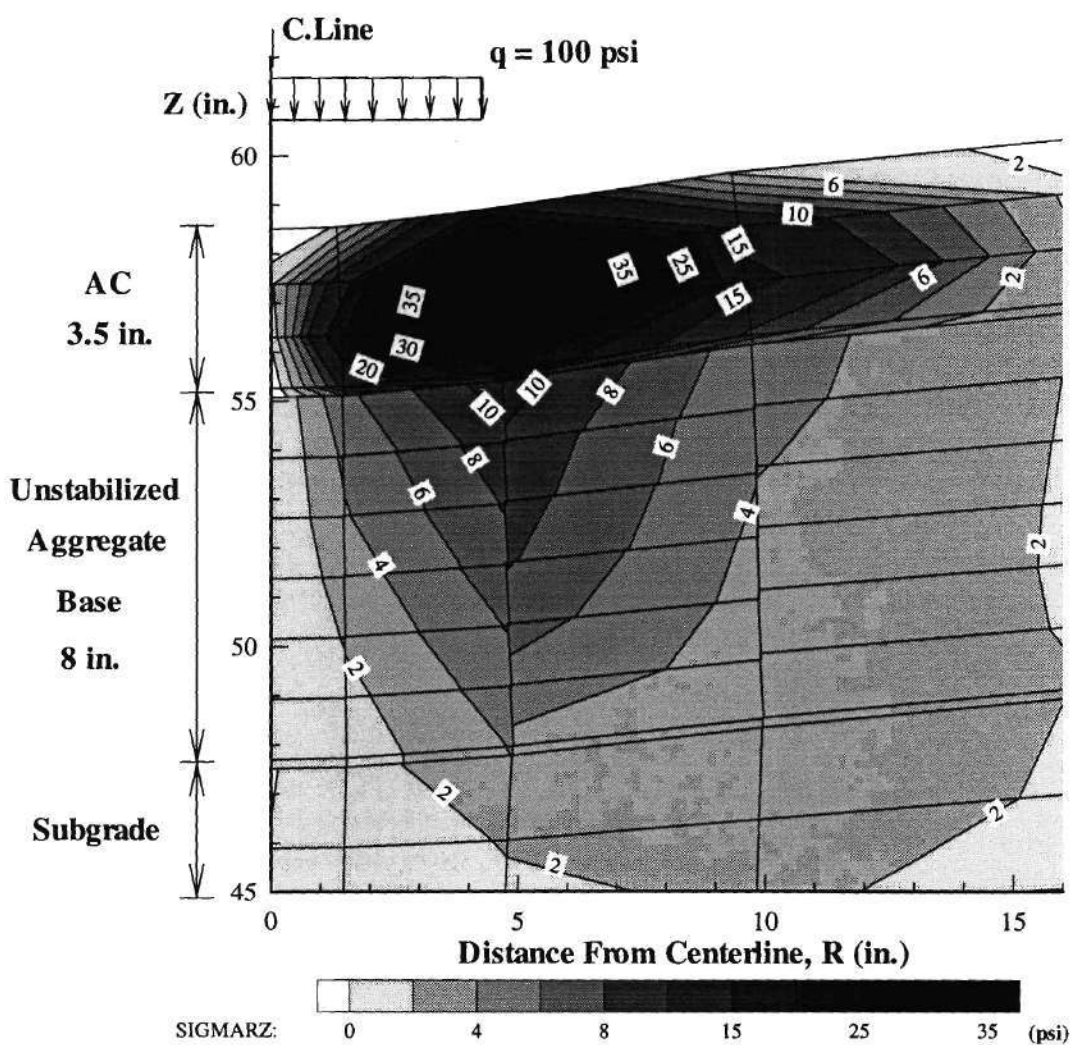
- Notes:**
1. Displacements are exaggerated by a factor of 100
 2. Tension is positive
 3. 1 in. = 25.4 mm, 1 psi = 6.85 kPa

Figure 8.18. Example 3: The Variation of Vertical Stresses Obtained from the Horizontal Interface Elements in The Crushed Stone Base.

therefore, not actually continuous in the blocks of crushed granitic gneiss. The continuity of stresses, however, is present in the subgrade and AC layers.

Due to the discontinuity between the blocks, interface stresses were non-existent in the vertical interfaces which had separated. Spreading laterally of the vertical stress from the wheel load in the base layer, therefore, did not occur in the block model. Spreading of the vertical stress did occur in the continuum representation. As a result, the vertical stress on the subgrade of the block model was predicted at the centerline to be 12.9 psi (88.9 kPa) which is higher than the measured value of 9.9 psi (68.3 kPa) as shown in Table 7.5. Similarly, the surface deflection at the centerline was computed to be 0.030 in. (0.76 mm) as compared to 0.028 in. (0.71 mm), and the horizontal tensile strain at the bottom of the AC was 554×10^{-6} in./in. when compared to the measured value of 330×10^{-6} in./in. A better geometric modeling of the discrete particle aggregate base can be achieved by using a staggered arrangement of blocks which allows better spreading of the wheel load.

Shear Resistance: Figure 8.19 presents a contour plot of the shear stresses predicted in the top portion of the finite element mesh at the end of the iterative block model equilibrium procedure. The shear stress contours shown in the crushed stone base correspond to the interface shear stresses determined at the horizontal interfaces. The shear stresses obtained from approximately 15 horizontal interface elements that experienced slip were limited to the failure shear stress values (τ_{\max}). The larger interface



- Notes: 1. Displacements are exaggerated by a factor of 100
 2. Tension is positive
 3. 1 in. = 25.4 mm, 1 psi = 6.85 kPa

Figure 8.19. Example 3: The Variation of Shear Stresses Obtained from Interface Elements In the Crushed Stone Base.

shear stresses are primarily concentrated in the upper portion of the base at a radial distance of approximately 4.55 in. (116 mm). This distance corresponds to the edge of the 100 psi (689 kPa) applied tire pressure.

A simple assembly of three spherical particles aligned and loaded vertically is shown in Figure 8.20. Under the applied normal load N , the friction forces F_1 and F_2 developed between the particles can resist the horizontal pull H applied on particle 2. The friction forces considered in this example are analogous to the shear resistance between blocks at the horizontal interfaces. The horizontal pull H then corresponds to tension load due to the predicted horizontal tensile stresses in the continuum representation of the base.

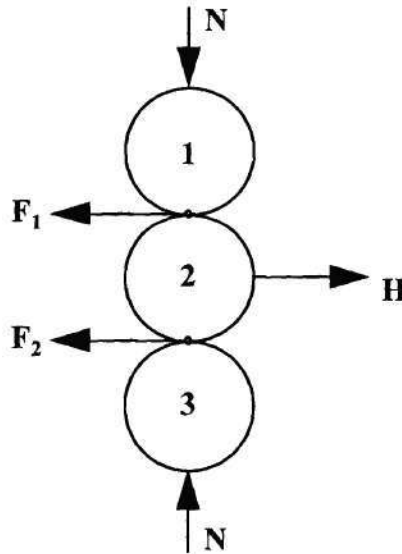
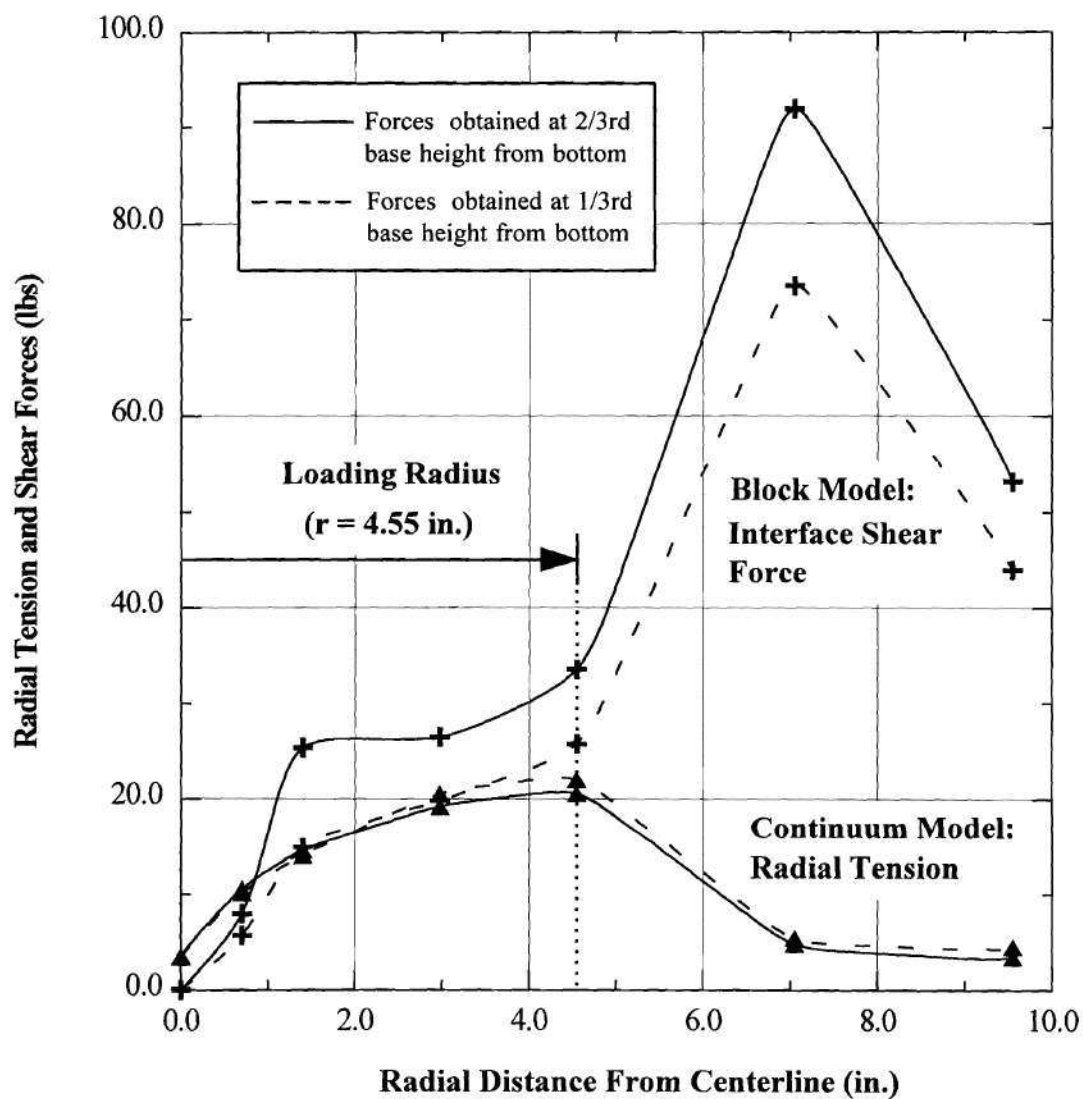


Figure 8.20. Frictional Shear Resistance Under Normal Stress in A Three Grain Assembly.

To demonstrate how shear forces developed between blocks to resist radial tension predicted in the continuum representation, the results are compared of the (1) block model and (2) “no tension” continuum approaches. (1) Using the block model, the internal shear spring forces at the interfaces are computed in the horizontal interface elements. (2) The radial tensile stresses predicted in the base layer using the continuum approach are shown in Figure 8.16. The nodal forces from the continuum solution due to these horizontal tensile stresses are calculated to obtain the tension in the horizontal direction.

Figure 8.21 shows the distribution of the radial tension forces predicted by both the “no tension” type elastic continuum and the block model at the horizontal interface nodes. Horizontal forces are plotted in the base at a height of both one-third and two-thirds above the bottom of the base. The interface shear stresses predicted at both heights in the base by the block model clearly exceed the radial tension obtained from the elastic continuum model. A maximum difference is indicated at a radial distance of 7 in. (178 mm) where the interface shear force is about 18 times larger than the tension force predicted by the continuum solution.

The most important finding from the block model analysis is that the blocks of aggregates develop very high peak shear resistance at the interfaces due to the application of large normal stress. The shear stresses are frictional forces which in turn are capable of resisting any apparent tension forces (such as those predicted by the elastic continuum solution) applied on the blocks (see Figure 8.20). Because of the development of this



Note: 1 in. = 25.4 mm; 1 lb. = 4.448 N

Figure 8.21. Example 3: Comparison of Radial Tension Force In Base from Elastic Continuum and Block Models.

shear resistance between the aggregates, flexible pavements with granular bases, therefore, do not usually fail in the field. The “no tension” problem of the continuum model is then at least partly explained by the shear resistance of unbound aggregates under vertical compressive stresses (see Figure 8.20) as demonstrated using particulate mechanics.

Comparison of the Block Model and Continuum Method: When compared to the elastic continuum approach, the block model analysis does not allow horizontal tension to develop in the unstabilized aggregate base at the block interfaces. The translation, sliding and separation of the blocks of aggregates are permitted in the model through an iterative procedure which solves for the equilibrium interactions between blocks. Load transfer in shear can, therefore, be modeled in aggregates using realistic interface friction properties between the blocks obtained from direct shear tests. On the other hand, the continuum model incorporates the stress transfer algorithm for a “no tension” type analysis which completely eliminates any predicted apparent tension in the continuum representation of the aggregate base.

Practical Findings of the Block Model Relevant to Design: The block model analysis proves that the frictional shear resistance calculated between the discrete blocks could allow an apparent limiting tension to be taken by the assembly of aggregates. This apparent tension is analogous to the tensile stresses predicted by the classical elastic

continuum approaches that do not use the “no tension” type analysis. For all practical design purposes, it is then of no use to have methods, such as the stress transfer method, which completely eliminate these tensile stresses. The continuum approach may well be adequate in most cases to design a flexible pavement provided that the tensile stresses predicted in the lower portion of the base are smaller than failure values. The failure stresses could, for example, be obtained from comparison charts, such as shown in Figure 8.21, that give the maximum amount of apparent tension permitted by the frictional resistance in the block interfaces. Residual compaction stresses, if known or measured, should also be included in the analyses.

Summary

A new block model approach was introduced for modeling granular bases in flexible pavements. The block model employs blocks of aggregates to approximately model the load transfer mechanisms of the real particulate nature of granular materials. The block model was proposed as an alternative method to investigate tension carrying ability of granular bases. The unbound aggregate bases were modeled as particulate media composed of blocks of aggregates which are able to transfer both shear and normal compressive loads through the interfaces. The modeling was achieved by using 6-node interface elements between the 8-node continuum elements in the finite element mesh.

The GT-PAVE program organization and subroutines related to the block model option were described and the interface element behavior was studied in detail.

The main purpose of applying the block model to granular bases was to realistically predict using a practical model the particulate nature of aggregate behavior and then explain in a rational way why unbound bases do not fail. It was shown that granular bases can take relatively large amounts of apparent horizontal tension in the form of shear resistance between aggregate particles subjected to vertical stresses. The classical elastic continuum solution of a granular base, therefore, may not include a "no tension" type analysis provided that the apparent horizontal tension do not exceed the frictional shear resistance between blocks of aggregates. Applying block model to the granular bases of Georgia Tech conventional test sections, the shear forces at the horizontal block interfaces were found to be the largest for radial distances greater than the radius of the wheel load. The vertical stress on the subgrade and other response variables were, however, overestimated by the block model due to the lack of spreading of the wheel load through the vertical interfaces.

CHAPTER IX

CONCLUSIONS AND RECOMMENDATIONS

Conclusions

A theoretical and analytical study was undertaken in this thesis to develop an improved analysis method for calculating the performance of flexible pavements with granular bases. Mathematical finite element formulations limited to resilient response were presented to analyze the pavement system when subjected to external wheel loads. Two different models were included in the GT-PAVE nonlinear finite element program developed for the current state of the art analysis of the unbound materials. These nonlinear methods are based upon a continuum approach and a new block model approach which permits modeling of the granular layers as discrete blocks of aggregates. To more correctly model flexible pavement behavior, the following essential features were included in the GT-PAVE program within the framework of the elastic continuum approach: (1) nonlinear behavior of granular bases and subgrade soils through elastic constitutive behavior laws, (2) cross-anisotropic representation of the granular materials, (3) incremental loading, (4) the compaction induced residual stresses, and (5) "no

tension” modifications. The block model approach models the real particulate nature of the granular media enabling translation, sliding and separation of the blocks in the base. The block model offers a new insight into the long abandoned “no tension” problem encountered in granular layers.

A new neural network model of the resilient modulus of granular materials was also proposed using laboratory measured results for different aggregate types. This modeling of the resilient modulus behavior is believed to be the first use of artificial neural networks (ANN) in granular material characterization. The neural network model was shown to quite accurately predict resilient modulus from a known stress state for a specific material type. The ANN model, however, memorized the data sets for different aggregate types and categorized each material according to its material properties such as dry unit weight, percent fines, and aggregate size. A larger experimental database is needed to correctly train a more generalized ANN model which would work for different aggregate types having various material properties.

The GT-PAVE program was verified using both theoretical examples and measured results of laboratory and full-scale tests. The theoretical verification consisted of a separate analysis of the various components of the method such as the cross-anisotropic formulation and convergence of nonlinear analysis. The results of the linear elastic computations compared quite well with the closed form solutions as well as with the results of other computer programs. Measured response from laboratory tests and full-scale flexible pavement test sections provided a second verification of the program.

The resilient behavior of five pavement test sections were predicted **at the same time** reasonably accurately for up to 8 response variables (i.e., displacements, stresses and strains) using a cross-anisotropic nonlinear analysis. Such predictions are hard to achieve and indicate the finite element model used is reasonably valid.

The general limitations of the finite element formulation presented include no provision to consider the dynamic inertia effects due to the moving traffic loads. Instead, a static analysis is performed for practical purposes to simulate wheel load. Special care should be given to the possibility of amplification of the computed response variables in a resonance condition. Resonance could occur, for example, when a shallow subgrade depth to bedrock exists. Other limitations of the program include: (1) neglecting viscoelastic AC layer behavior by using linear elastic material properties which assume that the loading time is relatively short and the stress levels on the pavement are small, (2) assuming small-displacement theory is valid, (3) solving only axisymmetric problems, and (4) neglecting the effects of dilation of granular particles at block interfaces. The present formulation implemented in the GT-PAVE finite element program, however, is considered to be an improvement of the current analysis methods for multilayered elastic pavement systems with granular layers.

The following specific conclusions can be made:

1. Simplified resilient modulus models, such as the Uzan (1985) and UT-Austin (Pezo, 1993) models consider both confinement and shear stress effects in granular

materials. These models were found to give sufficiently accurate results for pavement design and are also practical enough for routine design use.

2. A hardening type of granular material resilient behavior was fitted nicely using the Uzan (1985) model. As a result, a direct secant stiffness approach for nonlinear analysis adapted here in the program was found to be a more efficient method compared to the Newton-Raphson and tangent stiffness approaches.

3. To converge smoothly for each load increment in the nonlinear analysis, a damping factor of 0.3, as defined in the thesis, was employed to obtain an improved estimate of the resilient modulus to be used as the initial estimate in the next load increment.

4. A convergence criterion of a 5% maximum individual error was adapted between any two resilient moduli calculated in two subsequent nonlinear iterations. The 5% criterion mainly controlled convergence rather than the cumulative error criterion. This criterion was adequate for the required accuracy of the computed pavement response.

5. A cross-anisotropic representation of the base was shown to reduce the horizontal tension in the granular base by up to 75%. Use of 15% of the vertical modulus in the horizontal direction was found by trial and error to be necessary for: (1) predicting correctly the horizontal and vertical measured strains in the base layers, and (2) properly modeling the horizontal tension in the granular base layer.

6. An iterative tension modification procedure using the modified stress transfer approach was successfully adapted in the continuum model for the fast elimination of the horizontal tension in the base. The tensile stresses in the granular layer are balanced in this method by applying counteracting forces at the nodes.
7. Observed hardening type of resilient response of laboratory granular samples was successfully predicted at different stress levels using the incremental nonlinear procedure adapted in the program.
8. Compaction induced residual stresses in the base were shown to affect both the linear and nonlinear solutions by mainly reducing the amount of radial tension predicted in the granular layer. The effect of residual stresses was more prominent in the cross-anisotropic base.
9. The resilient behavior of 5 well instrumented full-scale pavement test sections were successfully predicted using the GT-PAVE program for up to 8 measured response variables, such as displacements, stresses and strains. A nonlinear cross-anisotropic analysis was found to be necessary for predicting at the same time these 8 variables thus validating the GT-PAVE program. The good predictions were unaffected when the "no tension" stress transfer approach was applied for eliminating tensile stresses in the granular base of the conventional test sections.
10. The vertical and horizontal resilient modulus distributions within the base and subgrade layers were shown to be highly nonlinear both vertically and radially.

11. The block model employed in granular layers used realistic properties obtained from direct shear tests to model the particulate media. Horizontal tension was not allowed to develop at the block interfaces. The load transfer in granular materials was shown to be done by shear and normal compressive stresses at block interfaces since tensile stresses can not occur.

12. The granular base of the conventional test sections was modeled using the block model approach. The frictional shear forces calculated in the horizontal block interfaces were found to be at least equal to or greater than the horizontal tension forces predicted by the continuum model.

13. The vertical stress on the subgrade and other critical response variables were overestimated by the block model due to the lack of spreading of the wheel load through the vertical interfaces. This deficiency needs be solved by offsetting blocks in a staggered arrangement.

14. The interface behavior formulated analytically must be verified by laboratory experiments for further improvements in the model.

Practical Findings:

15. Inverted pavement sections were found to make optimum use of the compressive characteristics of the unbound aggregate base when the base is sandwiched between a lower cement stabilized subbase and an upper AC surfacing.

16. A 6 in. (152 mm) unbound aggregate base and a 6 to 8 in. (152 to 203 mm) thick cement stabilized subbase were found by theoretical analyses to give a practical inverted section design which minimizes tensile strain in AC and vertical stress on the subgrade.

17. An inverted section and a conventional section having the same total cost give different performances as predicted using the GT-PAVE program. For equal AC thicknesses greater than 5.1 in. (130 mm), the inverted sections performed better than the conventional sections. Fatigue life was about 30% greater and subgrade stress was 10% less than for the conventional sections.

18. Applying block model to Georgia Tech conventional test sections, frictional shear resistance calculated in the granular base between the discrete blocks allowed an apparent limiting tension which was taken by the assembly of aggregates. This apparent tension is analogous to the tensile stresses predicted by the classical elastic continuum approach that do not use a "no tension" type analysis.

19. For all practical design purposes, it is probably not necessary to employ tension correction methods, such as the stress transfer approach, which completely eliminate predicted tensile stresses in granular bases. The continuum approach may well be adequate in most cases to design a flexible pavement provided that the tensile stresses predicted in the lower portion of the base do not exceed frictional resistance of aggregates under the compressive wheel load.

Recommendations for Future Work

The GT-PAVE finite element program developed in this thesis can be verified and further improved with additional work undertaken in the following research areas:

1. Measurements of several response variables need to be obtained from other well-instrumented experimental pavement sections to validate and improve the current analytical finite element model.
2. To determine realistic cross-anisotropic material properties to be assigned in the analysis, laboratory testing of pavement materials should be performed under various loading conditions.
3. Appropriate models should be researched and included in the analysis to model the viscoelastic asphalt concrete behavior.
4. Resilient behavior modeling of unbound materials using artificial neural networks (ANN) should be further investigated as a potential source for improvements in the area of material characterization. A successful implementation of a general ANN model into finite element computations can be quite beneficial in the future provided that a large database is used in the training of the model.
5. The block model proposed in this thesis should be verified by laboratory testing of aggregate blocks to show that the shear resistance and interlocking between

aggregates is responsible for any horizontal tension predicted in the granular bases. Improvements for the block model can be achieved by accounting for dilation of granular materials at the interfaces.

6. Better modeling of the base can be achieved using the block model when smaller blocks are considered in a staggered arrangement.

7. Large displacement and elastoplastic analysis can be included in the mathematical formulation for the continuum and block models. Permanent deformations can also be modeled for damage analysis in pavements. For example, plasticity models, such as the Cam-Clay model, can be considered for a cohesive subgrade soil in which consolidation effects are also included.

8. A soil fabric system can be included in the axisymmetric formulations where geosynthetics are used in the layered system as reinforcements. The soil-fabric model can be used to study fabric behavior at the interfaces, both the fabric and interface elements in the formulation.

APPENDIX A

RESILIENT MODULUS DATA FOR POTENTIAL ARTIFICIAL NEURAL NETWORK VARIABLES

Table A.1. GT Resilient Modulus Data For Potential ANN Variables

GT-BASES

(B#: Base #, B: Regular Gradation, F: Full Gradation,
C: Coarse Gradation, R: Replaced Gradation, S#: Sample #)

Sample Name:	B1BFS1	B1BFS2	B1CRS1	B1CRS2	B1BRS1	B1BRS2
Max. Aggregate Size, (in.):	1.5	1.5	2.5	2.5	1.5	1.5
Avg. Aggregate Size, D50 (in.):	0.25	0.25	0.35	0.35	0.35	0.35
Coefficient of Uniformity, Cu:	30	30	61	61	61	61
Dry Unit Weight (pcf.)						
Average:	143	143	143	143	143	143
Lab Result:	142.5	140.6	132.9	131.9	140.7	139.9
Water Content (%)						
Average:	5	5	5	5	5	5
Lab Result:	6.1	6.7	8.2	5.9	4.7	5.7
% Fines Content:	4	4	4	4	4	4
% Compaction of T-180:	100	100	100	100	100	100
Plasticity Index, (%):	-	-	-	-	-	-

Confining Pressure (psi)	Deviator Stress (psi)	Bulk Stress (psi)	MEASURED RESILIENT MODULUS (psi)					
3	3	12	19017.3	25751.7	21358.3	21603.5	19197.5	18545.3
3	6	15	22875.6	27789.4	22733.8	21804.2	20718.8	20893.5
3	9	18	24451.2	30649.7	23880	22450.6	22407.8	20897.4
5	5	20	24573.5	31062.5	22652.7	23754.5	23383.9	21571.6
5	10	25	29454.6	35176.3	29098.7	25719.5	26745.4	24891.8
5	15	30	33757	36834.4	30067.2	26703.5	27344.4	26031.4
10	10	40	42172	49737.3	39070.1	30228	36341.2	34897.6
10	20	50	45386.9	51574.2	42330	36135.2	37860.6	35381.3
10	30	60	46231.5	50181.4	43912.7	37231.7	38573.2	39684.8
15	10	55	50144.6	54730.9	44651.6	39485.9	43061	43091.1
15	15	60	49369.3	55582.8	46494.7	39971.8	43348.7	42271.6
15	30	75	56136.8	60698	50963.3	44180.8	48355.6	49135.9
20	15	75	59705	64644.5	55590.2	48928.8	54644.4	53311
20	20	80	61469.9	64246	55546.5	48285.2	53400.7	52541.6
20	40	100	65475.3	69820.9	60950.3	52467	57468	56697.2

Table A.1(cont'd). GT Resilient Modulus Data For Potential ANN Variables

GT-BASES

(B#: Base #, B: Regular Gradation, F: Full Gradation,
C: Coarse Gradation, R: Replaced Gradation, S#: Sample #)

Sample Name:	B2FS1	B2FS2	B2RS1	B2RS2	B4S5	B4S6
Max. Aggregate Size, (in.):	1.25	1.25	1.25	1.25	0.75	0.75
Avg. Aggregate Size, D50 (in.):	0.1	0.1	0.1	0.1	0.1	0.1
Coefficient of Uniformity, Cu:	67	67	67	67	73	73
Dry Unit Weight (pcf.)						
Average:	141.3	141.3	141.3	141.3	142.2	142.2
Lab Result:	138.7	136.9	138.5	138.5	130.3	136.65
Water Content (%)						
Average:	5.1	5.1	5.1	5.1	4.1	4.1
Lab Result:	6.7	5.1	3.9	3.9	5.63	5.75
% Fines Content:	10	10	10	10	-	-
% Compaction of T-180:	100	100	100	100	95	95
Plasticity Index, (%):	-	-	-	-	5	5

Confining Pressure (psi)	Deviator Stress (psi)	Bulk Stress (psi)	MEASURED RESILIENT MODULUS (psi)					
3	3	12	23221	31065	27460	29009	23555	26277.2
3	6	15	26261	30330	32143	31412	23083	27465.6
3	9	18	26858	32117	33050	32516	22986	26865.2
5	5	20	30534	36794	36824	34864	32426	32064.6
5	10	25	33901	38150	39644	38707	29805	32015.4
5	15	30	35374	40587	41392	39588	30579	32035.9
10	10	40	45927	53591	55049	51705	46884	47486.8
10	20	50	48064	53835	56194	52973	44796	47051.8
10	30	60	48380	53191	56030	52077	44052	47204.6
15	10	55	52998	57107	60072	55566	55551	58508.6
15	15	60	54724	58774	63603	56016	55732	56745.1
15	30	75	57146	64796	68799	62665	57787	59098.9
20	15	75	63992	69593	76123	69613	67753	72273
20	20	80	63535	69588	75343	67582	67929	71155.5
20	40	100	67444	72173	77558	70093	67088	71233.7

Table A.2. SHRP Resilient Modulus Data For Potential ANN Variables

SHRP BASES

Sample Name:	26A	26B	51A	51B	148A	148B
Max. Aggregate Size, (in.):	1.5	1.5	1.5	1.5	1.5	1.5
Avg. Aggregate Size, D50 (in.):	0.48	0.48	0.4	0.4	0.47	0.47
Coefficient of Uniformity, Cu:	40	40	14	14	42	42
Dry Unit Weight (pcf.)						
Average:	138.6	138.6	138.6	138.6	138.6	138.6
Lab Result:	140.6	138.9	135.4	138.5	141.8	138.8
Water Content (%)						
Average:	6	6	6	6	6	6
Lab Result:	6.4	4.8	5.5	5.5	5.4	5.7
% Fines Content:	3	3	1.5	1.5	2	2
% Compaction of T-180:	100	100	100	100	100	100
Plasticity Index, (%):	-	-	-	-	-	-

Confining Pressure (psi)	Deviator Stress (psi)	Bulk Stress (psi)	MEASURED RESILIENT MODULUS (psi)					
3	3	12	22201	20033	18568	16071	25461	21593
3	6	15	21886	21977	19947	16044	25846	25567
3	9	18	27977	22549	26059	21154	27563	25859
5	5	20	25521	23558	29684	23356	33086	33022
5	10	25	31963	28088	30740	23884	33483	30040
5	15	30	31347	26739	33261	24775	34672	32329
10	10	40	38997	32211	42781	32268	46227	45291
10	20	50	39552	38349	43157	33884	46027	46603
10	30	60	39505	36143	42737	35076	45386	46508
15	10	55	44939	41938	48828	38079	52966	50547
15	15	60	44108	41400	49100	37789	53226	51396
15	30	75	46224	46815	51325	47660	53475	55088
20	15	75	55695	50239	56071	41781	64299	61792
20	20	80	52664	51465	57078	46462	61324	62212
20	40	100	56380	52670	61010	51939	64440	65860

Table A.2 (cont'd.). SHRP Resilient Modulus Data For Potential
ANN Variables

SHRP BASES

Sample Name:	173A	173B	178A	178B	196A	196B
Max. Aggregate Size, (in.):	1.5	1.5	1.5	1.5	1.5	1.5
Avg. Aggregate Size, D50 (in.):	0.42	0.42	0.38	0.38	0.38	0.38
Coefficient of Uniformity, Cu:	21	21	11	11	21	21
Dry Unit Weight (pcf.)						
Average:	133.6	133.6	133.6	133.6	138.6	138.6
Lab Result:	133.5	136	130.7	134.1	139.8	138.4
Water Content (%)						
Average:	8	8	8	8	6	6
Lab Result:	8.1	6.1	8.9	11.7	5.1	5.4
% Fines Content:	0.3	0.3	0.1	0.1	0.2	0.2
% Compaction of T-180:	100	100	100	100	100	100
Plasticity Index, (%):	-	-	-	-	-	-

Confining Pressure (psi)	Deviator Stress (psi)	Bulk Stress (psi)	MEASURED RESILIENT MODULUS (psi)					
3	3	12	36118	35587	29811	21646	30519	39382
3	6	15	30505	31763	25153	30533	30191	40118
3	9	18	31192	30504	25021	28703	31198	28967
5	5	20	35590	35845	28348	22666	33599	40951
5	10	25	39356	36507	29040	26256	34731	32853
5	15	30	40560	39102	35705	31045	35510	34893
10	10	40	56202	51548	39136	41548	44405	54439
10	20	50	56057	52468	48659	47348	45646	55587
10	30	60	54962	53845	48640	45588	45622	55875
15	10	55	59967	63020	51243	49278	51790	61923
15	15	60	59618	64009	51254	51188	50777	62917
15	30	75	63643	64462	60359	54805	56407	66667
20	15	75	72354	75560	55907	64097	62438	69249
20	20	80	74021	76528	66787	63081	59605	70718
20	40	100	97820	79189	70493	67541	63643	75347

Table A.2 (cont'd.). SHRP Resilient Modulus Data For Potential
ANN Variables

SHRP BASES

Sample Name:	197A	197B	202A	202B
Max. Aggregate Size, (in.):	1.75	1.75	1.5	1.5
Avg. Aggregate Size, D50 (in.):	0.4	0.4	0.36	0.36
Coefficient of Uniformity, Cu:	39	39	47	47
Dry Unit Weight (pcf.)				
Average:	133.6	133.6	133.6	133.6
Lab Result:	-	132.7	131.6	132.7
Water Content (%)				
Average:	8	8	8	8
Lab Result:	-	7.5	9.8	8.2
% Fines Content:	2	2	2	2
% Compaction of T-180:	100	100	100	100
Plasticity Index, (%):	-	-	-	-

Confining Pressure (psi)	Deviator Stress (psi)	Bulk Stress (psi)	MEASURED RESILIENT MODULUS (psi)			
3	3	12	27917.8	26849	30113.2	29957
3	6	15	30935.9	24793.3	25808.9	28172.4
3	9	18	30228.5	23976	27339	27852.2
5	5	20	33374.2	30167.5	30483.5	28099.8
5	10	25	32646	29426	28978.4	31810.6
5	15	30	34275	31554.2	31561.3	29733.3
10	10	40	46857.1	37428.3	41654.6	40556
10	20	50	48215.8	39184.1	44672.9	43427.1
10	30	60	49719	39734.6	57625.1	41331.8
15	10	55	55312.1	43581	51196.4	56395.4
15	15	60	55500	45416.9	46497.4	55453.1
15	30	75	60250.3	51302	63315.6	59317.8
20	15	75	69164.4	56845.7	58769.7	68280.1
20	20	80	69493.6	57566.5	85412.2	66174
20	40	100	73479	69903.4	75128.3	64238.4

Table A.3. NC Resilient Modulus Data For Potential ANN Variables

NC BASES

(Sample A: MR After 50 Repetitions,
Sample B: MR After 100 Repetitions)

Sample Name:	10F3S1A	10F3S1B	10F3S2A	10F3S2B
Max. Aggregate Size, (in.):	1.5	1.5	1.5	1.5
Avg. Aggregate Size, D50 (in.):	0.25	0.25	0.25	0.25
Coefficient of Uniformity, Cu:	33	33	33	33
Dry Unit Weight (pcf.)				
Average:	151.1	151.1	151.1	151.1
Lab Result:	145.6	145.6	148.3	148.3
Water Content (%)				
Average:	3.5	3.5	3.5	3.5
Lab Result:	4.17	4.17	6.75	6.75
% Fines Content:	5	5	5	5
% Compaction of T-180:	100	100	100	100
Plasticity Index, (%):	-	-	-	-

Confining Pressure (psi)	Deviator Stress (psi)	Bulk Stress (psi)	MEASURED RESILIENT MODULUS (psi)			
3	3	12	41832.8	40142.8	22726.1	23670.6
3	6	15	33170.7	33317.8	22304.3	22348.2
3	9	18	32977.9	32548.7	22922	23134.7
5	5	20	46911.4	44988.7	25306.6	25575.9
5	10	25	40708.4	39662	28187.8	27893.1
5	15	30	39259.2	40832.5	30158.4	28963.7
10	10	40	64399.4	59527.6	39881.6	39649.1
10	20	50	58416	58491.9	41890.7	41771
10	30	60	60858.2	60653.7	43443.5	42983.4
15	10	55	74482.9	74127.3	50846.2	50843.8
15	15	60	74554.2	70763.5	49925.8	49470.5
15	30	75	75559.3	74988.2	54005.9	51461.4
20	15	75	91727.4	89994.5	60481.1	60662.5
20	20	80	83723.7	83277.4	59303.3	59008.8
20	40	100	88875.4	89459	64324.8	63220

Table A.3 (cont'd). NC Resilient Modulus Data For Potential
ANN Variables

NC BASES

(Sample A: MR After 50 Repetitions,
Sample B: MR After 100 Repetitions)

Sample Name:	20F3S2A	20F3S2B	30F3S2A	30F3S2B
Max. Aggregate Size, (in.):	1.5	1.5	1.5	1.5
Avg. Aggregate Size, D50 (in.):	0.25	0.25	0.25	0.25
Coefficient of Uniformity, Cu:	28	28	40	40
Dry Unit Weight (pcf.)				
Average:	149.7	149.7	149.7	149.7
Lab Result:	148.5	148.5	147.9	147.9
Water Content (%)				
Average:	5.6	5.6	5.6	5.6
Lab Result:	6.7	6.7	8.1	8.1
% Fines Content:	5	5	5	5
% Compaction of T-180:	100	100	100	100
Plasticity Index, (%):	-	-	-	-

Confining Pressure (psi)	Deviator Stress (psi)	Bulk Stress (psi)	MEASURED RESILIENT MODULUS (psi)			
3	3	12	24314.1	25003.3	27567.6	27065
3	6	15	22152.3	22057	25830.4	26125.4
3	9	18	22815.7	22668.7	26958	26768
5	5	20	29916.5	29789.8	28400.3	28385.4
5	10	25	27097.2	27588.9	30010.6	29903.6
5	15	30	29676.1	30453.8	30962.8	30710.2
10	10	40	41382.3	41333.6	38943.6	41060.3
10	20	50	41481.8	42633.2	42265.9	41200.4
10	30	60	44721.6	44851.6	41666	41795.6
15	10	55	51442.6	52748.3	47454.3	47573.7
15	15	60	52188.9	51765.3	47951.8	48100.5
15	30	75	55614.2	54970.3	50881.7	50589.7
20	15	75	62691.4	61298.3	57422.9	56807.2
20	20	80	60278.5	60217.3	55397.7	55611.9
20	40	100	63515.9	63646.7	60226.1	59830.6

APPENDIX B

GT-PAVE NONLINEAR FINITE ELEMENT PROGRAM

Input and Output Capabilities

The GT-PAVE finite element program requires as the input information the geometry, material properties, loading and boundary conditions, analysis type (linear or nonlinear), interface properties, and nonlinear analysis and tension modification parameters. The default values of units used in the GT-PAVE program are pounds, inches, and degrees Fahrenheit. Any consistent system of units, however, can be used in the analysis. The dimensional units F=force, L=length and ($^{\circ}$)=degrees are given in parentheses for the variables. The following steps present the detailed information that must be entered in a data file for each input category:

(a) Geometry:

Number of elements, nodal points, boundary points, and interface elements;

Number of zones for rectangular mesh generation,

For each zone: number of layers, number of columns, initial node number,

r and z coordinates of the initial node (L), initial element number, layer and column spacings (L);

(b) Material Properties:

Number of material types,

For each material type: specify if isotropic or cross-anisotropic,

(i) *isotropic*: resilient modulus (F/L^2), Poisson's ratio, coefficient of thermal expansion ($1/^\circ$), and unit weight (F/L^3),

(ii) *cross-anisotropic*: vertical resilient modulus (F/L^2), horizontal resilient modulus (F/L^2), vertical shear modulus (F/L^2), vertical Poisson's ratio, horizontal Poisson's ratio, thermal expansion coefficient ($1/^\circ$), unit weight (F/L^3);

For cross-anisotropic analyses, default values can be used in the granular bases.

Sublayering of the nonlinear layers is also suggested to input correct initial guesses.

(c) Loading Conditions:

Concentrated nodal point loads (F) and gravity loads (as the unit weight, F/L^3),

Temperature loads: constant temperature change ($T_f - T_i$) ($^\circ F$) creating initial strains,

Distributed edge loads: constant pressure (F/L^2),

Horizontal residual compaction stresses: initial stresses in granular layer (F/L^2);

(d) Boundary Conditions:

For each boundary node: support conditions (fixed or free) in r and z directions,
specified support settlements (L) in r and z directions;

(e) Analysis Type:

Linear or nonlinear elastic analysis:

Asphalt concrete (AC) layer taken only as linear elastic,
Continuum or block model employed in granular base layer;

(f) Interface Properties:

For the block model approach:

Normal and shear subgrade modulus (F/L^3) used in interface elements,
cohesion (F/L^2) and angle of friction ($^\circ$) of the unbound aggregates in base;

(g) Nonlinear Analysis:

Number of load increments for the gravity and the surface wheel loadings, moduli averaging coefficients (the damping factors λ) used for the gravity and surface wheel loadings, horizontal modulus reduction coefficient (n) used when tension is observed in granular bases,

For nonlinear bases and subgrades: model selection and model parameters;

(h) No Tension or Equilibrium Analysis:

For continuum approach: optional usage of modified stress transfer tension
modification approach (Doddihall and Pandey, 1984),

limiting tensile strength (F/L^2) of granular materials

(default value has been set at 0.1 psi, 0.689 kPa.),

For block model approach: shear stiffness reduction coefficient for slip,

number of maximum iterations for block equilibrium.

The output capabilities of the GT-PAVE program give a complete state of stress, strain and deformation of the finite element model. The program first prints the input information to an user specified output file for verification purposes. Then, the following information is printed for each load increment both on the screen and in the output file during the execution of the program:

The results of nonlinear iterations: iteration number, maximum individual error

and element number, maximum cumulative error,

convergence messages;

The results of tension/equilibrium iterations: iteration number, number of interface

elements in slip and separation; convergence

messages.

Finally, the computed output response variables are printed in the output file. The results of the analysis include by default the following:

- (i) the displacements of the nodal points,
- (ii) the stresses and strains calculated at the center of the elements,
- (iii) the principal stresses and strains at the center of the elements,

- (iv) the stresses and strains averaged at the nodes,
- (v) the maximum and minimum summary of the strains and stresses, and
- (vi) the interface stresses and strains if granular base has been modeled using the block model approach.

By specifying the element numbers in the input file, the stresses and strains calculated at the nodes in each element can also be printed in the output file. This option is best to use for the elements at the layer interfaces since the averaged nodal response values could be erroneous for the nodes shared by two neighboring layers.

A separate output file has been reserved in the GT-PAVE program for the fast output data visualization of the pavement sections using the Tecplot software (Amtec Engineering Inc., Bellevue, WA, 1993). The computed total displacements are printed in the first zone of this output file together with the geometry of the finite element mesh. The stresses and strains obtained at the integration points in each pavement layer are then printed in separate data zones to make possible the interpolation of the results on the nodes of the complete finite element mesh. The final output file, therefore, becomes automatically generated at the end of the GT-PAVE program run to be input into the Tecplot software. The results can then be easily visualized in the form of the deformed mesh and contour plots for different response variables such as vertical or radial stresses.

REFERENCES

- AASHTO T99-90. (1990). The Moisture Density Relations of Soils Using a 5.5-lb. [2.5 kg] Rammer and a 12-in. [305 mm] Drop. Standard Specifications for Transportation Materials and Methods of Sampling and Testing, 15th ed. American Association of State Highway and Transportation Officials, Washington, D.C., pp. 226-230.
- AASHTO T180-90. (1990). The Moisture Density Relations of Soils Using a 10-lb. [4.54 kg] Rammer and an 8-in. [457 mm] Drop. Standard Specifications for Transportation Materials and Methods of Sampling and Testing, 15th ed. American Association of State Highway and Transportation Officials, Washington, D.C., pp. 455-459.
- AbTech Corporation. (1992). AIM - User's Manual. AbTech Corporation, Charlottesville, VA.
- Ahlvin, R.G. and Ulery, H. H. (1962). Tabulated Values for Determining the Complete Pattern of Stresses, Strains and Deflections Beneath A Uniform Circular Load on A Homogeneous Half Space. Bulletin 342, Highway Research Board, pp. 1-13.
- Alba, J. L. (1993). *Laboratory Determination of Resilient Modulus of Granular Materials for Flexible Pavement Design*, Ph.D. Thesis, Georgia Institute of Technology, School of Civil and Environmental Engineering, December.
- Allaart, A. P. (1992). *Design Principles for Flexible Pavements - A Computational Model for Granular Bases*. Ph.D. Thesis, Delft Technical University, Delft, Netherlands.
- Amtec Engineering. (1993). Tecplot Data Visualization Software - User's Manual. Amtec Engineering, Inc., Bellevue, WA.
- The Asphalt Institute. (1982). Research and Development of the Asphalt Institute's Thickness Design Manual (MS-1). 9th Edition, Research Report 82-2., Asphalt Institute.
- Barden, L. (1963). Stresses and Displacements in A Cross-Anisotropic Soil. Geotechnique, September, p. 198 .

Barksdale, R. D., Robnett, Q., Lai, J., and Zeevaert, A. E. (1982). Experimental and Theoretical Behavior of Geotextile Reinforced Aggregate Soil Systems. Proceedings, 2nd International Conference on Geotextiles, Vol. 2, Las Vegas, pp. 375-380.

Barksdale, R. D., and Todres, H. A. (1983). A Study of Factors Affecting Crushed Stone Base Performance. Final Report, Georgia Institute of Technology Report SCEGIT-82-109, Atlanta, GA.

Barksdale, R. D. (1984). Crushed Stone Base Performance. In Transportation Research Record 954, TRB, National Research Council, Washington, D.C., pp.78-87.

Barksdale, R. D., Brown, S. F. and Chan, F. (1989). Potential Benefits of Geosynthetics in Flexible Pavements. NCHRP Report 315, Transportation Research Council, Washington D.C.

Barksdale, R. D. and Itani, S. Y. (1989). Influence of Aggregate Shape on Base Behavior. In Transportation Research Record 1227, TRB, National Research Council, Washington, D.C., pp. 173-182.

Barksdale, R. D. and Alba, J. L. (1993). Laboratory Determination of Resilient Modulus For Flexible Pavement Design. Interim Report No. 2, Prepared for NCHRP, Transportation Research Board, National Research Council, Washington, D.C.

Bathe, K. J. and Wilson, E. L. (1976). *Numerical Methods in Finite Element Analysis*. Prentice Hall, Inc., Englewood Cliffs, NJ.

Beer, G. (1985). An Isoparametric Joint/Interface Element for Finite Element Analysis. International Journal for Numerical Methods in Engineering, Vol. 21, pp. 585-600.

Borowicka, H. (1943). Pressure Distribution in a Halfspace with A Linearly Varying Modulus of Elasticity. *Ingenieur-Archiv*, 14 (2), pp. 75.

Boulanger, R. W., Bray, J D., Chew, S. H., Seed, R. B., Mitchell, J. K., and Duncan, J. M. (1991). SSCOMPPC: A Finite Element Analysis for Evaluation of Soil-Structure Interaction and Compaction Effects. Geotechnical Engineering Report No. UCB/GT/91-02, Department of Civil Engineering, University of California, Berkeley, April.

Boussinesq, J. (1885). Application des potentiels a l'etude de l'equilibre et du Mouvement des Solids Elastiques, Gauthier-Villars, Paris.

Boyce, J. R. (1976). *The Behavior of A Granular Material Under Repeated Load*. Ph.D. Thesis, University of Nottingham, Department of Civil Engineering, May., 174 pp.

Boyce, J. R. (1980). A Nonlinear Model for the Elastic Behavior of Granular Materials Under Repeated Loading. International Symposium on Soils Under Cyclic and Transient Loading, Swansea.

Broms, B. (1971). Lateral Earth Pressure Due to Compaction of Cohesionless Soils. Proceedings, 4th Budapest Conference on Soil Mechanics and Foundation Engineering, pp. 373-383.

Brown, S. F. and Pell, P. S. (1967). An Experimental Investigation of the Stresses, Strains and Deflections in a Layered Pavement Structure Subjected to Dynamic Loads. Proceedings, 2nd International Conference on the Structural Design of Asphalt Pavements, Ann Arbor, MI, pp. 487-504.

Brown, S. F. (1979). The Characterization of Cohesive Soils for Flexible Pavement Design. Proceedings, 7th European Conference on Soil Mechanics and Foundation Engineering, Vol. 2, pp. 15-22.

Brown, S. F., Pappin, J. W., and Brodrick, B. V. (1980). Permanent Deformation of Flexible Pavements. Final Report, European Research Office, U.S. Army, Univ. of Nottingham, England.

Brown, S. F. and Pappin, J. W. (1981). Analysis of Pavements with Granular Bases. In Transportation Research Record 810, TRB, National Research Council, Washington D.C., pp. 17-23.

Brown, S. F., Loach, S. C. and O'Reilly, M. P. (1987). Repeated Loading of Fine Grained Soils. Contractor's Report CR 72. U.K. Transport and Road Research Laboratory, Crawthorne, Berkshire, England.

Brunton, J. M. and De Almeida, J. R. (1992). Modeling Material Nonlinearity in a Pavement Backcalculation Procedure. In Transportation Research Record 1377, TRB, National Research Council, Washington D.C., pp. 99-106.

Burmister, D. M. (1943). The Theory of Stresses and Displacements in Layered Systems and Applications to the Design of Airport Runways. Proceedings, Highway Research Board, Vol. 23, pp. 126-144.

Burmister, D. M. (1945). The General Theory of Stresses and Displacements in Layered Soil Systems. Journal of Applied Physics, Vol. 16, pp. 84-94, 126-127, 296-302.

- Chan, F., Barksdale, R. D. and Brown, S. F. (1989). Aggregate Base Reinforcement of Surfaced Pavements. *Geotextiles and Geomembranes* 8, Elsevier Applied Science, pp. 165-189.
- Chang, C. S. (1988). Micromechanical Modeling of Constitutive Equation for Granular Material. *Micromechanics of Granular Materials*, M. Satake and J. K. Jenkins, eds., Elsevier, Amsterdam, The Netherlands, pp. 271-278.
- Chang, C. S., Chang, Y., and Kabir, M. G. (1992). Micromechanics Modeling for Stress-Strain Behavior of Granular Soils, I: Theory. *Journal of Geotechnical Engineering*, Vol. 118, No. 12, December, pp. 1959-1974.
- Chen, W. F. and Lui, E. M. (1987). *Structural Stability - Theory and Implementation*. Elsevier Science Publishing Co., Inc., New York, NY.
- Claussen, A. I. M., Edwards, J. M., Sommer, P., and Uge, P. (1977). Asphalt Pavement Design - The Shell Method. Proceedings, 4th International Conference on the Structural Design of Asphalt Pavements, Vol. 1, pp. 39-74.
- Clough, G. W. and Duncan, J. M. (1969). Finite Element Analyses of Port Allen and Old River Locks. Geotechnical Engineering Report, TE-69-3, Department of Civil Engineering, University of California, Berkeley, September.
- Cook, R. D., Malkus, D. S., and Plesha, M. E. (1989). *Concepts and Applications of Finite Element Analysis*. Third Edition, John Wiley and Sons, New York, NY.
- Crockford, W. W., Bendana, L. J., Yang, W. S., Rhee, S. K., and Senadheera, S. P. (1990). Modeling Stress and Strain States in Pavement Structures Incorporating Thick Granular Layers. Final Report, The Texas Transportation Institute, College Station, Texas, April, pp. 57-71.
- Cundall, P. A. and Strack O. D. L. (1979). A Discrete Numerical Model for Granular Assemblies. *Geotechnique*, Vol. 29, p. 47.
- Dantu, P., (1957). Contribution a l'Etude Mechanique et Geometrique des Milieux Pulverulents. Proceedings, 4th International Conference on Soil Mechanics, Vol. 1, London, UK.
- Dehlen, G. L. (1969). *The Effect of Nonlinear Material Response on the Behavior of Pavements Subjected to Traffic Loads*. Ph.D. Thesis, University of California, Berkeley.

De Jong, D. L., Peatz, M. G. F., and Korswagen, A. R. (1973). Computer Program Bisar, Layered Systems Under Normal and Tangential Loads, Konin Klijke Shell-Laboratorium, Amsterdam, External Report AMSR.0006.73.

Deresiewicz, H. (1958). Stress-Strain Relations for A Simple Model of A granular Medium. Journal of Applied Mechanics, Transactions of ASME, 25(3), pp. 402-406.

Desai, C. S. (1974). Numerical Design-Analysis for Piles in Sands. Journal of Geotechnical Engineering, ASCE, Vol. 100, No. GT6, June.

Desai, C. S., Zaman, M. M., Lightner, J. G., and Siriwardane H. J. (1984). Thin Layer Element for Interfaces and Joints. International Journal for Numerical and Analytical Methods in Geomechanics, Vol. 8, pp. 19-43.

Digby, P. J. (1981). The Effective Elastic Moduli of Porous Granular Rock. Journal of Applied Mechanics, Transactions of ASME, 48(4), pp. 803-808.

Dobry, R., Ng, T. T., and Petrakis, E. (1989). Deformation Characteristics of Granular Soil In the Light of Particulate Mechanics. Proceedings, 14th Conference on Geotechnics, Italian Geotechnical Association, Torino, November 28-30, 1989.

Doddihal, S. R. and Pandey, B. B. (1984). Stresses In Full Depth Granular Pavements. In Transportation Research Record 954, TRB, National Research Council, Washington D.C., pp. 94-100.

Dormon, G. M. and Metcalf, C. T. (1965). Design Curves for Flexible Pavements Based on Layered System Theory. Highway Research Record 71, Highway Research Board, pp. 69-84.

Duffy, J. and Mindlin, R. D. (1957). Stress-Strain Relations and Vibrations of Granular Media. Journal of Applied Mechanics, Transactions of ASME, 24(4), pp. 585-593.

Duncan, J. M., Monismith, C. L. and Wilson, E. L. (1968). Finite Element Analyses of Pavements. In Highway Research Record 228, TRB, National Research Council Washington D.C., pp. 18-33.

Duncan, J. M. and Seed, R. B. (1986). Compaction-Induced Earth Pressures Under K0-Conditions. Journal of Geotechnical Engineering, ASCE, Vol. 112, No. 1, pp. 1-21.

Ellis, G. W., Yao, C., and Zhao, R. (1992). Neural Network Modeling of the Mechanical Behavior of Sand. Proceedings, 9th Conference on Engineering Mechanics, College Station, Texas, pp. 421-424.

Feliberti, M. (1991). *Critical Evaluation of Parameters Affecting Resilient Modulus Tests on Subgrades*. M.S. Thesis, University of Texas at El Paso (UTEP), Department of Civil Engineering, November.

Felt, E. J., and M. S. Abrams. (1957). Strength and Elastic Properties of Compacted Soil-Cement Mixtures. ASTM Special Technical Publication, No. 206, pp. 152-173.

FHWA, Soil Stabilization In Pavement Structures - A User's Manual. (1979). Vol. I and II. Federal Highway Administration, Office of Development Implementation Division. Report FHWA-IP-80-2.

FHWA, Highway Statistics, (1990). Federal Highway Administration, Superintendent of Documents, U.S. Government Printing Office, Washington, D.C. 20402.

Foinquinos, R., Roesset, J. M., and Stokoe, K. H., II. (1994). Response of Pavement Systems to Dynamic Loads Imposed by Nondestructive Tests. Preprint No. 940678, 73rd Annual Meeting of the Transportation Research Board, Washington, D.C.

Foster, C. R., and Ahlvin, R. G. (1958). Development of Multiple-Wheel CBR Design Criteria. Journal of the Soil Mechanics and Foundations Division, ASCE, Vol. 84, No. SM2, May, pp. 1647-1 to 1647-12.

Galjaard, P. J. and Allaart, A. P. (1989). Mechanicabeschouwing van de relatie tussen laboratorium - en in situ stijfheden van ongebonden wegenbouwmaterialen. Report 7-89-209-11. Road and Railroad Research Laboratory, Delft University of Technology.

Gerard, C. M. and Mulholland, P. (1966). Stress-Strain and Displacement Distributions in Cross-Anisotropic and Two-Layer Isotropic Elastic Systems. Proceedings, 3rd Conference of Australian Road Research Board, Part 2, p. 1123.

Ghaboussi, J., Wilson, E. L., and Isenberg, J. (1973). Finite Element for Rock Joints and Interfaces. Journal of Soil Mechanics and Foundations Division, ASCE, Vol. 99, SM10.

Ghaboussi, J. (1988). Fully Deformable Discrete Element Analysis Using A Finite Element Approach. Computers and Geotechnics, Vol. 5, No. 3, pp. 175-195.

Ghaboussi, J., Garrett, J. H., and Wu, X. (1991). Knowledge-Based Modeling of Material Behavior with Neural Networks. Journal of Engineering Mechanics, Vol. 117, No. 1, pp. 132-153.

Golub, G. H. and Van Loan, C. F. (1989). *Matrix Computations*. Second Edition, The Johns Hopkins University Press, Baltimore, MD.

Goodman, R. E., Taylor, R. L., and Brekke, T. L. (1968). A Model for the Mechanics of Jointed Rocks. Journal of Soil Mechanics and Foundations Division, ASCE, Vol. 94, SM3.

Goodman, R. E., and Shi, G. H. (1981). Geology and Rock Slope Stability - Application of A "Keyblock" Concept for Rock Slopes. Proceedings, Third International Conference on Stability in Surface Mining, Vancouver, B.C., pp. 347-373.

Goodman, R. E., and Shi, G. H. (1985). *Block Theory and Its Application to Rock Engineering*. Edited by William J. Hall, Prentice-Hall, Inc., Englewood Cliffs, NJ, 07632.

Goodman, R. E., and Shi, G. H. (1989). Generalization of Two-Dimensional Discontinuous Deformation Analysis for Forward Modeling. International Journal for Numerical and Analytical Methods in Geomechanics, Vol. 13, No. 4, July-August, pp. 359-380.

Hadley, O. W. (1991). Material Characterization and Inherent Variation Analysis of Soil-Cement Field Cores. In Transportation Research Record 1295, TRB, National Research Council Washington, D.C., pp. 23-36.

Harichandran, R. S., Yeh, M. S. and Baladi, G. Y. (1989). MICH-PAVE: A Nonlinear Finite Element Program for Analysis of Pavements. In Transportation Research Record 1286, TRB, National Research Council, Washington D.C., pp. 123-131.

Hertz, J., Krogh A., and Palmer R. G. (1991). *Introduction to the Theory of Neural Computation*. Addison-Wesley, Reading, MA.

Heukelom, W. and Klomp, A. J. G. (1962). Dynamic Testing as A Means of Controlling Pavements During and After Construction. Proceedings, 1st International Conference on the Structural Design of Asphalt Pavements, pp. 667-685.

Hicks, R. G. (1970). *Factors Influencing the Resilient Properties of Granular Materials*. Ph.D. Thesis, University of California, Berkeley.

Hicks, R. G. and Monismith, C. L. (1971). Factors Influencing the Resilient Properties of Granular Materials. In Transportation Research Record 345, TRB, National Research Council, Washington D.C., pp. 15-31.

Holl, D. L. (1941). Plane Strain Distribution of Stress in Elastic Media. Iowa Engineering Experimentation Station Bulletin, pp. 148-163.

Hornik, K., Stinchcombe, M., and White, H. (1989). Multilayer Feedforward Networks are Universal Approximators. Neural Networks, 2, pp. 359-366.

Huang, Y. H. (1968). Stresses and Displacements in Nonlinear Soil Media. Journal of the Soil Mechanics and Foundations Division, ASCE, Vol. 94, No. SM1, pp. 1-19.

Huang, Y. H. (1993). *Pavement Analysis and Design*. 1st Edition, Prentice Hall, Englewood Cliffs, NJ, 805 pp.

Hwang, D. and Witczak, M. W. (1979). Program DAMA (Chevron) User's Manual. Department of Civil Engineering, University of Maryland, MD.

Ingold, T. S. (1979). The Effect of Compaction on Retaining Walls. Geotechnique, 29, No. 3, pp. 265-283.

Itani, S. Y. (1990). *Behavior of Base Materials Containing Large-Sized Particles*. Ph.D. Thesis, Georgia Institute of Technology, School of Civil and Environmental Engineering, September, 329 pp.

Jenkins, J. T. (1987). Volume Change in Small Strain Axisymmetric Deformations of A Granular Material. *Micromechanics of Granular Materials*, M. Satake and J. K. Jenkins, eds., Elsevier, Amsterdam, The Netherlands, pp. 143-152.

Jones, R. (1966). Measurement of Elastic and Strength Properties of Cemented Materials in Road Bases. In Highway Research Record 128, HRB, National Research Council, Washington, D.C., pp. 101-111.

Jouve, P., Martinez, J., Paute, J. L., and Ragneau, E. (1987). Rational Model for Flexible Pavements Deformations. Sixth International Conference on the Structural Design of Asphalt Pavements, Ann Arbor, MI.

Kasianchuk, D. A. (1968). *Fatigue Considerations in the Design of Asphalt Concrete Pavements*. Ph.D. Thesis, University of California, Berkeley, August.

Katona, M. G. (1983). A Simple Contact-Friction Interface Element with Applications to Buried Culverts. International Journal for Numerical and Analytical Methods in Geomechanics, Vol. 7, pp. 371-384.

Kirwan, R. W. and Glynn, T. E. (1969). Experimental and Theoretical Investigation of Pavement Deflections. Technical Report to the European Office, US Army, by Trinity College, Dublin.

Kirwan, R. W. and Snaith, M. S. (1975). Further Investigations Towards A Rational Method of Design for Flexible Pavements, Part II. Final Technical Report to the European Office, US Army, by Trinity College, Dublin.

Kopperman, S., Tiller, G., and Tseng, M. (1986). ELSYM5, Interactive Microcomputer Version, User's Manual. Report No. FHWA-TS-87-206, Federal Highway Administration, Washington, D.C.

Lister, N. W. and Powell, W. D. (1987). Design Practice for Bituminous Pavements in the United Kingdom. Proceedings, Sixth International Conference on the Structural Design of Asphalt Pavements, Vol. 1, pp. 220-231.

Loach, S. C. (1987). *Repeated Loading of Fine Grained Soils for Pavement Design*. Ph.D. Thesis, University of Nottingham, Department of Civil Engineering, Nottingham, UK.

Love, A. E. H. (1944). *A Treatise on the Mathematical Theory of Elasticity*. Fourth Edition, Dover Publications, New York, NY, pp. 643.

Makhlouf, H. and Stewart, J. J. (1967). Elastic Constants of Cubical-Tetrahedral and Tetragonal Sphenoidal Arrays of Uniform Spheres. Proceedings, International Symposium of Wave Propagation and Dynamic Properties of Earth Materials, ASCE, New York, NY, pp. 825-837.

Mamlouk, M. S. and Davies, T. G. (1984). Elastodynamic Analysis of Pavement Deflections. Journal of Transportation Engineering, ASCE, Vol. 110, No. 6, pp. 536-550.

Mamlouk, M. S. (1987). Dynamic Analysis of Multilayer Pavement Structures - Theory, Significance and Verification. Proceedings, Sixth International Conference on the Structural Design of Asphalt Pavements, Vol. 1, pp. 466-474.

May, R. W. and Witczak, M. W. (1981). Effective Granular Modulus to Model Pavement Responses. In Transportation Research Record 810, TRB, National Research Council, Washington D.C., pp. 1-9.

Mayhew, H. C. (1983). Resilient Properties of Unbound Roadbase Under Repeated Triaxial Loading. Transport and Road Research Laboratory, LR 1088.

Meier, R. W. (1995). *Backcalculation of Flexible Pavement Moduli from Falling Weight Deflectometer Data Using Artificial Neural Networks*. Ph.D. Thesis, Georgia Institute of Technology, School of Civil and Environmental Engineering, Atlanta, March.

Meier, R. and Rix, G. J. (1994). Backcalculation of Flexible Pavement Moduli Using Artificial Neural Networks. In Transportation Research Record 1448, TRB, National Research Council, Washington D.C., pp. 75-82.

Monismith, C. L., Sousa, J., and Lysmer, J. (1988). Modern Pavement Technology Including the Dynamic Loading Conditions. Vehicle/Pavement Interaction, Where the Truck Meets the Road, SP-765, Society of Automotive Engineers, Inc., pp. 33-52.

Oda, M. (1974) A Mechanical and Statistical Model of Granular Materials. Soils and Foundations, Vol. 14, Japanese Society of Soil Mechanics and Foundation Engineering,

Odemark, N. (1949). Undersoknig av Elasticitetegenskaperna hos Olika Jordarter Samt Teori for Berakning av Belagningar Enligt Elasticitetsteorin. Statens, Vaginstitut, Meddelande 77.

Okuda, H., Miyazaki, H., and Yagawa, G. (1994). Neural Network Modeling of Viscoplastic Material Behaviors. Advanced Computer Applications, ASME Pressure Vessels Piping Division Publications, Vol. 274, ASME New York, NY, pp. 141-145.

Pappin, J. W. (1979). *Characteristics of A Granular Material for Pavement Analysis*. Ph.D. Thesis, University of Nottingham, Nottingham, UK.

Penumadu, D. (1993). *Strain Rate Effects in Pressuremeter Testing and Neural Network Approach for Soil Modeling*. Ph.D. Thesis, Georgia Institute of Technology, School of Civil and Environmental Engineering, Atlanta, May.

Pezo, R. F. (1993). A General Method of Reporting Resilient Modulus Tests of Soils - A Pavement Engineer's Point of View. Paper No: 93082, Transportation Research Board, 72nd Annual Meeting, National Research Council, Washington D.C.

Pidaparti, R. M. and Palakal, M. J. (1993). Material Model for Composites Using Neural Networks. AIAA Journal, Vol. 31, No. 8, pp. 1533-1535.

Raad, L. and Figueroa, J. L. (1980). Load Response of Transportation Support Systems. Transportation Engineering Journal, ASCE, Vol. 16, No. TE1, pp. 111-128.

Rauhut, J. B. and Kennedy, T. W. (1982). Characterizing Fatigue Life of Asphalt Concrete Pavements. In Transportation Research Record 888, TRB, National Research Council, Washington D.C.

Rosenblatt, F. (1958). The Perceptron: A Probabilistic Model for Information Storage and Organization in the Brain. Psychological Review 65, pp. 386-408.

Round, D. J. (1976). *The Solution of Load/Deformation Behavior of A Discrete Particle Material by Digital Computer*. Ph.D. Thesis, University of Nottingham, Nottingham, UK.

Rumelhart, D. E., Hinton, G. E., and Williams, R. J. (1986). Learning Internal Representation by Error Propagation. *Parallel Distributed Processing: Explorations in the Microstructures of Cognition*, D. E. Rumelhart and J. L. McClelland (Eds.), MIT Press, Cambridge, MA, pp. 318-362.

Selig, E. T. (1987). Tensile Zone Effects on Performance of Layered Systems. Geotechnique, Vol. 37, No. 3. pp. 247-254.

Seridi, A., and Dobry, R. (1984). An Incremental Elastic-Plastic Model for the Force-Displacement Relation at the Contact Between Elastic Spheres. Research Report, Department of Civil Engineering, Rensselaer Polytechnic Institute, Troy, NY.

Shifley, L. H. (1967). *The Influence of Subgrade Characteristics on the Transient Deflections of Asphalt Concrete Pavements*. Ph.D. Thesis, University of California, Berkeley.

Shook, J. F., Finn, F. N., Witzak, M. W., and Monismith, C. L. (1982). Thickness Design of Asphalt Pavements - The Asphalt Institute Method. Proceedings, 5th International Conference on the Structural Design of Asphalt Pavements, Vol. 1, pp. 17-44.

SHRP Protocol P-46 (1993). Resilient Modulus of Granular Base/Subbase Materials and Subgrade Soils. Strategic Highway Research Program, SHRP-LAPP Laboratory Material Testing Guide, June.

Snyman, M. F. and Martin, J. B. (1992). A Consistent Formulation of A Dilatant Interface Element. International Journal for Numerical and Analytical Methods in Geomechanics, Vol. 16, pp. 493-527.

Stewart, E. H., Selig, E. T., and Norman-Gregory, G. H. (1985). Failure Criteria and Lateral Stresses in Track Foundations. In Transportation Research Record 1022, TRB, National Research Council, Washington D.C., pp. 59-64.

Stock, A. F., Brown, S. F., Pell, P. S. (1979). Analysis of Structural Performance of Flexible Pavements. Report No. AFS/3, Asphalt and Coated Macadam Association, University of Nottingham, Nottingham, UK.

Sweere, G. T. H., Penning, A., and Vos, E. (1987). Development of A Structural Design Procedure for Asphalt Pavements with Crushed Rubble Base Courses. Sixth International Conference on the Structural Design of Asphalt Pavements, Ann Arbor, MI.

Syriopoulos, N. and Barksdale, R. D. (1985). Shear Strength of Rock Discontinuities in Georgia. Final Report, prepared for Georgia Mining and Resources Institute, Research Project E20-501, School of Civil and Environmental Engineering, Georgia Institute of Technology, Atlanta, October.

Thom, N. H. (1988). *Design of Road Foundations*. Ph.D. Thesis, University of Nottingham, Department of Civil Engineering, May, 307 pp.

Thompson, M. R. and Elliot R. P. (1985). ILLI-PAVE Based Response Algorithms for Design of Conventional Flexible Pavements. In Transportation Research Record 1043, TRB, National Research Council, Washington D.C., pp. 50-57.

Timoshenko, S. P. and Goodier, J. N. (1970). *Theory of Elasticity*. Third Edition, McGraw-Hill Book. Co., New York, NY.

Ullidtz, P. (1995). Stresses and Strains in A Two-Dimensional Particulate Material. Paper No: 950142, Transportation Research Board, 74th Annual Meeting, National Research Council, Washington D.C.

Uzan, J. (1985). Characterization of Granular Materials. In Transportation Research Record 1022, TRB, National Research Council, Washington D.C., pp. 52-59.

Walton, K. (1987). The Effective Elastic Moduli of A Random Packing of Spheres. Journal of Mechanical of Physics of Solids, 35(3), pp. 213-226.

Wang, B., and Garga, V. K. (1991). Block-Spring Model for Analyzing Discontinuous Rocks. Proceedings, 44th Canadian Geotechnical Conference, Part 1 (of 2), Calgary, Alberta, September 29 - October 2, 1991.

Warren, H. and Dieckman, W. L. (1963). Numerical Computation of Stresses and Strains in A Multiple-Layer Asphalt Pavement System. International Report, Chevron Research Corporation, Richmond, CA.

Wasserman, P. D. (1989). *Neural Computing: Theory and Practice*. Van Nostrand Reinhold, New York, NY,

Williams, R. I. T. (1972). Properties of Cement Stabilized Materials. The Journal of the Institution of Highway Engineers, Vol. 19, No. 2, pp. 5-19.

Witczak, M. W. and Uzan, J. (1988). The Universal Airport Pavement Design System, Report I of V: Granular Material Characterization. University of Maryland, Department of Civil Engineering, MD.

Zeevaert, A. E. (1980). *Finite Element Formulation for the Analysis of Interfaces, Nonlinear and Large Displacement Problems in Geotechnical Engineering*. Ph.D. Thesis, Georgia Institute of Technology, School of Civil and Environmental Engineering, September.

Zeilmaker, J, and Henny, R. J. (1989). The Measurement of Residual Stresses Due to Compaction in Granular Materials. Proceedings of the International Symposium on Unbound Aggregates on Roads (UNBAR3), April, Unbound Aggregates in Roads, Edited by R. H. Jones and A. R. Dawson, Part of Reed International Publishing, UK.

Zienkiewicz, O. C., Cheung, Y. K., and Stagg, K. G. (1966). Particular Reference to Problems of Rock Mechanics. Journal of Strain Analysis, Vol. 1, No. 2, pp. 172-182.

Zienkiewicz, O. C., Valliappan, S. and King, I. P. (1968). Stress Analysis of Rock as a "No Tension" Material. Geotechnique 18, pp. 56-66.

Zienkiewicz, O. C. (1970). Analysis of Nonlinear Problems in Rock Mechanics with Particular Reference to Jointed Rock Systems. Proceedings, 2nd Congress of the International Society for Rock Mechanics, Belgrade.

Zienkiewicz, O. C. and Taylor, R. L. (1989). *The Finite Element Method*. Volume 1, Basic Formulation and Linear Problems, 4th Edition, McGraw Hill Book Co. (UK) Limited.

VITA

Erol Tutumluer was born on April 28, 1967 in Istanbul, Turkey. He completed his secondary studies at Kadikoy Anadolu Lisesi in Istanbul in 1985, and obtained his Bachelor of Science degree in Civil Engineering from Bogazici University in July, 1989.

In 1989, he started his graduate studies at Duke University, Durham, NC where he received his first Master of Science degree in Civil Engineering in May, 1991. During his master program at Duke University he worked under the supervision of Dr. Tomasz Hueckel for projects funded by ISMES Spa., a geotechnical engineering company in Bergamo, Italy. The MS thesis written was on the nonlinear elastic effects in overconsolidated clays. He co-authored with Dr. Tomasz Hueckel two papers which were published from this work.

In 1991, Erol Tutumluer started his Ph.D. studies at Georgia Institute of Technology in geotechnical engineering. He worked as a research assistant in the School of Civil and Environmental Engineering supervised by Dr. Richard D. Barksdale. In 1993, he received his second MS degree in Civil Engineering at Georgia Tech. He has been involved with modeling of flexible pavements with granular bases for his Ph.D. Erol published two papers with Dr. Barksdale and made 3 professional presentations in both national and international conferences. For his contribution to teaching at Georgia Tech as an instructor, Erol received the Outstanding Teaching Assistant Award from the School of Civil and Environmental Engineering in June 1995. He was also nominated twice for the George F. Sowers Distinguished Student Award by the Geosystems Engineering Department.